https://doi.org/10.15388/vu.thesis.110
https://orcid.org/0000-0001-5677-6631

VILNIUS UNIVERSITY
CENTRE FOR PHYSICAL SCIENCES AND TECHNOLOGY

Audrius
DRABAVIČIUS

Formation of chalcogenide solar cell absorber layers using electrochemical deposition of precursors

DOCTORAL DISSERTATION

Natural sciences,
Chemistry (N 003)

VILNIUS 2020

This dissertation was written between 2015 and 2019 in Center for Physical Sciences and Technology.

Academic supervisor:
Habil. Dr. Remigijus Juškėnas (Center for Physical Sciences and Technology, Natural sciences, Chemistry – N 003).

This doctoral dissertation will be defended in a public/closed meeting of the Dissertation Defence Panel:
Chairman – **Prof. Habil. Dr. Albertas Malinauskas** (Center for Physical Sciences and Technology, Natural sciences, Chemistry – N 003).

Members:
Prof. Dr. Kęstutis Arlauskas (Vilnius University, Natural sciences, Physics N 002).
Prof. Dr. Henrikas Cesiulis (Vilnius University, Natural sciences, Chemistry N 003).
Dr. Jurga Juodkazytė (Center for Physical Sciences and Technology, Natural sciences, Chemistry – N 003).
Dr. Andrius Stanulis (Swansea university, Natural sciences, Chemistry – N 003).

The dissertation shall be defended at a public meeting of the Dissertation Defence Panel at 11 a.m./ on 27 November 2020 in meeting room E302 of the Center for Physical Sciences and Technology.
Address: Saulėtekio av. 3, Vilnius, Lithuania
Tel. +37052648884; e-mail: office@ftmc.lt

The text of this dissertation can be accessed at the libraries of Center for Physical Sciences and Technology and Vilnius University, as well as on the website of Vilnius University: www.vu.lt/lt/naujienos/ivykiu-kalendorius

https://doi.org/10.15388/vu.thesis.110
https://orcid.org/0000-0001-5677-6631

VILNIAUS UNIVERSITETAS
FIZINIŲ IR TECHNOLOGIJOS MOKSLŲ CENTRAS

Audrius
DRABAVIČIUS

Chalkogenidinių saulės celių absorberio sluoksnių formavimas naudojant elektrocheminį pradinių medžiagų nusodinimą

DAKTARO DISERTACIJA

Gamtos mokslai,
Chemija (N 003)

VILNIUS 2020

Disertacija rengta 2015 – 2019 metais Fizinių ir technologijos mokslų centre.

Mokslinis vadovas:
Habil. dr. Remigijus Juškėnas (Fizinių ir technologijos mokslų centras, gamtos mokslai, chemija N 003).

Gynimo taryba:
Pirmininkas – Prof. habil. dr. Albertas Malinauskas (Fizinių ir technologijos mokslų centras, gamtos mokslai, chemija N 003).
Prof. dr. Kęstutis Arlauskas (Vilniaus universitetas, gamtos mokslai, fizika N 002).
Prof. dr. Henrikas Cesiulis (Vilniaus universitetas, gamtos mokslai, chemija N 003).
Dr. Jurga Juodkazytė (Fizinių ir technologijos mokslų centras, gamtos mokslai, chemija N 003).
Dr. Andrius Stanulis (Swansea universitetas, gamtos mokslai, chemija N 003).

Disertacija ginama viešame Gynimo tarybos posėdyje 2020 m. Lapkričio mėn. 27 d. 11 val. Fizinių ir technologijos mokslų centro posėdžių salėje E302. Adresas: Saulėtekio al. 3, Vilnius, Lietuva tel. +37052648884; el. paštas: office@ftmc.lt.

Disertaciją galima peržiūrėti Fizinių ir technologijos mokslų centro ir Vilniaus universiteto bibliotekose ir VU interneto svetainėje adresu: https://www.vu.lt/naujienos/ivykiu-kalendorius

ABBREVIATIONS

CE	Counter electrode
CIGS	$Cu(In, Ga)Se_2$
CV	Cyclic voltammetry
CZTS	Cu_2ZnSnS_4
CZTSe	$Cu_2ZnSnSe_4$
DC	Direct current
E	Potential
EDX	Energy dispersive x-ray spectroscopy
E_g	Band Gap
FF	Fill factor
FIB	Focused ion beam
FWHM	Full width at half maximum
HR-TEM	High-resolution transmission electron microscopy
ICP-OES	Inductively coupled plasma - optical emission spectroscopy
ITO	Indium tin oxide
J	Current density
j_{ph}	Photocurrent
J_{SC}	Short-circuit current density
MSA	Methane sulfonic acid
PCE	Power conversion efficiency
RE	Reference electrode
SEM	Scanning electron microscopy
SLG	Soda-lime glass
SLME	Spectroscopic limited maximum efficiency
TCO	Transparent – conducting oxide
TEM	Transmission electron microscopy
TFSC	Thin-film solar cell
V_{OC}	Open-circuic voltage
WE	Working electrode
XRD	X-ray diffraction

Table of contents

1. INTRODUCTION

1.1. Solar energy

The Sun – free, most abundant, and at the same time the most underused source of energy in the world as it generates an output of power equal to 120 000 Terawatts on the earth's surface regularly. Despite the vast amounts of free energy generated by the sun, solar energy harvesting is not competing with carbon-based sources of energy from oil, coal, or natural gas. Only 0.6 % of the Worlds energy is produced by using solar energy (Fig. 1).

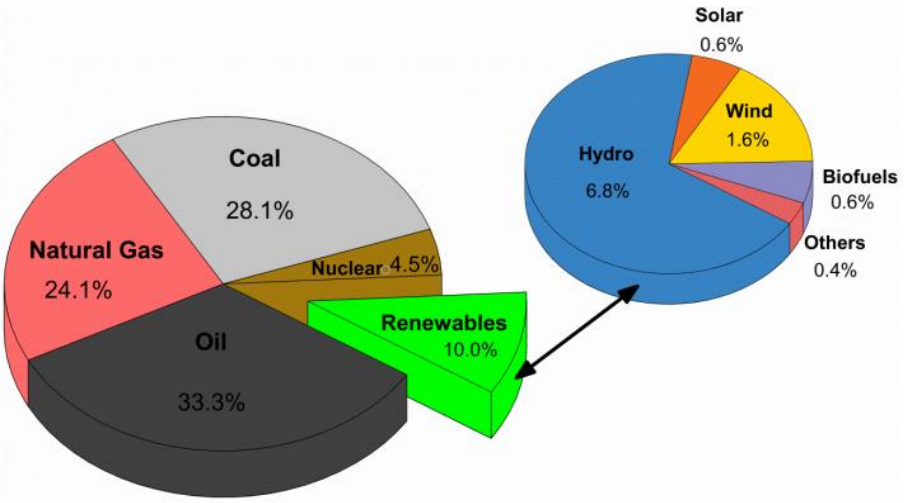

Figure 1. World energy consumption. BP statistical review of world energy [1].

The obvious question is – why the solar panels are not one of the primary sources of energy in the world? Several requirements need to be fulfilled for the technology to be attractive for the industry – non-toxic materials and waste (after synthesis), usage of only abundant materials, and the last and most important, it has to be cheap. Leading commercial technologies will be reviewed in the next paragraphs.

1.2. Crystalline Silicon solar cells

Silicon solar cells are the most common ones in the market. Around 80 % of all the solar cells manufactured in the world are silicon-based since the technology is the oldest (they are also called “the first generation”) and most developed. However, silicon is an indirect semiconductor, so in order to absorb all of the light from the sun, layers have to be at least 200 μm thick.

Also, the silicon required for the layers has to be very pure, thus, making the solar panel expensive. Crystalline silicon solar technology is around for 40 years now and has a record efficiency of 25 % PCE, but it is still not making any significant impact on global energy production.

1.3. Amorphous silicon solar cells

Amorphous silicon is a semiconductor made from non-crystalline silicon. The silicon chemical bond is still intact despite having no lattice structure. The elimination of crystalline structure changes the characteristics of light absorption, so the thinner layer is sufficient for the solar device. This type of solar cell is based on p-i-n structure, instead of p-n. The p-i-n structure is made up of very thin p-type and n-type layers with a thicker intrinsic layer for the light absorption. The junctions in this type of structure can be stacked to improve efficiency. However, even when the technology requires ~100 times less silicon than the crystalline silicon technology, the creation of a multilayered stacked structure increases the production costs drastically. Also, the amorphous silicon solar cells are not that stable. They tend to lose up to 20 % of the initial efficiency after a more extended period of usage.

1.4. Thin film solar cells

Thin film solar cells (TFSC) or second generation cells were developed to decrease the material quantity required for the manufacturing; thus, the cost of production. The key to lower the quantity of the materials needed was to find a compound with a high value of the absorption coefficient. The TFSC also does not require a monocrystalline layer and can be manufactured using less pure materials than for crystalline silicon. However, a downside of the TFSC is lesser efficiency than crystalline silicon SC, making it less attractive for industrial scale manufacturing. The only TFSC technologies that are manufactured on a large scale are cadmium telluride (CdTe) and copper indium gallium selenide (CIGS). These technologies have a drawback related to the costs of the raw materials. Figure 2 shows the relative abundance in the earth`s crust and the price of the materials used in these TFSC. Indium and gallium (used in the manufacturing of CIGS) are not that rare (0.9 ppm and 30 ppm, respectively), but their prices are very high (700000 $/ton and 800000 $/ton). In comparison, tellurium is not only expensive (400000 $/ton) also is quite a rare element (only 10^{-3} ppm). The low abundance and the prices of the raw materials make these two technologies not enough competition in the energy harvesting market.

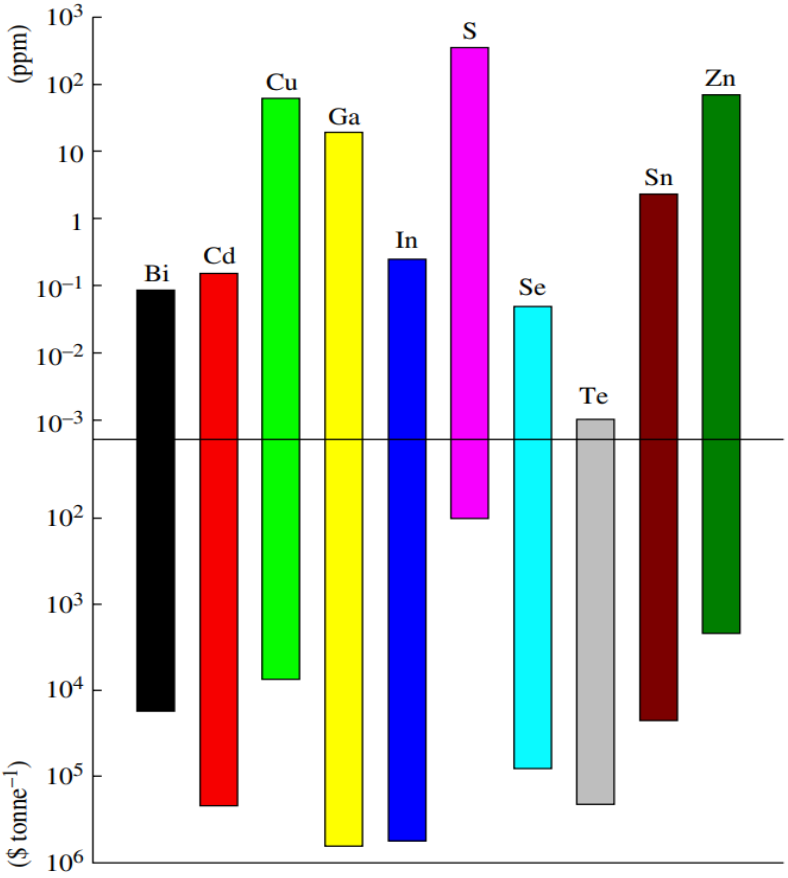

Figure 2. Bulk cost (bottom) and the abundance (top) of the elements used for the manufacturing of TFSC [1].

1.5. CZTS solar cells

For solar energy to compete in the global production of energy, the new compound had to be found. Around a decade ago, semiconductor material $Cu_2ZnSnS(Se)_4$ (CZTS(Se)) also known as kesterite draw attention as a promising compound for use in TFSC. The theoretical efficiency and light absorption were considered perfect for a solar device. Also, the elements needed for CZTS(Se) fabrication are relatively cheap, abundant, and non-toxic. The most expensive and least abundant (fig. 2) metal needed for the fabrication is Sn (4 ppm, 30000 $/ton). The price is still very low when compared to the elements needed for CIGS. Materials used in CZTS(Se) manufacturing are also efficiently mined, no shortage is foreseen in the near future, unlike the Cd and Te for CdTe solar devices.

Despite the theoretical compatibility for solar devices, CZTS(Se) absorbers are not quite there yet to compete with other technologies. The record efficiency is suffering a stagnation (fig 3). However, the technology is still considered the most promising and realistic option for the solar cells based on the inorganic compounds that do not contain any toxic and low availability (or high cost) materials. The main problem of the CZTS(Se) solar cells' low efficiency is the open circuit voltage, V_{OC} deficit. Various strategies are being developed to address the issue. The most common suggestion is the doping of kesterite. To increase the efficiency of kesterite TFSC, better detection, and understanding of the secondary phases and defects are necessary.

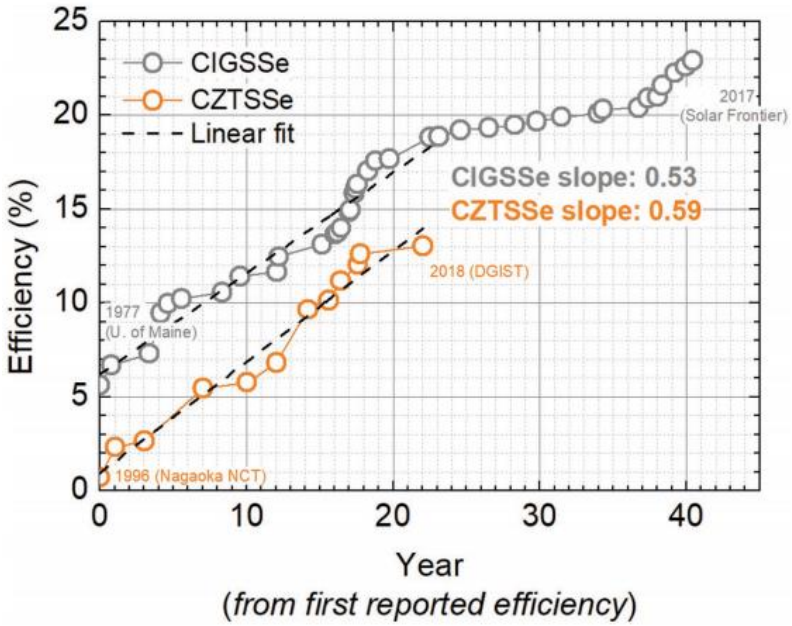

Figure 3. Evolution of the kesterite (bottom) and chalcopyrite (top) efficiency from the first reported solar cell. 0 year is 1977 for chalcopyrite and 1996 for the kesterite [2].

The relatively cheap materials need to be combined with a relatively cheap manufacturing method to compete in the energy production market. One of the cheapest production methods is the electrochemical deposition of the Cu-Zn-Sn (CZT) precursor layer with subsequent sulphurization/selenization at high temperature. Point defects were the least studied in CZTS layers formed by electrochemical deposition. Perhaps only two works attempted to use XRD with Cu $K_{\alpha 1}$ radiation for the study of point defects overall.

1.6. Major goal

Fabricate the kesterite layers using electrochemically deposited Cu-Sn-Zn precursors and investigate phase composition, surface morphology, and photoelectrohemical,properties of synthesized kesterite layers.

1.7. Objectives

* To fabricate high purity and continuous Cu-Zn-Sn precursor layer on SLG/Mo substrate using electrochemical deposition.
* To study and select the proper annealing and sulfurization/selenization conditions.
* To study the crystal structure, phase composition, surface morphology, and cross-sections using XRD, Raman spectroscopy, SEM, and SEM-FIB methods.
* To evaluate the point defects structure of kesterite using XRD, Raman spectroscopy, and photoluminescence spectroscopy methods.
* To investigate the relation between CZTS layers photoelectrochemical response and the point defects structure of kesterite.

1.8. Scientific novelty

* The modified electrolyte solution developed in our work yielded far more compact and smooth Cu-Sn precursor layers of higher purity in a significantly shorter time compared to other researchers which used similar conditions of the synthesis. The electrodeposition of Cu-Sn alloy for precursor layers proceeds with ~90 % current efficiency, which is around 20 % higher than in any of the electrolytes used by other researchers.
* The Raman spectra band at 77 cm^{-1} has been shown to be used as a marker of the monoclinic Cu_2SnSe_3 structure.
* For the first time, the kesterite manufactured by electrochemical deposition was investigated using XRD with Cu $K_{\alpha 1}$ radiation combined with Raman spectroscopy, PEC, and photoluminescence, for point defects analysis.
* The off-stoichiometric kesterite $Cu_{2.078}Zn_{0.909}Sn_{1.022}S_{4.000}$ is always formed despite different Zn/Sn ratios under conditions used in the current work.
* The XRD methods using Cu $K_{\alpha 1}$ radiation gives more plausible information both on the kesterite stoichiometry and the point defects than Raman spectroscopy.

1.9. Statements of defence

⁕ The electrodeposited Cu-Sn alloy and Zn on top yields more uniform and homogenous layers when sulfurized than those electrodeposited layer by layer (Cu/Sn/Cu/Zn).
⁕ Selenization of the Cu-Sn alloy at the temperature under 500 °C yields the cubic Cu_2SnSe_3, increasing temperature to 550 °C or more monoclinic Cu_2SnSe_3 is formed.
⁕ Post annealing of the Cu_2SnSe_3 films in 200 °C increases the photocurrent generated by the absorber layer.
⁕ The kesterite with Zn/Sn ratio of ~ 1.0 has a higher photocurrent density and less defective crystalline structure than Zn-rich or Zn-poor one.
⁕ The XRD method using Cu $K_{\alpha 1}$ radiation gives more reliant information for both kesterite stoichiometry and point defects than Raman spectroscopy, for kesterite absorber layer containing secondary phases.

1.10. Contribution of the author

The author participated in the fabrication of all the precursor films presented in the dissertation. Designed and engineered the unique flow cell that was tested in this work. Also, took part while choosing parameters of the annealing and selenization/sulfurization. Took part in the XRD and microscopy measurements. Furthermore, he was a part of the team analyzing the XRD, SEM, TEM, EDX, Raman spectroscopy, PEC, PL experimental data, designing the graphical illustration, and preparing the scientific publications. Additionally, obtained results were published by international journals and presented in the conferences, and, of course, the author wrote this dissertation.

1.11. Scientific publications

The main results of the doctoral thesis were published in 2 (Q1) scientific publications.

1. Juškėnas, R., Drabavičius, A., et al., Structural and photoelectrochemical characterization of Cu2SnSe3 thin films fabricated by electrochemical co-deposition and selenization. Journal of Alloys and Compounds, 2018. 767: p. 345-352. DOI: 10.1016/j.jallcom.2020.153853.
2. Drabavičius, A., Juškėnas, R., et al., Photoelectrochemical, Raman spectroscopy, XRD and photoluminescence study of disorder in electrochemically deposited kesterite thin film. Journal of Alloys and

Compounds, 2020. 824: p. 153853. DOI: 10.1016/j.jallcom.2018.06.276.

Other publications:

1. Jablonskiene, J., et al., *Synthesis, characterization and properties of the graphene supported platinum-cobalt nanocatalysts.* Chemija, 2015. 26: p. 159-164.
2. Semasko, M., et al., *Evaluation of Activity of Platinum-Ruthenium-Cobalt/Graphene Catalysts towards Methanol Oxidation.* ECS Transactions, 2015. 68(3): p. 55-62.
3. Raudonyte-Svirbutaviciene, E., et al., *Photochemical synthesis of CeO2 nanoscale particles using sodium azide as a photoactive material: effects of the annealing temperature and polyvinylpyrrolidone addition.* RSC Advances, 2016. 6(108): p. 107065-107074.
4. Ramanavičius, S., et al., *Shell-dependent antimicrobial efficiency of cobalt ferrite nanoparticles.* Nano-Structures & Nano-Objects, 2018. 15: p. 40-47.
5. Pushkarev, A.P., et al., *A Few-Minute Synthesis of CsPbBr3 Nanolasers with a High Quality Factor by Spraying at Ambient Conditions.* ACS Applied Materials & Interfaces, 2019. 11(1): p. 1040-1048.
6. Jablonskiene, J., et al., *Surfactant-assisted microwave synthesis of carbon supported MnO2 nanocomposites and their application for electrochemical supercapacitors.* Chemija, 2020. 31.
7. R. Stagniūnaitė, V. Kepenienė, Z. Sukackienė, A. Balčiūnaitė, G. Niaura, A. Drabavičius, M. Andrulevičius, I. Kruusenberg, K. Kaare, A. Volperts, G. Dobele, A. Zhurinsh, L. Tamašauskaitė-Tamašiūnaitė, E. Norkus, *N-doped carbon material modified with cobalt nanoparticles as catalyst for oxygen reduction*. Chemija, Vol 30 No 2 (2019).
8. Klimkevicius, V., et al., *Effect of Cationic Brush-Type Copolymers on the Colloidal Stability of GdPO4 Particles with Different Morphologies in Biological Aqueous Media.* Langmuir, 2020. 36(26): p. 7533-7544.

1.12. Conferences

C1. Drabavičius, A., Juškėnas, R., et al., *CulnSe2 absorber layer formation using different electrochemical approaches.* 19-th international conference-school "Advanced materials and technologies": 27-31 August, 2017, Palanga, Lithuania. (poster)
C2. Drabavičius, A., Juškėnas, R., et al., *Kesterite precursor film formation using electrochemical flow cell.* FizTech2017, Vilnius, Lithuania, 2017, (oral presentation).
C3. Drabavičius, A., Juškėnas, R., et al., *CuSnZn electrochemical deposition with further sulphurization for CZTS solar cells*. 20-th international conference-school "Advanced materials and technologies": 27-31 August, 2018, Palanga, Lithuania.
C4. Drabavičius, A., Juškėnas, R., et al., *Optimization of precursor layers for fabrication of kesterite solar cell absorber film.* FizTech2018, Vilnius, Lithuania, 2018, (oral presentation).

2. LITERATURE REVIEW

2.1. Molybdenum back contact

Molybdenum works as a back contact for kesterite solar cells. Molybdenum has to be well adhered to the glass because the electrodeposition of metals at a negative reduction potential can produce hydrogen gas, which occur at the working electrode and delaminate metal coating from the glass. Usually, Mo films are formed using the magnetron sputtering method [133, 134]. Layer characteristics mainly depend on the Ar gas pressure used during sputtering. It was found that the Mo layer deposited using constant pressure has a disadvantage: a well adhered layer has a higher resistance, and a more conductive layer has poor adhesion to glass. The solution was found sputtering two or even three layers of molybdenum on glass, the first one being the best adherent to glass [134] surface and second, having better conduction [133].

2.2. CIG(S,Se) absorber layers

A semiconductor suitable as an absorber material for a thin film solar cell has to meet criteria such as band gap between 1 and 1.5 eV, high optical absorption (at least 10^4 cm^{-1}) in the wavelength region of 350-1000 nm, high quantum yield for carriers, low recombination velocity, and high diffusion

length [3]. The second aspect of interest is the price, materials for the semiconductor absorber layer have to be widely available, preferably synthesized by a low-cost production technique. Meeting all of these criteria is crucial for large scale production.

CZTS(Se) as a solar cell material originally developed from CIGS(Se) chalcopyrite, replacing In and Ga with cheaper and more earth abundant Zinc and Tin. Since CIGS(Se) played a significant role in the development of kesterite absorber, a brief review is presented in this paragraph. CIGS(Se) technology is one of the most developed in the thin film solar cell field.

Postdeposition treatment of CIGS(Se) thin film with heavy alkalis (KF, RbF, CsF) was found to enhance Cu-depletion at the absorber surface combined with some passivation methods, and Ga amount enhancement [4] helped to achieve record power conversion efficiency (PCE) of 22.6 % [5]. Such high efficiency of a polycrystalline thin film with p-n hetero junction shows that this technology can neck-and-neck compete with other photovoltaic technologies.

CIGS(Se) semiconductor band gap varies from 1.05 eV for pure $CuInSe_2$ up to 1.65 eV for $CuGaSe_2$ (band gap can be adjusted by changing the ratio of In and Ga), absorption coefficient (α) of visible light spectrum for CIGS(Se) is greater than 10^4 cm^{-1}. These characteristics show that CIGS(Se) is very well suited for photovoltaic devices.

Fig. 4. shows a cross-section view of CIGS(Se) solar cell. The device consists of I) substrate and back contact; II) CIGS(Se) absorber; III) buffer and window layers.

I) The most commonly used substrate for thin film solar cells is soda-lime glass. Molybdenum coating on substrates is used as a back contact for solar cells. Some studies as an alternative used lightweight, flexible materials such as metal foils or polymers [6].

II) CIGS(Se) absorber layer formation can be divided into two major approaches: a) co-evaporation of all elements; b) deposition of metals/alloy precursor with subsequent sulfurization or selenization.

III) Usually, 50-60 nm thick CdS layer is used as a buffer. For several reasons, it is a naturally n-type semiconductor with a wide band gap of 2.4 eV, forms II-type heterojunction with CIGS(Se) – excellent electronical compatibility. CdS layer is formed using chemical bath deposition.

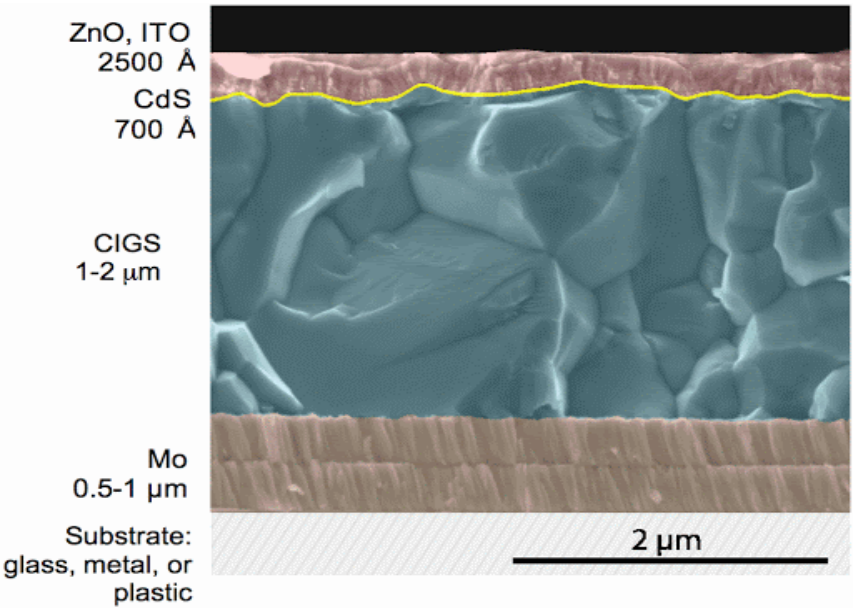

Figure 4. Coloured SEM cross-section image of standard CIGS solar cell structure [7].

The window layer for solar cell must be both transparent and conductive. The best option, considering these requirements, are transparent-conductive oxides (TCO). Commonly used are indium - tin oxide (ITO) and Al-doped zinc oxide (AZO). Usually, the TCO layer is formed using magnetron sputtering. Before sputtering, TCO, usually a thin protective layer of ZnO is formed to increase resistivity (prevent the solar cell from short-circuiting) and to protect the CdS buffer layer from damage caused by TCO sputtering.

2.3. Cu2ZnSnS4 and Cu2ZnSnSe4 development for solar cell application

Cu_2ZnSnS_4 first synthesis took place in Swiss and was performed by R. Nitsche, who was developing a variety of chalcogenides ($A_2^{I}B^{II}C^{IV}X_4$) using iodine vapor transport [8].

Due to the high price and low abundance of In and Ga for CIGS(Se) and high toxicity of Cd for CdTe absorbers, scientists were on a hunt for new semiconductor materials for thin film solar cell application. This led to the rediscovery of the kesterite. Nakazawa and Ito (Japan) synthesized Cu_2CdSnS_4 and Cu_2ZnSnS_4 using atomic beam sputtering. Optical and

physical properties showed that CZTS fits perfectly for thin film PV technology. They also developed a functioning solar cell, forming a heterojunction with cadmium tin oxide [9].

The p-type semiconductor CZTS(Se) has a direct band gap of 1.5 eV and 1.0 eV for Cu_2ZnSnS_4 and $Cu_2ZnSnSe_4$, respectively. Furthermore, in theory, it meets all of the optical and electronic parameters for high efficiency absorber. Since CZTS(Se) derived from CIGS(Se), similar band gap adjustments can be made by varying S and Se ratio. It is also compatible with the CdS buffer layer and ZnO window layer for solar cells, widely studied for CIGS(Se).

Katagiri suggested modern CZTS solar cells with structure SLG/Mo/CZTS/CdS/ZnO/TCO first time in 1997. CZTS was produced stacking Cu/Sn/Zn layers using electron beam deposition with later sulphurization in N_2+H_2S (5%) atmosphere. The developed solar cell produced PCE of 0.66 % [10] and is acknowledged as the starting point of the development rush of thin film CZTS solar cells. The main features that made CZTS material attractive for solar cell application is give in the Figure 5.

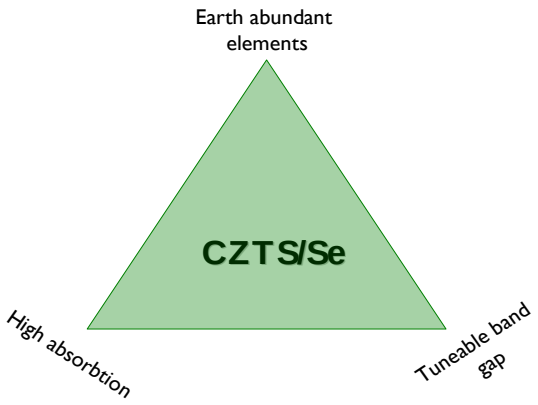

Figure 5. Main features that make CZTS(Se) very attractive for solar cell applications.

Since the first working cell was produced, lots of scientific groups started working towards the increase of PCE since CZTS theoretically can reach efficiency over 32 % according to the Shockley-Queisser limit. This most

universally used PV cell efficiency predictor depends only on the materials band gap, making it a very unreliable method. Photovoltaic device efficiency (η) is more complex: thermodynamics, defect structure, and optical characteristics, in addition to element abundance, cost, fabrication complexity, and toxicity, should be considered as a factor for semiconductor. Method called "Spectroscopic limited maximum efficiency" (SLME) was offered (fig. 6). The SLME captures the leading physics of absorption, emission, and recombination characteristics, resolving a spread of different efficiencies for materials having the same band gap [11].

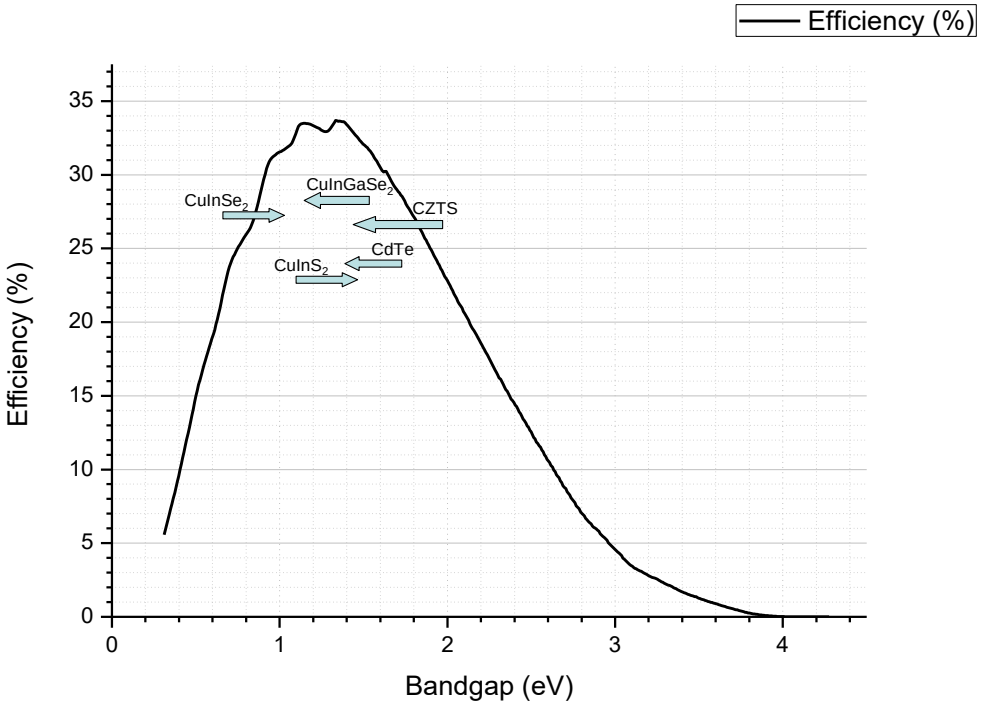

Figure 6. The most common types of thin films solar cells SLME versus Shockley-Queisser (black line) limit [12, 13].

2.4. Fundamental properties

2.4.1. Formation of kesterite material

For the past few years a tremendous amount of effort was put towards explaining the structure of the CZTS(Se) compound. Firstly, it was proven that kesterite compound has lower formation energy than the mono-crystalline $Cu_2ZnSnS(Se)_4$ stannite structure in the I_2-II-IV-VI_4 group. Therefore kesterite is a more stable compound[14]. Copper and zinc ions are in alternate positions of crystallographic planes 2a and 4d in the of the tetragonal lattice with an equal chance to take alternate statistically occupied positions [15]. Because Cu and Zn ions have a very similar ionic radius, antisite defects of Cu_{zn} and Zn_{Cu} occur both in kesterite and stannite compound. Due to the relatively high melting point of these elements, CZTS compound formation temperature is relatively high. Kesterite thin film is most commonly formed using two-step methods. First, Cu-Zn-Sn metal precursor is formed using one of the metal deposition methods. Then precursor is chalcogenized at a temperature of 500-600 °C in a sulfur or selenium atmosphere. Lower temperatures were found to be insufficient for a quality solid-state reaction. To prevent tin loss as the temperature rises, since Sn has the lowest melting point of used elements, chemical equilibrium can be adjusted by introducing SnS_2 or $SnSe_2$ to the chalcogenization treatment [16].

At the equilibrium state, the stoichiometric CZTS has a standard crystal lattice parameters: a = 0.5435 nm, c = 1.0843 nm. Element ratios can vary the lattice constant. The lattice constants of selenide are greater than those of sulfide in kesterite, shown in Table 1.

To explain the PV aspects of the CZTS semiconductor, more structural, physical, and chemical properties of CZTS kesterite are compared with CIGS (the leading thin-film solar cell semiconductor material) in Table 1. It is established that kesterite material possesses the potential to compete with CIGS; since, in theory, the majority of properties are very similar. CZTS even has a slightly higher concentration of the charge carriers and higher current density. The main factor why CIGS has a high efficiency is the remarkably long charge carriers lifetime (250 ns), while CZTS charge carriers lifetime is only 2.5-15 ns. Very high recombination rate is another major issue for CZTS. Typically, synthesis of pure CZTS is a challenging task; secondary phases occur during synthesis. Although detailed characterization of CZTS phase purity is challenging due to structural similarities of secondary phases, extensive research is ongoing.

Table 1. Properties of chalcogenide (CZTS, CZTSe, CZT(S,Se), CIGS, CIGSe) materials.

Properties	CZTS	CZTSe	CZT(S,Se)	CIGS	CIGSe	Ref.
Lattice constants (a,c) Å	a=5.427 c=10.820	a=5.40 c=10.846	a=5.40 c=10.846	a=5.6-5.8 c=11.0-11.5	a=5.6-5.8 c=11.0-11.5	[17, 18]
Space group	*I*4/I42m	*I*4/I42m	*I*4/I42m	*I*42d	*I*42d	
Crystal structure	Tetragonal	Tetragonal	Tetragonal	Tetragonal	Tetragonal	[19, 20]
Density (g/cm^3)	4.56	4.56	4.56	5.7	5.7	[19]
Band gap (eV)	1.5	1.0	1.1 - 1.5	1.0 – 1.7	1.0 – 1.7	[20]
Crystal energy (meV/atom)	2.86	2.86	2.86	-	-	[21]
Absorbtion coeff. (cm^{-1})	10^4	$10^4 – 10^5$	$10^4 – 10^5$	$10^4 – 10^5$	$10^4 – 10^5$	[22]
Carrier concentration (cm^{-1})	$10^{15} – 10^{20}$	$10^{15} – 10^{20}$	$10^{15} – 10^{20}$	$10^{17} – 10^{18}$	$10^{17} – 10^{18}$	[23]
Carriers lifetime (ns)	15	15	15	250	250	[24]
Melting point (°C)	990	990	990	990-1070	990-1070	[25, 26]
Record efficiency (%)	8.4	10.1	12.6	22.6		[5, 27-29]

2.4.2. Kesterite-specific secondary phases

As mentioned in the previous chapter, pure kesterite is very difficult to synthesize. In addition to quaternary compound (I_2-II-IV-VI_4), several ternary and binary phases can form Cu_2SnS_3, Cu_4SnS_4, and Cu_2S, CuS, SnS, SnS_2, ZnS. These secondary phases affect the physical properties of the absorber layer; their properties are described in Table 2.

Table 2. Properties of the CZTS and kesterite-specific secondary phases.

Properties	**CZTS**	**Cu_2SnS_3**	**Cu_2S**	**CuS**	**SnS_2**	**ZnS**
Structural properties	Kesterite type *I4*	Cubic and Tetragonal	Chalcocite	Hexagonal	Rhombohedral	Sphalerite and Wurtzite *I43m*
Electrical properties	P-type semiconductor	p-type semiconductor	Highly defective, metal like	P-type semiconductor	n-type semiconductor	Insulator
Effect on solar cell	Absorbing material	Affect carrier collection at the electrode	Short circuits solar cell		Forms barrier for carrier collection	Photocurrent reduce
Removal possibility		KCN etching	KCN etching	KCN etching	KCN etching	HCl etching
Band Gap (eV)	1,4 - 1,5	0,98-1,35	1,21	1,55	2,2	3,54-3,68

Phase equilibrium of the quasi-ternary compound system Cu_2S-ZnS-SnS_2 was investigated by Olekseyuk et al. [30]. The analysis led to a conclusion, even if we can adjust the amount of every element in the system, single-phase CZTS only exists in a narrow zone of elemental ratios. Even tiny alterations from the stoichiometry will result in the formation of secondary phases during synthesis. Scragg et al.[31] came up with a simpler phase diagram, based on the work of Olekseyuk, and assumed that the sulfur amount in the synthesized film is dependant on the phases created. The Diagram of the ternary phase for the Cu-Zn-Sn system at 400 ^oC is shown in Figure 7. Cu/(Zn+Sn) and Zn/Sn metal ratios are used to show the composition of CZTS films. Using theoretical calculations from the diagram, a series of experiments were carried out, confirming that stable CZTS has a very narrow window of elemental composition[32]. Pure phase CZTS can be obtained only with Cu/(Zn+Sn) = 0,92-0,95 and Zn/Sn = 1.0-1.03 metal ratios[33, 34].

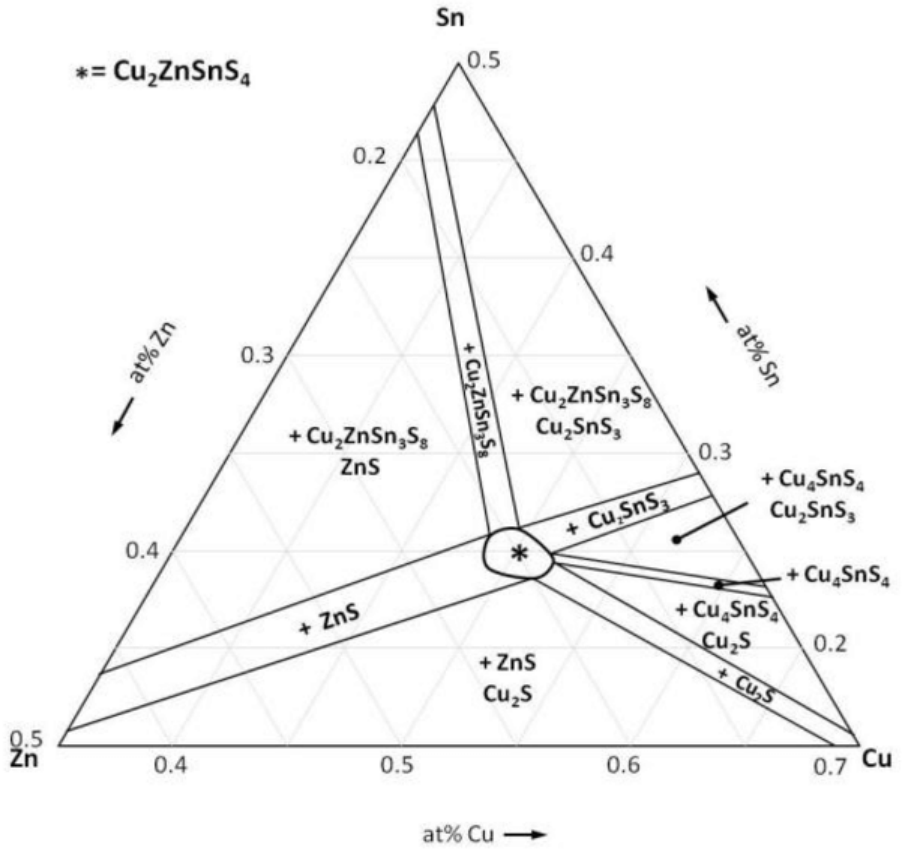

Figure 7. Phase diagram of the Cu-Zn-Sn system, predicting secondary phases at a temperature of 400 °C [32].

The optimal Zn-rich/Cu-poor element ratio for the CZTS film makes the appearance of the ZnS phase inevitable. Lots of published papers with Cu-poor/Zn-rich composition reports detecting this phase [20]. Clusters of the ZnS phase in kesterite film build insulation regions because of the high band gap of 3,6 eV [35]. In addition, due to the high resistivity of ZnS, it does not affect the V_{OC} of the solar cell but increases the series resistance, also. If the ZnS cluster is located at the p-n junction, loss in the current collection is observed [36].

The copper sulfide phases Cu_2S and CuS occur in CZTS films synthesized with Cu-rich composition. Both phases have p-type nature (high amount of holes in the valence band) and show good metallic conductivity [37, 38]. Because of excellent conductivity, copper sulfides can shunt solar devices.

Tin sulfides (SnS and SnS_2) can be found mainly in Sn-rich kesterite films. SnS semiconductor is already used in optoelectronics and PV. It can have both

n and p-type conductivity[39] with band gap of 1,2-1,7 eV [40-42]. SnS_2 is an n-type semiconductor with band gap of 2,18-2,44 eV [20, 39]. A significant amount of the n-type semiconductor in the p-type kesterite layer reduces fill factor and can perform as a diode that interferes with carrier collection. Ternary Cu_2SnS_3 (CTS) phase can occur in kesterite film, with Zn-poor configuration. CTS is a p-type semiconductor with metallic characteristics [43, 44]. CTS is polymorphic; it can crystalize in cubic, monoclinic, or tetragonal crystal structure [20]. Cubic crystal structure forms at 775 ^oC temperature, so it cannot be found in kesterite films, which are synthesized at 500-580 ^oC. Optical bandgap of CTS vary between 0,93 and 1,35 eV depending on the structure[45]. Similar to copper sulfide, CTS can shunt the solar device due to its high conductivity. Also, the low bandgap can reduce open-circuit voltage.

The undesired ZnS phase can be removed, immersing the thin film in the HCl solution (10%, 75 ^oC) [46]. To remove binary copper phases, KCN solution etching is used.

2.4.3. Identification of secondary phases

The identification of secondary phases in kesterite films is a challenging task. The essential method for compound identification, in general, is X-Ray diffraction (XRD). However, it has some flaws when the compound consists of phases with crystal structure similarities. In kesterite materials, CZTS, CTS, and ZnS, the highest intensity diffraction peaks overlap because of similar lattice parameters and crystalline structure [47]. Copper and tin sulfides can be easily identified using the XRD method.

To identify all of the phases in kesterite film, the Raman spectroscopy method is applied in addition to XRD. Kesterite CZTS material displays two peaks at 288-289 cm^{-1} and 338-339 cm^{-1}. The broad peak can also be observed at 368-373 cm^{-1-} [48]. The main peak for cubic ZnS is at 352 cm^{-1} secondary peaks at 271 cm^{-1}[49]. For cubic CTS Raman shifts appear at 267 cm^{-1}, 303 cm^{-1} and 256 cm^{-1} [50], for monoclinic CTS – 290 cm^{-1} and 352 cm^{-1} [51]. CTS with tetragonal crystal structure shows peaks at 337 cm^{-1}, 352 cm^{-1}, 297 cm^{-1}, broad peak at 280 cm^{-1} and 290 cm^{-1}[50]. Most commonly, Raman spectra for CZTS is performed under green and blue wavelength excitations of 532, 488, and 514.5 nm (mostly used in Raman spectroscopy for any materials). Dimitrievska et al. [52] employed six different excitation wavelengths, for CZTS, from near IR to UV, overall 18 peaks were associated with the the CZTS phase.

ZnS phase main Raman band at 352 overlaps with CZTS 351 band that makes it hard to determine the ZnS phase existence in film. Separating CZTS and ZnS phases in kesterite from Raman scattering was reported as a difficult task using the visible region excitation wavelengths [53]. Success in distinguishing ZnS and CZTS phases was achieved by using a UV excitation wavelengths of 325nm [54].

Table 3. Raman band positions of kesterite and possible secondary phases.

Phase	**Raman bands**	**Ref.**
CZTS	287, 338, 351, 368	[48, 55]
Cu_2SnS_3 (cubic)	267, 303, 356	[20]
Cu_2SnS_3 (tetragonal)	297, 337, 352	[20]
Cu_2SnS_3 (monoclinic)	290, 352	[56]
Cu_2SnS_3 (orthorhombic)	318	[20]
ZnS	275, 352	[49]
Cu_2S	264, 475	[57]
SnS	163, 189, 220	[58]
SnS_2	215, 315	[58]
Sn_2S_3	52, 60, 307	[58]

2.4.4. Solar cell performance

A significant amount of groups around the globe is working on kesterites for a solar cell application. However, CZTS still lacks the efficiency to be considered as a viable thin-film absorber for commercial-scale fabrication. CZTS/CdS devices efficiency (PCE) depends on the fill factor (FF), current density (J_{SC}), and open-circuit voltage (V_{OC}) (Fig. 8).

CZTS(Se)/CdS device has the record efficiency (PCE) of 12,6%[27]. Such deficit from theoretically calculated solar cell efficiency has forced researchers to investigate the junction characteristics, recombination, and current collection mechanisms.

CZTS solar cell current collection, junction characteristics, and recombination mechanisms can be altered by varying metal ratios in the layer, changing substrate temperature, annealing and sulfurization temperatures and time, pH, and concentration of salt solutions, etc. The CZTS absorber has a direct band gap of 1.4 – 1.6 eV, radiative, and non-radiative recombination has a high absorption coefficient in visible light range. CZTS displays a broad peak at 1.3 eV in PL spectra [20]. Two peaks of PL related to the random

distribution of defects were detected by Grossberg et al. [59]. Photoluminescence peaks are shifted to lower energies because of the perturbation of band structure [60].

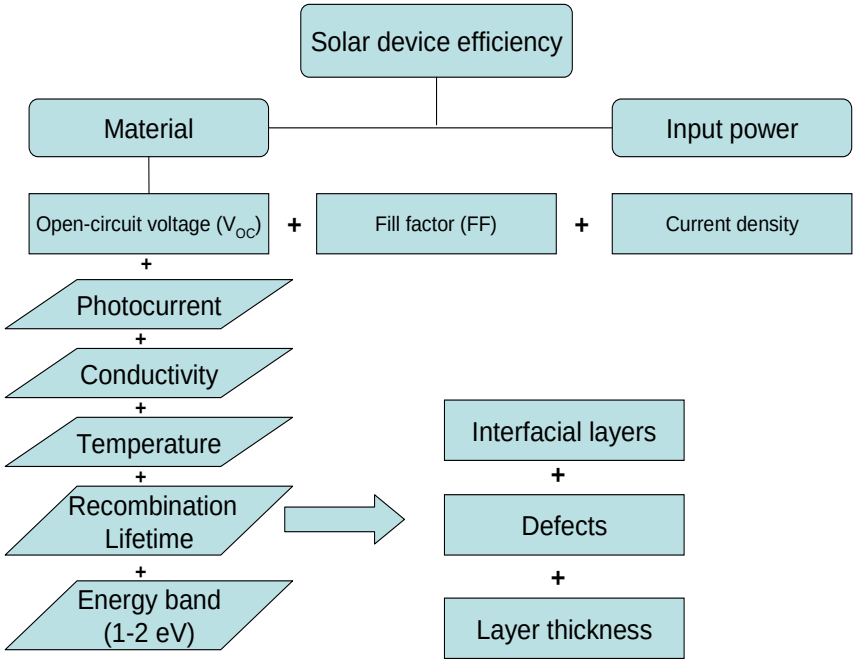

Figure 8. Parameters for solar device efficiency.

2.5. Defects in CZTS solar devices

By its nature, the CZTS compound is a p-type semiconductor because of the high concentration of copper vacancies (V_{Cu}) and Cu_{Zn} antisites, which both works as electron acceptors and is at ionized state at standard conditions. The antisite defect concentration relies mostly on Cu/(Zn+Sn) and Zn/Sn ratios used while synthesizing the film [61]. Defects that are near the band edge and have low enough energies to be ionized at standard conditions (shallow states). Separation energy is k_BT = 25 meV (when T is temperature constant 300K, k_B – Boltzmann constant). Shallow defects consist of localized electrons, which are weakly bound by Coulomb potential, only for a large volume of the crystal, that can ionize to the extended states of the crystal. Defects with charge carriers having ionization energies more than a couple of k_BT are more localized by the impurity potential and are called deep states [62]. Such

defects have a bigger impact on solar device efficiency since it is more likely that deep states will trap free charge carriers for a long time and act as recombination centers (when the charge carrier with opposite polarity is trapped before the first is emitted). Trap that is located closer to midgap is more likely to operate as a recombination center [63].

Defects in kesterite can also shape charge-neutral clusters that do not act as traps or recombination centers. E.g. defect complex with the lowest formation energy is the [Cu_{Zn}^{-} + Zn_{Cu}^{+}] [64-66]. The mentioned antisite defect complex has formation energy of 0.2 eV; it can be used to shift kesterite to stannite and vice-versa. The comprehensive influence of this defect on the optical and electronic properties is feeble, but the difference of stannite and kesterite bandgap might impact the overall effect on CZTS solar device performance.

Although some of the defect complexes are relatively harmless to solar device performance, other defects that come from off-stoichiometry are not so friendly. E.g., antisite complex [Zn_{Sn} + Sn_{Zn}] clusters lower the band gap of CZTS, which can cause a drop of V_{OC} and increase the chance of carrier trapping. While this defect cluster is one of the most damage causing, its formation energy is rather high, and concentration should be relatively low. Depositing excess amount of Sn in precursor films for kesterite to compensate SnS(Se) loss should be carefully considered.

Experimental results varying the stoichiometry of kesterite found that best device efficiencies are obtained when elemental ratio composition is Cu/(Zn+Sn) = 0.8 and Zn/Sn = 1 - 1.2. Theoretical defect formation energies and cluster concentrations support the experimental results. Defect clusters with lowest formation energy occurring due to non-stoichiometry are [V_{Cu}^{-} + Zn_{Cu}^{+}], [Zn_{Sn}^{2-} + $2Zn_{Cu}^{+}$] and [$2Cu_{Zn}^{-}$ + Sn_{Zn}^{2+}]. The last-mentioned defect cluster can cause a decrease in conduction band maximum, which can induce charge carrier trapping, the other two defect clusters have very little to no effect on conduction and valence bands maximum (CBM and VBM) [61]. So, the Cu-poor/Zn-rich composition leads to more benign off-stoichiometry induced defect complex formation.

2.6. Types of kesterite

Substitution of ions in copper-poor kesterites can be A-type in Cu-poor/Zn-rich compound when Cu is substituted with vacancy V_{Cu} and zinc substitute copper Zn_{Cu}, or B-type where Cu and Sn are subtituted with zinc ions forming Zn_{Cu} and Zn_{Sn} defects. Cation substitution in Cu-rich/Zn-poor compound can be C-type where copper and tin ions substitutes zinc, forming Cu_{Zn} and Sn_{Zn}

antisites, or D-type where copper substitutes zinc with additional copper interstitials forming Cu_{Zn} and Cu_i defects. Two additional types has been introduced by Valle-Rios et al. [67] E-type structure occurs in Cu-poor/Zn-poor/Sn-rich kesterite compound it is described by a general formula $Cu_{2-2w}Zn_{1-w}Sn_{1+w}S_4$ with $2V_{Cu}+Sn^{+4}{}_{Zn}$ or $Sn^{+4}{}_{Cu}+V_{Cu}+V_{Zn}$ defect complexes; F-type has Cu-rich/Zn-rich/Sn-poor composition and $Cu_{2(2-k)}Zn_{2-k}Sn_kS_4$ general formula, forming $Zn_{Sn} + 2Cu_i$ or $Cu_{Sn} + Cu_i + Zn_i$ defect complex.

2.7. Formation methods of kesterite layer

To obtain high-quality CZTS thin film, various deposition methods have been applied by several groups over the last decade, since kesterite caught such an enormous interest for solar cell application. The main challenge stands up till today – synthesizing homogenous, single-phase, large grain thin films with no cavities. Entirely, the method for synthesizing CZTS should be relatively cheap and fast.

Synthesis of CZTS can be categorized in to vacuum and non-vacuum depositions. It can be performed by the one-step process – when all elements (Cu, Zn, Sn, S(Se)) are deposited on a substrate at high temperatures, or a two-step process – when a metallic precursor (consisting of proper amounts of Cu, Zn, and Sn) are formed on the substrate, with the following annealing at high temperature in sulfur or selenium (or a mixture of both) atmosphere. Sulfide CZTS thin films are preferred because of sulfurs' lesser toxicity and price compared to selenium. Nevertheless, better efficiency (PCE) of solar devices was achieved by selenides or mixed (S, Se) kesterite thin-film solar cells.

In the two-step approach, precursors can be either formed by stacking metallic layers or co-depositing all of the elements (at the same time). Kesterite thin film properties such as grain size, band gap, stoichiometry, etc. were reported to rely on annealing temperature, deposition rates, and other synthesis related parameters [20, 68-70].

2.7.1. Vacuum methods

These methods require a high vacuum and, in some cases, high temperature for deposition of kesterites. Vacuum deposition methods (such as thermal evaporation, magnetron sputtering, pulsed laser deposition, etc.) grants a very high reproduction of films; it is also easy to manage ratios of elements deposited [71]. The most commonly used vacuum methods will be briefly reviewed in this paragraph.

Thermal evaporation. The Source of material is heated in a vacuum chamber, evaporated material then transfers onto a substrate. CIGS solar cells formed by using thermal evaporation showed very high efficiencies and filled factor [20]. Kesterite films can be formed either by using one-step evaporation [20] or two-step, evaporating precursor on a substrate, then annealing it at sulfur or selenium atmosphere [72, 73]. CZTS pure sulfide, synthesized using thermal evaporation, has reached 8.4% efficiency [29], and 11.6% for selenium based kesterite [74].

Magnetron sputtering. One of the most widely used methods to form thin films in general, no exception is CZTS films. Kesterite films usually are formed by a two-step approach. The first precursor is sputtered onto the substrate, following with annealing in sulfur or selenium atmosphere. The magnetron sputtering method can be performed either stacking metal layers, co-sputtering all of the metals, or sputtering precursor using the Cu-Zn-Sn-S alloy target. Stacking and co-sputtering can be performed by using separate targets [75, 76] or binary/ternary targets [77, 78]. Sequential layer stacking has an advantage. It is easier to control the composition of the precursor by depositing uniform layers of known thickness [79]. However, in co-sputtered precursor layers, elements are more mixed, which can prevent metals diffusion during annealing. A few study reports were showing the results of sputtering CZTS films from a quaternary target [80-82]. However, this approach proved to have some difficulties controlling the composition of elements [83]. Samples prepared by co-sputtering precursors hold records of 6.2% and 8.03% for CZTS and CZTS(Se) solar devices, respectively [84, 85].

Pulsed laser deposition (PLD). Vapor deposition technique for thin films. High power laser pulses are used to vaporize material from a target in a high vacuum—vaporized material deposits on the substrate. CZTS targets are prepared by a solid-state reaction from Cu_2S, ZnS, and SnS_2, a one-step technique [86, 87].

2.7.2. Non-vacuum deposition methods

These methods rely on much cheaper equipment than those of vacuum methods. Basically, all of the non-vacuum methods are solution-based. Adjusting stoichiometry can be easy for some of the solution-based methods by controlling the concentration of organometallic complex salts. Nevertheless, there are some drawbacks. For some of the solutions, it is necessary to use toxic substances and some of the solvents leave residue in the

films. In this chapter, standard non-vacuum methods for thin film formation will be discussed.

Ink-based methods. Ink – precursor metal salts solution. These techniques rely on solvent evaporation, leaving only precursor metals on the substrate, usually, a two-step method, requiring post-deposition annealing at high temperature in the sulfur/selenium atmosphere. A major drawback of ink-based methods is toxic solvents (e.g., hydrazine). Despite toxic materials used, CZTS devices formed by using these methods have shown very high efficiencies.

The first sol-gel synthesis of CZTS thin films dates back to the year 2007, performed by Tanaka et al. films had an almost stoichiometric composition of elements, with a direct band gap of 1.49 eV [89].

A group from IBM Research Center in 2010 synthesized the CZTS(Se) compound using the hydrazine slurry method. Best CZTS(Se) solar device of the series shown efficiency of 9.66% [94]. The same research group in the year 2012 twice improved the efficiency of the solar device, at first to 10.1% [95], then to 11.1% [96]. Finally, in 2014 they reached 12.6% efficiency (PCE) [27]. This record for efficiency stands to this day. Research showed that defects at the CZTS(Se)/CdS junction has a negative effect on the carrier lifetime, and so increasing the collection efficiency of carriers generated and diffusion length in the kesterite absorber.

Defects at the CZTS(Se)/CdS interface are the main reason for a V_{OC} deficit. A deeper understanding of the current collection, junction characteristics, and recombination mechanisms in kesterite devices are crucial to improving V_{OC} as well as the efficiency beyond 13%. However, this method has some issues, highly toxic solvents are used, and the reactivity of hydrazine, making this method very hard to industrialize. Diluting hydrazine with H_2O 1:1 makes this method possible for large-scale fabrication. CZTS(Se) devices formed using diluted hydrazine solution for precursors yield 8.1% efficiency [97].

Nanoparticle ink method. This method is based on depositing already synthesized CZTS nanoparticles from a suspension, onto the substrate, with later thermal treatments [98]. When a conventional ink-based method relies on very toxic hydrazine, nanoparticle deposition uses only common organic solvents for suspension used for deposition of the precursor layer [99, 100]. Also, this method is suitable for large-scale production. Suspensions can be used for large-area coating techniques like doctor blading or printing.

Since the first time CZTS nanocrystalline ink method was used to produce thin films, a number of studies tried to improve the quality of nanoparticles by investigating the synthesis route (changing organometallic salts, reaction times, temperatures, finding new ways to introduce sulfur into the system,

etc.) [20, 105]. All of these works were focused on nanocrystal CZTS growth. In 2012 Leidholm et al. from NREL reported a 9,85% kesterite solar device formed by using CZTS nanocrystal ink.

Spray pyrolysis. This method consists of spraying a solution, precursor metal salts (chlorides, acetates) dissolved in water (or, in some cases, other solvents) on a heated substrate. When solution droplets reach the heated substrate, high temperature initiates a pyrolytic reaction, forming the preferred compound [106]. In the year 1996, Nakayama and Ito were the first ones to use spray pyrolysis to form CZTS thin films. The films had a stannite structure with a band gap of 1,46 eV [107]. This technique was one of the first non-vacuum methods performed to produce kesterite thin film.

Chemical vapor deposition. In the year 2011, the first CZTS film was deposited using chemical vapor deposition (CVD). Ramasamy et al. prepared a solution made from diethyldithiocarbamate Cu and Zn and alkyl derivative of Sn (solvent toluene). The reduction of precursor elements to form the CZTS compound was found to enact in a narrow range of temperatures 280-300 ^{o}C. In other temperatures, ZnS, SnS, and Cu_xS phases occur. Nevertheless, the control over stoichiometry was very difficult. Films that were deposited at different substrate temperatures had different stoichiometry [109]. Record efficiency for CZTS films formed by using the CVD method is 6.03% with J_{SC}, V_{OC} and FF 16,5 mA/cm^2, 658 mV and 55.5% respectively [110].

Electrochemical deposition. Electrochemical deposition is a very appealing method for a couple of reasons - it is a low-cost method (no need for complicated high-vacuum equipment), which is easy to adapt for industrial-scale manufacturing [111]. This method was already successfully applied for other thin film PV device fabrication, the BP Appolo process for CdTe solar devices [112], and the CISEL project was developing CIGS solar cells, electrochemically deposited precursors were thermally treated to obtain high-quality thin films [113].

In the year 2008, the first CZTS synthesis using electrodeposition was carried out by Scragg et al. Mo-coated SLG was used as a substrate on which Cu, Sn, and Zn metal layers were deposited sequentially. They used copper chloride, sodium hydroxide, and sorbitol aqueous solution for Cu deposition, stannous chloride, sodium hydroxide, and sorbitol aqueous solution for Sn layer deposition, and zinc chloride aqueous solution buffered with Hydrion for Zn deposition [114, 115]. The precursor layer was then washed in deionized water and annealed at 550 ^{o}C in the sulfur vapor atmosphere for 2 hours. The solar cell developed from this CZTS layer showed V_{OC} = 295 mV, FF = 33%, J_{SC} = 8,7 mA/cm^2 and efficiency of 0,8% [111]. Due to the high series resistance and high shunt conductance, the solar cell had a very low

efficiency. In later work, they have studied the precursor composition effect on solar device performance. The study showed that the off-stoichiometric composition of precursor has to be used to achieve effective CZTS films, using layer-by-layer electrodeposition. Starting with a Cu/(Zn+Sn) ratio of as low as 0,7 may lead to high concentrations of secondary phases. The solution to this problem was introducing the co-electrodeposition of the constituents and optimizing the annealing process for single-phase kesterite growth. Large grain films were obtained, substituting the elemental sulfur vapor with H_2S gas when annealing [115]. In two years, by optimizing the deposition process, they increased the efficiency of the CZTS devices from 0,8% to 3,2%. Standard layer stacking Cu/Sn/Zn was substituted with Cu/Sn/Cu/Zn, rotating disc electrode was introduced for improving uniformity of layers, and finally, the KCN etching was used to dissolve the secondary Cu-rich phases from formed absorber layer. Kurihara et al. study of thin films deposited from unstirred electrochemical bath showed a latteral inhomogeneity in both film thickness and composition. This was caused by the difference in the ion flux to the surfaces of the electrodes at different points of the surface. The use of an RDE (rotating disc electrode) was suggested to control the ion flux to the surface deposition and increase in the uniformity of films both in thickness and in composition [116]. Electrochemical metal stacking of Cu/Sn/Zn layers with further sulfurization in nitrogen at temp. 300 – 600 ^oC were studied by Araki et al. Precursor films were deposited from metal acetate solutions. Back contact Mo was coated with a thin layer of Pd to increase adhesion. Device yielded 0,98% efficiency [117]. Later they changed the approach, using copper sulfate, zinc sulfate, and tin chloride salts instead of acetates. They co-electrodeposited Cu-Zn-Sn alloy and annealed the precursor in the N_2 atmosphere at 600 ^oC for two h. Kesterite films had a single-phase CZTS and were Zn-rich. The best device from this approach had an efficiency of 3,16% [118]. The crystallization of CZTS from co-electrodeposited Cu-Zn-Sn precursor films was studied by Schurr et al. Cu-poor, and Cu-rich precursor films were sulfurized and investigated by using angle-dispersive X-ray measurements. Two different reaction paths of Cu_2SnS_3 phase formation were found, dependent on the metal ratos in film. In both cases, CZTS kesterite growth was found to be the product of the solid-state reaction between Cu_2SnS_3 and ZnS, starting at no less than 570 ^oC. Some oxide impurities were found (Sn_2O and CuO) using the in-situ XRD method [119]. Ennaoui et al. [120] fabricated a CZTS device using a very similar procedure, Cu-Zn-Sn electroplated precursor was annealed in Ar + 5% H_2S atmosphere with a total 8 hours procedure, using very slow temperature ramping, and a maximum temperature of 550 ^oC. All of the samples were found to have Cu deficiency.

Still, KCN etching was performed to remove any unwanted Cu_xS phases. They found that films had strong mechanical adhesion, despite some voids found mainly at CZTS/Mo interface. Since films had a copper deficiency, ZnS phase was present, which contributed in reducing V_{OC} and FF values of solar cell. Best device had a 3,6% PCE [120].

Pawar et al. Have shown the possibility of preparing CZTS thin films using single-step electrodeposition of all the constituents. They used an aqueous solution containing copper, zinc, and tin sulfides and $Na_2S_2O_3$ for sulfur source. Films were electroplated at room temperature, using the stirring of the electrolyte. Films were annealed as-deposited, at temperatures 150-550 ^oC for 1h in an argon atmosphere. The best result in structure and band gap was obtained at 550 ^oC [121]. In the year 2012, Ahmed et al., using a three-step electrodeposition method, fabricated a CZTS device, with a record-breaking efficiency of 7,3% (record stands to this day for electrodeposited CZTS devices). Electrodeposited Cu/Sn/Zn or Cu/Zn/Sn sequential stacks were first annealed at a low temperature of 210-350 ^oC to facilitate phase separation and yield homogeneous (Cu, Zn) and (Cu, Sn) compounds. For the second annealing, temperatures were increased to 550-590 ^oC, and the sulfur vapor was introduced to process for 5-15min. A CZTS phase with high crystallinity was observed using X-ray diffraction. The record cell had a V_{OC}, J_{SC}, and FF of 567mV, 22mA/cm^2 and 58,1% respectively [122]

Table 4. Record efficiencies for kesterites achieved using different methods.

Type of kesterite	Parameters					Precursor		Annealing		Ref.
	E_g (eV)	V_{OC} (mV)	FF (%)	J_{SC} (mA/cm^2)	ŋ (%)	As deposited	Method	Atmosphere	T (°C)	
CZTS	**1.5**	**731**	**69.3**	**21.7**	**11.0**	**CuZnSnS**	**Co-sputtering**	**S+Sn**	**560**	**[123]**
	1.5	567	58.1	22.0	7.3	Cu/Zn/Sn	Electrodeposition	S	585	[122]
	1.5	746	62.0	19.1	8.8	CuZnSnS	Spin coating	S+Sn	560	[124]
	1.5	661	65.8	19.5	8.4	CuZnSnS	Co-evaporation	S	570	[29]
CZTSe	**1.0**	**423**	**67.3**	**40.6**	**11.6**	**CuZnSnSe**	**Co-evaporation**	**Se**	**590**	[125]
	1.04	463	66.3	36.0	11.0	Cu/Sn/Zn	Sputtering	Se	550	[126]
	1.03	443	68.0	38.1	11.4	Zn/Cu-Sn/Zn	Sputtering	Se	530	[127]
	1.06	400	66.2	35.2	9.3	CuZnSnS nanoink	Doctor blading	Se	550	[128]
	1.05	440	60.0	31.3	8.2	Cu/Sn/Zn	Electrodeposition	Se+Sn	550	[129]
CZTS(Se)	**1.13**	**466**	**69.8**	**38.9**	**12.6**	**CuZnSnSSe**	**Spin coating**	**-**	**500+**	[27]
	1.07	485	64.9	37.5	11.8	Zn/Sn/Cu	Sputtering	S+Se	520	[130]
	1.13	531	64.8	33.7	11.6	CuZnSnS	Spin coating	Se	540	[131]
	1.07	471	69.6	31.6	10.3	CuZnSnS	Doctor blading	Se	590	[132]

3. EXPERIMENTAL

In this chapter all of the experimental details of this work will be given. Firstly, the preparation of working electrode (back-contact of solar cell) molybdenum coated soda-lime glass will be reviewed. Secondly, electrochemical approaches of precursor fabrication and thermal treatment will be defined. Last part will be the description of the characterization methods.

3.1. Working electrode preparation

As a working electrode, molybdenum coated (~750 nm layer) soda-lime glass (ZSW, Germany) was used in this work. Molybdenum films tend to form a thin barrier layer of molybdenum oxide [135]. Which plays a major role in the electrodeposited layer adhesion to the electrode. Therefore, cleaning and preparation of the electrode are very important. Mo electrode was immersed in ethanol (99.5%) and cleaned using an ultrasonic bath for 5 minutes, then soaked in NH_4OH for 10 minutes, washed under a flow of distilled water, immersed in ethanol again for 1 minute, and dried under the flow of Ar gas (99.999%).

3.2. Electrochemical formation of precursor

Electrodeposition of precursor layers was performed galvanostaticaly for single elements and potentiostatically for the alloy. Gamry REF 600 potentiostat with a standard three-electrode system was used for the experiments (reference electrode - Ag/AgCl, 3M KCl, the counter electrode – polished Pt). As a working electrode, we used molybdenum coated soda-lime glass. All of the experiments were carried out at room temperature. For solution preparation, we used deionized water (18 MΩ).

Precursor films were deposited using two different routes:

1) Sequential electrodeposition of Cu/Sn/Cu/Zn metals with two different setups: using a unique 3D printed flow cell and a standard three-electrode setup with stirring.
2) Electrodeposition of Cu-Sn (bronze) alloy followed with the deposition of metallic Zn.

Many factors like pH of the electrochemical bath, salt and additives concentrations, temperature, electrical potential, or current density, determines the structure, morphology, and other properties of a precursor layer. It can be grown as a crystalline film or an amorphous layer. Crystal

growth mainly depends on overpotential. Films formed at a low overpotential consists of larger crystals than those formed at a high overpotential.

3.2.1. Sequential electrodeposition of Cu/Sn/Cu/Zn metals

The electrochemical deposition of metals was carried out galvanostaticaly. For the electrodeposition of the copper layer, we used a 0.075 M copper sulfate pentahydrate with 0.225 M sodium citrate solution. The natural pH level of the solution was used (not adjusted by any other substance) - ~5.5. The solution is non-toxic and does not require any surfactants. Copper complexes with citrate forms at a slightly acidic pH, which is obtained when salts are dissolved in distilled water [136]. Tin was electrodeposited from a solution containing 0.1 M $SnSO_4$, 1 M methanesulfonic acid (CH_3SO_3H), 0.6 ml/l triton X-100, and 1 g/l hydroquinone. The hydroquinone was used as an antioxidant agent for the solution (Sn tends to oxidize, forming an insoluble tin oxide). Triton X-100 was added to the solution as a surfactant to avoid the island growth. The methanesulfonic acid for tin electrodeposition was used instead of the tri-sodium citrate because the stability of the solution was found to be better. Tin in the solution containing MSA oxidizes slower, which means – the solution can be used for a longer period of time. The deposition of zinc on Cu/Sn/Cu layer stack was performed using an electrolyte solution containing 50 g/l of $ZnCl_2$, 200 g/l NH_4Cl, and 1 ml/l of Triton X-100. The same surface-active additive was used in the tin electrolyte solution.

Metals were deposited using two different setups: the flow cell and standard three-electrode electrochemical setup (stirred). The sequence of the metal deposition was Cu → Sn → Cu → Zn. An intermediate Cu layer was used in order to deposit a uniform, compact, continuous Zn layer since zinc is very difficult to deposit on the Sn surface. Also, a better distribution of the elements is achieved throughout the precursor film when metal layers are more mixed.

A unique 3D printed flow cell was adapted for layer-by-layer metal electrodeposition (Fig. 9). The same electrolytes solutions were used for the electrodeposition of metals both in conventional and flow cells (Table 5).

Table 5. Composition of solutions used for layer-by-layer electrodeposition.

Metal	Salt	Complex agent	Additives	pH
Cu	$CuSO_4$	$Na_3C_6H_5O_7$	-	~ 5.5
Sn	$SnSO_4$	CH_4O_3S	Triton X-100 Hydroquinone	~ 0
Zn	$ZnCl_2$	-	NH_4Cl, Triton X-100	~ 4

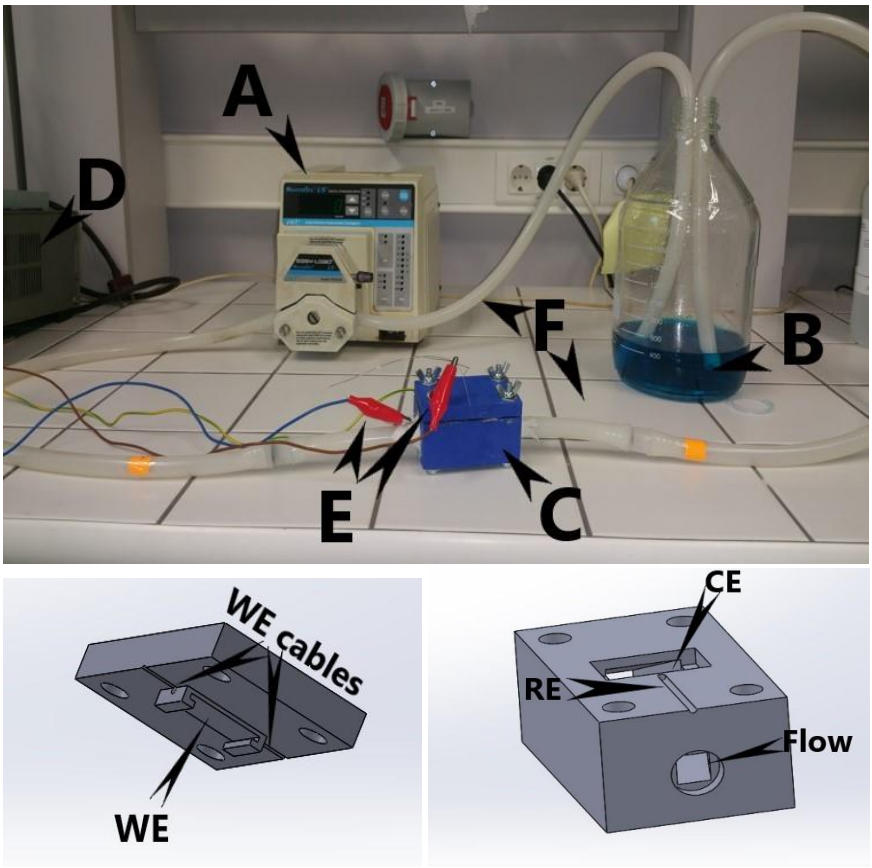

Figure 9. The unique 3D printed electrochemical flow cell. The top picture shows the whole system used for deposition A – peristaltic pump; B – electrolyte solution; C – flow cell; D – current supply; E – electrodes; F – silicon hoses. The bottom images show the design of two-piece flow cell left – bottom part; right – top part. WE – working electrode; RE – reference electrode; CE – counter electrode.

3.2.2. Electrochemical deposition of Cu-Sn (bronze) alloy followed with a top layer of Zn

Electrochemical co-deposition of copper and tin on molybdenum coated soda-lime glass was carried out in a stirred standard three-electrode electrochemical cell using potentiostatic conditions, the reference electrode (Ag/AgCl/KCl) was placed near the working electrode through the Lugin capillary.

The electrolyte solution containing 20 mM $CuSO_4$, 10 mM $SnSO_4$, and 0.1 M tri-sodium citrate was prepared. 1 mM hydroquinone was added to the solution to minimize the oxidation of tin ions. pH was adjusted to 5.75 using sodium hydroxide. Electrodeposition was performed at room temperature. Cu-Sn alloy was deposited at E_c −1.0 V. For Zn layer electrochemical deposition, we used a commercial $ZnCl_2$ solution (LIKONDA ZnRN). Zinc was electrodeposited using galvanostatic regime at 30 mA/cm^2. Stoichiometry was varied by adjusting the deposition time of zinc. Following, kesterite films with Cu-poor Zn-poor, Cu-poor Zn-stoichiometric, Cu-poor Zn-rich composition were manufactured (Zn layer thickness 170, 200, and 240 nm respectively).

Our method of stacking Cu-Sn (in our case Cu 65 at. %, Sn 35 at. %) with the following zinc layer originated from work by Khalil et al. [137]. Published work showed poor electrochemically deposited film quality. The zinc layer wasn't continuous, showing island growth. We improved layer quality by using different solutions and introducing magnetic stirring of the solution while electroplating.

3.3. Thermal treatment and sulfurization

For thermal procedures, we have used the tube furnace. In this work, we have used two-step thermal treatment. The first step was the annealing of precursor films for 60 minutes in a gas mixture (Ar 95% + H_2 5%) at a temperature of 350 ^oC for Cu-Sn/Zn films and at a temperature of 250 ^oC for Cu/Sn/Cu/Zn films under atmospheric pressure. Deposited metallic copper has a greater diffusion rate than that in the bronze alloy. Therefore, Cu/Sn/Cu/Zn films require a lower annealing temperature for elements to distribute evenly throughout the entire layer.

Sulfurization samples were placed in a graphite container along with 150 mg of elemental sulfur. The graphite container was placed in the tube furnace. To remove any oxygen from the tube, the entire system was flushed with Ar (99.9999%) gas three times. Sulfurization was carried out under the atmospheric pressure of Ar (99.9999%) at a temperature of 580 ^oC for 15 minutes. The temperature ramping rate was 2 $^oC\ s^{-1}$ after sulfurization samples were left to cool down naturally in the furnace.

3.4. Structural, morphological, and electronic characterization

The present chapter will be dedicated to briefly review the methods used in this work: XRD, Raman spectroscopy, SEM, TEM, photoluminescence, and photoelectrochemical study.

3.4.1. X-ray diffraction

XRD measurements were performed using a state of art X-ray diffractometer SmartLab (Rigaku) equipped with a 9kW rotating Cu anode X-ray tube. The lattice parameters of the kesterite and the quantity of zinc sulfide were determined using a CALSA (Crystal Array on Logarithmic Spiral Analyser) analyzer on a diffracted beam, which is capable of singling out and register only Cu $K_{\alpha 1}$ radiation (λ = 1.5405929 Å). The diffractometer was tested and calibrated using a certified standard LaB_6 SRM 660b powder.

3.4.2. Raman Spectroscopy

The Raman spectra were registered using a confocal microspectrometer inVia (Renishaw). The spectrometer is equipped with a CCD camera (thermoelectrically cooled to -70 °C) and a microscope. Spectra were excited using laser radiations of 325 nm (0.1 mW, 2400 lines mm^{-1} grating), 532 nm (0.06 mW, 3000 lines mm^{-1} grating) and 785 nm (1 mW, 1200 lines mm^{-1} grating). Silicon standard was used to calibrate the Raman frequencies according to the line at 520.7 cm^{-1} (532 nm excitation). Spectra were recorded using a 50x/0.75 NA (785 and 532 nm) and 15x/0.32 (325 nm) objective lens. The time of the integration was 100 s for 785 nm and 400 s for 532 and 325 nm. Band parameters were determined by adapting the experimental spectra with Gaussian-Lorentzian shape components using GRAMS/A1 8.0 software (Thermo Scientific).

3.4.3. Scanning and transmission electron microscopy

Surface morphology, chemical composition, and cross-section analysis of the films were carried out using a dual-beam system FE-SEM-FIB Helios Nanolab 650 (FEI Company) with an X-Max EDX spectrometer (Oxford instr.). Element distribution throughout the film thickness was observed using Tecnai F20 X-TWIN (FEI company) TEM with an accelerating voltage of 200 kV equipped with an EDX (EDAX) spectrometer, Gatan Orius CCD camera.

3.4.4. Photoelectrochemical analysis

Photoelectrochemical analysis of the kesterite films was performed using an electrochemical cell with a quartz window. A Standard three-electrode system was used (counter electrode – Pt wire, reference electrode - Ag/AgCl/KCl). Working solution – aqueous 0.2 M $Eu(NO_3)_3$ (deionized 18MΩ water). Photovoltamperometric measurements were conducted using a potentiostat

PI-50-1.1 with an analog-digital converter (ADC) for data collection. Films were illuminated by white LED Lumiled 3W. Area of the film exposed to the solution and illumination – 0.5 cm^2. The intensity of the light at the film surface was measured – about 100mW/cm^2 (measured with power meter VLP-2000).

3.4.5. Photoluminescence

Photoluminescence (PL) analysis was performed by using a self-made experimental setup. Kesterite films were mounted on the cold finger of a closed-cycle cryostat (SHI-4, Janis Research) and excited using a pulsed UV laser (266nm/4.66 eV, <0.6ns, >0.7 kW). PL spectra were recorded at a temperature of 3-300 K. NIR (near-1 dispersed by a 500 mm grating monochromator (Andor Shamrock SR-500i-D1; 600 1/mm, blaze @ 1000 nm) and focused into InGaAs photodetector (cooled thermoelectrically). Conventional lock-in methods were applied to process the electrical signal. For the temperatures below 250 K, asymmetrical spectra were analyzed by two Gaussian bands—full-range of spectra (temperature-dependent) allowed to estimate the activation energy (E_a). The potential fluctuation parameter γ was determined using excitation power-dependent spectra.

4. RESULTS AND DISCUSSION

4.1. Preparation of working electrode

The electrodeposition of metals on molybdenum rather complicated since the Mo surface is always covered by the oxide layer. As it was mentioned in the previous chapter, in this study, we used Mo coated SLG as a working electrode for precursor layer electrochemical deposition. To find the most suitable one, we have investigated three different preparation methods:

1. Mo layer cleaning with industrial detergent and washing it with distilled water.
2. Immersing Mo/SLG in ethanol for 1 min in an ultrasonic bath, then soaking it in ammonia for 10 min, rinsing with water, and again immersing in ethanol for 1 min (drying with Ar flow).
3. Magnetron etching of molybdenum surface.

Figure 10. The contact angle of the water/Mo surface. Left – molybdenum cleaning with detergent; middle – surface cleaning with ammonia and alcohol; right – magnetron etching of the surface.

The hydrophilic surfaces are more suited for electrochemical deposition. The most hydrophilic surface should provide the most uniform and compact films [138]. Hydrophilic properties were evaluated by measuring contact angle of water drop on the Mo surface after surface treatment. (Fig. 10). The most hydrophilic molybdenum surface was achieved by using magnetron etching, and the least hydrophilic was the one washed with industrial detergent. The in-between was the one washed with ethanol and etched with ammonia.

However, experimentally we found that adhesion of the electrochemically deposited layer on magnetron etched Mo films are very poor. Copper deposited film just peeled off of the Mo surface when washing it in water. This could be related to the roughness of the surface, which we determined using AFM (Fig. 11). Also, after the etching Mo surface is very active, the oxide layer may have formed while transferring the substrate from the magnetron to the electrochemical bath. The coating made on the surfaces cleaned with the industrial detergent also showed poor adhesion, which might be due to the residue of organic compounds left on the surface. The second most hydrophilic surface, obtained by preparing the Mo substrates using ethanol/NH_4OH/ethanol, showed great adhesion of deposited Cu films. Therefore, it was chosen to use throughout the research.

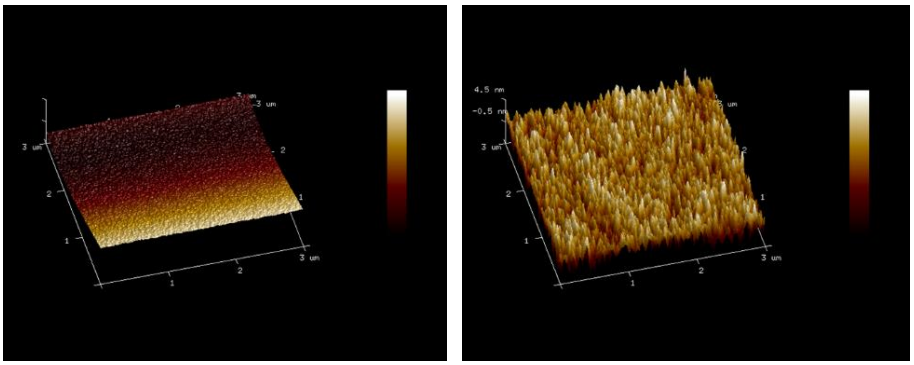

Figure 11. AFM image of Mo film after treatment in ethanol/NH_4OH/ethanol (left) and after magnetron etching (right).

4.2. Study of the kesterite films formed using electrochemically deposited Cu/Sn/Cu/Zn precursor

4.2.1. Electrochemical deposition of stacked layers

All of the separate layers were deposited using galvanostatic conditions. It is much easier to predict and control the thickness of the layers under this conditions and this conditions are much more common in the industrial electroplating.

The sequence of the metallic layers cannot be random. To prevent an oxidation of the previous layer, metals have to be electrodeposited in the certain order – starting from metal with the most positive deposition potential and finishing the most negative one (copper E^0=+0.34 V, tin E^0=-0.13 V, zinc E^0=-0.76 V). Also, copper is preferred to be the first layer on top of molybdenum, from the three metals which are present in the CZT precursor as it has the best cohesion to the Mo layer. In theory, the optimal sequence would be Cu/Sn/Zn [122, 139-141]. However, zinc electrodeposition on the tin layer is complicated due to the formation of zinc aggregates instead of a continuous layer. This phenomenon was already reported by Scragg [31] and is probably related to the formation of tin oxide on the electrodeposited tin surface. To prevent the zinc aggregation problem, Scragg [31] suggested stacking the metallic layers with an intermediate copper layer between tin and zinc, forming a Cu/Sn/Cu/Zn precursor layer.

Aiming towards industrial electrochemical layer deposition, the electrochemical flow cell was developed using SolidWorks CAD 3D design software. The flow cells' biggest advantage over the convenient solution mixing is the laminar flow – the constant exchange of the solution at the solution/electrode interface. The silicone hoses (10 mm inner diameter) were

used to transport the solution in a closed cycle by using a peristaltic pump. Precursor films were deposited on 3.1 cm^2 molybdenum surface. To assess the flow type, the method of injecting dye in the hose with flowing water was applied – in the presence of the turbulent flow, the dye would mix randomly in the tubes. The laminar flow was achieved with a flow rate of 1.1 l/min (high end of our system capabilities). At the lower flow rates, the strokes of the solution can be observed, and the flow was rather turbulent. This was caused by the working principles of the pump (only four bearings in a 360 degrees spin cycle of the pump pushing the solution in the hose). To keep the laminar flow throughout the entire system, the transition from the round hose to the rectangular electrochemical cell chamber had to be designed and evaluated by the 3D aerodynamics software tools.

Copper electrodeposition.

The current density for the electrodeposition of Cu was chosen using the voltammetry data (Figure 12) of our system.

A couple of samples were prepared using different current densities (chosen using voltammetry data) to examine the morphology and evaluate what current density is the best suited for the thin (the target thickness was ~350 nm) copper layer deposition.

Figure 13 shows the surface and cross-section images of the deposited films (pictures were taken from the middle of the sample). The current densities of 3.2 and 2.5 mA/cm^2 were chosen for the experiment, FC2, and FC1 samples (FC– Flow Cell sample series), respectively. From the SEM images, we can observe that both of the films have a similar copper grain size of about 500 to 800 nm. From the SEM cross-section images (FIB made), we can see that the sample deposited using the lower current density is not uniform in the thickness. The film thickness varies from 200 to 460 nm. However, the sample deposited using higher current density is more uniform, with an average thickness of ~350 nm (middle of the sample).

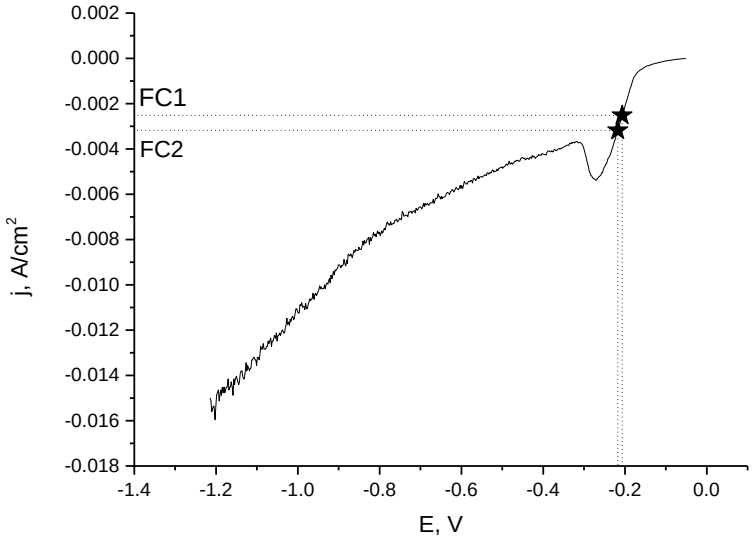

Figure 12. Cu polarization curve of the Cu/Mo/glass working electrode was measured in the electrolyte solution (pH = ~5.5) containing: $CuSO_4$ – 75 mM and 225 mM tri-sodium citrate. Potential scan rate: 2 mV s^{-1}. It is measured in the flow cell.

To assess the distribution of copper deposits throughout the entire sample, the EDX measurements were used. The copper coating thickness is relatively low, so the Mo peaks of characteristic x-ray spectrum can be found in the EDX spectra. The peak intensities of Mo and Cu can be used to evaluate the thickness of the copper (top) layer. The higher the Mo peak – the lower thickness of the copper layer. Figure 14 depicts the scheme of the samples and indicates the measured copper atomic percentage (the rest is molybdenum). The atomic percentage is directly related with the thickness of the copper layer (the higher atomic percentage of copper – thicker the layer of copper).

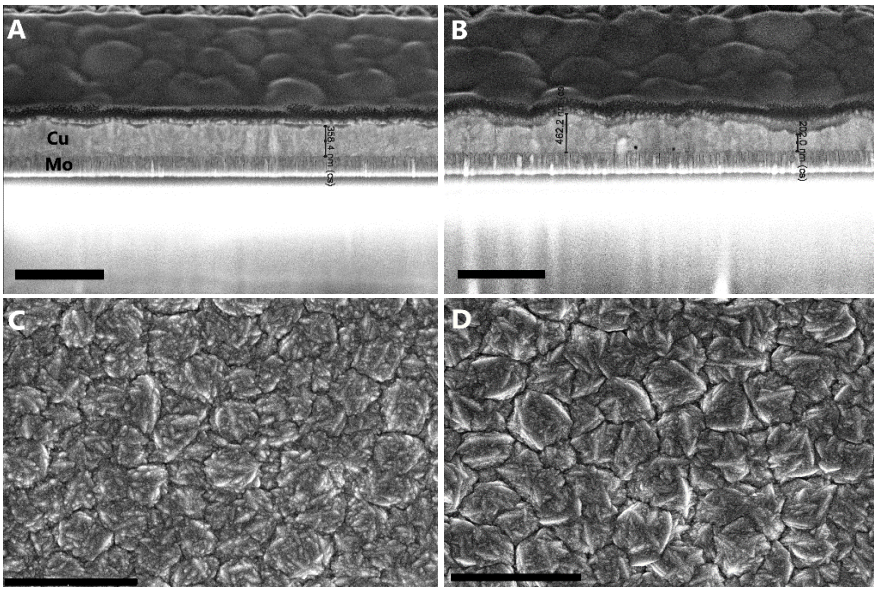

Figure 13. The SEM surface and cross-section images of the copper layer deposited at current density: 3.2 mA/cm^2 A and C (point FC2 in Fig.13) and 2.5 mA/cm^2 B and D (point FC1). The scale bar denotes 1 μm.

The sample deposited using lower current density was found to have a thicker layer of copper on the bottom side (where electrolyte solution flows into the cell), and the thickness lowers in the direction of the flow. That could be caused by the depletion of Cu ions in the abovementioned direction due to exhaustion of the ions during deposition and insufficient supply of the latter by the too slow flow rate of electrolyte. On the other hand, the thickness of the copper increases from left to the right side of the sample (parallel to the direction of the flow). Such thickness distribution may result from a certain degree of turbulence of electrolyte flow. The film thickness of the sample deposited at a higher current density also lowers in the direction of the electrolyte solution flow. The thickness in the corners parallel to the flow distributes unevenly alike in the previous sample. The right side has a slightly thicker coating of copper than the left side. An explanation of such thickness distribution could be the unequal distance between the working and counter electrode at the right and left side along the direction of electrolyte flow.

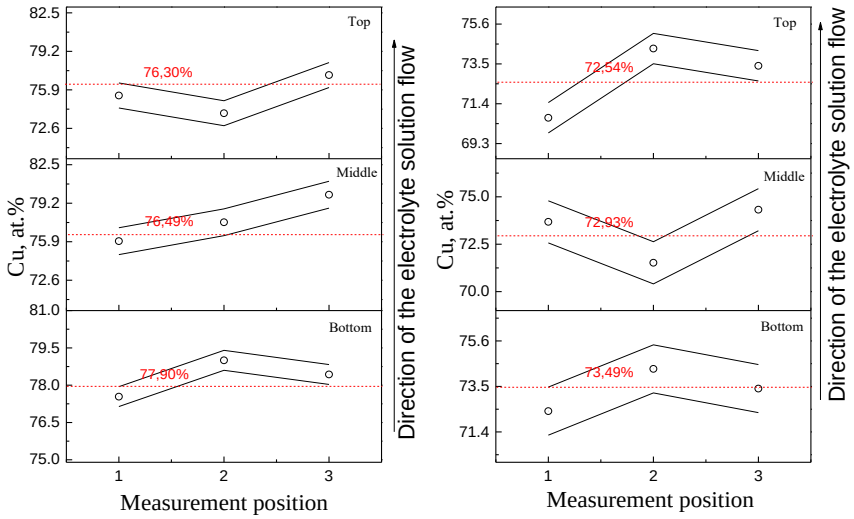

Figure 14. Schematic representation for the EDX measurements for Cu samples FC1 (left) and FC2 (right) electrodeposited at current density of 3.2 and 2.5 mA/cm^2, respectively.

The EDX results agree well with the SEM images. The average thickness of the sample deposited at a higher current density is larger at every measured location compared to the sample deposited at a lower current density. The layer deposited at 3.2 mA/cm^2 is more homogeneous due to the higher number of the crystallization canters formed at higher overpotential.

Tin electrodeposition.

The Sn layer is electrodeposited under galvanostatic conditions. The flow rate was used the exact same as for the copper to retain the laminar flow.

We have chosen the Sn deposition current density of 9.5 mA/cm^2. A compact layer of metal usually grows at higher current densities while at lower values takes place electrocrystallization of island-like deposits, and at the higher densities, a dendritic deposit starts to grow. The tin films were deposited on SLG/Mo electrodes coated with a copper layer of ~100 nm. To increase the number of crystallization centers at the beginning of the deposition, the strike of 41.3 mA/cm^2 current density was applied for 2 seconds, and further deposition was conducted at a current density of 9.5 mA/cm^2. To achieve a compact and homogeneous Sn layer, Triton X-100, as surface-active material (SAM), was added to the electrolyte solution. The dependence of the Sn layer morphology on a concentration of the Triton X-100 was studied. Additives

can leave residue in the layer, so the amount of it used has to be the minimum needed to achieve a uniform layer.

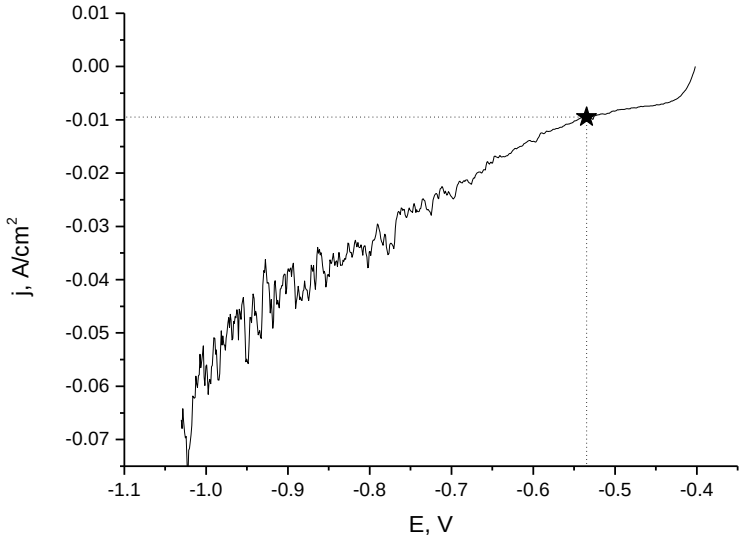

Figure 15. Sn polarization curve of Sn/Cu/Mo/glass working electrode measured in the electrolyte solution containing: $SnSO_4$ – 100 mM, MSA – 1 M, Triton X-100 – 0.6 ml/l; (pH = ~0). Potential scan rate 2 mV/s.

The Cu/Sn precursor layers were investigated, measuring the atomic composition (Cu at. % + Sn at. % = 100 at. %) at the different locations of the samples. The sample FC7 was electrodeposited in the solution with 0.3 ml/l of the Triton X-100 and the sample FC9 with 0.6 ml/l. Both of the samples were deposited at the same current density, and the deposition duration was exactly the same. We can see (Fig. 16) that in the sample FC7 the tin quantity is maximum in the middle of the sample and lowers at the end of the sample from the flow direction perspective. The averages of the deposited tin layer thickness are very inconsistent throughout the layer. The first section (where the solution goes into the cell) has an average of 38.33 % of tin, the middle section – 44.52 %, and the third section – 14.26 %. The sample FC9 (Fig. 16), which has a higher concentration of Triton X-100 tin amount values, a very slight decrease in the direction of the solution flow. The first section has an atomic tin percentage of 46.93 %, the middle section – 46.53 %, and the third section – 44.53 %. We can also see that the sides of the sample are not evenly coated by tin. The right side has a significantly thicker layer of Sn. The Sn

layer of the sample FC9 is more uniform and thicker overall than the FC7 sample.

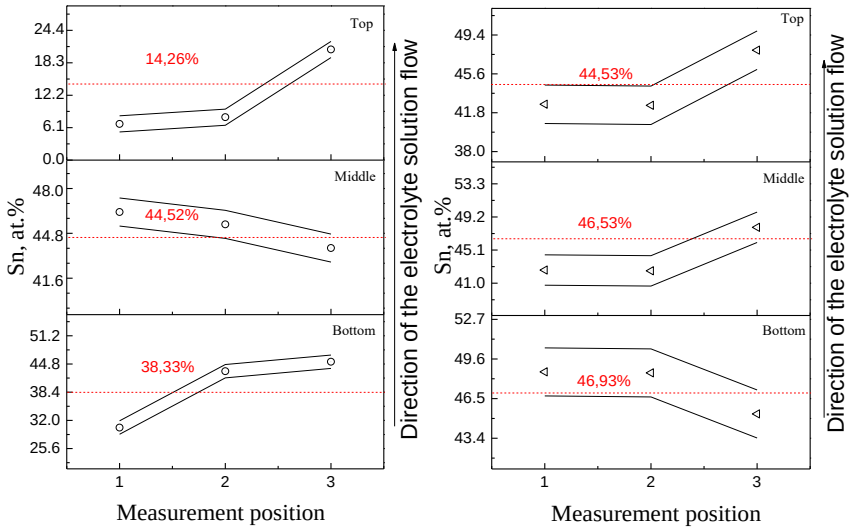

Figure 16. The schematic representation of Sn quantity (at.%) at different locations of the samples electrodeposited in solution with different concentrations of Triton X-100: 0.3 ml/l (sample FC7, left graph) and 0.6 ml/l (sample FC9, right graph).

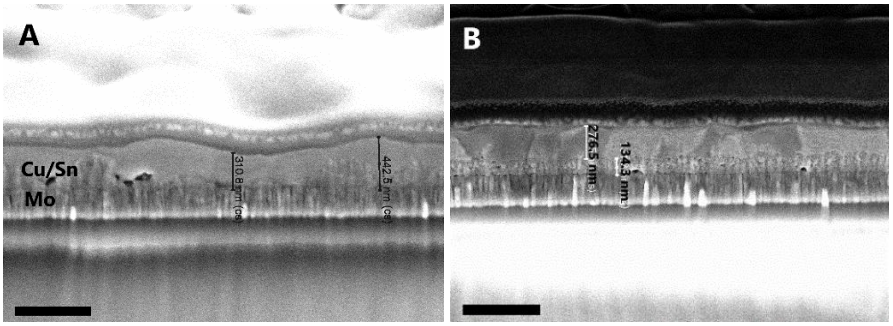

Figure 17. The SEM cross-section images of the sequentially electrodeposited Cu/Sn layers on the molybdenum substrate. A – FC7 sample; B – FC9 sample. The scale bar denotes 500 nm.

The SEM images (fig. 17) of the FC7 sample shows that the Cu/Sn precursor layer is not very uniform (thickness varies from ~310 up to ~440 nm). That can indicate the insufficient amount of surface-active additive. The FC9 sample shows a great thickness distribution in the SEM cross-section image. The amount of surface-active additive is sufficient since we do not see any traces of island growth, which is very typical for the electrodeposited tin layers. The SEM images agree very well with EDX data. In the case of the FC9 sample, where the layer is uniform and overall thicker – the copper atomic percentage is only 53.82 % (measured with EDX), whereas in the FC7 sample, which has an inconsistent layer thickness – the measured copper atomic percentage is 64.88 %.

Zinc layer electrodeposition.

The zinc layer deposition was carried out on the SLG/Mo electrode coated with electro-deposited copper (135 nm thickness). Two samples were deposited at a different current density FC13 at 9.5 mA/cm^2 and FC14 at 15.9 mA/cm^2. The starting current density pulse of 41.26 mA/cm^2 and 47.60 mA/cm^2 was applied for FC13 and FC14, respectively. The same method of measuring the relative thickness using EDX data was applied (Cu at. % + Zn at. % = 100 %).

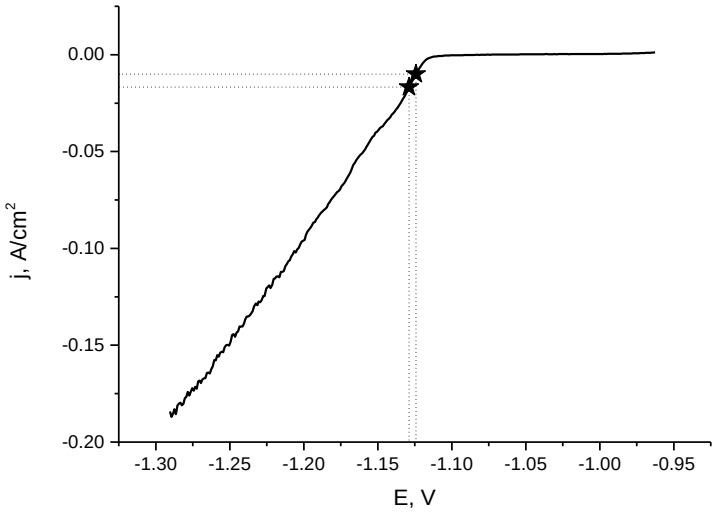

Figure 18. The Zn polarization curve of the Zn/Cu/Mo/glass working electrode was measured in the electrolyte solution containing: ZnCl – 50 g/l, NH_4Cl – 200 g/l and Triton X-100 – 1 ml/l. Potential scan rate: 2 mV s^{-1}. It is measured in the electrochemical flow cell.

In figure 19 (left), we see that in the sample FC13 the amount of zinc (thickness of the Zn layer) is decreasing in the direction of the solution flow. The average amount of the zinc in the section where the solution first enters the cell is – 55.53 % in the middle section – 51.29 % and in the third section – 24.71 %.

The zinc layer thickness increases significantly from left to the right side. The FC14 sample (fig. 19 right) shows a much lower thickness decrease in the direction of the solution flow. The first section average amount of the zinc is 53.42 %, the second section – 57.31 %, and the third section – 48.77 %. Also, the amount of zinc is increasing in the same direction as in the FC13 sample - from left to the right side. From the EDX measurements, we can obviously see that the FC14 sample is more uniform, and the overall amount of deposited zinc is greater (53.17 % compared to 43.84 %) than in the FC13 sample.

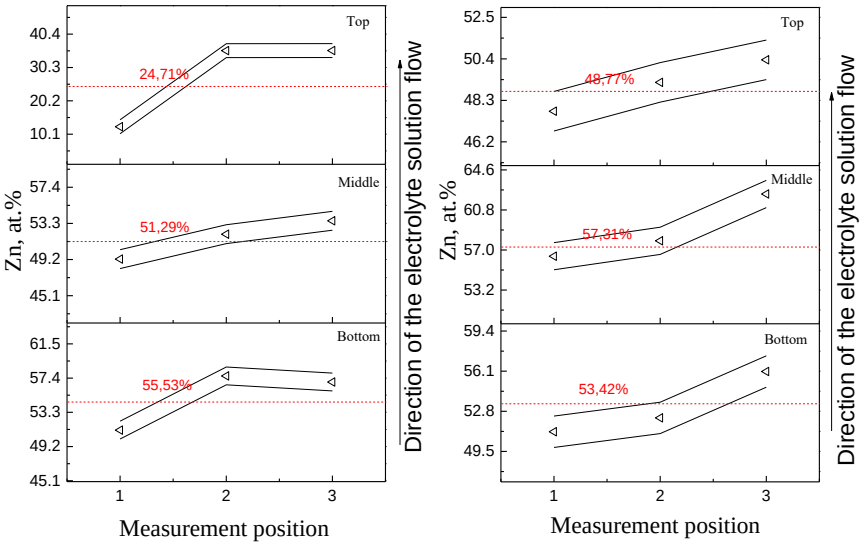

Figure 19. The schematic representation of zinc quantity in samples FC13 (left) and FC14 (right) electrodeposited at a current density of 9.5 and 15.9 mA/cm^2, respectively.

Fig. 20 shows SEM cross-section (left) and surface (right) images of the sample FC14. The surface image presents characteristic disc-like growth of Zn. The large surface of the discs is parallel to (001) crystallographic plane of hexagonal Zn crystal lattice. Most of the plates are oriented perpendicular to

the surface, and that is the reason for the serrated profile of the cross-sectional image of the Zn layer.

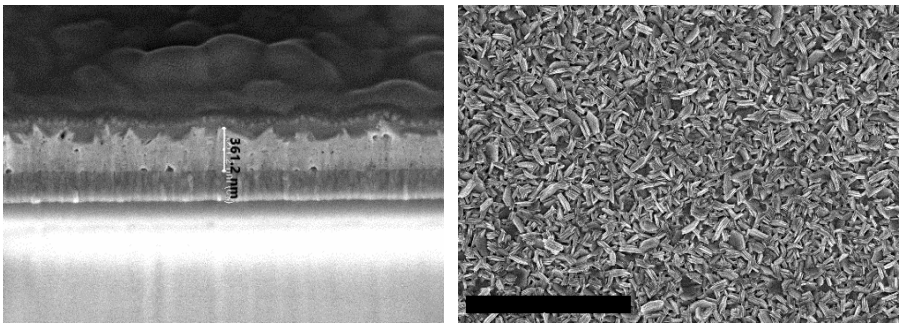

Figure 20. The SEM cross-section (left) and surface image (right) of the sample FC14. The scale bar denotes 2 μm.

4.2.2. Cu/Sn/Cu/Zn precursor layer

After evaluating the results of the electrochemically deposited separate metallic layers, the Cu/Sn/Cu/Zn (CTCZ) precursor layer was formed. The details of FC19 sample fabrication and deposited separate layers thicknesses are given in table 6. The precursor presented the following ratios of metals quantities in at. %: Cu/(Sn+Zn)=0.7; Zn/Sn=1.15 which corresponded to Cu-poor and Zn-rich precursor composition.

Table 6. Parameters used for the formation of the sample FC19.

Sample	Starting current density impulse (Cu/Sn/Cu/Zn), mA/cm^2	Current density (Cu/Sn/Cu/Zn), mA/cm^2	Deposition duration (Cu/Sn/Cu/Zn), s
FC19	34.9/41.3/34.9/63.5	3.2/9.5/3.2/15.9	75/26/60/10

From the schemes in figure 21. we can see that in the FC19 sample the Sn amount slightly decreases in the direction of the solution flow, 31.1 %, 29.72%, and 26.14 % for the first, second, and third sections, respectively. We can also see that the amount of tin is increasing from the left to the right side of the sample. The zinc distribution throughout the entire surface is similar to tin. The amount of Zn decreases in the direction of the solution flow – 38.66 %, 37.93 %, and 34.93 % for the first, second, and the third sections, respectively. Also, the zinc amount is increasing from the left side to the right.

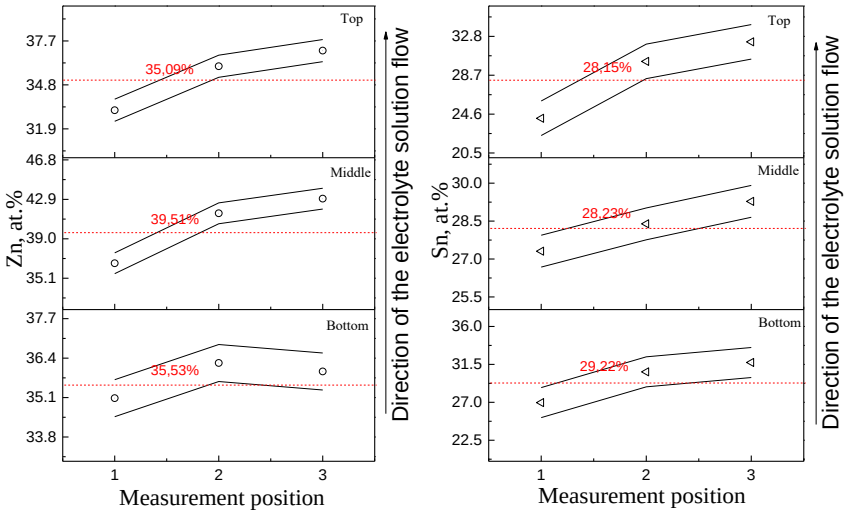

Figure 21. The schematic representation of the Zn (left) and Sn (right) amount in different FC19 sample locations.

Summarizing the results of the electrodeposition of Cu, Sn, and Zn layers in the electrochemical flow cell, we concluded that the cell is suitable for electrodeposition of thin films of Cu, Sn, and Zn under galvanostatic conditions. However, the uniform thickness of the films can be obtained in a small area only. The character of uneven distribution of film thickness on the larger area is common for all of the studied metals. That could mean the main reason for poor thickness distribution is the uneven distance between working and counter electrodes (cathode and anode). This distance is very sensitive, especially in the case then the electrodes are positioned very close to each other like in the case of our flow electrolytic cell. Dimensions of the cell are restricted by the electrolyte flow rate. The decrease in the film thickness in the flow direction implies that the flow rate possibly was too slow, and that means that the cell should be even of smaller dimensions for the peristaltic pump we used in our work.

4.2.3. Electrodeposition using a conventional electrochemical cell

The transition from the electrochemical flow cell to the conventional electrochemical cell was mainly done because of the geometry flaws in the flow cell deposition chamber. The tubes we used were very small in diameter, and there was no possibility to use bigger ones with our pump. To sustain the

laminar flow of the solution, the electrodes in the deposition chamber had to be very close to each other (the distance of around only 2 mm). Having such a small distance between the electrodes meant that any imbalance of the working electrode while mounting it causes the uneven distribution of the deposited layer thickness.

To deposit the samples studied in this paragraph, we used a standard three-electrode electrochemical cell. As a working electrode, we used SLG/Mo substrates, the counter electrode – Pt plate (larger surface area than WE), reference electrode – Ag/AgCl/KCl. The electrochemical cell volume was 100 ml, the distance between WE and the counter electrode was fixed – 4 cm.

Copper electrodeposition.

The current density for the electrodeposition was chosen using the voltammetry data (Figure 23) of our system - copper layers were formed at three different j values (chosen from the j - E pattern).

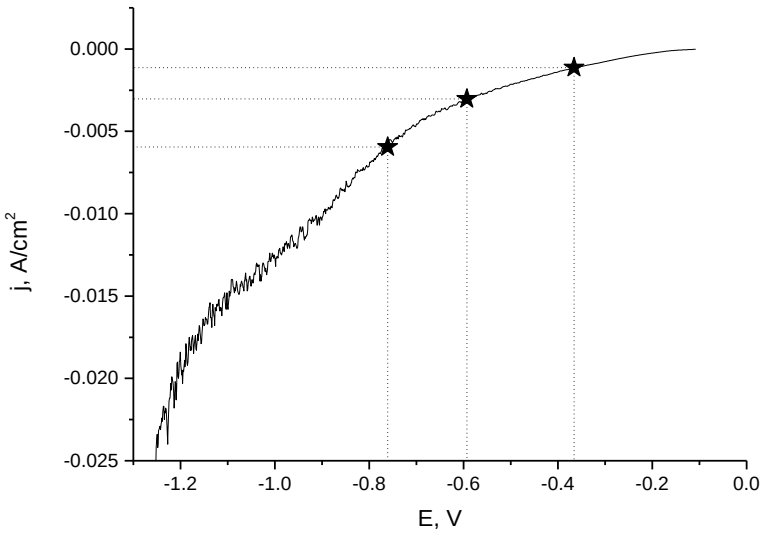

Figure 22. Cu polarization curve of Cu/Mo/glass working electrode measured in the electrolyte solution containing: $CuSO_4$ – 75 mM and $Na_3C_6H_5O_7$ – 225 mM, Potential scan rate: 2 mV s^{-1}.

Figure 23 shows the surface and cross-section images of copper layers formed at different current densities. The grain size decreased with the increase in current density. The most uniform layer of copper was obtained

using a current density of 3 mA/cm^2 for electrodeposition. Also the layer thickness was near to the calculated one (Faraday`s law). The layer deposited at a current density of 1 mA/cm^2 was not uniform, island growth can be observed, and the layer formed at the 6 mA/cm^2 showed a quite poor yield of copper deposit, and the grains were smaller than those of the sample deposited at a 3 mA/cm^2.

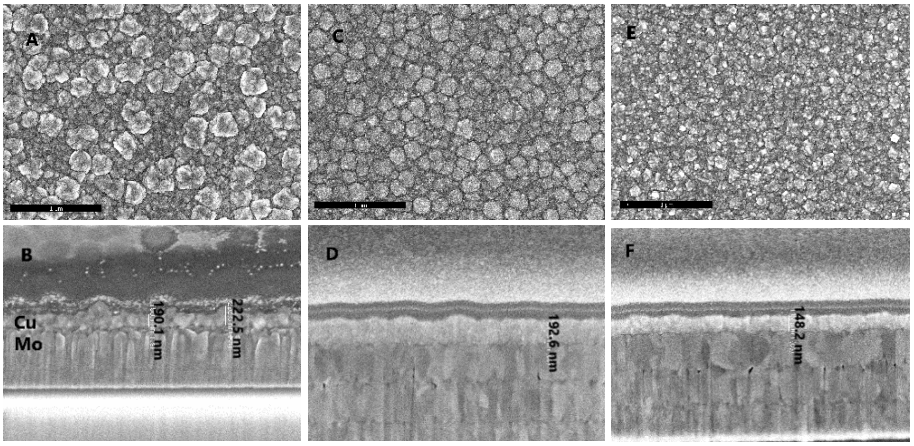

Figure 23. The SEM surface and cross-section images of the electrodeposited copper layer. A and B – deposited at a current density of 1 mA/cm^2; C and D – at 3 mA/cm^2; E and F – at 6 mA/cm^2. The scale bar denotes 1 μm.

Tin electrodeposition.

The voltammetry data was used to determine the region of Sn reduction (Figure 24). Using the voltammetry data, four values of current density were tested for thin film deposition.

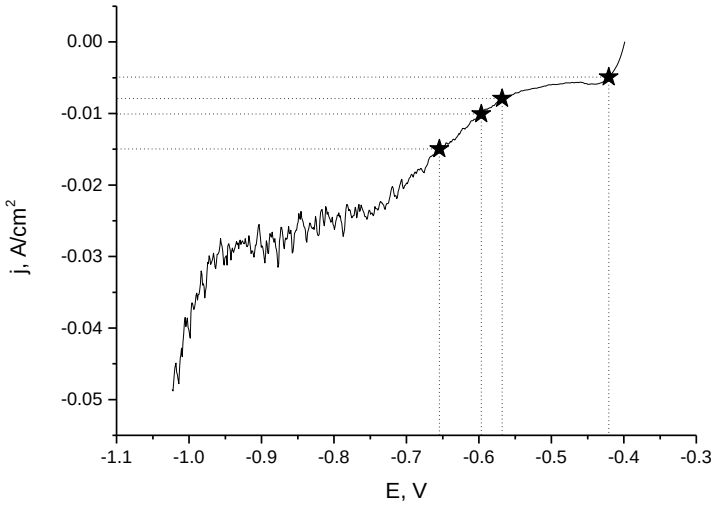

Figure 24. Sn polarization curve of Sn/Cu/Mo/glass working electrode measured in the electrolyte solution containing: $SnSO_4$ – 100 mM, MSA – 1 M and Triton X-100 – 0.6 ml/l. Potential scan rate: 2 mV s^{-1}. Measured in the conventional cell.

Figure 25 and Figure 26 shows us the SEM surface and cross-section images of the SLG/Mo/Cu/Sn stacked films, respectively (copper deposited by using the previously chosen conditions). The current density for Sn electrodeposition for sample in the picture A was 5 mA/cm^2; B – 8 mA/cm^2; C - 10 mA/cm^2; and D - 15 mA/cm^2.

The film where Sn was deposited at a current density of 5 mA/cm^2 island growth was observed, and no continuous layer was formed, when the current density was raised to 8 mA/$cm^{2,}$ the surface coverage improved, yet, some gaps can still be observed from the SEM surface image, cross-section image showed that the surface of the film is not very smooth. However, when the tin electrodeposition is carried out at a current density of 10 mA/$cm^{2,}$ the surface of the deposited film is very smooth, and no gaps are observed from the surface image. Further increase of the current density (up to 15 mA/cm^2) for the Sn deposition results in the rough surface and a porous precursor layer that might be the result of the hydrogen evolution occurring at the surface of the electrode. In all of the SEM micrographs, we can see that the copper layer below the tin is very thin and a bit porous that can be explained – copper diffusion coefficient value is high, Cu from the bottom layer diffuses into the deposited tin on top, forming a Cu-Sn alloy.

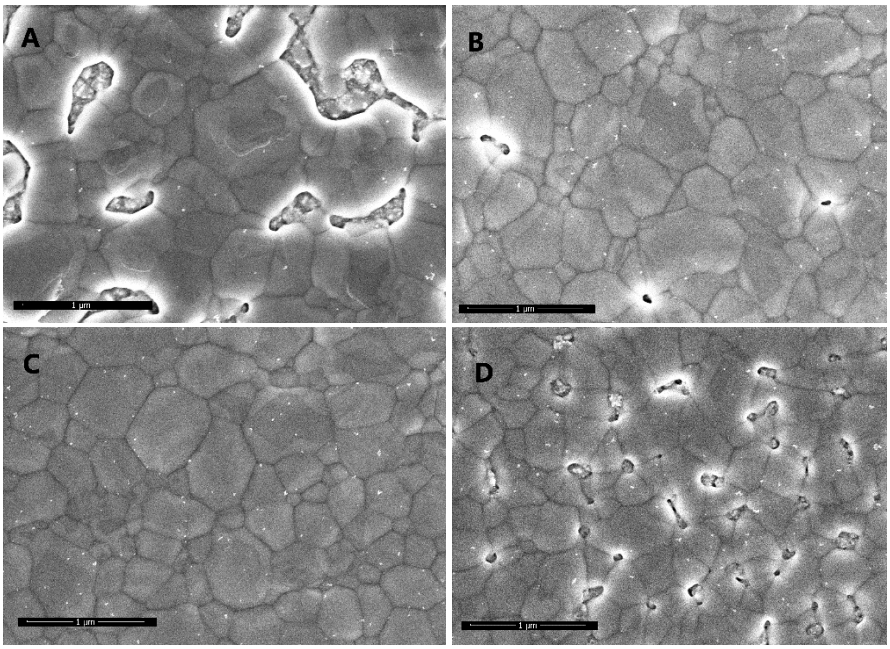

Figure 25. The SEM surface images of the tin layers deposited on copper coated molybdenum substrates at the different current densities. A – 5 mA/cm^2; B – 8 mA/cm^2; C – 10 mA/cm^2; D – 15 mA/cm^2. The scale bar denotes 1 μm.

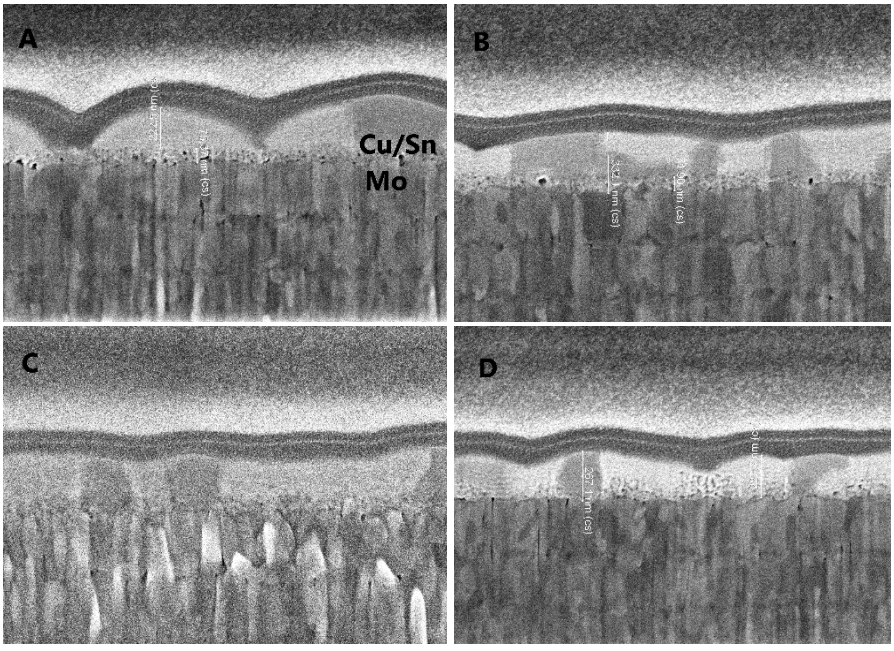

Figure 26. SEM cross-section images of the tin layers deposited on copper coated molybdenum substrates at the different current densities. A – 5 mA/cm^2; B – 8 mA/cm^2; C – 10 mA/cm^2; D – 15 mA/cm^2.

Intermediate Copper layer deposition.

As mentioned before, the copper layer between tin and zinc is necessary. The same electrolyte solution and current density as in the first Cu layer were applied to deposit the intermediate layer. To obtain the optimal Cu/Sn/Cu layer for later zinc deposition we tried a few different thickness of the bottom and intermediate copper layers. The Cu/Sn/Cu samples list with deposition information is given in Table 7.

Table 7. Thicknesses of Cu and Sn layers of studied samples.

Sample	1st Cu layer thickness*	Sn layer thickness*	2nd Cu layer thickness*
A122	70 nm	200 nm	70 nm
A123	40 nm	200 nm	100 nm
A124	100 nm	200 nm	40 nm

* - In the table, the calculated thicknesses are given, the actual thickness of the layer may differ.

SEM cross-section imagess of the samples are given in Figure 27. The A124 sample with the thicker bottom layer of copper showed the least amount of voids at the Mo/precursor interface and the smoothest surface of the sample series. The samples with copper layers of equal thickness and with the thinner bottom layer were more porous or even had significant voids at the Mo/precursor interface. The surfaces of both A122 and A123 samples had some gaps between the grains. The interfaces of metals cannot be distinguished precisely due to the formation of Cu-Sn alloy (due to interdiffusion of copper and tin).

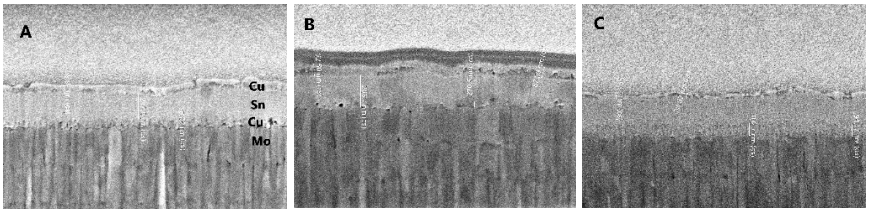

Figure 27. SEM cross-section images of the Cu/Sn/Cu layers. A – A122; B – A123; C – A124. The sample details are given in Table 7.

Zinc layer electrodeposition.

To investigate the zinc layers, three samples were deposited at the different current densities on the SLG/Mo electrodes coated with electrochemically deposited copper layer (~80 nm thickness). The polarization curve was very

similar to the one measured in the electrochemical flow cell (fig. 18). The current densities for zinc electrodepositions are given in Table 8.

Table 8. Zinc electrodeposition parameters.

Sample	The current density for Zn electrodeposition, mA/cm^2	Electrodeposition time of Zn, s
A119	15	31
A120	20	23
A121	25	18

The sample A119 (deposited at the lowest current density) was found to have the smoothest surface of the sample series. When increasing the current density of the deposition surface roughness increases. The surface of the sample A121 deposited at 25 mA/cm^2 had a lot of blisters. Having such poor adhesion to the substrate, it was decided not to do cross-section measurements.

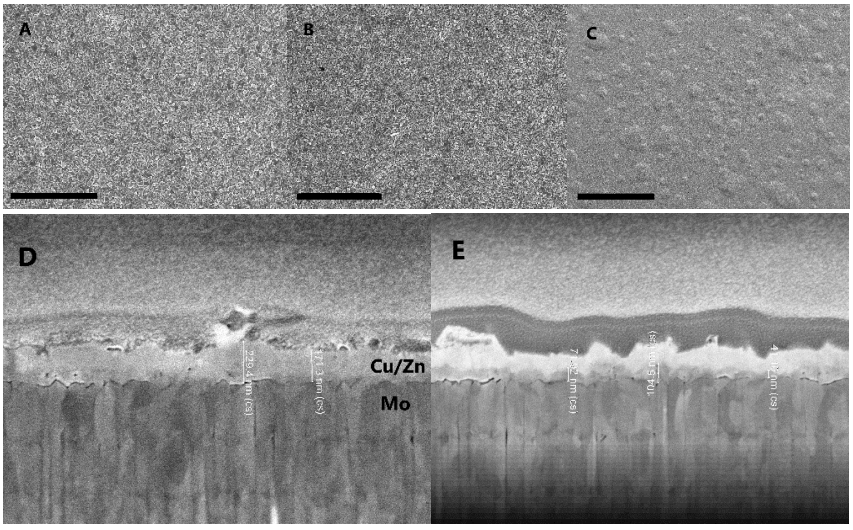

Figure 28. The surface and cross-section SEM images of the zinc layers deposited on copper coated Mo/glass substrates. A and D – A119 sample; B and E – A120 sample; C – A121 sample. The scale bar denotes 5 µm (except C, which is 100 µm).

The optimal current density for the deposition of zinc for Cu/Sn/Cu/Zn had to be investigated further since the deposition ratio and morphology can differ when depositing on Cu/Sn/Cu rather than on just the Cu layer. Further

investigation of zinc layer deposition was carried out. Current densities of Zn layers deposition and substrate compositions are given in Table 9.

Table 9. Substrate layer composition and current density of Zn electrodeposition for investigated samples.

Sample	1st Cu layer thickness, nm	Sn layer thickness, nm	2nd Cu layer thickness, nm	The current density for Zn electrodeposition, mA/cm^2
A125	100	200	40	15
A126	70	200	70	15
A127	70	200	70	20
A128	100	200	40	20

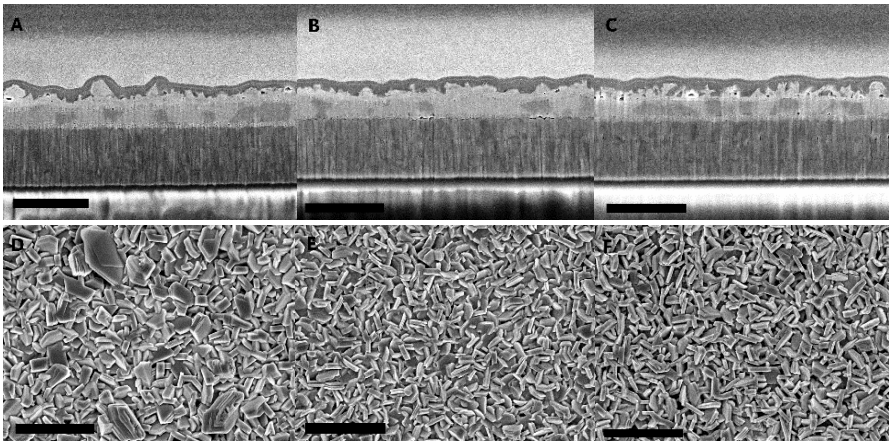

Figure 29. SEM surface and cross-section images of the Cu/Sn/Cu/Zn precursor layers deposited using Cu layers of different thickness and Zn current density (specifications on how the samples were deposited given in Table 9). A and D images are of A126 sample; B and E – A127 sample; C and F – A128 sample. The scale bar denotes 1 μm.

Sample A125 was not successful – zinc was not seen on the surface; therefore, SEM images are not included in Figure 29. The surface of the sample A126 was very rough; the zinc islands can be observed. The zinc in the samples A127 and A128 were both deposited at the same current density on the substrates with different thickness distribution of the bottom and intermediate copper layers. The surface of sample A127 (thicker Cu top layer) shows that the zinc layer is rather continuous and obviously smoothest of the

sample series. The sample A128 (thinner Cu top layer) had a very rough surface. From the cross-section view, it is visible that the zinc did not form a continuous layer. The cross-section images also show the importance of the intermediate Cu layer, for Zn electrodeposition. Zinc formed more uniform and continuous layers only on the Cu/Sn/Cu surfaces with the thicker intermediate Cu layer.

4.2.4. Annealing of the Cu/Sn/Cu/Zn precursor layers

An interdiffusion between Cu and Sn layers takes place even at room temperature [142, 143]. A low temperature (preliminary) annealing must be conducted to form a homogeneous and compact layer of Cu-Zn-Sn (CZT) precursor, which should lead to more pure and homogeneous CTZS layer after sulphurization.

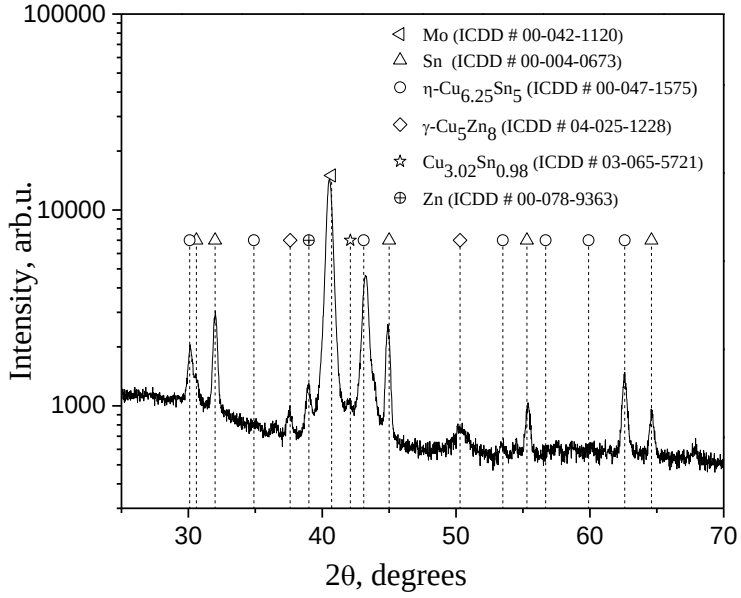

Figure 30. X-ray diffraction pattern of the Cu/Sn/Cu/Zn sample recorded at a temperature of 24 °C, before annealing.

The temperature dependence of the phase composition of the electrochemically deposited Cu/Sn/Cu/Zn precursor was investigated by in-situ x-ray phase analysis in a high-temperature x-ray stage in He atmosphere at a temperatures of 24; 200; 250; 300; 350 and again at 24 °C when sample

cooled down. In this temperature range the annealed precursor coating becomes more homogeneous, intermetallic compounds are formed, and the residue from the organic compounds that may have been adsorbed in the layer during electrochemical deposition is removed. However, to remove the organic residue from the deposition H_2 atmosphere is necessary.

The presented x-ray diffraction (XRD) pattern (Fig. 30) recorded at 24 °C before annealing shows intermetallic phases already formed due to the ongoing intense diffusion between the copper, tin, and zinc layers both during deposition and after the formation of the precursor layer even at room temperature. Intense diffraction peaks of Mo (ICDD # 00-042-1120); Sn (ICDD # 00-004-0673); Zn (ICDD 00-078-9363) were observed. Pure Cu peaks were not found in the pattern, indicating that copper diffused into Sn and Zn layers to form intermetallic compounds: γ-Cu_5Zn_8 (ICDD # 04-025-1228), η-$Cu_{6,25}Sn_5$ (ICDD #00-047-1575); $Cu_{3,02}Sn_{0,98}$ (ICDD # 03-065-5721).

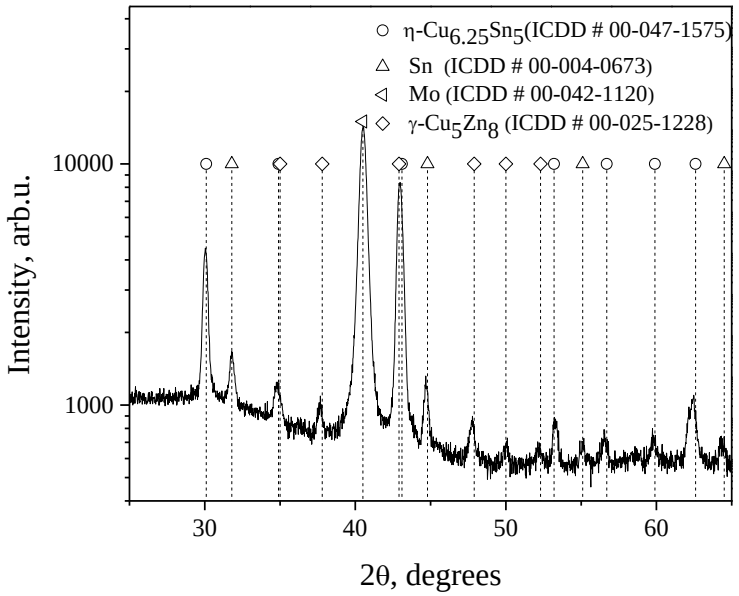

Figure 31. The XRD pattern of the Cu/Sn/Cu/Zn sample measured at a temperature of 200 °C.

In the XRD pattern (Fig. 31), we see that no Zn phase was detected at 200 °C, but low-intensity tin phase peaks are still visible. This indicates that all of the zinc diffused into the copper layer to form the γ-Cu_5Zn_8 intermetallic compound. Cu-Zn intermetallic compounds formation energy is twice lower

than the formation energy of Cu-Sn compounds; therefore, the γ-Cu_5Zn_8 phase is formed first, and only later η-$Cu_{6,25}Sn_5$ is formed. In this XRD pattern, we can see that the intensity of the η-$Cu_{6,25}Sn_5$ phase peak is higher than in the one recorded at room temperature.

In the XRD diffraction pattern recorded at a temperature of 250 °C (Fig. 32), we see that the tin (which has the lowest melting point of 231.9 °C) melted because its diffraction peaks were no longer present. Also, the XRD peaks of cubic γ-Cu_5Zn_8 are visible at the angles of 34.9; 37.9; 43.0; 47.9; 50.1; 52.2, and 62.2°. The peaks are narrowed, indicating an increase in crystallites size.

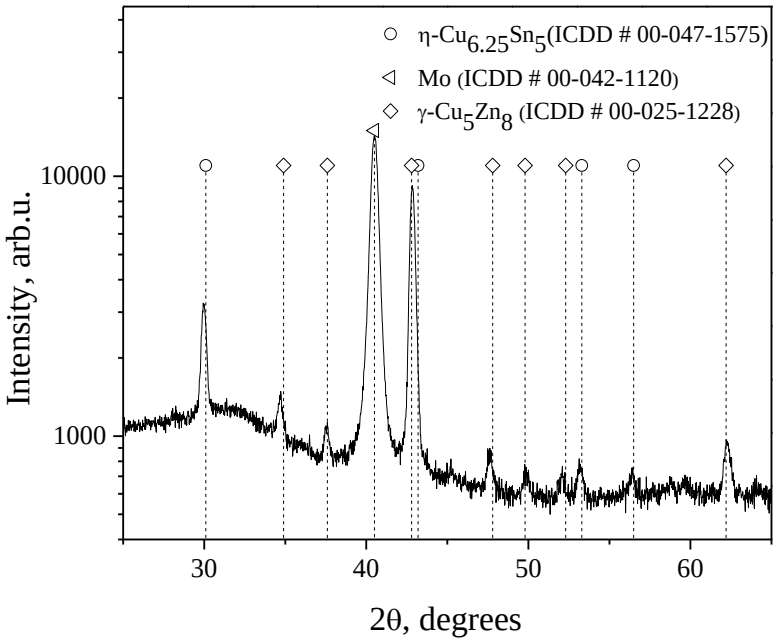

Figure 32. The X-ray diffraction pattern of the Cu/Sn/Cu/Zn sample measured at a temperature of 250 °C.

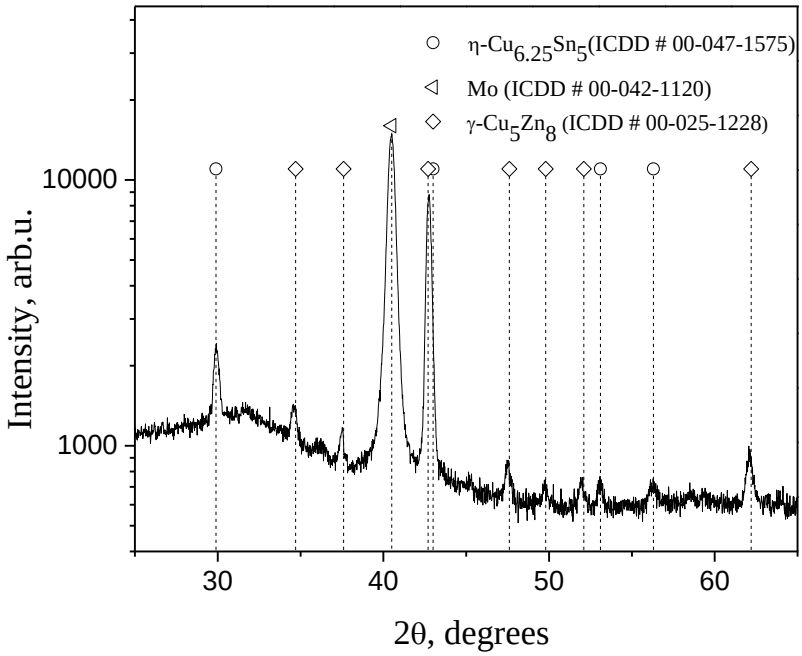

Figure 33. The XRD pattern of the Cu/Sn/Cu/Zn sample measured at a temperature of 300 °C.

XRD (Fig. 33) at 300 °C clearly shows that peaks of η-$Cu_{6,25}Sn_5$ (ICDD # 00-047-1575); γ-Cu_5Zn_8 (ICDD # 04-025-1228), and Mo (ICDD # 00-042-1120) are even narrower due to further increase in crystallites size compared to those at 200 and 250 °C. Low intensity peaks are visible at diffraction angles of 32.0 and 36.2 °, which can be attributed to ZnO.

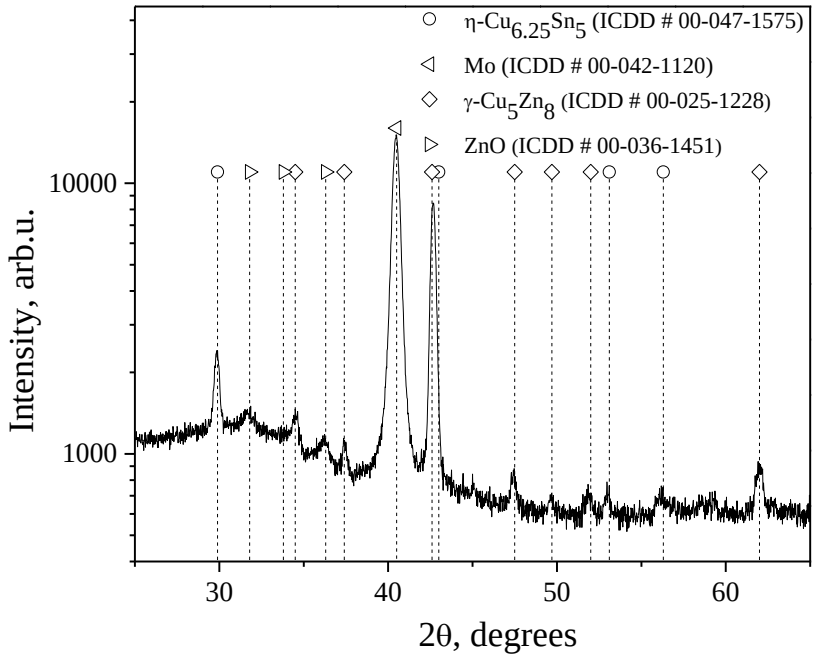

Figure 34. The XRD pattern of the Cu/Sn/Cu/Zn sample measured at a temperature of 350 °C.

Figure 34 shows the XRD pattern at a temperature of 350 °C. More low-intensity peaks of hexagonal ZnO appear at the angles of 32.0; 34.1; 36.2; 47.3; 56.9, and 62.6°. The Zn layer is electrochemically deposited using a rather negative potential (-1.1 V), so not only the Zn reduction reaction takes place, but also electrochemical hydrogen evolution is present, so the amorphous $Zn(OH)_2$ may form on the surface of the zinc layer. At higher temperatures, in this case, 350 °C, $Zn(OH)_2$ decomposes, leaving crystalline ZnO on the surface.

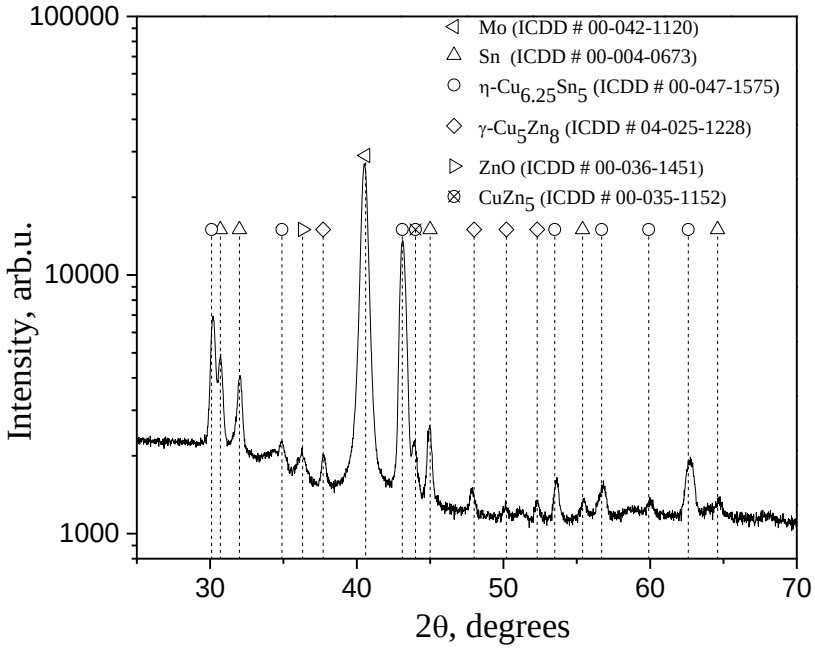

Figure 35. XRD pattern of the Cu/Sn/Cu/Zn sample measured at a temperature of 24 °C, after the annealing.

After annealing and cooling, the XRD pattern of the sample was recorded at 24 °C (Fig. 35) again. Peaks of pure Sn (ICDD # 00-004-0673) were present, indicating that molten tin crystallized when the precursor layer cooled down. The peaks are visibly broader, indicating a decrease in crystallites size. Also, another phase - $CuZn_5$ (ICDD # 00-035-1152) was detected.

To evaluate the real annealing conditions, several Cu/Sn/Cu/Zn precursors were formed and annealed at temperatures of 250, 300, and 350 °C, in Ar 95% + H_2 5% atmosphere for 1 hour. XRD patterns were recorded using the grazing incidence beam method, where the primary x-ray beam hits the sample surface at a constant ω angle, in our case ω=0.5°, and the diffracted x-rays are recorded with only a change in the angle between the sample surface and the detector. The elemental composition of the coatings was determined before and after annealing using an induced plasma optical emission spectrometer (ICP-OES). All of the samples were divided in half, one half for determination of chemical composition using ICP-OES before annealing and the other one after annealing. The results obtained are presented in Table 10. All the samples

were Cu-poor. Samples AA250 and AA300 showed nearly stoichiometric values for ratio Zn/Sn before annealing. The sample AA350 was Zn-poor and

Table 10. The elemental composition (at. %) of the samples, before and after the annealing.

	Elemental composition				
Sample	Cu, at.%	Sn, at.%	Zn, at.%	Zn/Sn	Cu/ (Zn+Sn)
AA250, before annealing	43,44	28,54	28,02	0,98	0,77
AA250 (T=250 °C, Ar 95 % + H_2 5 %)	44,71	24,87	30,42	1,22	0,81
AA300, before annealing	43,49	27,75	28,76	1,04	0,77
AA300 (T=300 °C, Ar 95 % + H_2 5 %)	45,13	27,23	27,64	1,02	0,82
AA350, before annealing	42,00	31,14	26,86	0,86	0,72
AA350 (T=350 °C, Ar 95 % + H_2 5 %)	40,74	33,49	25,77	0,77	0,69

strongly enriched in Sn. The annealing had strong impact on Zn quantity: the ratio Zn/Sn increased after the annealing at temperature of 250 °C, remained approximately the same at temperature of 300 °C, and decreased at that of 350 °C. At this temperature quantity of Cu also decreased in contrast to other temperatures, at which the ratio Cu/(Zn+Sn) had increased.

The figure 36 depicts XRD patterns of Cu/Sn/Cu/Zn precursors annealed at different temperatures. All the patterns presented three intermetallic compounds: γ-Cu_5Zn_8 η-$Cu_{6,25}Sn_5$; ε-Cu_3Sn; and pure Sn. The XRD peaks attributable to γ-Cu_5Zn_8 phase were of higher intensity for samples AA250 and AA300, while in the XRD pattern of AA350 these peaks were of much lower intensity, which was in agreement with the results of chemical composition (Table 10). In contrast, the XRD peaks of Sn showed the highest intensity in the pattern of sample AA350. One more phase presented in all of the patterns was that of ZnO. The intensity of peaks attributable to the latter compound increased with annealing temperature. The annealing was provided in slightly reducing atmosphere (Ar 95 % + H_2 5 %) so it was unlikely that ZnO could be formed through an oxidation of zinc during the annealing. Most probably the Cu/Sn/Cu/Zn precursors contained small amount of amorphous

$Zn(OH)_2$ on the surface (Zn was the topmost layer). The amorphous $Zn(OH)_2$ transformed into crystalline ZnO at the elevated temperatures. The increase in intensity of ZnO peaks with the annealing temperature supported this assumption. Interestingly, the higher losses of Sn were obtained at lower annealing temperatures. It can be assumed that temperature of 250 °C was sufficient for partial evaporation of Sn (melting temperature 230 °C). At higher temperatures, liquid Sn may have been able to remove Zn from the γ-Cu_5Zn_8 intermetallic compound, while the removed Zn atoms were evaporated.

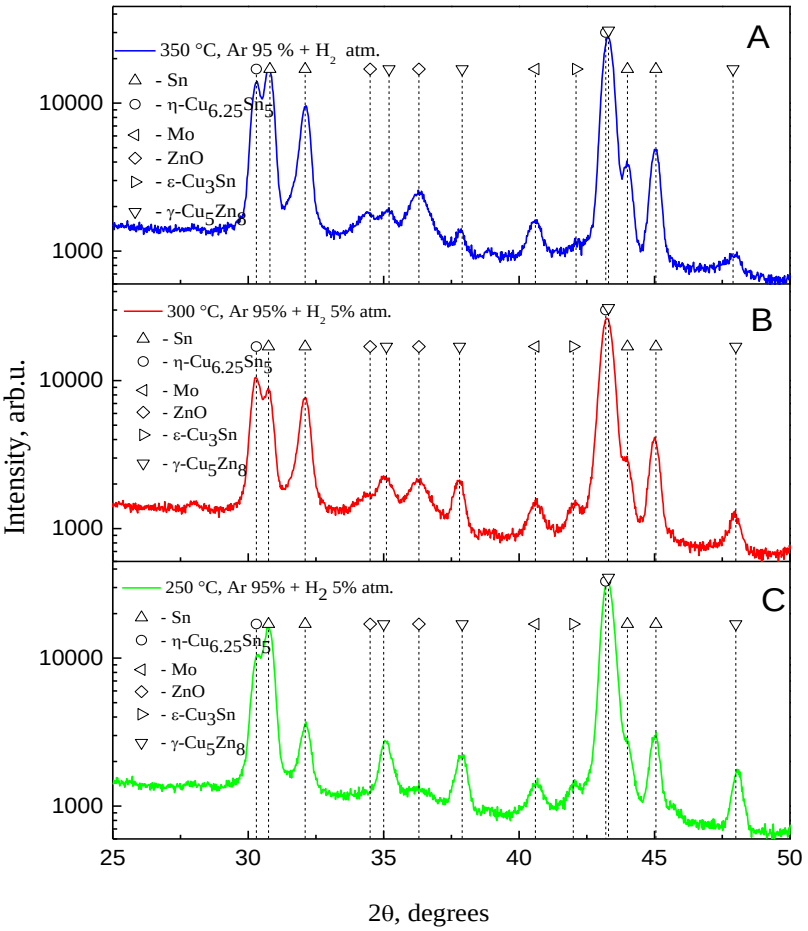

Figure 36. Cu/Sn/Cu/Zn precursor XRD patterns after the annealing of the films in Ar 95 % + H_2 5 % atmosphere at different temperatures: A – at a temperature of 350 °C; B – 300 °C; C- 250 °C.

4.2.5. Sulfurization of the CTCZ precursor films

Electrochemically deposited copper-poor and zinc-rich Cu/Sn/Cu/Zn precursor layers annealed at 250 ºC were sulfurized in a vacuum tube furnace at the temperatures 540, 560, and 580 ºC. To remove Cu_xS_y phases from the surface of the CZTS layer – samples were immersed in a 5 % KCN solution for 1 minute.

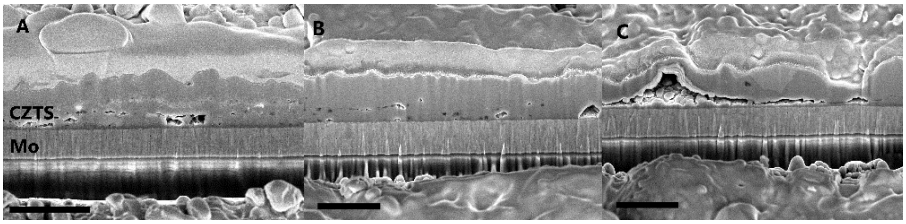

Figure 37. SEM cross-section views of the CZTS samples. Picture A – sulfurized at a temperature of 540 ºC; B – 560 ºC; C- 580 ºC. The scale bar denotes 2 μm.

From the SEM cross-section images (fig. 37), we can see that samples sulfurized at a temperature of 540 and 560 ºC are much more uniform and has fewer voids than that sulfurized at 580 ºC, which has a lot of high diameter voids and overall poor adhesion to the substrate. Since the quality of the sample sulfurized at a temperature of 580 ºC was so poor, it was decided not to proceed with the phase composition study of the sample.

Table 11. Elemental composition of the samples after sulfurization at different temperatures.

	Elemental composition, at. %			
Sample sulfurization temperature, ºC	Cu	Sn	Zn	S
540	21.51	12.52	6.88	59.09
560	23.75	11.75	3.96	60.54
580	23.97	11.82	4.90	59.31

The elemental composition of the samples was measured using the EDX method (table 11). Sample sulfurized at the lowest temperature – 540 ºC showed the largest amount of zinc – 6.88 at. %, while the samples sulfurized at a temperature of 560 and 580 ºC had only 3.96 and 4.90 at. % of zinc,

respectively. The zinc loss at high temperatures can be explained by the volatility of ZnS, which was mostly forming at the sample surface since the Zn layer had been deposited on the top of the precursor layers. While having zinc deficiency in the kesterite, there is a better chance that secondary copper tin sulfide phases will form.

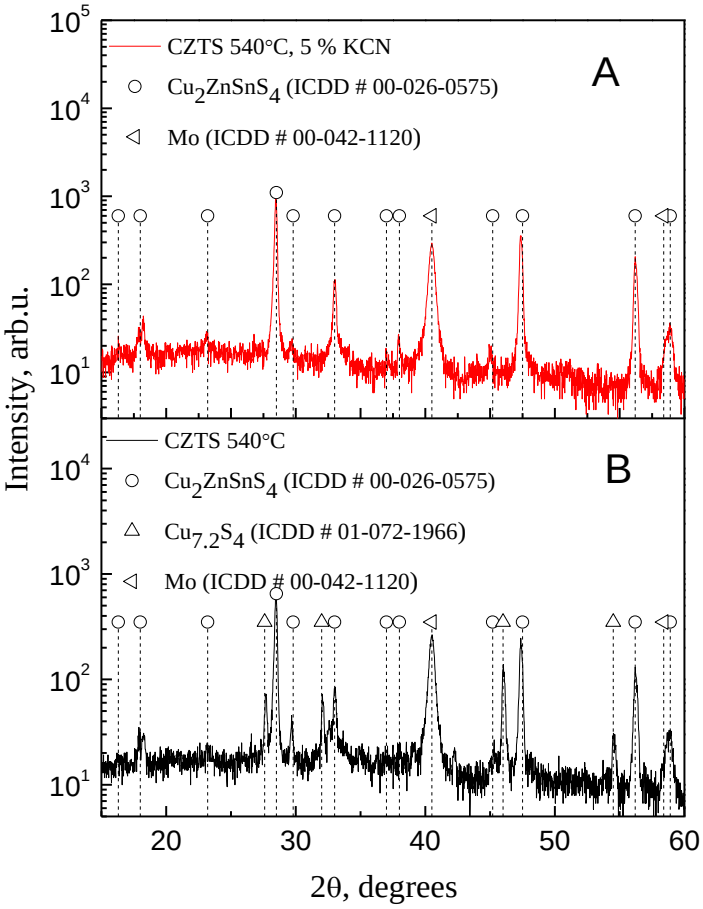

Figure 38. XRD pattern of the CZTS sample sulfurized at the temperature of 540 ºC. A – after the KCN etching; B – before the etching.

In the presented XRD pattern of the CZTS layer obtained by sulfurizing the Cu/Sn/Cu/Zn precursor layer at a temperature of 540 ºC (fig. 38 B), intense peaks at 2Θ angles 18; 28.5; 29.8; 33; 47.5; 56.2; 58.9 º are characteristic for Cu_2ZnSnS_4 (ICDD # 00-026-0575) phase. Sharp profile of the peaks indicate that the kesterite crystallites are rather large. Peaks of copper sulfide phase $Cu_{7.2}S_4$ (ICDD # 01-072-1966) are also present. The formation of this phase

can be the consequence of zinc loss at higher temperatures – in this case, 540 ºC. The copper sulfide phase was removed by dissolving it in a 5% KCN solution. In the XRD pattern (fig. 38 A) measured after the treatment with KCN solution, $Cu_{7.2}S_4$ phase peaks at 2Θ angles 27.6; 32; 46; 54.5 º are not present. The diffraction peaks of Mo at 40.5; 58.4 º are also observed in both of the patterns.

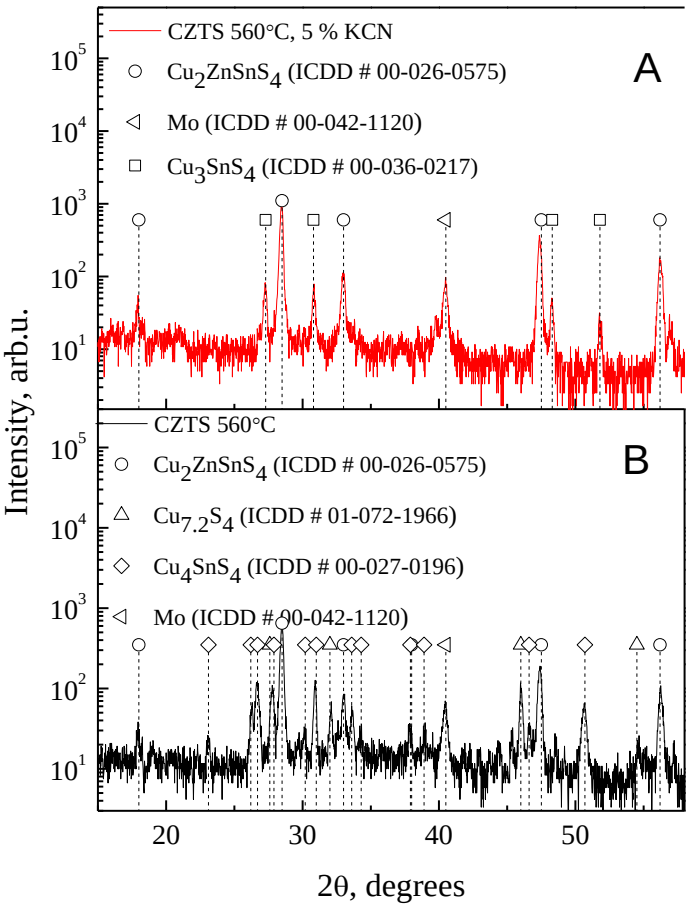

Figure 39. XRD pattern of the CZTS sample sulfurized at the temperature of 560 ºC. A – after the KCN etching; B – before the etching.

Figure 39 shows the XRD pattern of the CZTS sample sulfurized at a temperature of 560 ºC (B). Intense and sharp peaks can be observed at the diffraction angles of 18; 28,5; 33; 56.2 º, which are attributable to the tetragonal Cu_2ZnSnS_4 phase. This proves that the formed CZTS layer contains large crystals. However, peaks of the secondary phases $Cu_{7.2}S_4$ (ICDD # 01-

072-1966) and Cu_4SnS_4 (ICDD # 00-027-0196) are also present in the pattern. Both secondary phases found in the layer are a consequence of the zinc loss (in the form of ZnS) during the high-temperature procedure. Figure 40 A shows the diffraction pattern of the same sample after etching it in the KCN solution. All of the $Cu_{7.2}S_4$ phase diffraction peaks disappeared. Also, the selective etching with KCN dissolved some of the copper from the Cu_4SnS_4 (ICDD # 00-027-0196) phase, and the diffraction peaks can be seen at an angle of 27,3; 30,8; 48,3; 51,8 indicating the stoichiometry shift of copper-tin sulfide to Cu_3SnS_4 (ICDD # 00-036-0217).

The XRD method is insufficient for the study of kesterite purity since XRD peaks of some secondary phases such as ZnS, Cu_2SnS_3 overlap with XRD peaks of kesterite. To get more reliable information on phase purity, samples sulfurized at a temperature of 540 and 560 ºC were investigated using Raman spectroscopy. Both of the samples were etched in a 5 % KCN solution before the measurement.

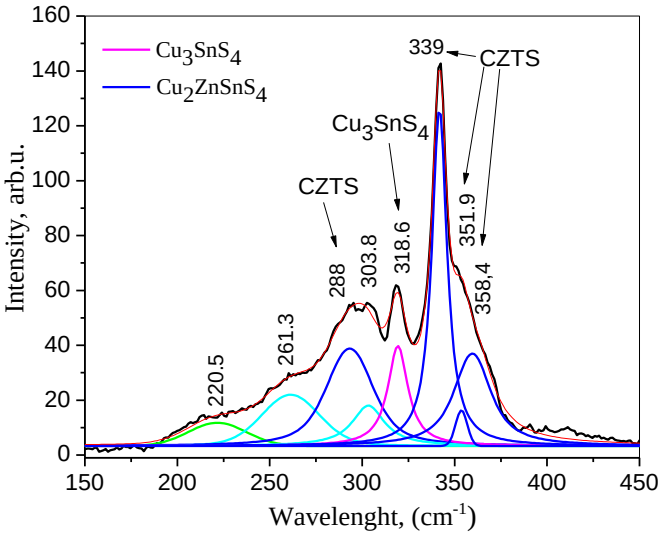

Figure 40. Raman spectrum of the CZTS sample sulfurized at a temperature of 560 ºC. Excitation wavelength 542 nm.

Figure 40 presents the Raman spectrum of the sample sulfurized at the temperature of 560 ºC. The main peak of the tetragonal Cu_2ZnSnS_4 phase can be seen at the 339 cm^{-1} wavenumber and the lower intensity peaks at 288; 351.9, and 358.4 cm^{-1}. Also, a low-intensity peak of the Cu_3SnS_4 phase can be seen at 318.6 cm^{-1} wavenumber. This phase was also was present in the X-ray pattern of the sample.

The Raman spectrum of the sample sulfurized at a temperature of 540 ºC (fig. 41) showed a high intensity peak at 338.7 cm^{-1} and two lower intensity peaks at 288.2 and 366.3 cm^{-1} wavenumbers attributed to the Cu_2ZnSnS_4 phase. Also, an intense peak can be observed at 322.4 cm^{-1} and three lower ones at 264.1, 301.7, and 355.1 $cm^{-1,}$ which are attributable to the Cu_3SnS_4 phase. It shows that the kesterite layer has a significant amount of secondary copper tin sulfide phase.

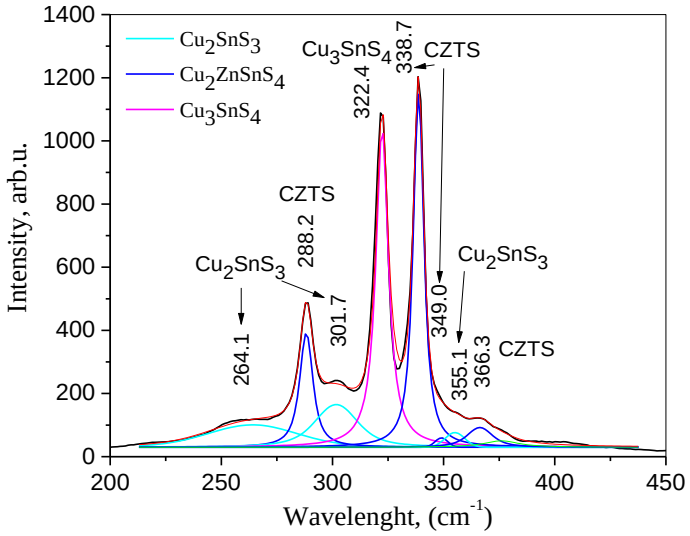

Figure 41. Raman spectrum of the CZTS sample sulfurized at a temperature of 540 ºC.

Table 12. Kesterite layer composition (at. %) of the samples with different Zn layer thickness.

	Elemental composition, at. %			
Zn layer thickness, nm	Cu	Sn	Zn	S
130	23,75	11,75	3,96	60,54
200	18,47	11,20	14,06	56,38

To obtain the zinc-rich kesterite, the sample was prepared with a much thicker layer of zinc on top (200 nm instead of 130 nm). The EDX measurements after the sulfurization of precursor and KCN etching of the layer showed that the elemental composition of the sample is Cu-poor, Zn-rich (table 12) kesterite.

The sample with a 200 nm zinc layer was sulfurized at the temperature of 560 ºC. The Raman spectrum of the sample (fig. 42) showed one intense peak at 339.3 cm^{-1} and two lower value peaks at 288.4 and 368.2 cm^{-1} wavenumbers attributable to the tetragonal Cu_2ZnSnS_4 phase. Only a low-intensity peak at 320.6 cm^{-1} wavenumber attributable to Cu_3SnS_4 phase was present. Also, three unidentified peaks were found at 264.4; 304.4, and 354.3 cm^{-1} wavenumbers, which according to Ref. [57], are attributable to cubic Cu_2SnS_3.

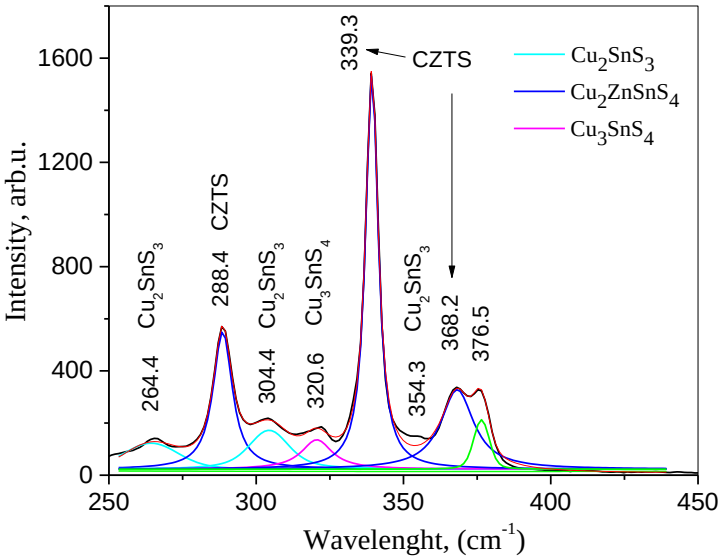

Figure 42. Raman spectrum of the Cu-poor, Zn-rich CZTS sample, sulfurized at a temperature of 560 ºC.

Even in the Zn-rich Cu-poor sample, the secondary phase without zinc was present. This might be the consequence of copper-tin interdiffusion occurring when layer by layer deposition takes place. The copper-tin alloy grains sulfurizes, resulting in copper tin sulfide, while the zinc forms volatile zinc sulfide on top. The formation of the CZTS compound takes place at the zinc sulfide/copper tin sulfide interface. Some copper-tin sulfide grains can have a very small area of contact with zinc sulfide. This results in the only partial formation of the CZTS compound. The probable solution to the elemental distribution problem might be the co-electrodeposition of Cu-Sn alloy (bronze) and the zinc on top, to form a stable precursor and minimize the interdiffusion in the precursor layer.

4.3. Study of CTSe

4.3.1. Electrodeposition of Cu-Sn alloy

Kesterite compound formation is a very complex process. Chalcogenization of an alloy containing three different metals is a difficult task. For a better understanding of the alloy chalcogenization, the study of CTSe (copper tin selenide) was carried out. Cu-Sn precursor layer was deposited onto the SLG/Mo substrate using a standard three-electrode electrochemical cell. Mo surface was cleaned prior to the deposition, as described in the previous chapter. The reference electrode (Ag/AgCl/KCl) was placed near the WE through the Lugin capillary, and as a counter electrode, Pt plate was used. Potential values (E_C) reported in this chapter will be with respect to Ag/AgCl/KCl reference electrode.

The solution used for electrochemical deposition contained 20 mM $CuSO_4$, 10 mM $SnSO_4$ and 0,1 M of tri-sodium citrate. The pH was adjusted to value of 5.75 using NaOH. Usually, Cu-Sn precursor is formed by sequential electrodeposition of copper and tin. The Co-deposition of Cu-Sn alloy is more complicated than single metal deposition but more convenient and a lot faster. Previous work [144] on the electrodeposition of Cu-Sn alloy suggests using 0.5 M of sodium citrate in electrolyte solution. A large amount of sodium citrate in the solution can lead to the incorporation of significant quantity of citrate ions into the electrodeposited Cu-Sn film. We reduced-sodium citrate amount five times, to 0.1 M. Reducing below 0.1 M resulted in a loss of electrolyte solution stability. Potentiostatic polarisation curves of the WE (SLG/Mo) in the electrolyte solutions containing different amounts of tri-sodium citrate are given in figure 43. The dashed line represents the curve of the solution containing 0.5 M trisodium citrate and the solid line – 0.1 M tri-sodium citrate. The lower curves belong to stirred solutions. Dotted vertical lines separate the potential ranges of Cu, Cu with underpotential Sn, and Cu-Sn alloy electrodeposition. Hydrogen gas electrochemical reduction potential is also marked. The cathodic potential E_C of -1.0 V (the potential of limiting current density for Cu and Sn reduction) was chosen for the deposition of precursor films. The electrochemical evolution of the hydrogen gas at this potential was rather slow. The electrolyte solution was constantly stirred throughout the experiment; this leads to increased current density by a factor of ~5.

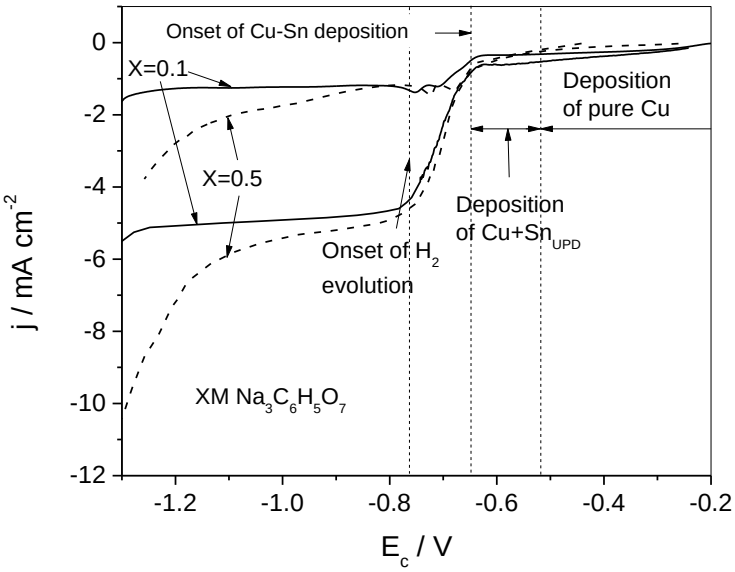

Figure 43. Potentiostatic polarisation curves of Mo working electrode in an electrolytic solution containing 20 mM $CuSO_4$, 10 mM $SnSO_4$ and different tri-sodium citrate concentrations (solid line 0.1 M and dashed line 0.5 M). Lower curves depict stirred solution, upper non-stirred. Potential scan rate: 2 mV s^{-1}.

To control the ratio of Cu/Sn, we did a series of experiments with electrolyte solutions containing various quantities of $SnSO_4$ (sodium citrate concentration in all of the solutions was 0.1 M), which yielded linear dependency Cu/Sn ratio on $SnSO_4$ concentration in the electrolyte solution given in fig. 44.

In figure 45, we see SEM surface images of the Cu-Sn samples deposited from the solution containing 0.5 M of tri-sodium citrate (image a) and 0.1 M (image b). The surface morphology advantage (continuous and uniform layer compared to rough surface composed of large agglomerates of small crystallites) of the Cu-Sn layer electrodeposited from electrolyte solution containing 0.1 M tri-sodium citrate (fig. 45 b)) can be observed compared to the surface formed in the solution containing 0.5 M the latter (fig. 45 a)).

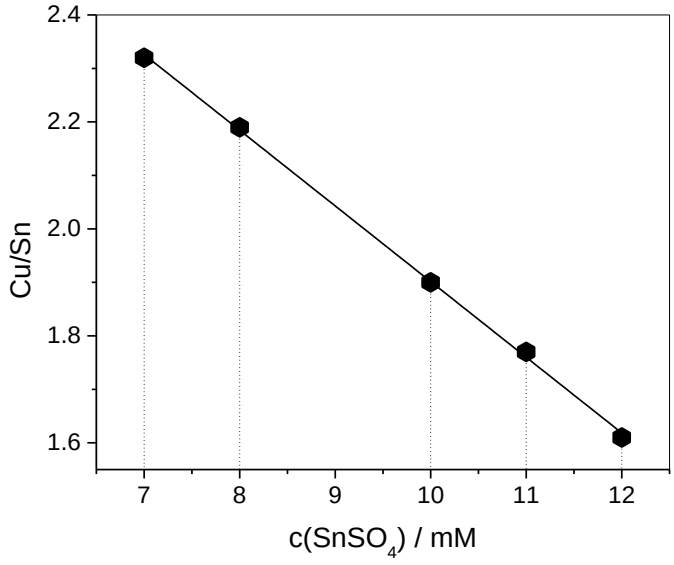

Figure 44. The dependency of Cu/Sn ratio in the deposited films on $SnSO_4$ concentration in the electrolyte solution. The elemental composition was determined using EDX measurements.

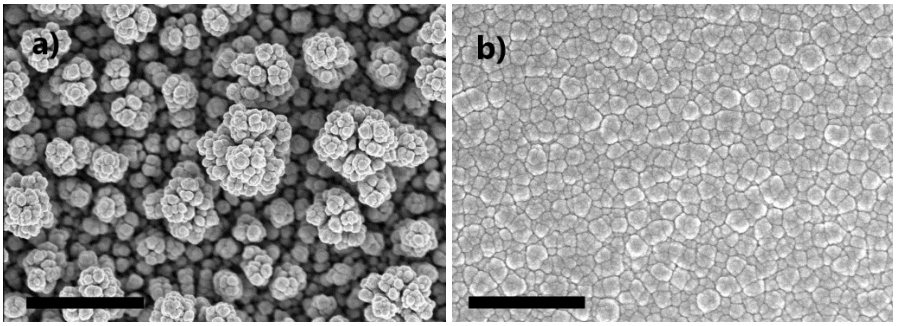

Figure 45. The surface morphology of Cu-Sn layers deposited from the solution containing 20 mM $CuSO_4$, 10 mM $SnSO_4$, and 0.5 M of tri-sodium citrate - a); and from solution containing 0.1 M of tri-sodium citrate - b), both layers were deposited from stirred solutions. The scale bar denotes 2 µm.

4.3.2. Selenization of Cu-Sn films

The co-electrodeposited Cu-Sn films were selenized in a range of temperatures to observe the impact of temperature on phase composition and

CTSe crystalline structure. The surface and cross-section SEM images of CTSe films, fabricated by selenizing Cu-Sn precursors co-electrodeposited from the solutions with different quantities of sodium citrate, are given in the fig. 46. The selenization was performed at a temperature of 500 °C. The images A and B depict CTSe film formed from Cu-Sn precursor with 0.5 M sodium citrate concentration in solution, C, and D images of the CTSe film from 0.1 M sodium citrate solution. The film obtained by using Cu-Sn precursor, with fewer $Na_3C_6H_5O_7$ in the electrolyte solution, is smoother and more compact. Cross-section view of CTSe films showed a lower amount of voids, and a better thickness distribution throughout the entire layer for the film fabricated using a lower amount of sodium citrate in the electrolyte solution.

The modification of the Cu-Sn electrolyte solution showed an improvement in surface morphology. Obtained good quality of the Cu-Sn precursor layer suggests using it in the further work (Cu-Sn/Zn two-step deposition instead of standard three-step Cu/Sn/Zn or two-step Cu-Zn/Sn precursor formation) to fabricate Cu-Sn-Zn precursor for CZTS(Se) solar devices.

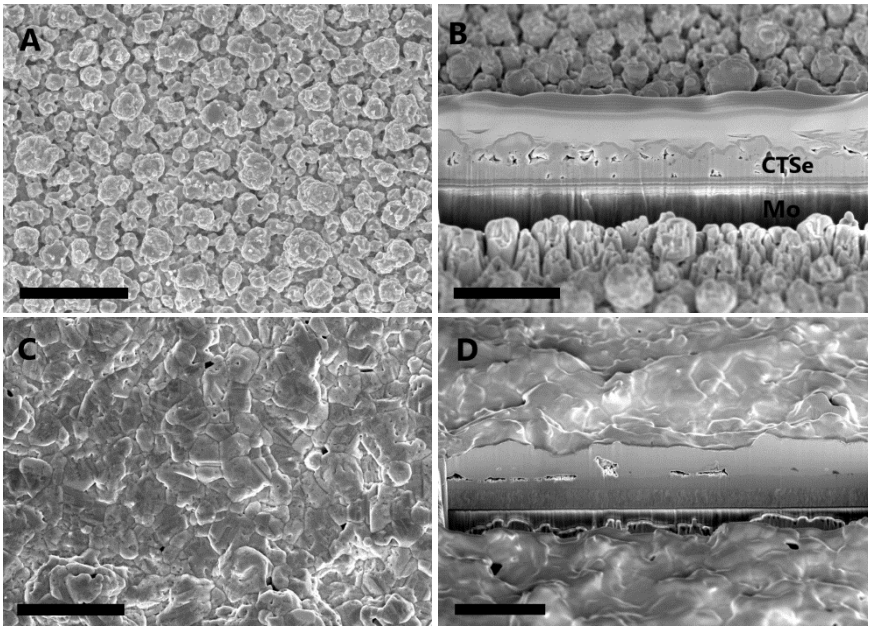

Figure 46. SEM surface and cross-section images of the CTSe films manufactured using Cu-Sn precursors electrodeposited in solutions containing different quantity of sodium citrate: A and B images - 0.5 M; C and D images - 0.1 M. Scale bar denotes 4 μm.

4.3.3. Selenization temperature impact on phase composition

The Cu-Sn precursor layers deposited from an electrolyte solution containing 0.1 M sodium citrate was used to determine the relation between selenization temperature and CTSe film crystalline structure and phase composition. XRD patterns are given in Figure 47 for CTSe films selenized at different temperatures between 400 and 560 °C for 20 minutes. The composition of all precursor films was about 65 at.% copper, ~ 35 at.% tin (Cu/Sn = 1.86).

After the selenization Cu/Sn ratio increased to 1.91 – 1.94, indicating a loss of tin during the thermal treatment. Lower temperatures were also considered and tested. At a temperature of 350 °C, not all of the Cu-Sn precursor was selenized, XRD pattern not presented.

The phase of the intermetallic compound η-$Cu_{6,26}Sn_5$ (ICDD card # 00-047-1575) was present along with orthorhombic Cu_2Se (# 00-037-1187) and SnSe (# 00-048-1224) phases. Some of the XRD peaks could be attributed to Cu_2Se (# 01-088-2043) and Cu_2SnSe_3 (# 01-089-2879) with the cubic structure.

The intermetallic Cu-Sn phases became untraceable by the XRD method at a temperature of 400 °C. Still, low amounts of $Cu_{1.8}Se$ (# 01-088-2046) and CuSe (# 00-049-1457) copper selenides were present in the layer.

Increasing the selenization temperature up to 450 °C, the XRD pattern showed peaks of cubic Cu_2SnSe_3 (# 01-089-2879) and one peak of CuSe (# 00-049-1457) at 2Θ angle of 31.15 °. The $MoSe_2$ layer thickening can be observed since the intensity of $MoSe_2$ peaks apparently increased.

CTSe film selenized at a 500 °C still consisted of the cubic Cu_2SnSe_3 and a small amount of CuSe phases. The $MoSe_2$ thickness further increased. Increasing the selenisation temperature to 560 °C led to the emergence of small XRD peaks at 2Θ angles of 15.35 and 19.88 ° suggesting the monoclinic Cu_2SnSe_3 structure (# 00-056-1111, and # 04-012-4693) was formed. After all, the presence of cubic Cu_2SnSe_3 cannot be ruled out, since the most intense peaks of both structures completely overlap if the lattice parameter of the cubic phase equals to 0.569 nm. The dependence of the cubic lattice parameter on the selenization temperature is shown in Figure 48.

The cubic Cu_2SnSe_3 lattice parameter was calculated using XRD patterns. It was determined that the lattice parameter of cubic Cu_2SnSe_3 increases when the selenization temperature is raised, 0.5645±0.0015 nm at a temperature of 385 °C up to 0.570±0.002 nm at 560 °C (Figure 48).

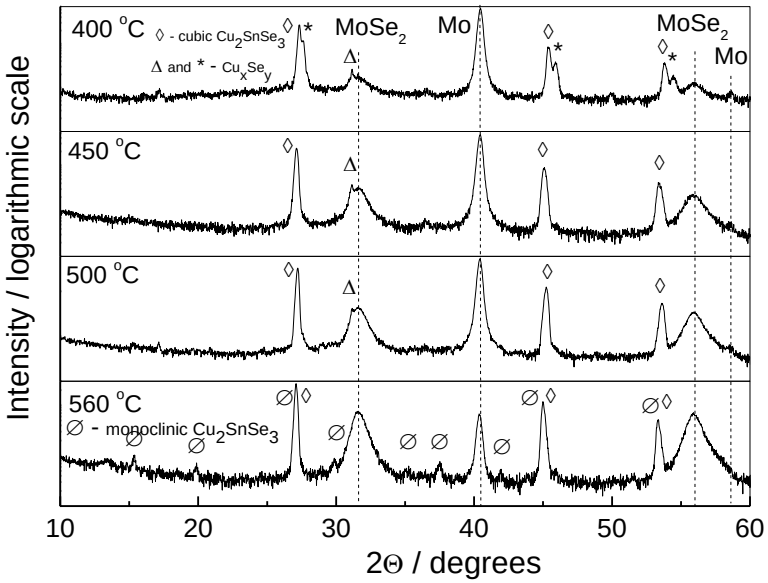

Figure 47. The XRD patterns of CTSe films synthesized in the temperature range from 400 to 560 °C. The atomic composition of the Cu-Sn precursors was 65.4±1.0 at.% of Cu and 34.6±1.0 at.% of Sn. ◊ - cubic Cu_2SnSe_3; * - cubic $Cu_{1,8}Se$; Δ - hexagonal CuSe; ∅ - monoclinic Cu_2SnSe_3.

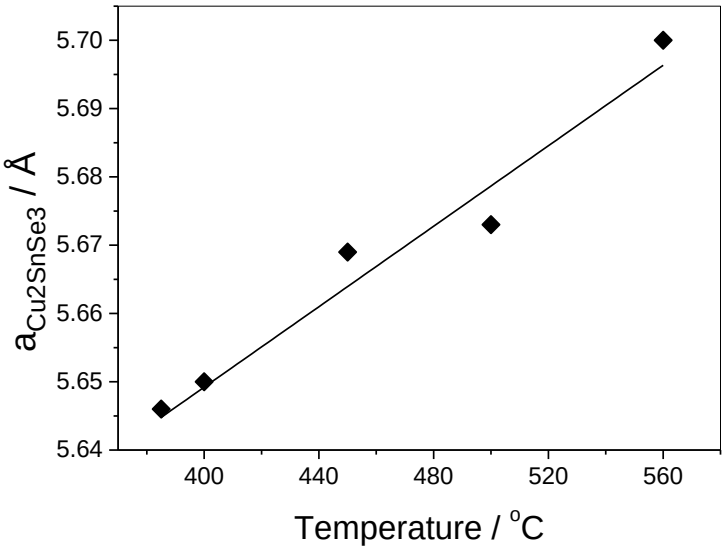

Figure 48. The dependence of the cubic Cu_2SnSe_3 lattice parameter *a* on the selenization temperature.

4.3.4. Raman spectroscopy of cubic and monoclinic Cu2SnSe3

To get more reliable information on phases present in the synthesized CTSe layers Raman spectroscopy has been used. Before measuring the Raman spectrum, CTSe films were immersed in a 5 % KCN solution to dissolve the copper selenides. Figure 49 shows the Raman spectra of CTSe films selenized at the temperatures of 500 °C (A) and 560 °C (B). Voigt function was used to deconvolve the Raman spectra into separate bands.

The Raman spectrum for the cubic only structure of Cu_2SnSe_3 (according to XRD) contains bands (fig. 49 A), which wavenumbers correlates well with those calculated for the monoclinic structure of Cu_2SnSe_3 [145] (Table 13.).

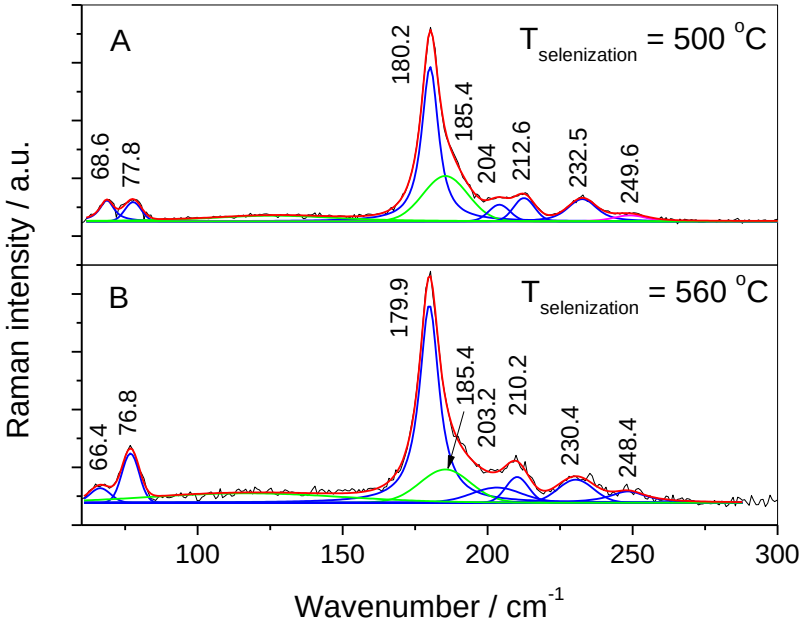

Figure 49. Raman spectra of the CTSe samples: A – annealed at the temperature of 500 °C, and B – at 560 °C. Excitation wavelength used 632.8 nm (0.05 mW); spectral region is 50–300 cm^{-1}.

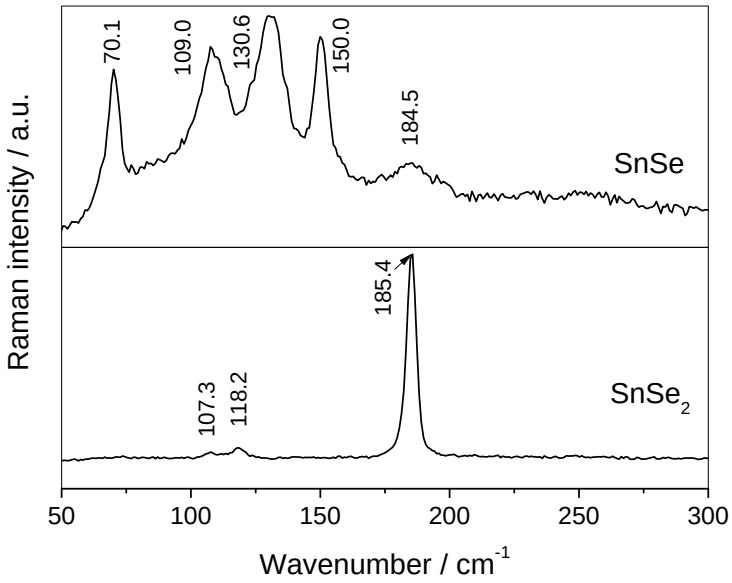

Figure 50. The Raman spectra of pure SnSe (top) and pure $SnSe_2$ (bottom) in the 50-300 cm^{-1} spectral region. An excitation wavelength of 532 nm (0.06 mW) was used.

Table 13. Calculated and measured band wavenumbers of Raman spectrum for monoclinic and cubic CTSe structures.

Spectrum	Band wavenumber, cm^{-1}						
Calc. [43]	67.7	78.6	181.6	203.8	211.7	230.5	-
Fig. 51 A	68.7	77.7	180.2	204.1	212.6	232.7	249.1
Fig. 51 B	66.4	76.8	179.9	203.2	210.2	230.4	248.4
Exper.[15]			179	199		233	250
Exper.[44]		83	178	204		231	244

The peaks of the cubic structure Raman spectrum were marginally shifted to higher energies (compared to the calculated values), only the main peak (180.2 cm^{-1}) was shifted to lower energies. However, these shifts are very modest and may occur due to the equipment inaccuracy. Also, a broad band was observed at 185.4 cm^{-1}. It can be attributed to $SnSe_2$ [146, 147]. To verify the presence of $SnSe_2$ in CTSe films, we measured the Raman spectrum of pure SnSe and $SnSe_2$ (Figure 50).

The $SnSe_2$ spectrum shows an intensive band at 185.4 cm^{-1} and two low-intensity bands at 107.3 and 118.2 cm^{-1}. Pure SnSe (Alfa-Aesar, 99.999%)

Raman spectrum presents one low-intensity feature at 184.5 cm^{-1} and four high-intensity bands at 70.1, 109.0, 130.6, and 150.0 cm^{-1}. Pure spectra of $SnSe_2$ (Ossila, 99.995%) confirmed that CTSe films contained a very small amount of precisely $SnSe_2$.

Raman spectrum of CTSe film synthesized at a temperature of 560 °C showed the same bands as the spectrum of cubic Cu_2SnSe_3 only. Nonetheless, all bands had a minor shift to the lower energies (compared to the calculated values). This abnormality can be due to the lower structure ordering in the layer. The relative intensity of the Raman band at 76.8 cm^{-1} was fairly increased compared to that of 77.8 cm^{-1} of the cubic Cu_2SnSe_3 spectrum. That could indicate the presence of both cubic and monoclinic Cu_2SnSe_3 structures in both samples. In the CTSe samples synthesized at a temperature of 500 °C, cubic polymorph was dominant, while in the sample selenized at a temperature of 560 °C, the dominant polymorph was monoclinic.

Study of the monoclinic Cu_2SnSe_3 [145] suggests only one band in the low energy region, at 83 cm^{-1}. In our work, we can assume that band at 76.8 cm^{-1} could indicate the monoclinic structure. The band intensity is much greater in the Raman spectrum of the sample containing monoclinic Cu_2SnSe_3 than in the sample containing only cubic Cu_2SnSe_3 (according to the XRD data). Therefore, we argue that this band can be used as a marker of the monoclinic Cu_2SnSe_3 structure.

4.3.5. Photoelectrochemical studies of CTSe films

Photovoltammetric studies were performed for CTSe films synthesized at different selenization temperatures. Pulses of photocurrent were measured while illuminating a film immersed in a 0.2 M $Eu(NO_3)_3$ aqueous solution. Photocurrent pulses of CTSe film selenized at a temperature of 500 °C are depicted in Figure 51. Pulses were measured at different cathodic potentials, E_C. Top row (A) shows the photovoltammetric pattern of as-synthesized CTSe, bottom row (B) synthesized and annealed after the selenization in air at a temperature of 200 °C for 2 hours. Indications “On” and “Off” represent the points at which illumination of the film started and ended. CTSe films under illumination produced negative photocurrent that shows p-doping of CTSe films, proving p-type conductivity. CTSe films were synthesized on Mo films (conductive layer). Therefore, it was impossible to measure conductivity and doping level by using the Hall method as it was performed for CTSe films deposited on glass substrates by other research groups [147-151].

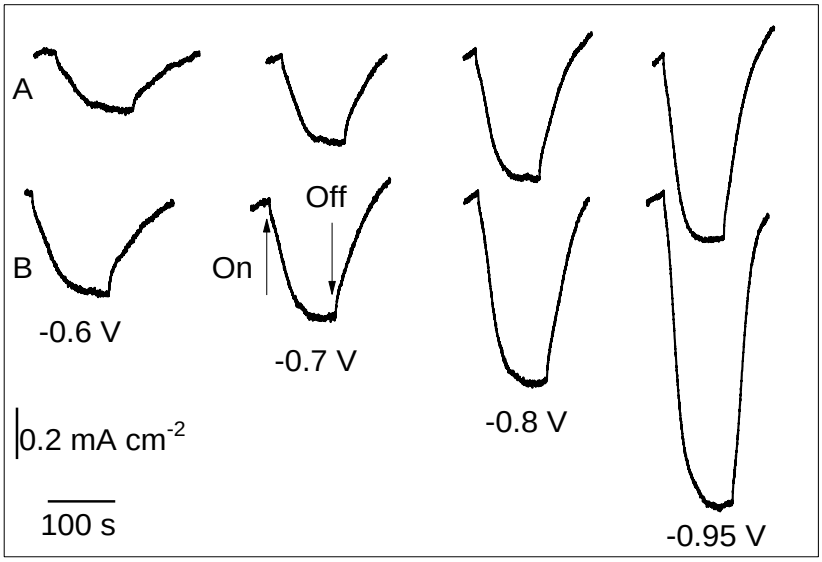

Figure 51. Photocurrent pulses for CTSe film (in 0.2 M $Eu(NO_3)_3$ solution) selenized at a temperature of 500 °C. A – as-synthesized; B – after post-annealing in air for 2 h at a temperature of 200 °C. The photocurrent density significantly increased after annealing the CTSe samples at the temperature of 200 °C.

Dependence of photocurrent density (j_{photo}) on selenization temperature is given in fig. 52. The photocurrent density was measured at the potential of – 0.8 V. CTSe films were immersed in KCN 5 % solution prior to the measurements to dissolve the copper selenides.

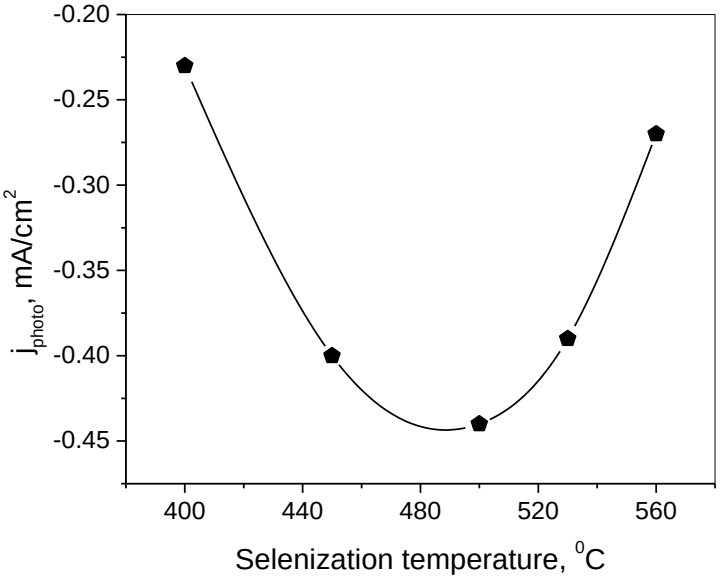

Figure 52. Dependence of the Cu_2SnSe_3 film produced photocurrent (in 0.2 M $Eu(NO_3)_3$ solution) on the selenization temperature at the cathodic potential of –0.8 V. Photocurrents were measured before the post-annealing in 200 °C.

CTSe film selenized at a temperature of 500 °C presented the largest photocurrent. The film consisted of mostly cubic Cu_2SnSe_3. Films prepared at a higher selenization temperature showed lower photocurrent, which is very unexpected since reference [152] suggests that cubic Cu_2SnSe_3 has a higher hole concentration compared to the monoclinic Cu_2SnSe_3, that basically means it should be more photoactive. Anyhow, the performance of the solar device is also affected by the presence of binary selenides [146], antisite defects, and vacancies [153]. Series resistance can also have an impact on photocurrent; this points to Mo back contact and the thickness of the $MoSe_2$ layer. SEM images of the CTSe/Mo cross-section showed an increase of $MoSe_2$ thickness related to higher selenization temperature (fig. 53). Increasing the selenization temperature reaction between Mo and Se is more intense, resulting in thicker $MoSe_2$ layer. It is possible that the thicker molybdenum selenide layer had an impact on the photoactivity of CTSe films selenized at a higher temperature.

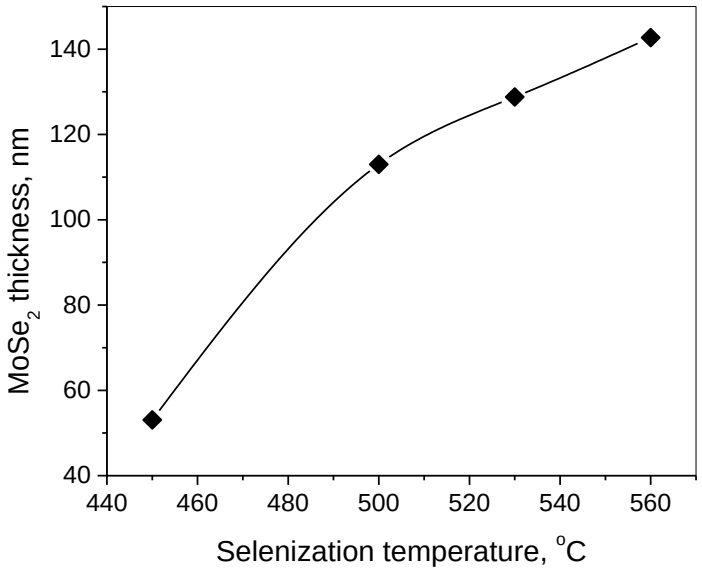

Figure 53. The dependency of the thickness of the $MoSe_2$ layer on the selenization temperature.

Low-temperature post-treatment of Cu_2SnSe_3 films in nitrogen gas [154] and annealing of Cu_2SnS_3 films in vacuum [153] were suggested to lower the concentration of copper vacancies, copper and zinc antisite defects (V_{Cu}, Cu_{Zn}, Zn_{Cu}) and thus, improve the photovoltaic characteristics of the device. We applied this method for the films selenized at a temperature of 500 °C. First, we tried a film treatment at a temperature of 100 °C for 24 hours. No impact on photocurrent was noticed.

Increasing the post-annealing temperature to 200 °C showed a substantial increase in CTSe films generated photocurrent even after 2 hours of treatment. An even greater increase in photocurrent was recorded after 18 hours of post-annealing (fig. 54). The study presented in ref. [153] suggests that 200 °C is a critical temperature (T_C) for the kesterite material. At the temperature below T_C, the ordering equilibrium degree increases, while at the temperature above T_C, the kesterite is considered to be in the disordered equilibrium state. The Cu_2SnSe_3 photoelectrochemical response has decreased after post-annealing in the N_2 atmosphere at a temperatures in the range of 150 – 300 °C [154]. This decrease can be due to undissolved copper selenides. In our experience, CTSe films photoelectrochemical response can be lower by as much as 30 % if not treated in a KCN 5 % solution after the synthesis.

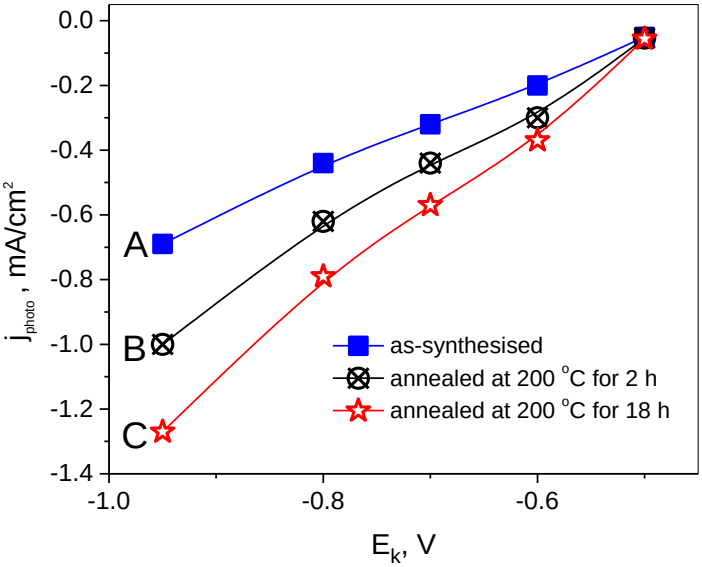

Figure 54. Photocurrent of the CTSe (Cu/Sn = 1.9) layer selenized at a temperature of 500 °C for 20 min. as a function of cathodic potential E_c in 0.2 M $Eu(NO_3)_3$ solution. A – as-synthesized CTSe sample; B – annealed for 2h at a temperature of 200 °C; C – annealed for 18 h. Annealing was performed in air atmosphere.

The electrolyte solution developed in the CTSe research was used in the later study of CZTS films for electrodeposition of precursor films. It was found that Cu-Sn alloy forms only cubic CTSe when selenized in temperatures up to 500 °C, monoclinic CTSe was found only in the films selenized at a temperature of 560 °C. Also, we found that it is possible to separate the cubic and monoclinic CTSe phases using the Raman spectroscopy.

4.4. Study of kesterite films formed using Cu-Sn/Zn precursor

4.4.1. CZTS samples and photoelectrochemical response

This part of the work presents the results of a kesterite study where the Cu-Sn-Zn precursor was formed by electrodeposition of the Cu-Sn alloy and zinc layer on the top. We have synthesized and studied three groups kesterite films with different stoichiometry. Samples with chemical composition Cu-poor Zn-poor, Cu-poor Zn-stoichiometric, and Cu-poor Zn-rich were synthesized. The chemical composition of the samples was controlled by the thickness of

the Zn layer. The chemical composition of synthesized kesterite was determined after KCN and HCl treatments (for removing secondary phases). Atomic ratios (Cu/(Zn+Sn), Zn/Sn) of elements in each sample group are given in Table 14.

Table 14. The chemical composition (at. %) and atomic ratios of elements of the studied samples.

Sample	Cu	Zn	Sn	S	Cu/(Zn+Sn)	Zn/Sn
Zn-rich	18.48	14.48	11.32	55.72	0.72	1.28
Stoichiometric	17.86	12.15	11.94	58.05	0.74	1.02
Zn-poor	18.89	10.81	12.8	57.5	0.80	0.84

The compositions shown in Table 14 are of one of the samples from every group with composition closest to the average of the sample group. Photocurrent density j_{ph} as a function of the CZTS/Mo electrode potential E (versus Ag/AgCl/KCl reference electrode) is given in fig. 55. The j_{ph} values presented in graphs are for potential of -0.5 V.

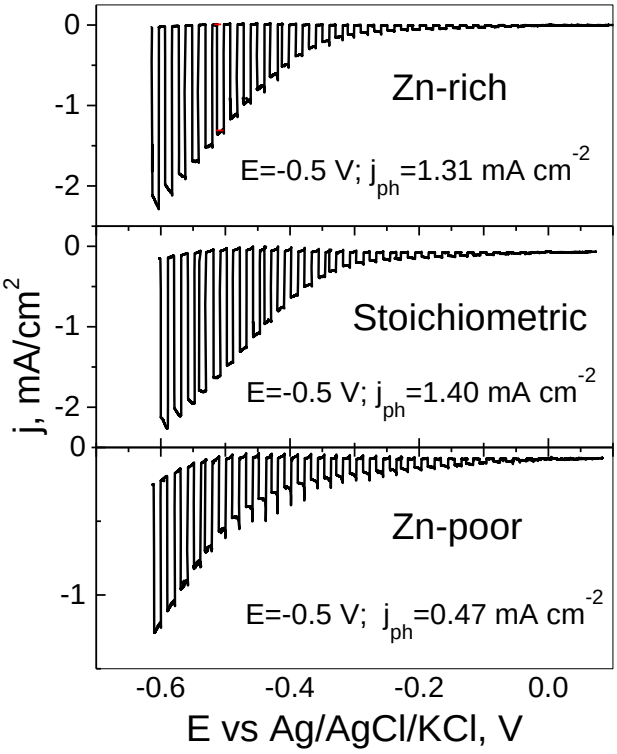

Figure 55. Photoelectrochemical current density (j_{ph}) as a function of potential E for the CZTS films under chopped illumination. (in a 0.1 M $Eu(NO_3)_3$ solution) The potential scan rate is 1 mV/s. Light intensity 100 mW/cm^2.

The highest photo-response was shown by the Stoichiometric CZTS sample. The lowest j_{ph} was of the Zn-poor sample. Pulses of j_{ph} show a spike at the light turning On and turning Off moments. These spikes and their size are related to a slow recombination kinetics of trap states [155]. The current density occurring due to this phenomenon is marked as j_{tr}. Figure 56 depicts the photocurrent pulse. That fragment of j~f(E) dependence was taken from the measurements of the CZTS sample Stoichiometric. The total current density consists of the photo-current j_{ph} and spike j_{tr}. The values of j_{tr} were measured 0.040, 0.025, and 0.044 mA/cm^2 for Zn-poor, Stoichiometric and Zn-rich samples, respectively. The lowest j_{tr} was observed for the Stoichiometric sample.

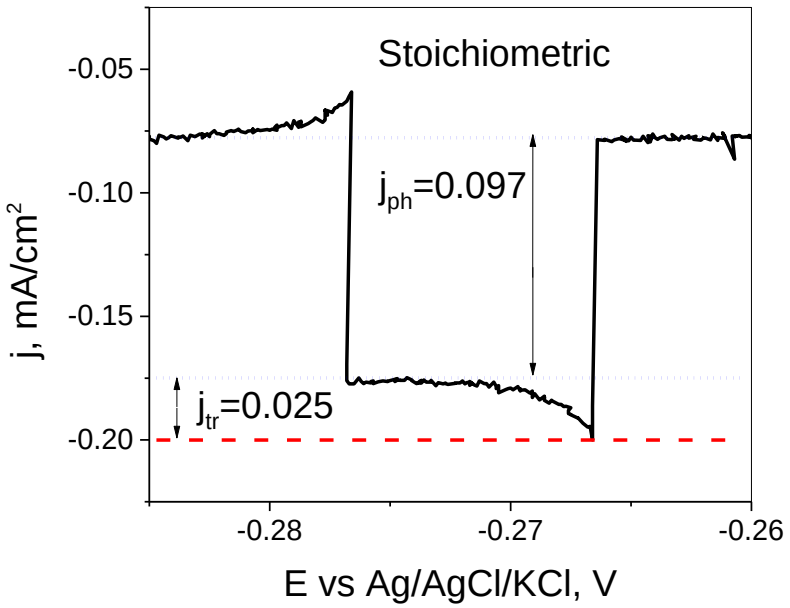

Figure 56. The fragment of the measured photovoltammogram (Stoichiometric CZTS sample in a 0.1 M $Eu(NO_3)_3$ solution under chopped illumination). The potential scan rate is 1 mV/s. Light intensity is 100 mW/cm^2.

CZTS film processing in KCN and HCl solutions made a large impact on the recombination effect. Figure 57 shows the decrease of j_{tr} as compared to the unprocessed samples. Along with recombination decrease at the CZTS/$Eu(NO_3)_3$ interface, film processing with KCN and HCl gave a positive effect on j_{ph}, the current density value (for Stoichiometric sample) increased by a factor of 7 (at a potential of -0.5 V). Also, the active surface of kesterite films increased after dissolving zinc and copper sulfides [156]. These binary phases, when located on the surface of kesterite, acts as a resistive barrier for carriers in p-type CZTS or as traps [52]. After the treatments with KCN and HCl, it is possible to use parameter j_{ph} to evaluate the photovoltaic efficiency of the kesterite film in bulk, because all of the samples were treated with the same KCN and HCl solutions.

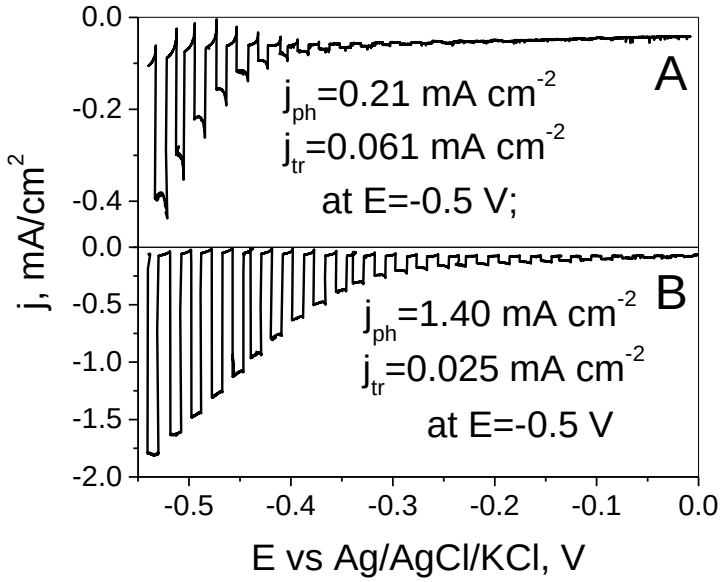

Figure 57. Current density as a function of the potential (CZTS sample Stoichiometric in a 0.1 M $Eu(NO_3)_3$ solution under chopped illumination): A - as-synthesized sample; B - the same sample after treatment in the KCN and HCl solutions.

4.4.2. Phase composition and order/disorder in CZTS

To establish a relation between photocurrent and point defects the Raman spectroscopy was used first. Also the ordering level S was ascertained where

value 0 means completely disordered and 1 – complete ordered. The Q and Q′ parameters were established by using the Raman spectra of the CZTS samples (near-resonant excitation wavelength of 785 nm was used) (fig. 58). $Q = I_{288}/I_{304}$ and $Q' = I_{338}/(I_{367} + I_{375})$ and I_i is an integral intensity of the respective kesterite Raman band [157]. The results are given in Table 15.

Table 15. The Q and Q′ parameters, type of structure, and ordering level S of the studied samples.

Sample	Cu/(Zn+Sn)	Zn/Sn	Q	Q′	Type of structure	S
Stoichiometric	0.66	1.02	2.5	2.0	B_S	0.4
Zn-rich	0.72	1.28	1.5	2.1	B_S	0.3
Zn-poor	0.80	0.84	2.4	2.5	B_S	0.4

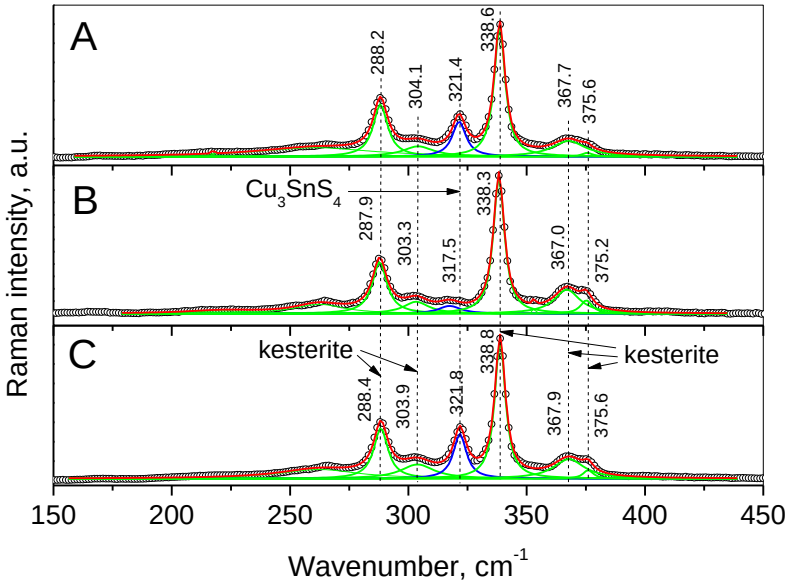

Figure 58. Raman spectra of the CZTS films. A – Zn-poor sample; B – Stoichiometric sample; C – Zn-rich sample. An excitation wavelength 785 nm.

The parameters Q and Q′ of the CZTS samples show B_S type structure (according to Ref. [157]. B_S type structure is an off-stoichiometric ordered CZTS with the stoichiometry of $Cu_{1.95}Zn_{1.06}Sn_{0.99}S_4$, using slow cooling after

the sulphuriztion. The disordered kesterite of the stoichiometry – B_Q is obtained by fast cooling or quenching after the sulphuriztion [157]. The Q and Q′ parameters for the fast cooled kesterite structure should be ≤ 1.0. Point defect clusters [$2Zn_{Cu}^{+}$ + Zn_{Sn}^{2-}] are characteristic of the B-type kesterite [157]. According to Ref. [21], ordering level S has a linear dependence on the Q parameter. Therefore, we adapted our measured Q values of CZTS samples (Table 15) to obtain ordering level S from the linear graph given in Ref. [18]. The samples showed ordering level S values of 0.28 – 0.45. The values are similar to those of the kesterite films synthesized using the tube furnace processing [158].

Order/disorder level in kesterites can also be evaluated by using the Raman spectrum parameter - full width at half maximum (FWHM) of the bands at 287 and 338 cm^{-1} [159]. FWHM values obtained from our samples Raman spectra and FWHM values for ordered (slow cooled) and disordered (quenched) kesterite samples from Ref. [159] are given in Table 16.

Table 16. FWHM values of our investigated samples and ones from literature.

Raman band	Slow cooled CZTS [23]	Quenched CZTS [23]	CZTS Stoichiometric	CZTS Zn-rich	CZTS Zn-poor
287 cm^{-1}	5.9 – 7.0	14.0 – 20.2	7.8	7.2	7.4
338 cm^{-1}	3.8 – 5.5	8.0 – 9.2	5.5	5.3	5.5

The FWHM values of our CZTS samples are very similar to the ordered kesterite (slow cooled) values. From our FWHM data, the CZTS film with Zn-rich composition showed the most ordered structure, i.e. lowest quantity of antisite defects. Nevertheless, the same Zn-rich sample had the largest quantity of Cu_3SnS_4 phase, according to the Raman spectra. Cu_3SnS_4 phase was indicated from the Raman spectra, specifically from the band at ~320 cm^{-1} (orthorhombic Cu_3SnS_4). The normalised intensities of the band were 11.5, 33.5, and 39.5 in arbitrary units for Stoichiometric, Zn-poor, and Zn-rich kesterite films, respectively.

To detect the presence and relative quantity of zinc sulfide secondary phase in kesterite samples, the Raman spectrum with an excitation wavelength of 325 nm was used, it provides the possibility to attain resonantly enhanced Raman spectrum for ZnS (fig. 59). The intense bands near 698.4, 1045.3, 1394.5, and low-intensity feature at 1743.3 cm^{-1} are associated with the second, third, fourth, and fifth-order peaks of fundamental longitudinal optical

(LO) phonon mode of ZnS at 351.5 cm^{-1}, respectively [160, 161]. The lower intensity bands visible at 633, 981.8, and 1318.4 cm^{-1} are due to higher-order combination bands of the fundamental LO and transverse optical (TO) phonon modes of ZnS [161]. Using resonantly enhanced Raman measurements, very low quantities of ZnS can be detected on the surface of the sample. The spectra showed that the sample with Zn-poor composition showed the lowest amounts of zinc sulfide, while the Zn-rich sample had the highest amount of ZnS secondary phase.

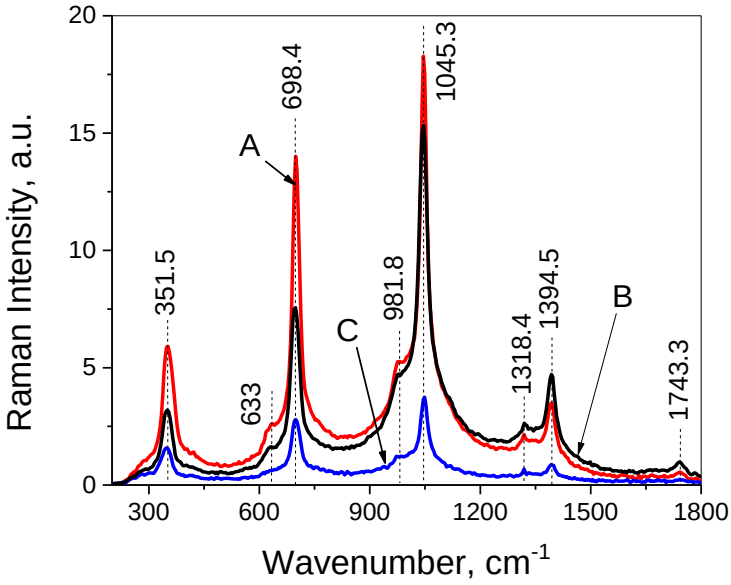

Figure 59. Raman spectra of the CZTS films. A – Zn-rich sample; B – Stoichiometric; C- Zn-poor. The excitation wavelength is 325 nm.

We also applied XRD measurements to analyse the layer phase composition and see how it correlate with the Raman analysis. Firstly, we conducted the XRD measurements using the Cu $K_{\alpha 1,2}$ radiation for determination of phase composition. XRD patterns of all the samples showed peaks attributable to off-stoichiometric kesterite $Cu_{1,885}Zn_{1,058}SnS_4$ (ICDD #01-080-8226). Also, in the as-synthesized CZTS samples, the secondary phase Cu_2S (#00-002-1284) was detected. Anyhow, XRD data of our CZTS samples showed no presence of zinc sulfide or ternary secondary phases. The main peaks of ZnS and ternary phases overlap with kesterite peaks and cannot be distinguished. After the KCN treatment of the films, copper sulfide peaks disappeared completely,

which indicates that all of the Cu_2S phase was on the surface of the kesterite film.

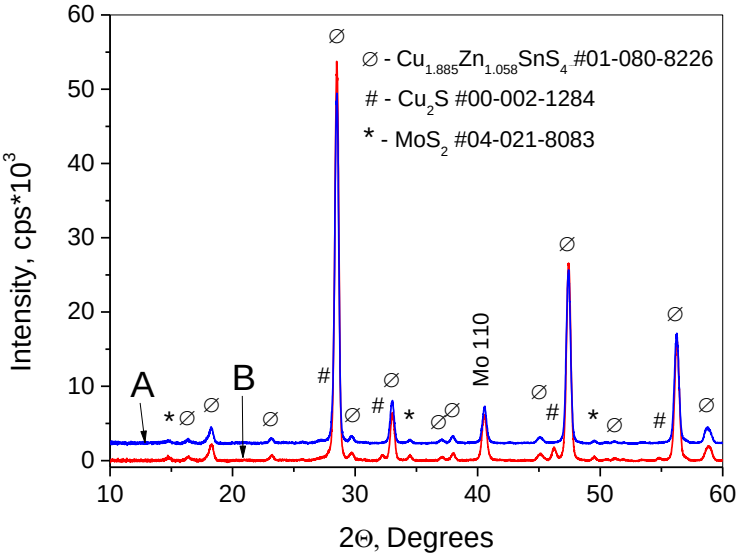

Figure 60. The Cu $K_{\alpha 1,2}$ radiation XRD patterns of CZTS sample Stoichiometric. Lower (B) pattern of as-synthesized, upper (A) after the treatment in the KCN solution.

The XRD patterns of the Stoichiometric kesterite sample are presented in fig. 60, which, according to the Raman measurements, had the lowest quantity of Cu_3SnS_4 (orthorhombic) phase. Nonetheless, XRD patterns of Zn-poor and Zn-rich films also did not show any peaks of the orthorhombic Cu_3SnS_4 phase, but in the Raman spectra, the bands were clearly visible. This discrepancy can be due to Raman`s better sensitivity for this particular phase when excitation wavelength was 758 nm. This excitation wavelength could be near-resonant for this compound since the second harmonic of the 1st order Raman signal at 321 cm^{-1} is seen at the wavenumber of 642 cm^{-1}. The Raman spectrum of the Zn-poor sample did not show the bands attributable to the orthorhombic Cu_3SnS_4 when the excitation wavelength of 532 nm was used, as you can see in Figure 61. Therefore, we can assume that in the Zn-rich sample, the excess zinc reacted with sulfur making large grains of binary ZnS compound, which did not participate in the kesterite synthesis. The lack of zinc resulted in the formation of the orthorhombic CTS phase.

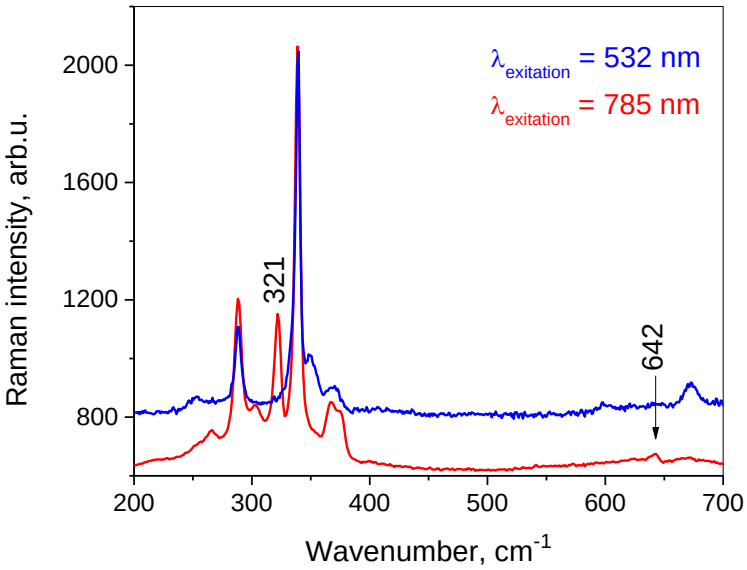

Figure 61. Raman spectra for the Zn-poor sample. The excitation wavelength for the blue spectrum – 532 nm, for the red one – 785 nm.

To support the results of XRD and Raman spectroscopy, we used SEM and TEM (EDX) analysis. Figure 62 shows the SEM and TEM cross-section images (samples for TEM analysis were prepared by using SEM/FIB) and elemental distribution profiles throughout the layer. The SEM cross-section image of the Stoichiometric kesterite sample showed that ZnS (white color areas) were located throughout the whole layer, and the quantity of zinc sulfide is greater than that in the Zn-rich sample. Also, the zinc sulfide grains were located closer to the surface of the kesterite layer in the latter sample.

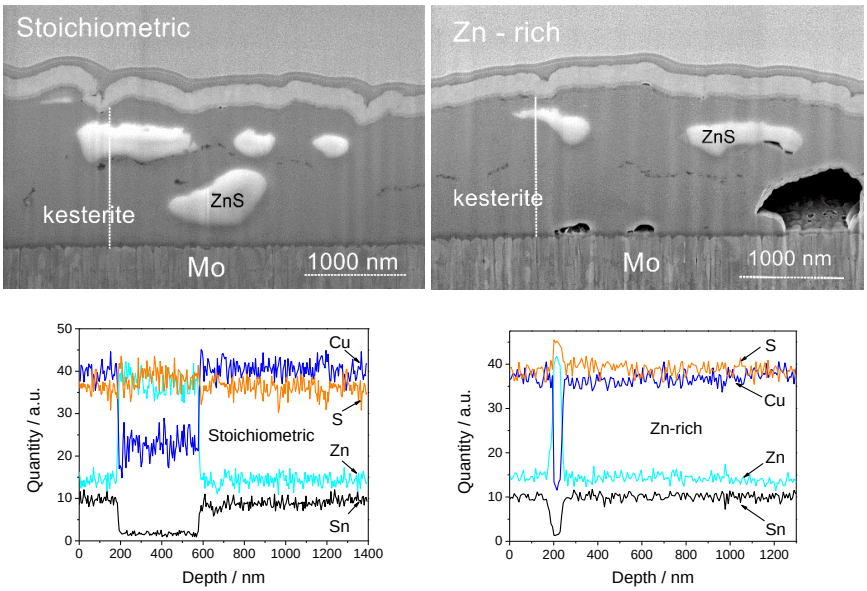

Figure 62. SEM images of FIB-made cross-sections and the elemental composition depth profiles of Stoichiometric (left) and Zn-rich (right) CZTS samples.

The EDX depth profiles of copper, zinc, tin, and sulphur are presented in figure 62. It shows that the distribution of the elements is uniform throughout the layer, we don't see any gradient towards the direction of molybdenum back contact, and that the white inclusions (as seen in SEM images) are definitely zinc sulfide.

4.4.3. High-resolution XRD measurements

The XRD measurements using Cu $K_{\alpha 1,2}$ did not yield sufficient information about the secondary phases in kesterite layers. The high-resolution XRD measurements were performed for our CZTS layers, using only Cu $K_{\alpha 1}$ radiation. Using these XRD patterns, we were able to determine the exact kesterite lattice parameters (more precise than those from Cu $K_{\alpha 1,2}$) and evaluate the order/disorder level in the kesterite structure. Also, high-resolution XRD gives us the possibility to determine the quantity of zinc sulfide in our samples. The fragment of the high-resolution XRD pattern of the Zn-rich sample is given in figure 63. The peaks 220 and 204 of the kesterite and peak 220 of ZnS (#00-005-0566) are well determined, so their integral peak intensity and FWHM can be precisely measured. CZTS 220 and ZnS 220

peak integrated intensities were used to calculate the quantity (volume percentage) of zinc sulfide in the kesterite layer.

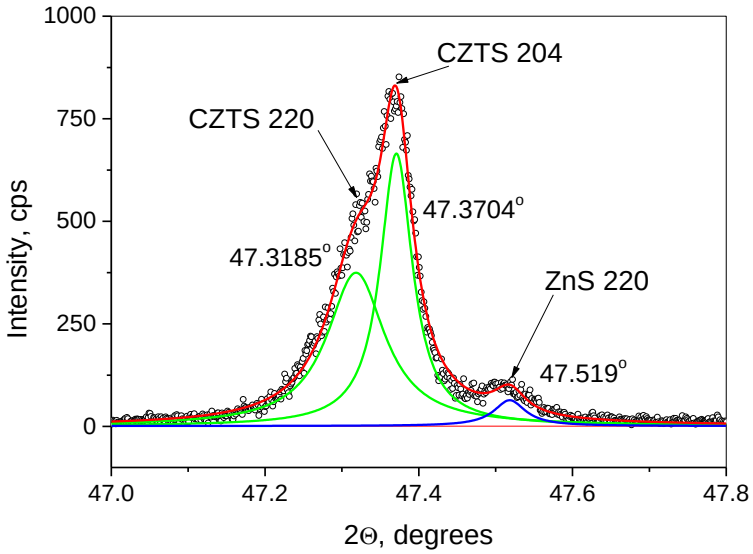

Figure 63. XRD pattern fragment of the Zn-rich sample, measured using Cu $K_{\alpha 1}$ radiation.

Table 17. Lattice parameters a and c, $2\Theta_{004}$-$2\Theta_{200}$ and FWHM values, crystallite size D_{200}, and amounts of ZnS in our investigated samples.

Sample	a, Å	c, Å	($2\Theta_{004}$-$2\Theta_{200}$)	FWHM 200	FWHM 004	D_{200}, nm	ZnS, vol. %
Stoichiometric	5.4288	10.8288	0.089± 0.005°	0.0913°	0.0340°	157	13.9
Zn-rich	5.4281	10.8308	0.080± 0.004°	0.1187°	0.0327°	107	6.6
Zn-poor	5.4281	10.8319	0.076± 0.006°	0.1290°	0.0384°	95	2.3

Calculation results are presented in Table 17. According to XRD measurements, the HCl treatment of synthesized CZTS samples did not affect

the quantity (XRD peak intensity) of ZnS. We assume that a very small part of the zinc sulfide present in the layer was located on the film surface.

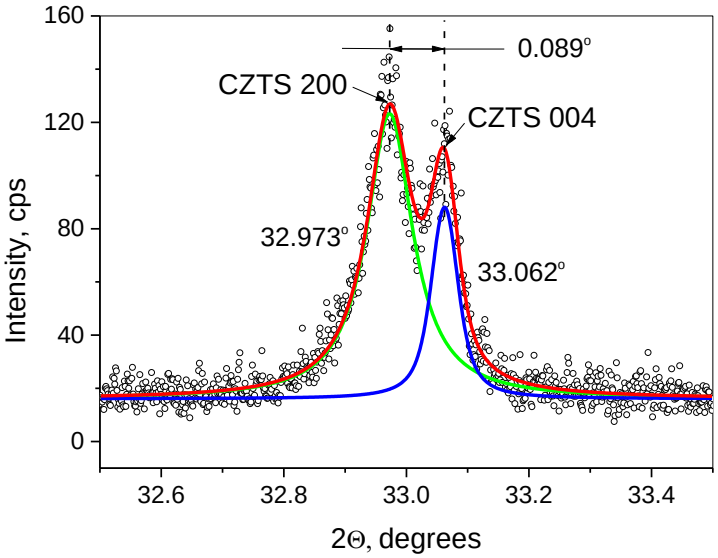

Figure 64. Fragment of XRD pattern of the Stoichiometric sample, measured using Cu $K_{\alpha 1}$ radiation.

Figure 64 shows a fragment of XRD pattern of the Stoichiometric sample. In this fragment we see the 200 and 004 peaks of the kesterite. The difference between $2\Theta_{max}$ values at the maximum peaks intensity shows the order/disorder level of the kesterite structure. The 2Θ difference for the ordered Zn-rich Cu-poor kesterite (A-type) structure is ~ 0.119°, when the difference for the Cu-rich Zn-poor kesterite structure (C-type) is only 0.061° [162]. Table 17 presents the measured difference of $2\Theta_{max}$ values for our CZTS samples. All of our samples yielded values between 0.076° and 0.089°. Results agree well with the order/disorder levels S, very similar to the ones determined using the Raman spectroscopy method.

$2\Theta_{max}$ values were also used to determine the lattice parameters of kesterite, a and c were calculated using the peaks 200 and 004, respectively. Calculated kesterite lattice parameters of our CZTS samples have shown lower values than the ones characteristic of the Cu-poor and stoichiometric kesterite [163]. Our kesterite lattice parameters were compared to the ones given in Ref. [163] the best match for a and c values of our kesterite was the off-stoichiometric Zn-poor Cu-rich kesterite ($Cu_{2.078}Zn_{0.909}Sn_{1.022}S_{4.000}$). The difference between 200 and 004 peaks equals 0.085° for this structure and is very similar with

those obtained for our samples. This particular off-stoichiometry (C-type) in kesterite is known to contain [$2Cu_{Zn}^{-} + Sn_{Zn}^{2+}$] clusters of antisite defects [67]. These point defects have a big (negative) impact on the performance of CZTS as a solar device.

The size of crystallites D_{200} was calculated using the Scherer equation, FWHM values of the peak 200 from XRD pattern were processed. As an instrumental broadening, the FWHM value of the LaB_6 peak 110 was subtracted from the FWHM values of the kesterite peak 200. The LaB_6 standard FWHM value was similar to the FWHM value of kesterite peak 004, which means the crystallites size in the crystallographic direction [001], D_{004} is larger than 250 nm in all of the measured samples. For all of the measured samples, the FWHM of kesterite peaks with indices h00 and hk0 were always about 3 times broder than the FWHM of peaks h01 or 001 indices, which means that the order level in the crystallographic directions of <100> and <110> was lower than order level of <001> and <h01>. Therefore, crystallites size in <100> and <110> directions is a sensitive parameter when evaluating the order/disorder level in kesterites, unlike the averaged crystallite size independent of crystallographic direction.

The correlation between the crystallites size D_{200} and generated photocurrent density was found. The samples with larger D_{200} crystallites showed higher j_{ph} and lower j_{tr} values. In our case, the CZTS sample Stoichiometric had the largest crystallites (D_{200}). The height of the spikes j_{tr} should be greater for the kesterite with smaller crystallites and grains since the j_{tr} is a consequence of the recombination at the interface of kesterite film and $Eu(NO_3)_3$ solution. These predictions agree very well with our results. The lowest values of j_{tr} were observed in the sample with the biggest crystallites and grains – Stoichiometric CZTS, the highest value of j_{tr} showed the sample with the lowest crystallinity – Zn-poor CZTS.

The value of the difference between the XRD peaks 200 and 004 correlates with the kesterite order/disorder. The higher difference means a more ordered structure of the kesterite (higher S value). The largest difference between the mentioned peaks was found in the Stoichiometric CZTS film, which also contained the highest amount of ZnS. The ZnS clusters should have a negative effect on the performance of the solar device, but Reference [155] suggests that if the zinc sulfide clusters are near the surface of the film, it can even improve the performance of the cell.

4.4.4. Photoluminescence measurements of CZTS layers

Photoluminescence (PL) spectroscopy is used very often to investigate the point defects in semiconductors generally, with no exception for kesterites [164, 165].

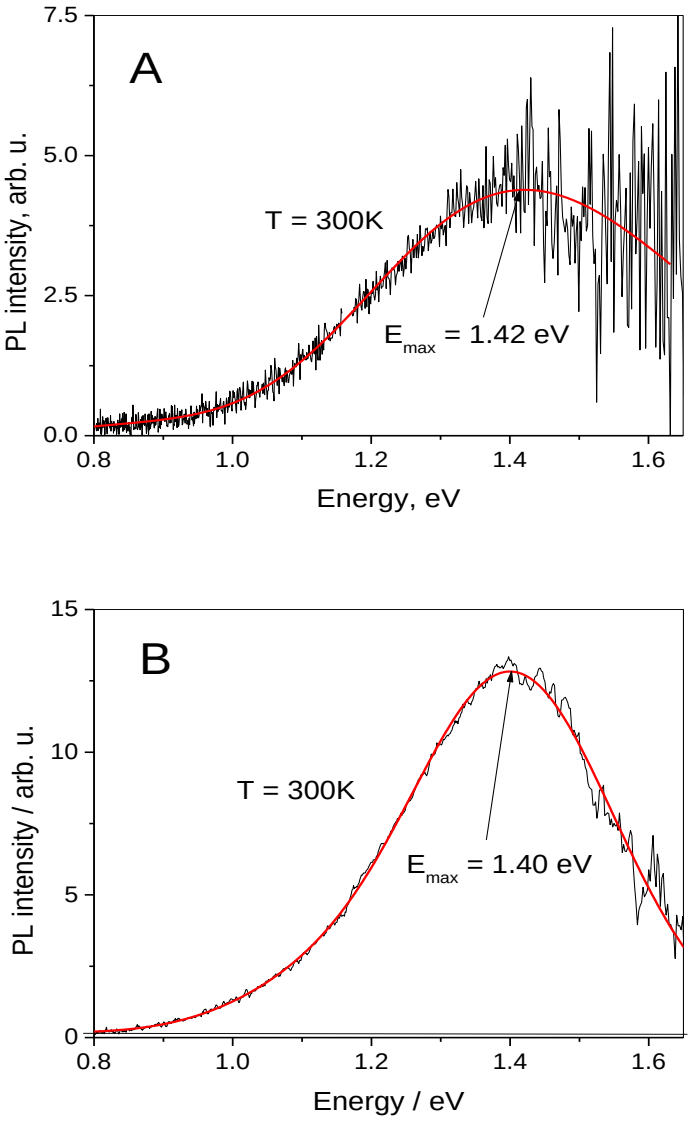

Figure 65. PL spectra (room temperature) of the CZTS samples. A – Zn-rich sample; B – Stoichiometric. The solid red curve depicts approximation by Gauss function.

The PL spectra of Stoichiometric and Zn-rich samples were measured at room temperature (300 K) and are shown in Figure 65. Band maximum energies for Stoichiometric and Zn-rich CZTS samples were 1.40 and 1.42 eV, respectively, the PL spectrum data were approximated using the Gauss function. Similar PL band maxima values (at room temperature) indicates band-to-tail (BT) recombination according to Ref. [164, 165].

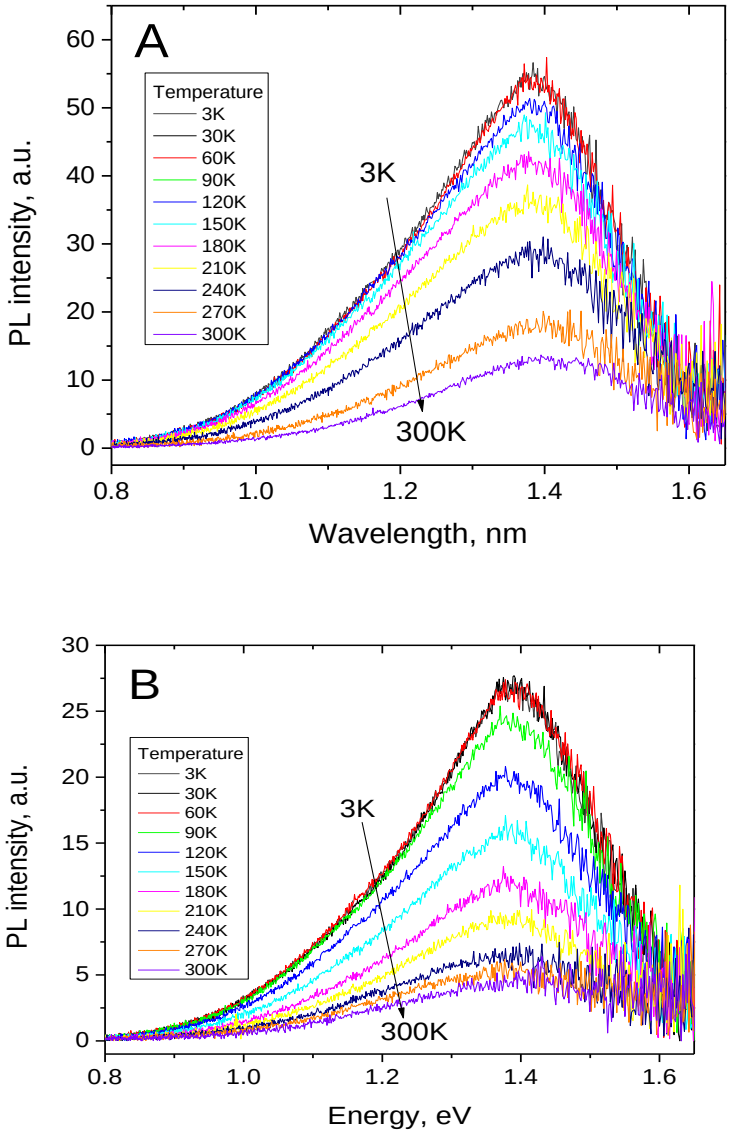

Figure 66. PL spectra (temp. dependent) of CZTS samples. A – Stoichiometric sample; B – Zn-rich one.

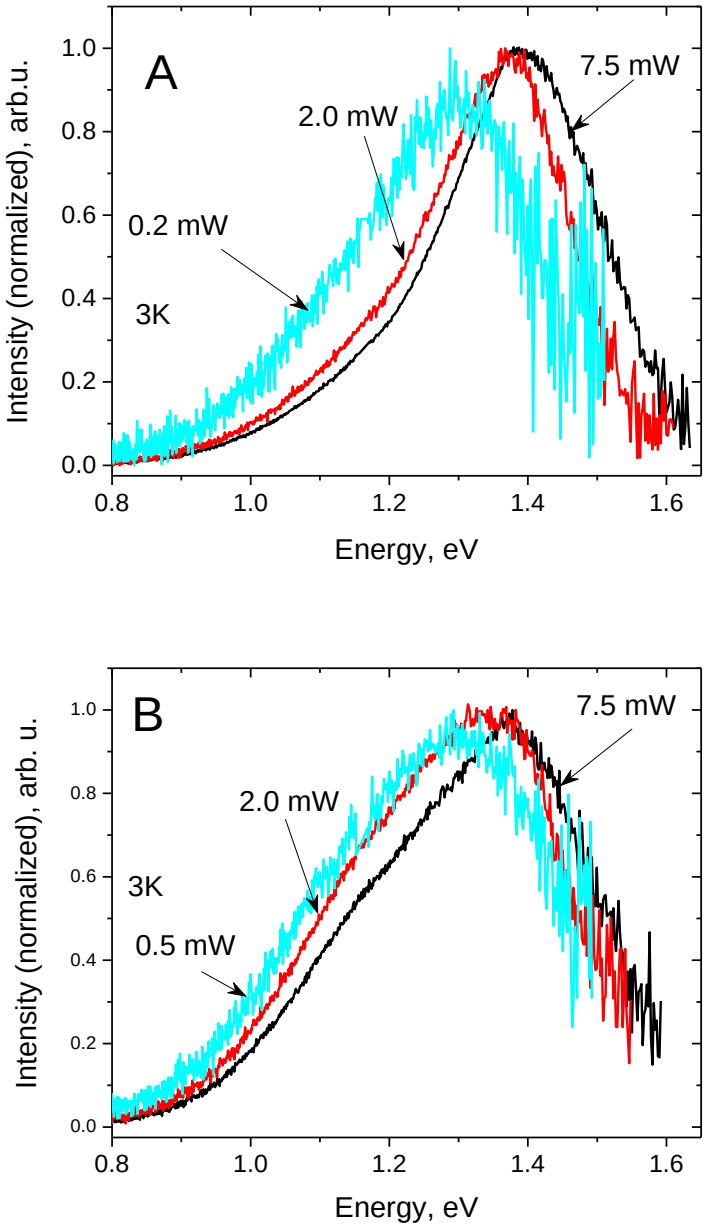

Figure 67. PL spectra (excitation power dependent) for A - Stoichiometric and B - Zn-rich CZTS samples.

Band-to-tail recombination in the Zn-rich and the Stoichiometric samples was also detected by using temperature (fig. 66) and excitation power-dependent (fig. 67) photoluminescence band blue shift.

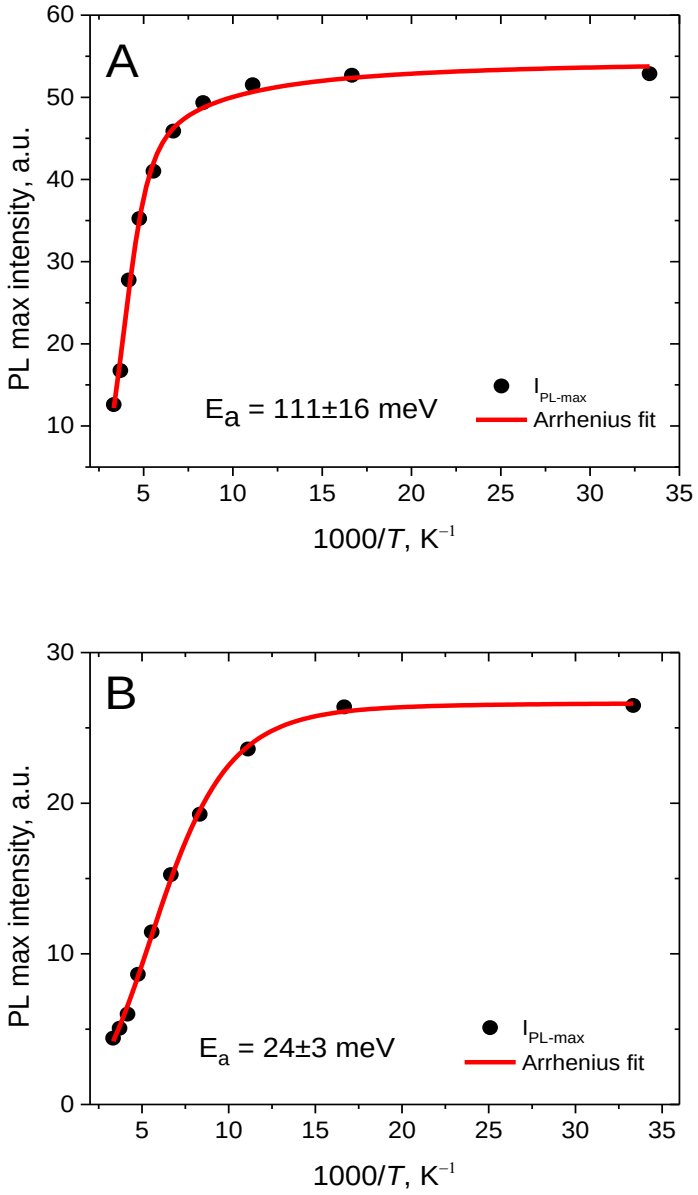

Figure 68. The Arrhenius plots for CZTS samples. A – Stoichiometric sample; B – Zn-rich.

Anyhow, the Arrhenius study (fig. 68) showed that the Zn-rich sample has much lower activation energy (E_a=24±3 meV) compared to the Stoichiometric sample (E_a=111±16 meV). According to Ref. [164], E_a of around 24 meV is attributed to the shallow acceptor (vacancy – V_{Cu}), and E_a of about 120 meV is associated with the acceptor defects, in this case, antisite defect Cu_{Zn}. The results of the Arrhenius study are compatible with the chemical composition of our samples – Zn-rich has less copper than the Stoichiometric one.

The analysis of the exponential decay of the low-energy side of the PL spectra at 3K was performed. Zn-rich and Stoichiometric samples yielded the average depth of potential fluctuation (γ) values of 176 meV and 147 meV, respectively. The typical potential fluctuation γ value for a single-phase kesterite is around 50 meV, sometimes even lower [165], although, sometimes γ value was reported much higher – 172 meV [165]. The depth of potential fluctuation, in general, is proportional to the concentration of ionized acceptors and donors [166]. The photoluminescence study of our CZTS samples very well agree with the XRD measurements data – all of the samples present an off-stoichiometric C-type kesterite structure with [$2Cu_{Zn}^{-} + Sn_{Zn}^{2+}$] clusters of point defects. The Stoichiometric sample showed a higher value of $2\Theta_{004} - 2\Theta_{200}$ indicating a higher-order and lower concentration of Cu_{Zn}^{-} antisite defects than the Zn-rich sample. Anyhow, the high value of potential fluctuation γ complicated the investigation of photoluminescence processes of the kesterite material, since the optimal γ value suggested for reliable PL spectra analysis should be less than 25 meV [165]. The higher phase purity and crystallinity of kesterite films are necessary for a more precise analysis of antisites and point defects in CZTS films.

From all of the methods we applied to examine our samples, it was determined that photoelectrochemical analysis data agrees with the data of the XRD study much better than with the Raman spectroscopy. The lowest value of j_{tr} was yielded by the CZTS sample Stoichiometric which also had the highest photocurrent density j_{ph}. The Stoichiometric sample had the best crystallinity and the structure of the highest order of the examined samples (biggest difference between 2Θ angle positions of the peaks 004 and 200). Also, Raman spectroscopy measurements suggested that the CZTS sample – Stoichiometric could be the highest quality absorber since the amount of Cu_3SnS_4 secondary phase was the lowest. But, to determine the amount of zinc sulfide present in the film, XRD data was not compatible with Raman spectroscopy results. The conflict of results might be related to the depth of which the data was acquirered – the laser radiation (325 nm) does not penetrate the film so deep when compared to x-rays. While the Raman

spectroscopy provides the information from only around 100 nm of depth and a couple of square microns area, the x-ray diffraction gives information from the entire film (~ 1500 nm) and the much larger area of around 10 square millimeters. Zn-rich CZTS sample yielded a larger amount of zinc sulfide near the surface of the film. ZnS clusters near the surface can be considered logical because the metallic zinc layer in the precursor film was a lot thicker than in other samples. Not only the amount of zinc sulfide in the films has been different. The distribution throughout the layer was also not the same in the Zn-rich and Stoichiometric CZTS samples. That was proven by the SEM and TEM analysis. The cross-section images and EDX profile measurements (fig. 63) showed that the zinc sulfide is more concentrated near the surface for the Zn-rich sample and was distributed more randomly in the Stoichiometric CZTS sample.

Photoluminescence spectroscopy analysis proved the presence of the ionized donors and acceptors and suggested the BT recombination. The ionized donors and acceptors might be antisite clusters [$2Cu_{Zn}^{-} + Sn_{Zn}^{2+}$] according to the XRD data. Anyhow, the high potential fluctuation γ value denied us to obtain more reliable information on the type of point defects from PL spectroscopy.

The biggest flaw of Raman spectroscopy measurements for our particular samples was that the presence of the secondary phases hinders the results of the kesterite stoichiometry and the order/disorder level, while the XRD results are less altered (or not affected at all) by the presence of the secondary phases.

CONCLUSIONS

1. The homogeneity and phase purity of the CZTS samples prepared by sulfurizing Cu-Sn/Zn precursors are superior to those prepared by sulfurizing Cu/Sn/Cu/Zn precursors. Cu-Sn alloy deposition significantly increases the elemental distribution of the Cu and Sn throughout the layer compared to Cu/Sn/Cu layer stacking.
2. The largest photoelectrochemical response yielded the Cu_2SnSe_3 films selenized at a temperature of 500 °C. The performance of Cu_2SnSe_3 film increases when post-annealed in the air at a temperature of 200 °C. It could be assumed that after post-annealing the crystalline structure ordering has improved and the density of V_{Cu} decreased.

3. The cubic Cu_2SnSe_3 forms when Cu-Sn precursor is selenized at temperatures in the range from 350 to 500 °C. The lattice parameter of the cubic Cu_2SnSe_3 linearly increases with temperature. The monoclinic Cu_2SnSe_3 is formed only when selenization occurs at 560 °C, according to XRD measurements.
4. The Raman spectrum band at 77 cm^{-1} has been shown to be used as a marker of the monoclinic Cu_2SnSe_3 structure. Intensity of the peak was found to be much greater for the samples where monoclinic structure is dominant.
5. The PEC analysis revealed that the kesterite with Zn/Sn = 1 had the highest photocurrent density j_{ph} and the smallest j_{tr} spikes. The PEC results are legitimate because Stoichiometric sample had the largest crystallites and the highest order level S in comparison with Zn-rich and Zn-poor samples.
6. Raman spectroscopy using the excitation wavenumber of 785 cm^{-1} was found to be resonant for the orthorhombic Cu_3SnS_4 phase.
7. According to XRD data, off-stoichiometric kesterite $Cu_{2.078}Zn_{0.909}Sn_{1.022}S_{4.000}$ was formed in every sample, irrespective of the Zn/Sn ratio in the film.
8. In our work, the XRD method using Cu $K_{\alpha 1}$ radiation was found to give more reliant information for both kesterite stoichiometry and point defects than Raman spectroscopy. The X-rays penetrates much deeper into the layer than laser used in Raman measurements, so it gives information from a much larger volume of the sample.

SUMMARY/SANTRAUKA

ĮVADAS

Saulė - nemokamas, lengviausiai prieinamas ir tuo pačiu labiausiai neišnaudojamas energijos šaltinis pasaulyje, generuojantis 120 000 Teravatų galią žemės paviršiuje reguliariai. Nepaisant didelio generuojamos energijos kiekio, saulės jėgainės nekonkuruoja su iškastinio kuro energijos šaltiniais iš naftos, anglies ar gamtinių dujų. Tik 0,6 % pasaulio sunaudojamos energijos pagaminama naudojant saulės jėgaines.

Iškyla akivaizdus klausimas - kodėl saulės jėgainės nėra vienas iš pagrindinių energijos šaltinių pasaulyje? Yra kelios saulės energijos išgavimo technologijos, tačiau kiekviena iš jų turi trūkumų, kurie neleidžia konkuruoti energijos gamybos rinkoje su iškastiniu kuru. Kad technologija būtų patraukli pramonei, turi atitikti pagrindinius reikalavimus – gamybai naudojamos lengvai prieinamos, sąlyginai pigios, netoksiškos medžiagos (ir atliekos po sintezės), kuo nesudėtingesni ir pigesni gamybos procesai. Pagrindinės komercinės technologijos apžvelgtos tolimesnėse pastraipose.

Kristalinio silicio saulės elementai yra labiausiai paplitę rinkoje. Maždaug 80% visų pasaulyje pagamintų saulės elementų yra pagaminti iš silicio. Ši fotoelektros technologija yra pati seniausia (dar vadinami „pirmosios kartos“) ir labiausiai išvystyta. Silicis yra netiesioginis puslaidininkis, todėl, norint sugerti visą saulės šviesą, silicio sluoksnio storis turi būti bent 200 μm. Taip pat sluoksniams reikalingas silicis turi būti labai grynas, todėl šie saulės kolektoriai yra brangūs. Kristalinio silicio saulės technologija naudojama jau 40 metų ir yra rekordiškai efektyvi – energijos konversijos našumas (EKN) apie 25%, tačiau dėl didelės kainos, nekonkurencinga pasaulinėje energijos rinkoje.

Amorfinio silicio saulės elementai. Pašalinus kristalinę struktūrą, keičiasi šviesos sugerties savybės, todėl saulės kolektoriui pakanka plonesnio sluoksnio. Šio tipo saulės elementai yra grįsti p-i-n sandūra, o ne tradicine p-n. „P-i-n“ sandūra yra sudaryta iš labai plonų p ir n tipo sluoksnių su storesniu tarpiniu sluoksniu, skirtu šviesai sugerti. Padidinti efektyvumui tokio tipo sandūros gali būti formuojamos viena ant kitos keletą kartų. Technologijai reikia ~ 100 kartų mažiau silicio nei kristalinio silicio technologijai, tačiau daugiasluoksnės struktūros formavimas padidina gamybos sąnaudas. Be to, amorfiniai silicio saulės elementai nėra tokie stabilūs, po ilgesnio naudojimo jie paprastai praranda iki 20% pradinio efektyvumo.

Plonasluoksniai saulės elementai arba antros kartos elementai buvo sukurti siekiant sumažinti gamybos sąnaudas, formuojant labai plonus absorberio sluoksnius. Svarbiausias uždavinys - rasti junginį, kurio absorbcijos koeficientas būtų didelis. Plonasluoksniams saulės elementams nereikia monokristalinio sluoksnio ir jis gali būti gaminamas naudojant mažiau grynas medžiagas nei kristalinis silicis. Tačiau šių saulės elementų efektyvumas yra mažesnis nei kristalinio silicio saulės elementų, todėl jis yra mažiau patrauklus pramoniniam naudojimui. Vienintelės plonasluoksnių saulės elementų technologijos, gaminamos dideliu mastu, yra kadmio telūrido (CdTe) ir vario indžio galio selenido (CIGS). Šios technologijos turi trūkumų, susijusių su didelėmis žaliavų kainomis ir ganėtinai mažu elementų, reikalingų jų gamybai, paplitimu žemėje.

Norint, kad saulės energija konkuruotų pasaulinėje energijos gamyboje, reikėjo rasti naują junginį. Maždaug prieš du dešimtmečius puslaidininkis Cu_2ZnSnS_4 (CZTS) atkreipė mokslininkų dėmesį kaip perspektyvus junginys, skirtas naudoti plonasluoksniams saulės elementams. Teorinis efektyvumas ir absorbcija buvo laikomi tobulais saulės elementams. Taip pat medžiagos, reikalingos CZTS gamybai, yra palyginti pigios, gausiai paplitusios ir netoksiškos.

DARBO TIKSLAS

Suformuoti kesterito absorberio sluoksnius naudojant elektrochemiškai nusodintus Cu-Sn-Zn pirmtakus ant Mo/stiklas padėklų ir ištyrinėti jų morfologiją, fazinę sudėtį ir fotoelektrocheminį atsaką.

DARBO UŽDAVINIAI

* Suformuoti Cu-Zn-Sn (CZT) pirmtako sluoksnį ant Mo/stiklas pagrindo, naudojant elektrocheminį nusodinimą.
* Ištirti CZT prekursoriaus atkaitinimo ir įsierinimo/įseleninimo sąlygų įtaką kesterito sluoksnio cheminei ir fazinei sudėčiai, struktūrai fotoelektriniam aktyvumui.
* Ištirti kristalinę struktūrą, fazinę sudėtį, paviršiaus morfologiją ir skerspjūvius naudojant XRD, Ramano spektroskopijos, SEM ir SEM-FIB metodus.
* Įvertinti defektinę kesterito struktūrą XRD, Ramano spektroskopijos ir fotoliuminescensinės spektroskopijos metodais.
* Ištirti sąryšį tarp CZTS sluoksnių fotoelektrocheminio atsako ir defektinės struktūros.

DARBO NAUJUMAS

⁕ Mūsų darbe buvo modifikuotas elektrolito tirpalas ir tai leido suformuoti žymiai grynesnius, kompaktiškesnius ir lygesnius Cu-Sn pirmtakų sluoksnius per ženkliai trumpesnį laiką. Gauta pirmtakų sluoksnių Cu-Sn lydinio elektrocheminio nusodinimo išeiga siekia 90 %.

⁕ Nustatyta, kad Ramano spektro smailė ties 77 cm^{-1} gali būti naudojama kaip monoklininės struktūros Cu_2SnSe_3 žymuo.

⁕ Pirmą kartą elektrocheminiu nusodinimu, pagamintas kesteritas buvo tyrinėtas naudojant Rentgeno spindulių difrakciją (RSD) su Cu $K_{\alpha 1}$ spinduliuote kartu su Ramano spektroskopija, fotoelektrocheminiais tyrimais ir fotoliuminescencija, taškiniams defektams nustatyti.

⁕ Nustatyta, kad šio darbo sąlygomis nestechiometrinis kesteritas $Cu_{2.078}Zn_{0.909}Sn_{1.022}S_{4.000}$ susiformuoja visuomet, nepaisant skirtingo Zn/Sn santykio.

⁕ Nustatyta, kad RSD metodai, naudojant Cu $K_{\alpha 1}$ spinduliuotę, suteikia patikimesnę informacijos apie kesterito stechiometriją ir taškinius defektus, nei Ramano spektroskopija.

GINAMIEJI TEIGINIAI

⁕ CZTS sluoksnis, kuriame Zn/Sn artimas vienetui, pasižymi didesniu fotosrovės tankiu ir mažesne rekombinacija, nei Zn praturtintas ar Zn nuskurdintas CZTS sluoksniai.

⁕ Įsierinti kesterito sluoksniai suformuoti iš elektrochemiškai nusodinto Cu-Sn lydinio ir ant jo nusodinto Zn sluoksnio pasižymi geresniu sudėties homogeniškumu ir sluoksnio kompaktiškumu, nei CZTS sluoksniai, gauti įsierinus pasluoksniui suformuotą (Cu/Sn/Cu/Zn) pirmtaką.

⁕ Cu-Sn lydinio selenizaciją vykdant žemesnėje nei 500 °C temperatūroje susidaro kubinis Cu_2SnSe_3, padidinus temperatūrą iki 550 °C susidaro daugiau fotoelektriškai aktyvios monoklininės Cu_2SnSe_3 fazės.

⁕ Suformuotų Cu_2SnSe_3 sluoksnių atkaitinimas 200 °C temperatūroje padidina fotoelektrocheminį atsaką.

⁕ RDS metodas naudojant Cu $K_{\alpha 1}$ spinduliuotę suteikia patikimesnės informacijos apie kesterito stechiometriją ir taškinius defektus, nei Ramano spektroskopijos metodas, CZTS sluoksniams turintiems priemaišinių fazių.

AUTORIAUS INDĖLIS

Suprojektavo ir, naudodamas 3D spausdintuvą, pagamino unikalią darbe išbandytą pratekamą elektrocheminę celę. Atliko tyrimus, leidusius parinkti tinkamiausią Mo paviršiaus paruošimo elektrocheminiam nusodinimui būdą. Pats elektrochemiškai nusodino ir, kai kuriais, atvejais aktyviai dalyvavo elektrochemiškai nusodinant disertacijoje tirtų kesterito sluoksnių pirmtakus. Dalyvavo parenkant atkaitinimo ir įseleninimo/įsierinimo sąlygas. Pats atliko dalį RSD ir elektroninės mikroskopijos matavimų. Be to, svariai prisidėjo prie RSD, SEM, PEM, EDS, Ramano spektroskopijos, FEC, fotoliuminescencijos eksperimentinių duomenų analizavimo ir apdorojimo. Kūrė grafines iliustracijas ir rengė mokslines publikacijas. Gautus rezultatus publikavo tarptautiniuose žurnaluose ir pristatė konferencijose, ir, be abejo, autorius parašė šią disertaciją.

5. LITERATŪROS APŽVALGA

Plonasluoksnio saulės elemento absorberiu gali būti naudojamas puslaidininkis, atitinkantis tokius reikalavimus: 1) draustinės energijos juosta turi būti intervale 1 - 1,5 eV, 2) efektyviai absorbuoti šviesą (absorbcijos koeficientas $\alpha > 104$ cm-1) bangų ilgių intervale nuo 350 iki 1000 nm, 3) pasižymėti dideliu krūvininkų kvantiniu našumu ir lėta jų rekombinacija [2]. Antrasis svarbus aspektas yra kaina - absorberio sluoksnį sudarantys cheminiai elementai ir sintezei naudojami metodai turėtų būti nebrangūs. Visų šių kriterijų išpildymas yra labai svarbus didelės apimties produkcijai.

Kesteritas – $Cu_2ZnSn(S,Se)_4$ arba CZT(S,Se), kaip medžiaga saulės elementams, sukurta naudojantis CIG(S,Se) chalkopirito modeliu, bandant In ir Ga pakeisti pigesniais ir žemėje gausiu paplitusiais Zn ir Sn. CIG(S,Se) technologija yra viena iš labiausiai išvystytų plonasluoksnių saulės elementų srityje. CIG(S,Se) plonų sluoksnių saulės elementų rekordinis energijos konversijos našumas (EKN) siekia 22,6% [4]. Toks didelis polikristalinės plonos plėvelės su p-n hetero-sandūra efektyvumas rodo, kad ši technologija galėtų konkuruoti su plačiai naudojamais silicio saulės elementais. CIG(S,Se) puslaidininkių draustinės energijos juosta kinta nuo 1,05 eV grynajam $CuInSe_2$ iki 1,65 eV $CuGaSe_2$ (draustinių energijų juostą galima kontroliuoti keičiant In ir Ga santykį), CIG(S,Se) matomos šviesos spektro absorbcijos koeficientas (α) yra didesnis už 10^4 cm^{-1}. Šios savybės rodo, kad CIG(S,Se) labai gerai tinka saulės elemento absorberiams.

Pirmoji Cu_2ZnSnS_4 sintezė įvykdyta Šveicarijoje, ją atliko R. Nitsche, kurdamas ($A_2^IB^{II}C^{IV}X_4$) chalkogenidus naudojant jodo garų pernešimo metodą [7].

Dėl didelės CIGS(Se) naudojamų In ir Ga žaliavų kainos ir nedidelio paplitimo žemėje, bei Cd toksiškumo CdTe saulės elementuose, mokslininkai ieškojo naujų puslaidininkių, tinkančių plonasluoksniams saulės elementams. Nakazawa ir Ito (Japonija) susintetino Cu_2CdSnS_4 ir Cu_2ZnSnS_4 (CZTS) sluoksnius, magnetroninio dulkinimo metodu. Optinių ir fizikinių savybių tyrimai parodė, kad CZTS puikiai tinka plonasluoksnių saulės elementų technologijai. Jie taip pat sukūrė veikiantį CZTS/kadmio-alavo oksido hetero-sandūros saulės lementą [8].

Kesterito Cu_2ZnSnS_4 ir $Cu_2ZnSnSe_4$, kuris yra p tipo puslaidininkis, draustinės energijos juosta yra atitinkamai 1,5 ir 1,0 eV. Teoriškai kesteritas atitinka visus optinius ir elektroninius parametrus, keliamus aukšto efektyvumo saulės elemento absorberiui.

Pirmoji šiuolaikinio CZTS saulės elemento sukūrimas priskiriamas Katagiri, kai 1997 m. pagamintas SLG/Mo/CZTS/CdS/ZnO/TCO struktūros saulės elementas. Šis saulės elementas, kurio našumas buvo 0,66%, ir yra pripažintas kaip plonasluoksnių CZTS saulės elementų vystymosi pradžios taškas [9]. Praėjus daugiau nei dviem dešimtmečiam po pirmojo CZTS saulės elemento sukūrimo pasiektas rekordinis 13,7 % našumas, kuris nėra toks aukštas, kokio galbūt galėjome tikėtis. Pastaruoju metu ypatingas dėmesys skiriamas CZTS būdingiems taškiniams defektams.

CZTS junginys yra p tipo puslaidininkis dėl didelės vario vakansijų (V_{Cu}) ir pakaitinių Cu_{Zn} taškinių defektų (kai kesterito gardelėje Cu jonai užima Zn jonų pozicijas dėl beveik vienodų jų joninių radiusų) koncentracijos, kurie veikia kaip elektronų akceptoriai ir standartinėmis sąlygomis yra jonizuotos būklės. Taškinių defektų koncentracija labiausiai priklauso nuo Cu/(Zn + Sn) ir Zn/Sn santykio prekursoriuje [60].

Nors vieni taškinių defektų kompleksai yra ganėtinai nekenksmingi saulės elementų veikimui, kiti, atsirandantys dėl sudėties nukrypimų nuo stechiometrinės, nėra tokie nereikšmingi. Pvz.: defektų kompleksas [Zn_{Sn} + Sn_{Zn}] sumažina CZTS draustinės energijos juostą, dėl to gali sumažėti atviros grandinės įtampa (V_{OC}) ir padidėti krūvininkų „pagavimo“ tikimybė. Nors ši defektų grupė yra viena labiausiai žalingų, jos formavimosi energija yra gana didelė, todėl koncentracija sluoksniuose turėtų būti palyginti maža.

Remiantis eksperimentiniais rezultatais, keičiančiant kesterito stechiometriją, nustatyta, kad geriausias saulės elemento efektyvumas gaunamas, kai yra tokie koncentracijų (at. %) santykiai: Cu/(Zn + Sn) = 0,8 ir Zn/Sn = 1 - 1,2. Tokiose sąlygose susidaro defektų klasteriai, turintys

mažiausią formavimosi energiją [$V_{Cu}^{-} + Zn_{Cu}^{+}$], [$Zn_{Sn}^{2-} + 2Zn_{Cu}^{+}$] ir nedarantys jokio poveikio laidumo ir valentinės juostos maksimumams [60]. Taigi, Cu-nuskurdinta/Zn-praturtinta sudėtis lemia, kad susidaro nekenksmingi saulės elemento veikimui defektų klasteriai. Kai kesterito sudėtis yra Cu-praturtinta/Zn-nuskurdinta susidaro [$2Cu_{Zn}^{-} + Sn_{Zn}^{2+}$] klasteriai, galintys sukelti laidumo juostos maksimumo sumažėjimą bei paskatinti krūvio nešėjų pagavimą. Šie klasteriai labai sumažina saulės elemento energijos konversijos koeficientą.

Norint gauti aukštos kokybės CZTS plonasluoksnį saulės elementą, pastarąjį dešimtmetį mokslininkų grupės taikė įvairius formavimo metodus. Tačiau pagrindinis iššūkis išlieka iki šių dienų - susintetinti homogenišką, grynos fazės, puikių morfologinių savybių (stambių grūdelių, be ertmių) sluoksnį. Labai svarbus aspektas gamyboje, kad CZTS sintezės metodas būtų kuo pigesnis ir greitesnis. Todėl šiame darbe pasirinktas elektrocheminis pirmtako nusodinimo metodas. Jis nereikalauja brangios vakuumines įrangos, naudojami sąlyginai nepavojingi tirpalai.

6. EKSPERIMENTO METODIKA

Šiame darbe Cu-Sn-Zn pirmtako sluoksniai buvo formuojami elektrocheminio nusodinimo metodu ir vėliau įsierinami/įselenidinami. Elektrocheminis nusodinimas buvo atliekamas galvanostatinėmis sąlygomis, naudojant standartinę trijų elektrodų celę. Darbo pradžioje buvo suprojektuota, pagaminta ir išbandyta pratekama celė elektrocheminiam nusodinimui. Tikėtasi, kad joje bus efektyvus elektrolito maišymas, leisiantis gauti tolygaus storio ir sudėties plonus pirmtako sluoksnius. Pirmtako sluoksnio formavimas buvo atliekamas skirtingais metodais – pasluoksniui nusodinant pavienius metalus pratekamoje ir standartinėje celėje bei elektrochemiškai nusodinant Cu-Sn lydinį (baltąją bronzą) ir ant viršaus Zn sluoksnį. Kaip darbinį elektrodą naudojome ant stiklo magnetroninio dulkinimo būdu suformuotą Mo sluoksnį (storis ~ 1 μm), kuris tarnauja apatiniu saulės elemento kontaktu. Kaip anodas naudota Pt plokštelė. Prekursoriaus atkaitinimui ir po to sekančiam įsierinimui/įseleninimui naudota vakuuminė vamzdinė krosnis.

Rentgeno spindulių difrakcijos tyrimai atlikti difraktometru SmartLab (Rigaku). RSD metodu nustatant kesterito kristalinės gardelės parametrus, cinko sulfido kiekį ir tiriant taškinius defektus naudotas CALSA (Crystal Array on Logarithmic Spiral Analyser) analizatorius, kurio dėka į detektorių patenka tik difragavę Cu $K_{\alpha 1}$ bangos ilgio rentgeno spinduliai. Ramano

spektroskopijos tyrimai atlikti naudojant inVia (Renishaw) konfokalinį mikrospektrometrą. Spektrams sužadinti buvo naudojami 325, 532 ir 785 nm bangos ilgio lazerio spinduliai. Paviršiaus morfologijos, elementinės sudėties ir skerspjūvių tyrimams naudotas skenuojantis elektroninis mikroskopas (dviejų spindulių sistema) FE-SEM-FIB Helios NanoLab 650 (FEI Company) su X-Max EDX spektrometru. Elementų pasiskirstymas per sluoksnio storį tirtas Tecnai G2 F20 X-Twin (FEI Company) peršviečiamuoju mikroskopu su EDX (EDAX) spektrometru ir Gatan Orius CCD kamera. Fotoelektrocheminiai tyrimai atlikti specialioje elektrocheminėje celėje su kvarciniu langeliu ir trijų elektrodų standartine sistema (pagalbinis elektrodas - Pt viela, palyginamasis – Ag/AgCl/KCl). Tyrimuose naudotas 0,2 M $Eu(NO_3)_3$ vandeninis tirpalas. Darbinis elektrodas (CZTS) buvo apšviečiamas baltos šviesos LED šviestuku (Lumiled 3 W), išmatuotas šviesos intensyvumas ant elektrodo paviršiaus – 100 mW/cm^2. Atliekant fotoliuminescencinės spektroskopijos tyrimus bandinys buvo įmontuojamas ant šaldomo padėklo prijungto prie uždaro ciklo kriostato (SHI-ė, Janis Research) sužadinimui naudotas UV lazeris (266 nm bangos ilgio). Spektrai fiksuoti temperatūrose nuo 3 iki 300 K.

7. REZULTATAI IR JŲ APTARIMAS

7.1. Padėklų paruošimas

Elektrocheminis metalų nusodinimas ant Mo padėklų yra pakankamai sudėtinga užduotis, nes Mo paviršius yra itin linkęs oksiduotis. Todėl, paviršiaus apdorojimas prieš elektrocheminį nusodinimą yra labai svarbus. Šiame darbe, mes išmėginome tris Mo paviršiaus paruošimo būdus:

1. Mo valymas industriniu valikliu, po to nuplaunant distiliuoto vandens srove.
2. Mo nuriebalinimas etanolyje (1 min. ultragarsinėje vonelėje), Mo oksidų nutirpinimas NH_4OH tirpale (10 min.), praplovimas distiliuotu vandeniu ir etanoliu (1 min. ultragarsinėje vonelėje).
3. Paviršiaus ėsdinimas plazma, magnetrone.

Hidrofiliniai paviršiai labiau tinka elektrocheminiam nusodinimui. Sluoksniai nusodinti ant hidrofiliškų paviršių turėtų būti tolygiausi ir kompaktiškiausi [138]. Mo paviršiaus hidrofilinės savybės po paruošimo buvo ištirtos nustatant kontaktinį kampą tarp apdoroto paviršiaus ir vandens (1 pav.). Labiausiai hidrofilinis Mo paviršius gautas naudojant magnetroninį ėsdinimą, o mažiausiai hidrofilinis nuvalius paviršių industriniu valikliu.

1 pav. Mo/vanduo kontaktinio kampo matavimų rezultatai. Kairėje – Mo paviršiaus nuvalyto su industriniu valikliu; viduryje – nuvalyto etanoliu ir amoniaku; dešinėje – plazma nuėsdinto (magnetrone).

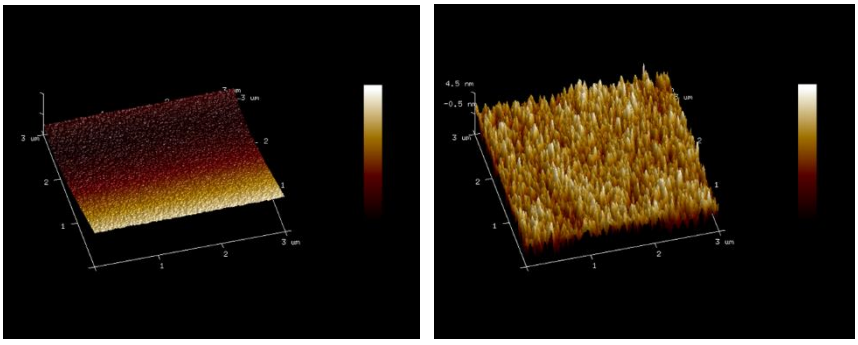

2 pav. Apdorotų Mo paviršių AFM vaizdai. Kairėje –paviršius, apdorotas etanoliu ir amoniaku; dešinėje – plazma nuėsdintas Mo (magnetrone).

Eksperimentiškai nustatėme, kad elektrochemiškai nusodintų sluoksnių sukibimas su magnetrone plazma ėsdintu Mo paviršiumi yra nekokybiškas. Vario sluoksnis po nusodinimo praplaunant vandens srove atsilupdavo. Tai gali būti susiję su paviršiaus šiurkštumu, kurį nustatėme naudodami AFM (2 pav.). Be to, magnetrone plazma nuėsdinti Mo paviršiai yra labai aktyvūs, išėmus Mo iš magnetrono kameros jo paviršius galėjo greitai oksiduotis. Pramoniniu plovikliu nuvalyti paviršiai taip pat demonstravo prastą sukibimą su elekrochemiškai nusodintu Cu sluoksniu, kurį galėjo lemti ant paviršiaus adsorbavęsi organiniai junginiai. Antras pagal hidrofiliškumą Mo paviršius, gautas naudojant etanolį/NH_4OH/etanolį, demonstravo puikią nusėdusių Cu sluoksnių adheziją. Todėl jis buvo pasirinktas naudoti viso tyrimo metu.

7.2. Elektrocheminis pirmtako sluoksnio nusodinimas

7.2.1. Pirmtako nusodinimas naudojant pratekamą elektrocheminę celę

Norint, kad pirmtako sluoksnių elektrochminio nusodinimo procesas būtų patrauklesnis pramoniniam sluoksnių formavimui ir pasiekti geresnį tirpalo maišymą, buvo išbandyta originali pratekama elektrocheminė celė, sukurtą naudojant „SolidWorks CAD 3D“ projektavimo programinę įrangą ir pagaminta 3D spausdintuvu (3 pav.).

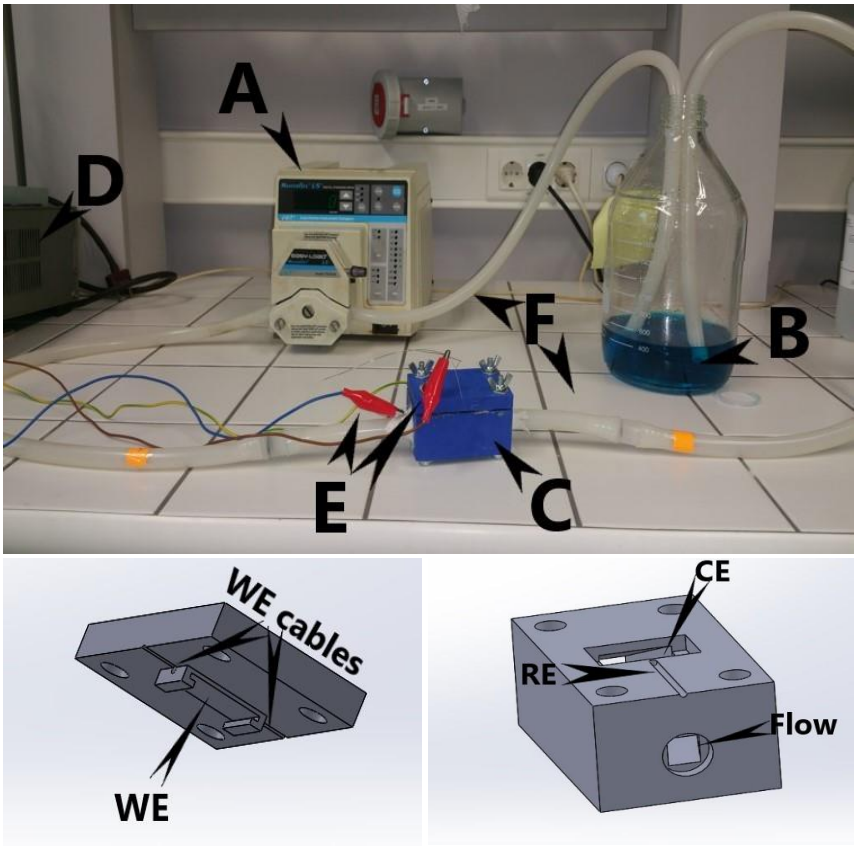

3 pav. Pratekamos elektrocheminės celės sistemos vaizdas ir 3D brėžiniai. Sistemos komponentai: A – peristaltinis siurblys; B – elektrolito tirpalo talpa; C – pratekama celė; E – elektrodai; F – silikoninės žarnos. WE – darbinis elektrodas; CE – pagalbinis elektrodas; RE – palyginamasis elektrodas.

Didžiausias pratekamos celės privalumas yra laminarinis elektrolito tekėjimas - pastovus tirpalo keitimasis tirpalo/elektrodo sandūroje. Išvengiama dengiamojo bandinio išėmimo iš elektrolitinės celės po kiekvieno

metalo nusodinimo. Silikoninės žarnos (10 mm vidinio skersmens) buvo naudojamos tirpalui cirkuliuoti uždarame cikle, tirpalo srautui sukurti naudotas peristaltinis siurblys.

Atskirų metalų sluoksniai buvo nusodinti naudojant galvanostatines sąlygas. Esant pastoviam srovės tankiui (j) yra daug lengviau kontroliuoti sluoksnių storį. Galvanostatinės sąlygos taip pat dažniau naudojamos elektrochemiškai nusodinant metalų dangas pramonėje.

Metalų sluoksnių seka negalėjo būti atsitiktinė. Norint užkirsti kelią ankstesniojo sluoksnio oksidacijai (nutirpimui), metalų seka turi būti: nuo teigiamiausio nusodinimo potencialo iki neigiamiausio (Cu E_0 = + 0,34 V, Sn E_0 = -0,13 V, Zn E_0 = -0,76 V). Be to, elektrochemiškai nusodintas Cu turi geriausią sankabumą su Mo, iš trijų metalų, sudarančių CZTS pirmtaką.

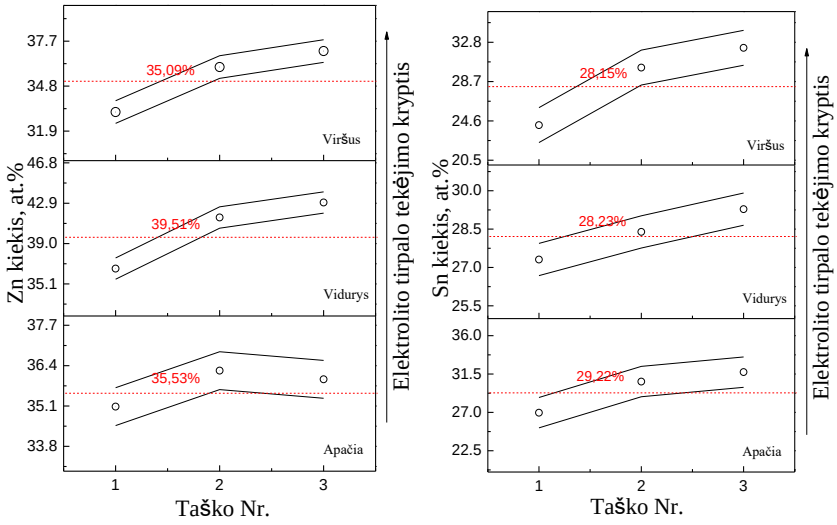

4 pav. Zn (kairėje) ir Sn (dešinėje) kiekio priklausomybė skirtinguose katodo su nusodintu Cu/Sn/Cu/Zn pirmtaku taškuose (at. %). Bandinys suformuotas pratekamoje elektrocheminėje celėje, Zn ir Sn kiekio matavimai atlikti SEM EDX spektrometru.

Tikrindami nusodintų metalų sluoksnių storio tolygumą išmatavome metalų kiekį (at.%) 9-uose padengto ploto taškuose. Trys taškai buvo išdėstyti ant tiesės atkarpos, statmenos elektrolito srauto krypčiai. Vienas jų buvo ploto viduryje (taškas Nr.2), kiti du (Nr.1 ir 3) abiejose pusėse vienodai nutolę nuo vidurio. Kiti šeši taškai išsidėstė ant linijų, lygiagrečių centrinei ir vienodai nutolusių nuo jos į abi puses. Išmatuoti metalų kiekiai yra tiesiogiai proporcingi jų sluoksnių storiams. Pav. 4 grafikuose pažymėti taškai rodo

metalo koncentracijas atitinkamuose taškuose, o punktyrinės linijos – koncentracijos vidurkį atitinkamoje linijoje, paskaičiuotą pagal tris šioje linijoje esančių taškų vertes. Nustatėme, kad Sn kiekis (4 pav., grafikas kairėje) nežymiai mažėja elektrolito tirpalo tekėjimo kryptimi. Pagal Sn kiekį kairėje (taškas Nr.1), centre (Nr.2) ir dešinėje (Nr.3) pasirinktuose taškuose, atitinkamai 26,14±1,7; 29,72±1,2 %; 31,1±1,6 % %, galima teigti, kad Sn kiekis mažėja iš dešinės į kairę. Ant Cu/Sn/Cu sluoksnių nusodintas Zn, kurio kiekio vidutinių verčių mažėjimas ir tirpalo tekėjimo kryptis sutampa su alavo sluoksnio storio nežymiu mažėjimu šia kryptimi. Pagal Zn kiekius taškuose 1, 2 ir 3, atitinkamai 34,93±1,2 %; 37,93±3,1 %; ir 38,66±3,8 %, matome, kad ir Zn sluoksnio storis mažėja iš dešinės į kairę. Galime daryti išvadą, kad sluoksnio storio nežymus mažėjimas elektrolito srauto kryptimi gali būti susijęs su tirpalo nuskurdimu atitinkamo metalo jonais vykstant elektrocheminei reakcijai. Tuo tarpu storio nevienodumas skirtingose pusėse gali būti aiškinamas nevienodais atstumais tarp katodo ir anodo dėl net nežymių Pt plokštelės paviršiaus nelygumų, kurie pratekamoje celėje gali turėti didelės įtakos dėl vos 2 mm atstumo tarp elektrodų. Kita galima priežastis – srauto turbulencija.

7.2.2. Pirmtako nusodinimas naudojant standartinę elektrocheminę celę

Nepavykus išvengti pratekamoje celėje suformuotų Cu/Sn/Cu/Zn pirmtako sluoksnių storio netolygumo atsisakyta tolimesnio šios celės naudojimo ir pereita prie pirmtako sluoksnių formavimo įprastinėje elektrocheminėje celėje.

Lentelė Nr 1. Cu/Sn/Cu/Zn pirmtako sluoksnių formavimo parametrai.

Bandinys	1-ojo Cu sluoksnio storis, nm	Sn sluoksnio storis, nm	2-ojo Cu sluoksnio storis, nm	Srovės tankis Zn elektronusodinimui, mA/cm^2
A125	100	200	40	15
A126	70	200	70	15
A127	70	200	70	20
A128	100	200	40	20

Naudota trijų elektrodų sistema, darbinis elektrodas – Stiklas/Mo; pagalbinis elektrodas – Pt plokštelė (4 cm^2 ploto); palyginamasis elektrodas Ag/AgCl/KCl. Atstumas tarp darbinio ir pagalbinio elektrodų 4 cm, celės tūris

– 100 ml. Atlikus tyrimus nusodinant atskirus metalus, buvo suformuoti tolygesnio storio Cu/Sn/Cu/Zn pirmtako sluoksniai (2 pav.).

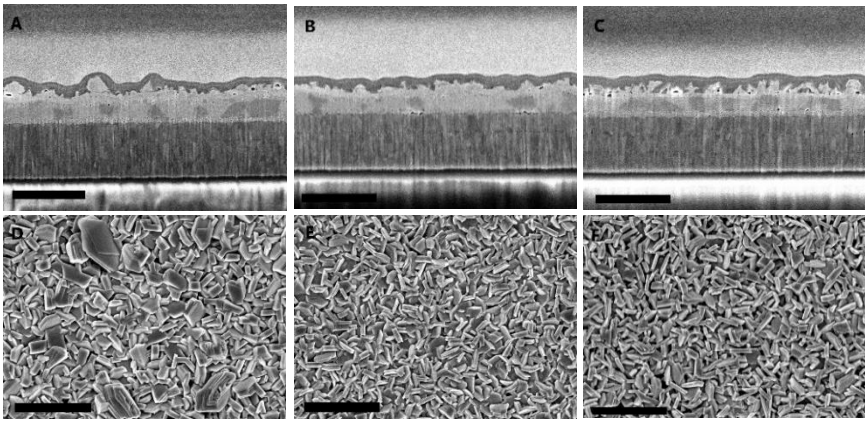

5 pav. Suformuotų Cu/Sn/Cu/Zn pirmtako sluoksnių skerspjūvių (A, B, C) ir paviršiaus (D, E, F) SEM vaizdai. Nusodinimo sąlygos pateiktos 1 lentelėje. A ir D vaizdai A126 bandinio; B ir E - A127 bandinio; C ir F – A128 bandinio. Skalės mastelis 1 μm.

A125 pavyzdyje cinko kristalų ant paviršiaus mikroskope nesimatė, todėl SEM vaizdai 5 pav. nepateikti. A126 bandinio paviršius buvo labai šiurkštus, pjūvio vaizde matomi įvairaus dydžio Zn kristalai (nuo ~200 iki 20-30 nm). Bandiniuose A127 ir A128 Zn buvo nusodintas naudojant vienodą srovės tankį, bet ant skirtingo storio Cu pasluoksnių 70 ir 40 nm, atitinkamai. A127 bandinio paviršius (storesnis Cu pasluoksnis) rodo, kad cinko sluoksnis yra ištisinis ir akivaizdžiai lygiausias iš aptarinėjamų bandinių. Bandinys A128 (plonesnis Cu pasluoksnis) pasižymėjo labai šiurkščiu paviršiumi, skerspjūvio vaizde matome, kad cinkas nesudarė ištisinio sluoksnio.

7.2.3. Cu-Sn lydinio elektrocheminis nusodinimas

Kesterito sintezė yra sudėtingas procesas, nes visų trijų sulfidai/selenidai susidaro esant skirtingoms temperatūroms. Siekiant geriau suprasti lydinio chalkogenizaciją, buvo atliktas vario alavo selenido (CTSe) susidarimo tyrimas. Cu-Sn pirmtako sluoksnis buvo nusodintas ant SLG/Mo pagrindo, naudojant standartinę trijų elektrodų elektrocheminę celę. Mo paviršius prieš nusodinimą buvo nuvalytas darbo pradžioje pasirinktu būdu. Palyginamasis elektrodas (Ag/AgCl/KCl) buvo patalpintas šalia darbinio elektrodo per Lugino kapiliarą. Kaip pagalbinį elektrodą naudojome Pt plokštelę.

Elektrocheminiam nusodinimui naudojamo tirpalo sudėtis: 20 mM $CuSO_4$, 10 mM $SnSO_4$ ir 0,1 M tri-natrio citrato. Tirpalo pH 5,75 nustatyta naudojant

NaOH. Paprastai Cu-Sn pirmtakas formuojamas paeiliui nusodinant Cu ir Sn sluoksnelius. Cu-Sn lydinio nusodinimas yra sudėtingesnis, nei pavienių metalų nusodinimas, tačiau patogesnis ir daug greitesnis.

Kitų autorių darbe [144] $Na_3C_6H_5O_7$ kiekis elektrolito tirpale buvo 0,5 M. Naudojant tokį tirpalą į dangą galėtų įsiterpti didokas anglies kiekis. Šiame darbe išbandytos mažesnės citrato koncentracijos. Atlikti tyrimai parodė, kad mažiausias citrato kiekis, kuriam esant elektrolito tirpalas išlieka stabilus, buvo 0,1 M. Ramano spektroskopijos tyrimai parodė, kad Cu-Sn lydinyje, nusodintame tirpale su 0,5 M $Na_3C_6H_5O_7$ yra aiškiai matoma angliai priskirtina juosta ties 2926 cm^{-1}, kuri išnyko, kai Cu-Sn buvo nusodintas tirpale su 0,1 M citrato.

Darbinio elektrodo (Stiklas/Mo) poliarizacijos kreivė mūsų tirtuose elektrolitų tirpaluose pateikta 6 paveiksle. Taškinės vertikalios linijos atskiria potencialų zonas, kuriose vyksta: 1) Cu redukcija, 2) Cu redukcija ir ikipotencialine (*angl*. underpotential) Sn redukcija, 3) Cu ir Sn elektrocheminis sasėdis. Taip pat pažymėtas vandenilio elektrocheminės redukcijos pradžios potencialas. Pirmtakų sluoksniams nusodinti buvo pasirinktas katodinis potencialas E_C -1,0 V (Cu ir Sn sasėdžio ribinės srovės potencialas). Elektrocheminė vandenilio dujų redukcija esant šiam potencialui buvo dar ganėtinai lėta. Naudojant elektrolito tirpalo maišymą magnetine maišykle srovės tankio vertės padidėjo apie 4 kartus.

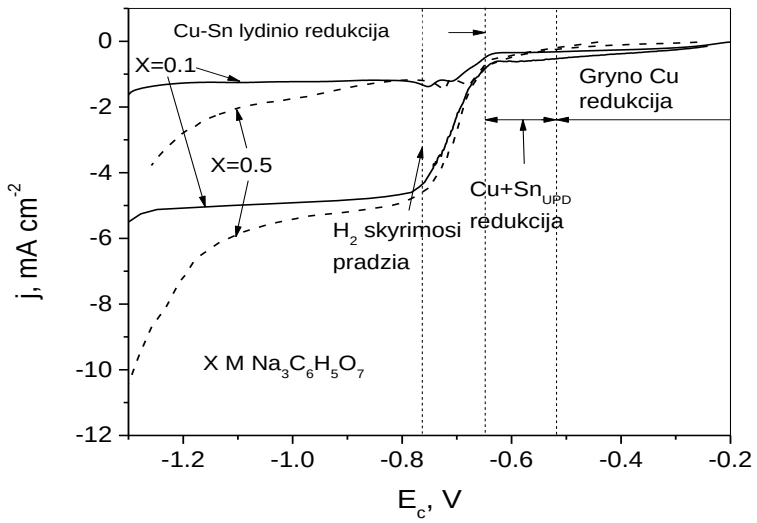

6 pav. Cu-Sn lydinio elektrocheminio nusodinimo voltamperograma. Punktyrinės linijos – poliarizacinės kreivės tirpale su 0,5 M $Na_3C_6H_5O_7$, ištisinės linijos – 0,1 M. Apačioje poliarizacinės kreivės užrašytos maišant elektrolitą, viršuje – be maišymo.

Cu-Sn elektrochemiškai nusodintas elektrolito tirpale su 0,5 M tri-natrio citrato (7 pav. a) ir 0,1 M tri-natrio citrato (7 pav. b). Matome, kad bandinio nusodinto naudojant didesnę citrato koncentraciją paviršius gautas šiurkštus, sudarytas iš smulkių kristalitų aglomeratų, o iš tirpalo su mažesniu $Na_3C_6H_5O_7$ kiekiu, paviršius yra vientisas ir tolygus.

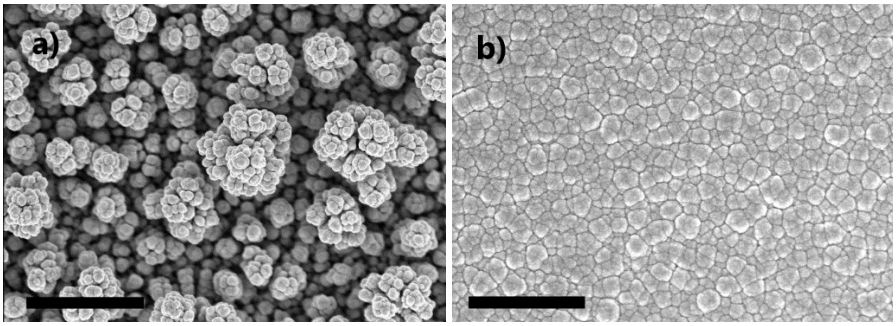

7 pav. Cu-Sn sluoksnių paviršiaus SEM vaizdai. Sluoksniai elektrochemiškai nusodinti iš 20 mM $CuSO_4$, 10 mM $SnSO_4$, ir 0,5 M $Na_3C_6H_5O_7$ tirpalo - a); 20 mM $CuSO_4$, 10 mM $SnSO_4$, ir 0,1 M $Na_3C_6H_5O_7$ – b). Mastelio skalė 2 μm.

7.3. Cu-Sn selenizacija ir fazinė sudėtis

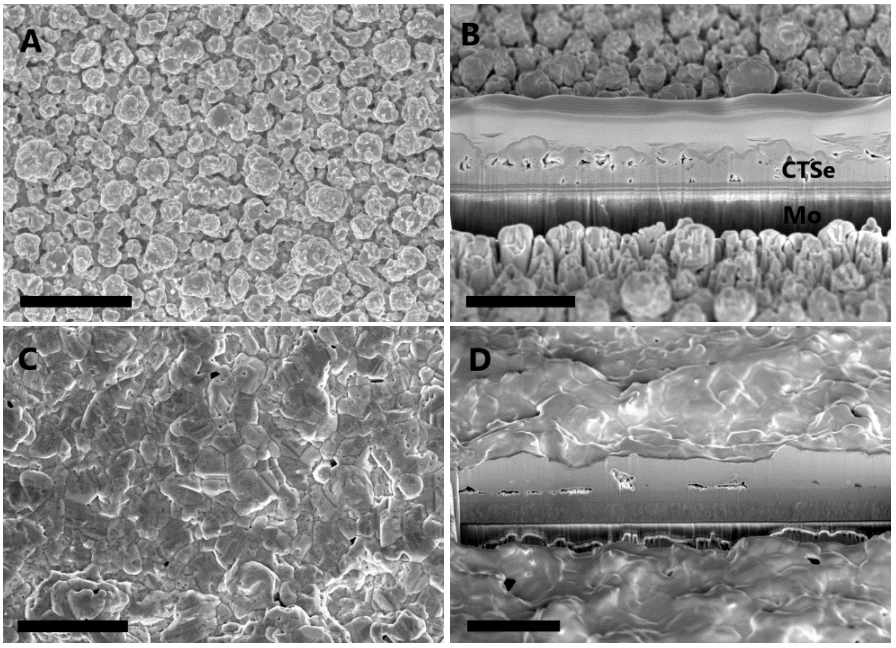

8 pav. CTSe sluoksnių SEM paviršiaus ir skerspjūvio vaizdai. CTSe sluoksniai suformuoti iš Cu-Sn pirmtako nusodinto tirpale: su 0,5 M natrio citrato (A ir B); su 0,1 M natrio citrato (C ir D). Mastelio skalė 4 μm.

Cu-Sn pirmtako sluoksniai įseleninti 500 °C temperatūroje. 8 paveiksle parodyti paviršius (A) ir skersinis pjūvis (B) CTSe sluoksnio, kurio pirmtakas nusodintas iš tirpalo su 0,5 M natrio citrato. C ir D rodo atitinkamus vaizdus CTSe sluoknio, kurį formuojant naudotas elektrolito tirpalas su 0,1 M $Na_3C_6H_5O_7$. Sluoksniai, gauti naudojant Cu-Sn pirmtaką, kurio elektrolito tirpale buvo mažiau $Na_3C_6H_5O_7$, yra lygesni ir kompaktiškesi. CTSe sluoksnių pagamintų naudojant mažesnį natrio citrato kiekį elektrolito tirpale skerspjūvio vaizdas parodė mažesnį plyšių kiekį ir vienodesnį storį. Gauta gera Cu-Sn pirmtako sluoksnio kokybė paskatino šio lydinio naudojimą tolesniame darbe (Cu-Sn/Zn dviejų etapų nusodinimas vietoj keturių Cu/Sn/Cu/Zn) Cu-Sn-Zn formavimui.

Cu-Sn pirmtakų sluoksniai, nusodinti iš elektrolito tirpalo, kuriame yra 0,1 M natrio citrato, buvo naudojami sąryšiui tarp selenizacijos temperatūros ir CTSe sluoksnio kristalinės struktūros bei fazinės sudėties nustatymui. 9 paveiksle pateikti RSD tyrimų rezultatai CTSe sluoksniams, įselenintiems per 20 minučių skirtingose temperatūrose nuo 400 iki 560 °C. Visų pirmtakų sluoksnių sudėtis buvo apie 65 at. % vario, ~ 35 at.% alavo (Cu / Sn = 1,86).

Po selenizacijos Cu/Sn santykis padidėjo iki 1,91 - 1,94, tai rodo alavo praradimą aukštoje temperatūroje.

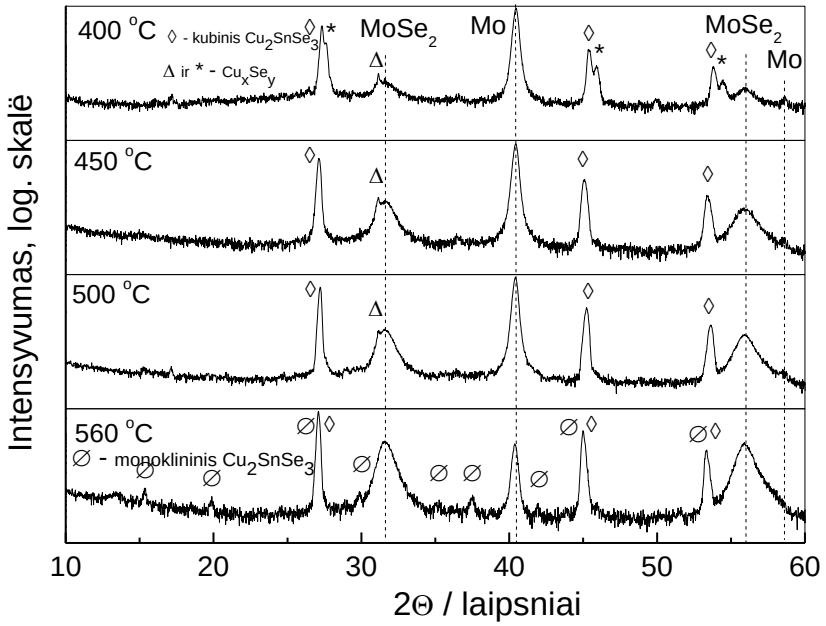

9 pav. Rentgenogramos CTSe sluoksnių, gautų įseleninant skirtingose temperatūrose (nuo 400 iki 560 °C). Cu-Sn pirmtakų sudėtis: Cu 65.4±1.0 at.% ir Sn 34.6±1.0 at.%. Identifikuotų fazių žymėjimas: ◊ - kubinė Cu_2SnSe; * - kubinė $Cu_{1,8}Se$; Δ - heksagoninė CuSe; ∅ - monoklininė Cu_2SnSe_3.

Įseleninus Cu-Sn lydinį 400 °C temperatūroje jau susidaro Cu_2SnSe_3 (# 01-089-2879), turintis kubinę kristalinę gardelę. Be to sluoksnyje aptinkami nedideli $Cu_{1.8}Se$ (# 01-088-2046) ir CuSe (# 00-049-1457) kiekiai.

Padidinus įseleninimo temperatūrą iki 450 °C, rentgenogramoje matome kubinio Cu_2SnSe_3 ir vieną CuSe fazės smailę ties 31,15° 2Θ kampu. Taip pat galima teigti, kad susidarė storesnis $MoSe_2$ sluoksnis.

CTSe sluoksnis, suformuotas 500 °C temperatūroje, sudarytas iš kubinės Cu_2SnSe_3 fazės ir nedidelio kiekio CuSe fazės. $MoSe_2$ storis dar padidėjo. Padidinus įseleninimo temperatūrą iki 560 °C, atsirado mažų XRD smailių ties 2Θ kampais 15,35 ir 19,88°, būdingų monoklininei Cu_2SnSe_3 struktūrai (# 00-056-1111 ir # 04-012-4693). Bet kokiu atveju negalima atmesti kubinio Cu_2SnSe_3 buvimo, nes intensyviausios abiejų struktūrų smailės visiškai sutampa, jei kubinės fazės gardelės parametras yra 0,569 nm. Nustatėme, kad kubinės gardelės parametras a tiesiškai priklauso nuo įseleninimo temperatūros (10 pav.).

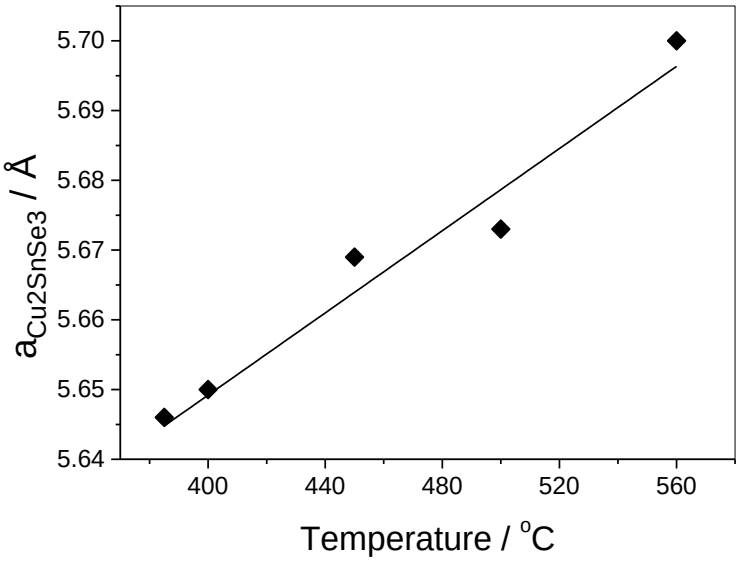

10 pav. CTSe kubinės gardelės parametro a priklausomybė nuo selenizacijos temperatūros.

560 °C temperatūroje įselenidinto CTSe sluoksnio Ramano spektre matomos smailės ties tais pačiais bangos skaičiais kaip ir CTSe įseleninto 500 °C temperatūroje, kuriame pagal RSD turėtų būti tik kubinis Cu_2SnSe_3 (11 pav.). Nepaisant to, visos juostos turėjo nedidelį poslinkį link mažesnių energijų (palyginti su apskaičiuotomis vertėmis). Ši anomalija galėjo atsirasti dėl prastesnės tvarkos sluoksnio struktūroje. Santykinis Ramano juostos intensyvumas ties 76,8 cm^{-1} ženkliai padidėjęs, palyginti su kubinio Cu_2SnSe_3 spektro intensyvumu ties 77,8 cm^{-1}. Tai gali reikšti, kad abiejuose mėginiuose yra ir kubinės, ir monoklininės struktūros Cu_2SnSe_3. CTSe mėginiuose, susintetintuose 500 °C temperatūroje, dominavo kubinis CTSe, o įselenintame 560 °C temperatūroje dominuojanti buvo monoklininė struktūra.

Monoklininio Cu_2SnSe_3 tyrimai [138] parodė tik vieną juostą, esančią mažų energijų srityje ties 83 cm^{-1}. Mūsų darbe atlikti tyrimai leidžia daryti prielaidą, kad smailė ties 76,8 cm^{-1} gali būti priskiriama monoklininei struktūrai. Bandinio, kuriame yra monoklininio Cu_2SnSe_3, šios Ramano spektro juostos intensyvumas yra daug didesnis nei spektre CTSe, kuriame pagal XRD yra tik kubinė Cu_2SnSe_3 struktūra. Todėl šią juostą galima laikyti monoklininio Cu_2SnSe_3 žymeniu.

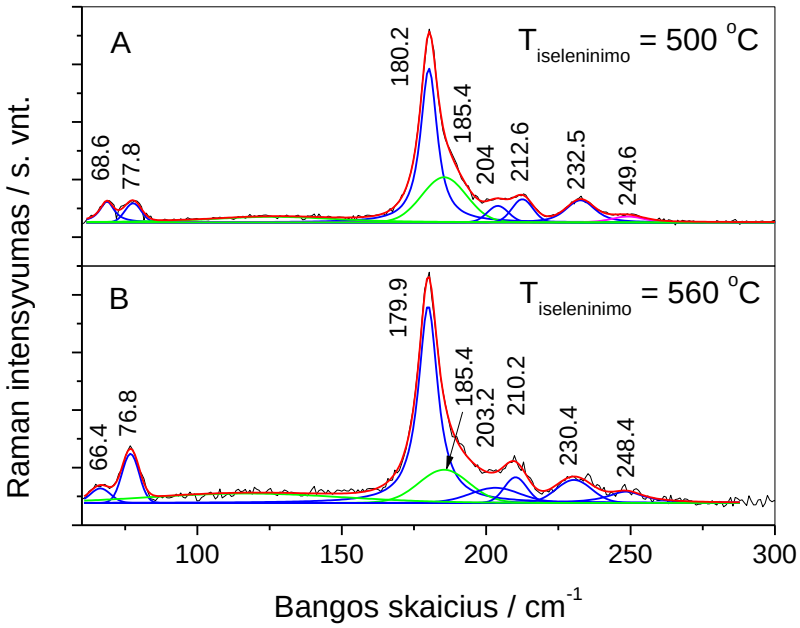

11 pav. CTSe bandinių Ramano spektrai. A – kubinės struktūros spektras, įseleninimo temperatūra 500 °C; B – maišytos struktūros (kubinės ir monoklininės) spektras, įseleninimo temperatūra 560 °C. Sužadinimui naudotas 632,8 nm lazeris (0,05 mW).

Skirtingose temperatūrose įselenintų CTSe dangų fotovoltamperometriniai tyrimai buvo atliekami 0,2 M $Eu(NO_3)_3$ tirpale. Chronoamperogramose matomi sukurtos fotosrovės impulsai. 500 °C temperatūroje įseleninto CTSe sluoksnio fotosrovės impulsai pavaizduoti 12 paveiksle. Impulsai buvo matuojami esant skirtingiems katodiniams potencialams, E_C. Viršutinėje eilėje (A) tik įseleninto CTSe fotosrovės impulsai, apatinėje eilėje (B) įseleninto ir atkaitinto 2 valandas oro atmosferoje, 200 °C temperatūroje impulsai. Pažymėtos LED šviestuko įjungimo ir išjungimo vietos „On“ ir „Off“ reiškia taškus, nuo kurių prasidėjo ir baigėsi bandinio apšvietimas. Apšviesti CTSe bandiniai generavo neigiamą fotosrovę, kuri rodo p-tipo laidumą CTSe sluoksniuose. Bandiniai po atkaitinimo 200 °C temperatūroje generavo didesnę fotosrovę, nei tik įseleninti bandiniai. Galime daryti prielaidą, kad atkaitinimas po įseleninimo daro teigiamą įtaką gardelės struktūrai, t.y. eliminuoja susidariusius žalingus defektų klasterius. 12 pav. pavaizduotos tik įselenintų ir po įseleninimo atkaitintų CTSe bandinių fotosrovės prie skirtingų potencialų.

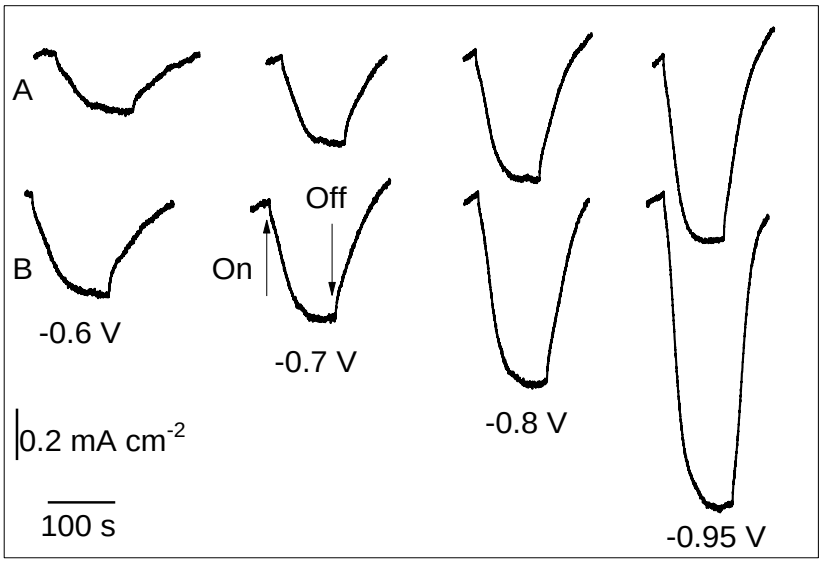

12 pav. CTSe bandinių fotosrovės impulsai (0,2 M $Eu(NO_3)_3$ tirpale). Bandiniai įseleninti 500 °C. A eilėje įseleninti CTSe bandiniai, B eilėje įseleninti ir atkaitinti 2 valandas 200 °C temperatūroje, oro atmosferoje.

CTSe bandinys, įselenintas 500 °C temperatūroje, pasižymėjo didžiausia foto srove. Sluoksnį sudarė daugiausia kubinės struktūros Cu_2SnSe_3. Sluoksniai, paruošti esant aukštesnei įseleninimo temperatūrai, pasižymėjo mažesne fotosrove, šis rezultatas prieštarauja rezultatams pateiktiems darbe [152], kuriame teigiama, kad kubinės struktūros Cu_2SnSe_3 skylių koncentracija yra didesnė, palyginti su monoklininės struktūros Cu_2SnSe_3, tai reiškia, kad pastaroji turėtų būti labiau fotoaktyvi. Tačiau, saulės elemento veikimui įtakos turi ir dvinariai selenidai [146], taškiniai defektai bei vakansijos [153].

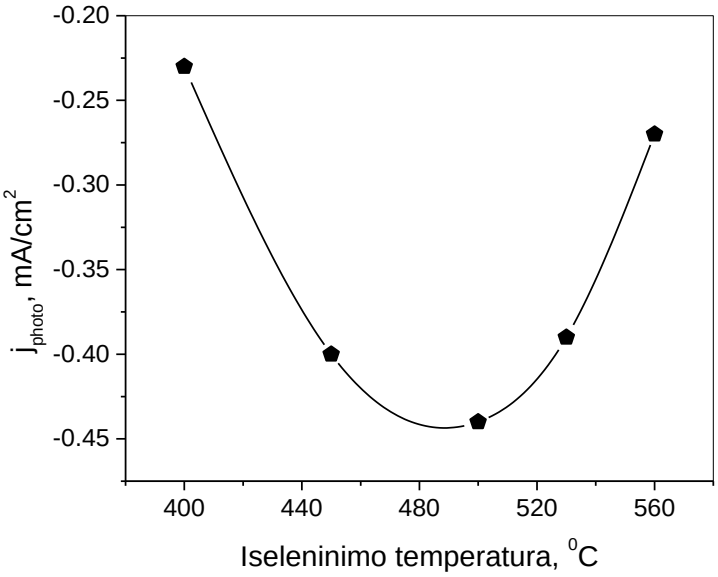

13 pav. Cu_2SnSe_3 sluoksnių fotosrovės priklausomybė nuo įseleninimo temperatūros (matuota 0,2 M $Eu(NO_3)_3$ tirpale), esant -0,8 V katodiniam potencialui.

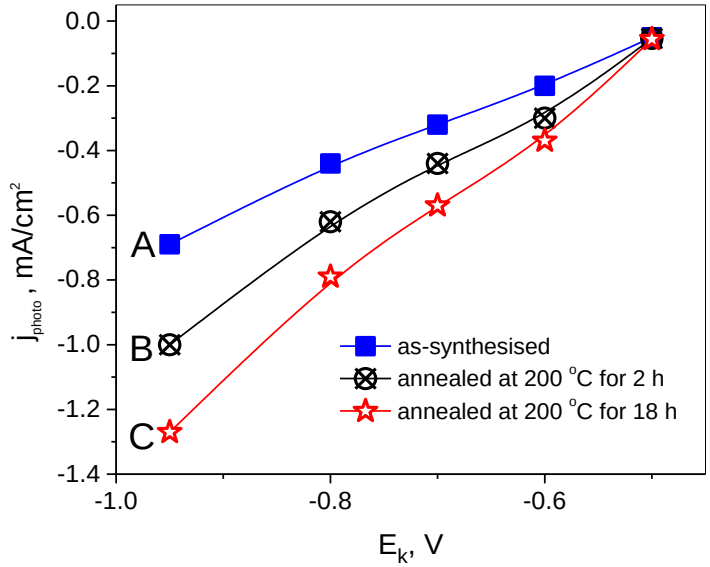

14 pav. CTSe bandinių (Cu/Sn = 1,9), įselenintų 500 °C temperatūroje, fotosrovių priklausomybė nuo katodinio potencialo E_k (0,2 M $Eu(NO_3)_3$ tirpale). A – tik įseleninto bandinio; B – įseleninto ir atkaitinto 2 valandas 200 °C temperatūroje; C - įseleninto ir atkaitinto 18 valandų 200 °C temperatūroje.

Atkaitinus įselenintą CTSe sluoksnį 200 °C temperatūroje (2 valandas), pastebimai padidėjo CTSe sluoksnių sukuriama fotosrovė. Dar didesnis fotosrovės padidėjimas buvo užfiksuotas po 18 valandų kaitinimo (14 pav.). Straipsnyje [153] teigiama, kad 200 °C yra kritinė temperatūra (T_C) kesterito junginiui. Viršijus kritinę temperatūrą T_C kesterito struktūroje tvarkingo Cu ir Zn išsidėstymo lygis mažėja. Kiti autoriai nustatė, kad priešingai nei mūsų darbe, Cu_2SnSe_3 fotoelektrocheminis atsakas sumažėjo po atkaitinimo N_2 atmosferoje, esant 150–300 ° C temperatūrai [154]. Šį sumažėjimą galėjo lemti neištirpinti vario selenidai, neištirpinti prieš fotoelektrocheminius tyrimus. Mūsų patirtis rodo, kad CTSe sluoksnių fotoelektrocheminis atsakas gali būti net 30% mažesnis, jei po įseleninimo sluoksnis neapdorojamas 5% KCN tirpale.

CTSe tyrime sukurtas elektrolito tirpalas buvo naudojamas formuoti pirmtako sluoksniams CZTS sintezėje. Nustatyta, kad Cu-Sn lydinys įseleninant ne aukštesnėje temperatūroje už 500 °C sudaro tik kubinės struktūros CTSe, monoklininė CTSe struktūra RSD metodu aptikta tik 560 °C temperatūroje įselenintose dangose. Be to, mes nustatėme, kad naudojant Raman spektroskopiją galima atskirti kubinę ir monoklininę CTSe fazes.

7.4. CZTS sluoksnių, suformuotų iš Cu-Sn/Zn pirmtako tyrimai

Šioje darbo dalyje pateikti CZTS sluoksnių tyrimo rezultatai. Cu-Sn-Zn pirmtakas buvo suformuotas elektrochemiškai nusodinant Cu-Sn lydinį ir cinko sluoksnį ant viršaus. Suformuoti trijų skirtingų sudėčių kesterito sluoksniai. Bandiniai, kurių cheminė sudėtis yra Cu-nuskurdinta Zn-nuskurdinta, Cu-nuskurdinta Zn-stechiometrinė ir Cu-nuskurdinta Zn-praturtinta. Mėginių cheminė sudėtis buvo kontroliuojama varijuojant Zn sluoksnio storį. Cheminė kesterito sudėtis buvo nustatoma po apdorojimo KCN ir HCl tirpaluose, t.y., pašalinus nuo paviršiaus vario ir cinko sulfidus. Kiekvienos mėginių grupės elementų atominiai santykiai (Cu/(Zn+Sn), Zn/Sn) pateikti 2 lentelėje.

Lentelė nr. 2. Tyrinėtų CZTS bandinių cheminė sudėtis atominiais procentais.

Bandinys	Cu	Zn	Sn	S	Cu/(Zn+Sn)	Zn/Sn
Zn-praturtintas	18.48	14.48	11.32	55.72	0.72	1.28
Stechiometrinis	17.86	12.15	11.94	58.05	0.74	1.02
Zn-nuskurdintas	18.89	10.81	12.8	57.5	0.80	0.84

Kesterito bandinių fotoelektrinis aktyvumas įvertintas matuojant fotosrovės priklausomybę nuo katodinio potencialo, apšviečiant bandinį baltos šviesos impulsais.

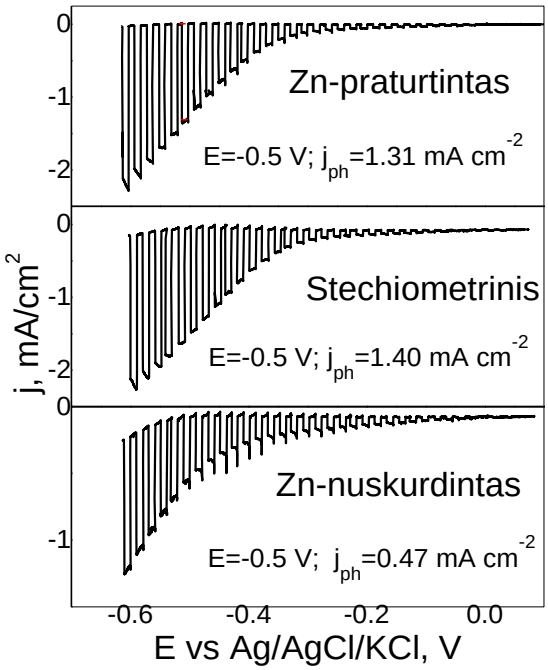

15 pav. Fotosrovės tankis j_{ph} kaip CZTS/Mo elektrodo potencialo E funkcija (palyginamasis elektrodas Ag/AgCl/KCl). Fotosrovė matuota vandeniniame 0,1 M $Eu(NO_3)_3$ tirpale. Potencialo skleidimo greitis 1 mV/s. Šviesos intensyvumas 100 mW/cm^2.

Didžiausią fotoatsaką pademonstravo stechiometrinį Zn kiekį turintis CZTS bandinys, mažiausias j_{ph} buvo Zn-nuskurdinto bandinio. Fotosrovės impulsai nėra taisyklingos stčiakampės formos. Kai šviesa įjungiama ir išjungiama j_{ph} pasiekia atitinkamai didesnes ar mažesnes vertes, už tas kurios nusistovi po tam tikro laiko. Šie fotosrovės šuoliai ir jų dydis yra susiję su lėta pagautų krūvininkų rekombinacijos kinetika [148]. Srovės tankis, atsirandantis dėl šio reiškinio, pažymėtas j_{tr}. 16 paveiksle pavaizduotas fotosrovės impulsas. Šis j ~ f (E) priklausomybės fragmentas buvo paimtas iš Stechiometrinio CZTS bandinio matavimų. Bendras srovės tankis susideda iš foto srovės j_{ph} ir srovės šuolio j_{tr}, kurios vertės Zn-nuskurdintam, Stechiometriniam ir Zn-

praturtinatam mėginiams atitinkamai buvo 0,040, 0,025 ir 0,044 mA/cm^2. Mažiausia j_{tr} gauta Stechiometriniam bandiniui.

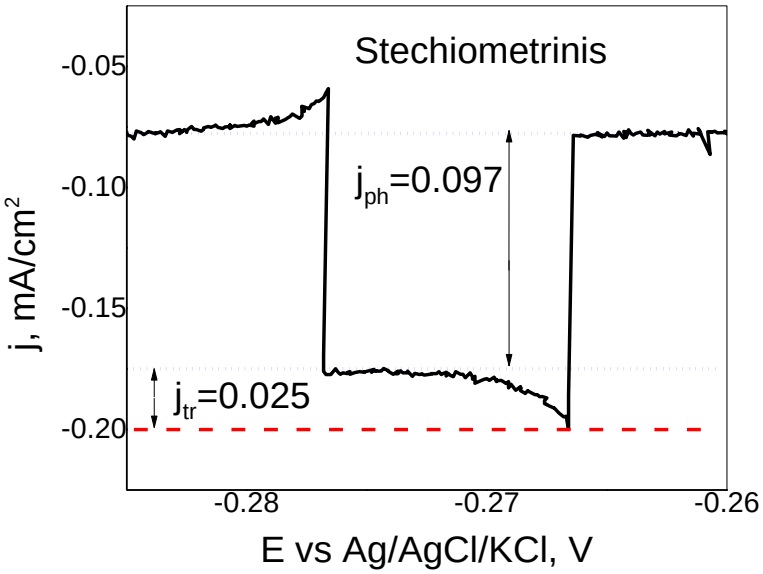

16 pav. Stechiometrinio CZTS bandinio fotovoltamperogramos fragmentas. Potencialo skleidimo greitis 1 mV/s. Šviesos intensyvumas 100 mW/cm^2.

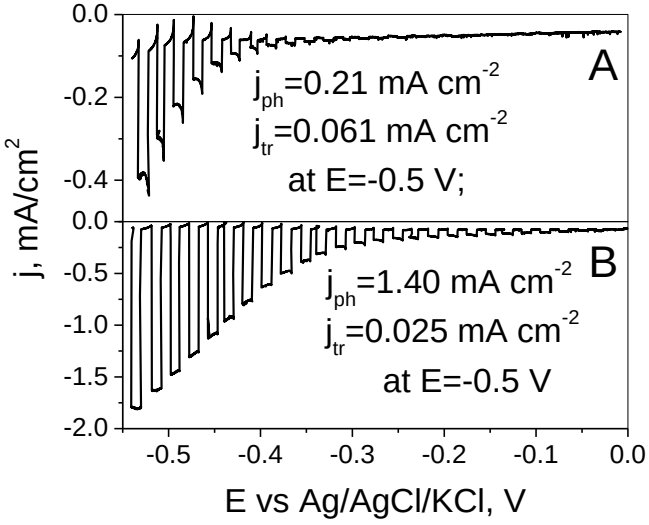

17 pav. CZTS Stechiometrinio bandinio fotovoltamperogramos (0,1 M $Eu(NO_3)_3$ tirpale). A – tik įseleninto bandinio; B – įseleninto ir apdoroto KCN ir HCl tirpaluose.

CZTS sluoksnių apdorojimas KCN ir HCl tirpaluose stipriai teigiamai įtakojo rekombinacijos efektą. 17 paveiksle matomas ryškus j_{tr} sumažėjimas, palyginti su neapdorotu bandiniu. Kartu su rekombinacijos sumažėjimu CZTS/Eu $(NO_3)_3$ sąlyčio taške, sluoksnių apdorojimas su KCN ir HCl taip pat turėjo teigiamą poveikį j_{ph}, srovės tankio vertė (Stechiometrinio bandinio) padidėjo 7 kartus (esant -0,5 V potencialui).

Lentelė Nr. 3. Apskaičiuoti CZTS bandinių Q ir Q′ parametrai, juos atitinkantis struktūros tipas bei tvarkingumo lygis S.

Bandinys	Cu/(Zn+ Sn)	Zn/Sn	Q	Q′	Struktūros tipas	S
Stechiometrinis	0.66	1.02	2.5	2.0	B_S	0.4
Zn-praturtintas	0.72	1.28	1.5	2.1	B_S	0.3
Zn-nuskurdintas	0.80	0.84	2.4	2.5	B_S	0.4

Iš pradžių, norint nustatyti taškinių defektų skaičių ir kilmę kesterito sluoksnyje, buvo naudojama Ramano spektroskopija, taip pat buvo nustatytas tvarkingumo lygis S, kurio vertė 0 reiškia visiškai netvarkingą, o 1 - visiškai tvarkingą kesterito struktūrą. Q ir Q′ parametrai buvo apskaičiuoti naudojant CZTS mėginių Ramano spektrus (sužadinimo bangos ilgis 785 nm) (18 pav.) $Q = I_{288}/I_{304}$ ir $Q' = I_{338}/ I_{367} + I_{375}$), kur I_i yra kesterito Ramano atitinkamos juostos integralinis intensyvumas [151]. Rezultatai pateikti 3 lentelėje

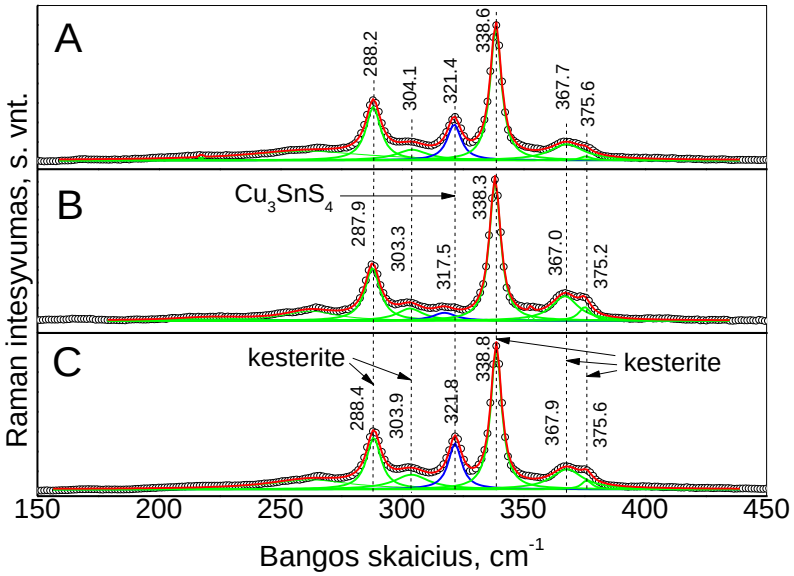

18 pav. CZTS sluoksnių Ramano spektrai. A – Zn-nuskurdinto; B – Stechiometrinio; C – Zn-praturtinto bandinio. Naudotas sužadinimo bangos ilgis 785 nm.

CZTS mėginių Q ir Q′ parametrai rodo B_S tipo struktūrą (pagal [151]). B_S tipo struktūra yra tvarkingas (mažai Cu_{Zn} ir Zn_{Cu} taškinių defektų) nestechiometrinis kesteritas ($Cu_{1.95}Zn_{1.06}Sn_{0.99}S_4$) gaunamas lėtai aušinant bandinius po įsierinimo. Netvarkingo nestechiometrinio kesterito tipas - B_Q gaunamas greitai aušinant [151] bandinius po įsierinimo. Greitai aušinamo kesterito struktūros Q ir Q′ parametrai turėtų būti ≤ 1,0. B tipo kesterito struktūrai būdingi [$2Zn_{Cu}^{+}$ + $ZnSn_2^{-}$] taškinių defektų klasteriai [151]. Remiantis [20], tvarkos vertė S turi tiesinę priklausomybę nuo Q parametro. Pagal šią priklausomybę ir mūsų išmatuotas CZTS mėginių Q reikšmes (3 lentelė) įvertinome tvarkos lygį S mūsų bandiniuose. Mėginiuose nustatytos S vertės buvo 0,28 - 0,45 intervale. Vertės atitinka kesterito sluoksnių, suformuotų naudojant vamzdinę krosnį darbe [152] pateiktas vertes.

Fazinei sudėčiai nustatyti CZTS bandiniai pirmiausia buvo analizuojami naudojant RSD metodą su Cu $K_{\alpha 1,2}$ spinduliuote. Rentgenogramos rodo, kad visuose mėginiuose yra $Cu_{1,885}Zn_{1,058}SnS_4$ (ICDD # 01-080-8226) nestechiometrinė kesterito fazė. Visuose tik suformuotuose CZTS bandiniuose aptikta antrinė fazė Cu_2S (# 00-002-1284). CZTS mėginių RSD

duomenys negali nei patvirtinti nei paneigti cinko sulfido ar trinarių antrinių fazių būvimą, pagrindinės ZnS ir trinarių antrinių fazių RSD smailės sutampa su kesterito smailėmis. Rentgenogramose, užrašytose apdorojus CZTS sluoksnius KCN tirpale, vario sulfido smailės visiškai išnyko. Tai rodo, kad Cu_2S fazė buvo tik ant kesterito sluoksnio paviršiaus.

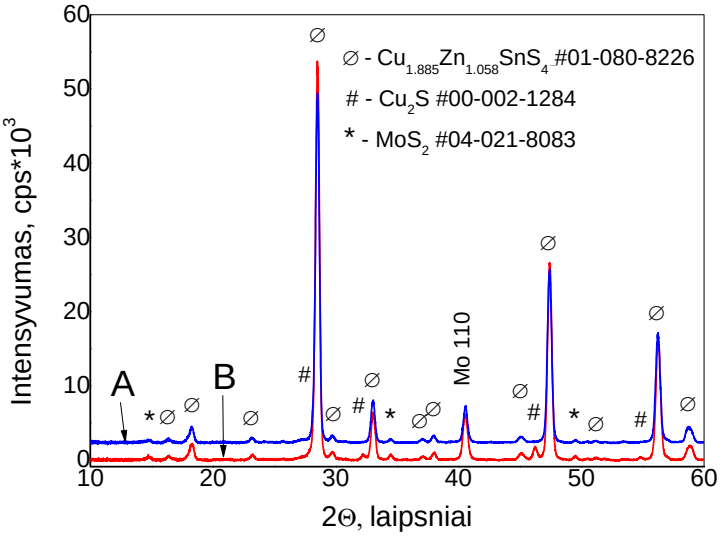

19 pav. CZTS stechiometrinio bandinio rentgenogramos, užrašytos naudojant Cu $K_{\alpha 1,2}$ spinduliuotę. B – tik suformuoto sluoksnio rentgenograma; A – to paties bandinio, apdoroto KCN tirpale, rentgenograma.

19 paveiksle parodytos rentgenogramos Stechiometrinio kesterito mėginio, kuris pagal Ramano matavimus turėjo mažiausią ortorombinės Cu_3SnS_4 fazės kiekį. Tačiau ir Zn-nuskurdinto bei Zn-praturtinto sluoksnių rentgenogramose nėra jokių ortorombinės Cu_3SnS_4 fazės smailių, tuo tarpu Ramano spektruose šios fazės juostos buvo aiškiai matomos (16 pav. raudonas spektras, juostos 321 ir 642 cm^{-1}). Šis neatitikimas gali būti dėl didesnio Ramano spektroskopijos jautrumo šiai konkrečiai fazei, kai sužadinimui naudojamas 785 nm bangos ilgis, t.y., šis bangos ilgis gali būti rezonansinis šiam junginiui. Tai patvirtina Zn-nuskurdinto mėginio Ramano spektras, kai sužadinimui buvo naudojamas 532 nm bangos ilgis, neparodęs juostų, priklausančių ortorombiniam Cu_3SnS_4, (20 pav. mėlynas spektras). Tai, kad Zn-praturtintame mėginyje, esant cinko pertekliui, sudarė ortorombinis Cu_3SnS_4 galima aiškinti tuo, kad dideli ZnS dariniai susidarė dar prieš pradedant

formuotis ortorombinei CTS fazei ir todėl negalėjo pilnai sureaguoti su pastaraja susidarant kesteritui.

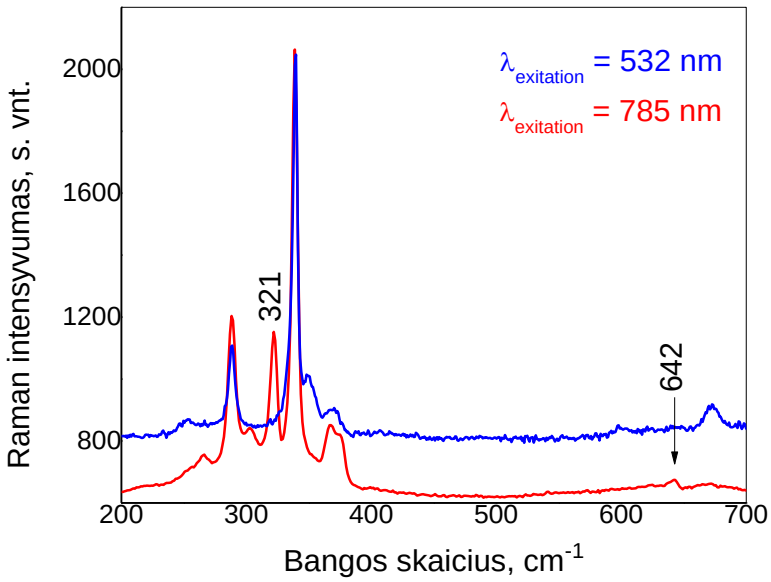

20 pav. Zn-nuskurdinto CZTS bandinio Ramano spektrai. Sužadinimo bangos ilgiai mėlynai pažymėtam spektrui – 532 nm, raudonai pažymėtam – 785.

Siekdami įvertinti kesterito taškinių defektų kiekį RSD metodu panaudojome didelės skiriamosios gebos RSD matavimus, naudojant tik Cu $K_{\alpha 1}$ spinduliuotę. Naudodami šį RSD metodą, mes galėjome nustatyti tikslius kesterito gardelės parametrus (matavimu rezultatai pakoreguoti pagal NIST LaB_6 etaloną) ir įvertinti tvarkos/netvarkos lygį kesterito struktūroje. Taip pat dėl didelės skiriamosios gebos šis RSD metodas suteikia galimybę įvertinti cinko sulfido kiekį mūsų mėginiuose. Zn-praturtinto bandinio didelės skyros rentgenogramos fragmentas pateiktas 21 paveiksle. Kesterito smailės 220 ir 204 bei ZnS 220 (# 00-005-0566) smailės gerai atsiskiria, todėl jų maksimumų padėtis, integralinius intensyvumus ir puspločius (FWHM) galima tiksliai išmatuoti. CZTS 220 ir ZnS 220 smailių integraliniai intensyvumai buvo naudojami cinko sulfido kiekiui (tūrio procentais) apskaičiuoti kesterito sluoksnyje, rezultatai pateikti 4 lentelėje.

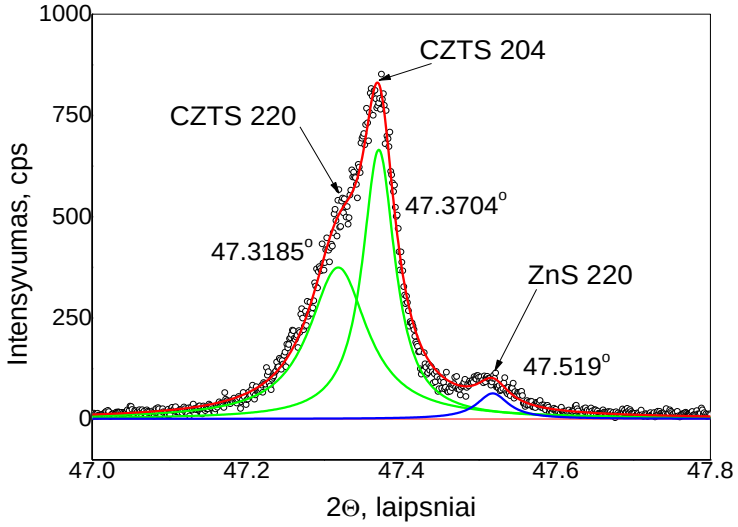

21 pav. Zn-praturtinto CZTS bandinio rentgenogramos fragmentas, užrašytas naudojant Cu $K_{\alpha 1}$ spinduliuotę.

Lentelė Nr. 4. CZTS bandinių tetragoninės gardelės parametrai a ir c, atstumas tarp kesterito smailių 004 ir 200, šių smailių puspločiai (FWHM) ir ZnS kiekis (tūrio procentais).

Bandinys	a, Å	c, Å	($2\Theta_{004}$-$2\Theta_{200}$)	FWHM 200	FWHM 004	D_{200}, nm	ZnS, vol. %
Stechiometrinis	5.4288	10.8288	0.089± 0.005°	0.0913°	0.0340°	157	13.9
Zn-praturtintas	5.4281	10.8308	0.080± 0.004°	0.1187°	0.0327°	107	6.6
Zn-nuskurdintas	5.4281	10.8319	0.076± 0.006°	0.1290°	0.0384°	95	2.3

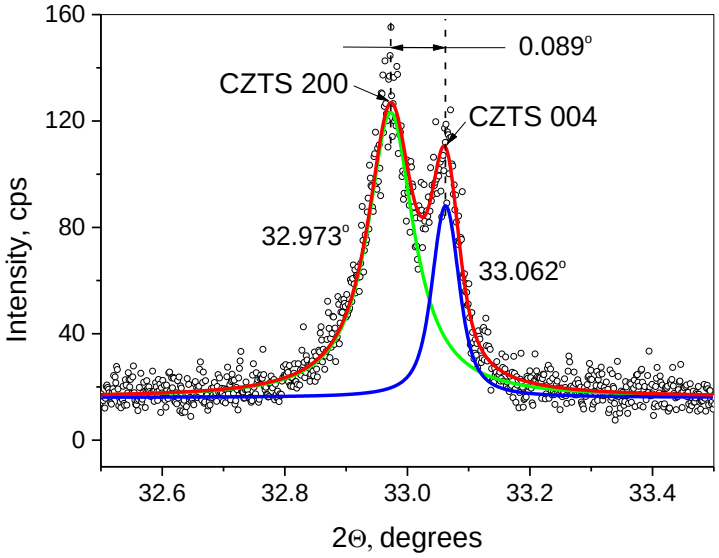

22 pav. CZTS Stechiometrinio bandinio rentgenogramos fragmentas. Matavimas atliktas naudojant Cu $K_{\alpha 1}$ spinduliuotę.

22 paveiksle parodytas stechiometrinio mėginio rentgenogramos fragmentas. Šiame fragmente matome 200 ir 004 kesterito smailes. Skirtumas tarp šių smailių 2Θ max verčių rodo kesterito struktūros tvarkos/netvarkos lygį. Tvarkingos Zn-praturtinto Cu-nuskurdinto kesterito (A tipo) struktūros 2Θ max skirtumas yra ~ 0,119°, Cu-praturtinto Zn-nuskurdinto netvarkingo kesterito struktūros (C tipo) skirtumas yra tik 0,061° [163] . 4 lentelėje pateikti išmatuoti 2Θ max verčių skirtumai mūsų tirtiems CZTS bandiniams. Visų mūsų matuotų bandinių 2Θ max verčių skirtumas buvo tarp 0,076° ir 0,089°. Rezultatai daugmaž sutampa su S tvarkos/netvarkos vertėmis, nustatytomis Ramano spektroskopijos metodu.

2Θ max vertės taip pat buvo naudojamos nustatant kesterito gardelės parametrus. Parametrai a ir c buvo apskaičiuoti naudojant atitinkamai 200 ir 004 smailes. Mūsų CZTS mėginių gauti kesterito gardelės parametrai turėjo mažesnes vertes, nei būdingos Cu-nuskurdintam ir pagal Zn stechiometriniam kesteritui [164]. Geriausiai su [164] pateiktomis vertėmis mūsų kesterito a ir c vertės atitiko ne-stechiometrinį Zn-nuskurdintą, Cu-praturtintą kesteritą ($Cu_{2.078}Zn_{0.909}Sn_{1.022}S_{4.000}$). Žinoma, kad tokiam ne-stechiometriniam kesteritui (C tipo) yra būdingos [$2Cu_{Zn}^{-} + Sn_{Zn}^{2+}$] defektų poros [67]. Šie taškiniai defektai daro didelę (neigiamą) įtaką CZTS saulės elemento efektyvumui.

Skirtumo tarp RSD smailių 200 ir 004 vertė koreliuoja su kesterito tvarka/netvarka, didesnis skirtumas reiškia tvarkingesnę kesterito struktūrą (didesnė S vertė). Didžiausias skirtumas tarp minėtų smailių nustatytas Stechiometriniame CZTS sluoksnyje, kuriame tačiau buvo ir didžiausias ZnS kiekis. ZnS sankaupos turėtų neigiamai paveikti saulės elemento našumą, tačiau pagal [148], jei cinko sulfido sankaupos yra šalia sluoksnio paviršiaus, tai gali netgi pagerinti elemento fotoelektrines savybes.

Iš visų metodų, kuriuos taikėme mėginių fazinės sudėties, struktūros ir taškinių defektų tyrimams šiame darbe, buvo nustatyta, kad fotoelektrocheminių tyrimų duomenys daug geriau sutampa su RSD tyrimo rezultatais, nei su Ramano spektroskopija. Mažiausią j_{tr} vertę demonstravo CZTS bandinys Stechiometrinis, kurio foto srovės tankis taip pat buvo didžiausias. Stechiometrinis bandinys turėjo didžiausius kristalitus ir aukščiausią tvarkos vertę (didžiausias skirtumas tarp kesterito smailių 004 ir 200) iš tirtų trijų bandinių grupių. Taip pat ir Ramano spektroskopijos matavimai parodė, kad CZTS bandinys Stechiometrinis galėtų būti aukščiausios kokybės absorberis, nes ortorombinės Cu_3SnS_4 antrinės fazės kiekis jame buvo mažiausias. Tačiau cinko sulfido kiekiai nustatyti RSD metodu nesutapo su Ramano spektroskopijos rezultatais. Rezultatų nesutapimas gali būti susijęs su skirtingais bandinių gyliais, iš kurių gaunama informacija - lazerio spinduliuotė (325 nm) neprasiskverbia į tiriamąjį sluoksnį taip giliai, kaip rentgeno spinduliai. Ramano spektroskopija teikia informaciją tik iš maždaug 100 nm gylio ir kelių kvadratinių mikronų ploto, tuo tarpu rentgeno spindulių difrakcija suteikia informaciją iš viso CZTS sluoksnio storio (~ 1500 nm) ir daug didesnio, maždaug 10 kvadratinių milimetrų ploto. Zn-praturtintas CZTS mėginys turėjo didesnį cinko sulfido kiekį šalia sluoksnio paviršiaus. Netoli paviršiaus esančius ZnS klasterius galima laikyti normaliu reiškiniu, nes metalinis cinko sluoksnis šio bandinio pirmtake buvo daug storesnis nei kituose bandiniuose. Zn-praturtintame ir Stechiometriniame bandiniuose ne tik cinko sulfido kiekis buvo skirtingas, bet taip pat ir ZnS pasiskirstymas sluoksnyje pagal gylį. Tai įrodyta atlikus SEM ir TEM analizę. Skerspjūvio vaizdai ir EDX profilio matavimai parodė, kad cinko sulfidas yra labiau koncentruotas šalia paviršiaus Zn-praturtintame bandinyje ir labiau atsitiktinai pasiskirstęs Stechiometriniame CZTS.

IŠVADOS

1. CZTS bandinių, pagamintų įsierinant Cu-Sn/Zn pirmtakus, homogeniškumas ir fazių grynumas yra pranašesnis už tuos, kurie buvo pagaminti įsierinant Cu/Sn/Cu/Zn pirmtakus. Elektrochemiškai nusodinus Cu-Sn lydinį Cu ir Sn pasiskirstymas sluoksnyje yra geresnis nei pasluoksniui nusodinus Cu/Sn/Cu metalus.
2. Didžiausią fotoelektrocheminį atsaką demonstravo Cu_2SnSe_3 sluoksniai įseleninti 500 °C temperatūroje. Cu_2SnSe_3 sluoksnių našumas padidėja po jų atkaitinimo ore 200 °C temperatūroje. Darome prielaidą, kad atkaitinimas po įseleninimo pagerino atomų išsidėstymo tvarką kristalinėje struktūroje ir sumažino V_{Cu} defektų kiekį.
3. Kubinis Cu_2SnSe_3 susiformuoja bandiniuose, įseleninant Cu-Sn pirmtaką 350–500 °C temperatūrų intervale. Kubinės gardelės parametras tiesiškai didėja keliant temperatūrą. Monoklininis Cu_2SnSe_3 RSD metodu buvo aptiktas tik 560 °C temperatūroje įselenintuose sluoksniuose.
4. Atlikus Cu_2SnSe_3 sluoksnių tyrimus Ramano spektroskopijos metodu įrodyta, kad juosta ties ~77 cm^{-1} gali būti šio junginio monoklininės struktūros žymekliu siekiant ją atskirti nuo kubinės. Ši juosta gerokai intensyvesnė bandiniui kuriame, pagal RSD tyrimus, dominuojanti fazė – monoklininė.
5. Fotoelektrocheminiai tyrimai parodė, kad Stechiometrinis bandinys turėjo didžiausią fotosrovės tankį j_{ph} ir mažiausias j_{tr} vertes, rezultatas puikiai koreliuoja su kitų tyrimų rezultatais – Stechiometriniame bandinyje nustatyti didžiausi kristalitai, taip pat tvarkos lygis S buvo geriausias iš tyrinėtų Zn-praturtinto, pagal Zn stechiometrinio ir Zn-nuskurdinto bandinių.
6. Nustatyta, kad tiriant Cu_2ZnSnS_4 fazinį grynumą Ramano spektroskopijos metodu sužadinimo bangos ilgis 785 cm^{-1} yra rezonansinis ortorombinei Cu_3SnS_4 fazei.
7. Pagal RSD duomenis, ne stechiometrinis kesteritas $Cu_{2.078}Zn_{0.909}Sn_{1.022}S_{4.000}$ susidarė visuose tirtuose bandiniuose, nepriklausomai nuo Zn/Sn santykio sluoksnyje.
8. Mūsų darbe RSD metodas, naudojant Cu $K_{\alpha 1}$ spinduliuotę, suteikia labiau patikimą informaciją apie kesterito stechiometriją ir taškinius defektus, nei Ramano spektroskopija. Rentgeno spinduliai prasiskverbia daug giliau nei Ramano spektroskopijoje naudojamo lazerio spinduliai, todėl RSD metodu gaunama informacija iš daug didesnio bandinio tūrio.

BIBLIOGRAPHY

1. Peter, L.M., *Towards sustainable photovoltaics: the search for new materials.* Philosophical Transactions of the Royal Society A: Mathematical, Physical and Engineering Sciences, 2011. **369**(1942): p. 1840-1856.
2. Giraldo, S., et al., *Progress and Perspectives of Thin Film Kesterite Photovoltaic Technology: A Critical Review.* Advanced Materials, 2019. **31**(16): p. 1806692.
3. Arkhipov, J.P.a.V., *Thin Film Solar Cells, Fabrication, Characterization and Applications*. 2006, John Wiley & Sons Ltd: Chichester, West Sussex, England.
4. Jackson, P., et al., *Effects of heavy alkali elements in Cu(In,Ga)Se2 solar cells with efficiencies up to 22.6%.* physica status solidi (RRL) – Rapid Research Letters, 2016. **10**(8): p. 583-586.
5. Jackson, P., et al., *Effects of heavy alkali elements in Cu(In,Ga)Se2 solar cells with efficiencies up to 22.6 %.* physica status solidi (RRL) - Rapid Research Letters, 2016.
6. Yazici, S., et al., *Growth of Cu 2 ZnSnS 4 absorber layer on flexible metallic substrates for thin film solar cell applications*. Vol. 589. 2015. 563-573.
7. Repins, I., et al., *19·9%-efficient ZnO/CdS/CuInGaSe2 solar cell with 81·2% fill factor.* Progress in Photovoltaics: Research and Applications, 2008. **16**(3): p. 235-239.
8. Nitsche, R., D.F. Sargent, and P. Wild, *Crystal growth of quaternary 122464 chalcogenides by iodine vapor transport.* Journal of Crystal Growth, 1967. **1**(1): p. 52-53.
9. Ito, K. and T. Nakazawa, *Electrical and Optical Properties of Stannite-Type Quaternary Semiconductor Thin Films.* Japanese Journal of Applied Physics, 1988. **27**(Part 1, No. 11): p. 2094-2097.
10. Katagiri, H., et al., *Preparation and evaluation of Cu2ZnSnS4 thin films by sulfurization of E-B evaporated precursors.* Solar Energy Materials and Solar Cells, 1997. **49**(1): p. 407-414.
11. Yu, L. and A. Zunger, *Identification of Potential Photovoltaic Absorbers Based on First-Principles Spectroscopic Screening of Materials.* Physical Review Letters, 2012. **108**(6).
12. Phillips, L.a.S., Christopher and Hutter, Oliver and Mariotti, Silvia and Bowen, Leon and Birkett, Max and Scanlon, David and Major, Jonathan and Yates, P and Shiel, Huw and Mariotti, S and Birkett, Max and Durose, K. and Major, J, *Current Enhancement via a TiO2*

Window Layer for CSS Sb2Se3 Solar Cells: Performance Limits and High Voc. IEEE Journal of Photovoltaics, 2018. **9**: p. 544 - 551.
13. Shockley, W. and H.J. Queisser, *Detailed Balance Limit of Efficiency of p-n Junction Solar Cells.* Journal of Applied Physics, 1961. **32**(3): p. 510-519.
14. Olekseyuk, I.D., et al., *Single crystal preparation and crystal structure of the Cu2Zn/Cd,Hg/SnSe4 compounds.* Journal of Alloys and Compounds, 2002. **340**(1): p. 141-145.
15. Nateprov, A., et al., *Single crystal X-ray structure investigation of Cu2ZnSnSe4.* Surface Engineering and Applied Electrochemistry, 2013. **49**(5): p. 423-426.
16. P. Atkince, J.d.P., *Elements of Physical Chemistry*. 2009: Oxford University press.
17. *JCPDS Card: 26-0575.*
18. Wang, H., *Progress in Thin Film Solar Cells Based on Cu 2 ZnSnS 4.* International Journal of Photoenergy, 2011. **2011**.
19. Guen, L. and W.S. Glaunsinger, *Electrical, magnetic, and EPR studies of the quaternary chalcogenides Cu2AIIBIVX4 prepared by iodine transport.* Journal of Solid State Chemistry, 1980. **35**(1): p. 10-21.
20. Schorr, S., *The crystal structure of kesterite type compounds: A neutron and X-ray diffraction study.* Solar Energy Materials and Solar Cells, 2011. **95**(6): p. 1482-1488.
21. Chen, S., et al., *Crystal and electronic band structure of Cu2ZnSnX4 (X=S and Se) photovoltaic absorbers: First-principles insights.* Applied Physics Letters, 2009. **94**(4): p. 041903.
22. Zhang, X., et al., *Efficient thermolysis route to monodisperse Cu_2ZnSnS_4 nanocrystals with controlled shape and structure.* Scientific reports, 2014. **4**: p. 5086-5086.
23. Hages, C. and R. Agrawal, *Copper Zinc Tin Sulfide-Based Thin Film Solar Cells*. 2015. p. 239-270.
24. Andrade-Arvizu, J., et al., *Is It Possible To Develop Complex S–Se Graded Band Gap Profiles in Kesterite-Based Solar Cells?* ACS Applied Materials & Interfaces, 2019. **11**(36): p. 32945-32956.
25. Matsushita, H., T. Ichikawa, and A. Katsui, *Structural, thermodynamical and optical properties of Cu2-II-IV-VI4 quaternary compounds.* Journal of Materials Science, 2005. **40**(8): p. 2003-2005.
26. Jones, R.M., *Mechanics of Composite Materials*. second ed. ed. 1999, Philadelphia, PA: Taylor and Francis.

27. Wang, W., et al., *Device Characteristics of CZTSSe Thin-Film Solar Cells with 12.6% Efficiency.* Advanced Energy Materials, 2014. **4**(7): p. 1301465.
28. Zhang, Y., et al., *Earth-abundant and low-cost CZTS solar cell on flexible molybdenum foil.* RSC Advances, 2014. **4**: p. 23666.
29. Shin, B., et al., *Thin film solar cell with 8.4% power conversion efficiency using an earth-abundant Cu2ZnSnS4 absorber.* Progress in Photovoltaics: Research and Applications, 2013. **21**(1): p. 72-76.
30. Olekseyuk, I.D., I.V. Dudchak, and L.V. Piskach, *Phase equilibria in the Cu2S–ZnS–SnS2 system.* Journal of Alloys and Compounds, 2004. **368**(1): p. 135-143.
31. Scragg, J., *Studies of Cu2ZnSnS4 films prepared by sulphurisation of electrodeposited precursors*. 2010, University of Bath.
32. Muska, K., et al., *Synthesis of Cu2ZnSnS4 monograin powders with different compositions.* Energy Procedia, 2011. **10**: p. 203-207.
33. Nagoya, A., et al., *Defect formation and phase stability of Cu_ {2} ZnSnS_ {4} photovoltaic material.* Phys. Rev. B, 2010. **81**.
34. Chen, S., et al., *Defect physics of the kesterite thin-film solar cell absorber Cu2ZnSnS4.* Applied Physics Letters, 2010. **96**(2): p. 021902.
35. Li, Z., et al., *The Study of Structural Transition of ZnS Nanorods under High Pressure.* The Journal of Physical Chemistry C, 2011. **115**(2): p. 357-361.
36. Siebentritt, S. and S. Schorr, *Kesterites-a challenging material for solar cells.* Progress in Photovoltaics: Research and Applications, 2012. **20**(5): p. 512-519.
37. Nozaki, H., K. Shibata, and N. Ohhashi, *Metallic hole conduction in CuS.* Journal of Solid State Chemistry, 1991. **91**(2): p. 306-311.
38. Liang, W. and M.H. Whangbo, *Conductivity anisotropy and structural phase transition in Covellite CuS.* Solid State Communications, 1993. **85**(5): p. 405-408.
39. Thangaraju, B. and P. Kaliannan, *Spray pyrolytic deposition and characterization of SnS and SnS2thin films.* Journal of Physics D: Applied Physics, 2000. **33**(9): p. 1054-1059.
40. Ogah, O.E., et al., *Thin films of tin sulphide for use in thin film solar cell devices.* Thin Solid Films, 2009. **517**(7): p. 2485-2488.
41. Calixto-Rodriguez, M., et al., *Structural, optical, and electrical properties of tin sulfide thin films grown by spray pyrolysis.* Thin Solid Films, 2009. **517**(7): p. 2497-2499.

42. Avellaneda, D., M.T.S. Nair, and P.K. Nair, *Photovoltaic structures using chemically deposited tin sulfide thin films.* Thin Solid Films, 2009. **517**(7): p. 2500-2502.
43. Tiwari, D., et al., *Non-toxic, earth-abundant 2% efficient Cu2SnS3 solar cell based on tetragonal films direct-coated from single metal-organic precursor solution.* Solar Energy Materials and Solar Cells, 2013. **113**: p. 165-170.
44. Wu, C., et al., *Hexagonal Cu2SnS3 with metallic character: Another category of conducting sulfides.* Applied Physics Letters, 2007. **91**: p. 143104-143104.
45. Baranowski, L.L., et al., *Control of Doping in Cu2SnS3 through Defects and Alloying.* Chemistry of Materials, 2014. **26**(17): p. 4951-4959.
46. Lu, Y., et al., *The characteristic of Cu2ZnSnS4 thin film solar cells prepared by sputtering CuSn and CuZn alloy targets.* Current Applied Physics, 2018. **18**(12): p. 1571-1576.
47. Shin, S.W., et al., *Studies on Cu2ZnSnS4 (CZTS) absorber layer using different stacking orders in precursor thin films.* Solar Energy Materials and Solar Cells, 2011. **95**(12): p. 3202-3206.
48. Fernandes, P., P. Salomé, and A.F. da Cunha, *Growth and Raman scattering characterization of Cu2ZnSnS4 thin films.* Thin Solid Films, 2009. **517**.
49. Nilsen, W.G., *Raman Spectrum of Cubic ZnS.* Physical Review, 1969. **182**(3): p. 838-850.
50. Fernandes, P.A., P.M.P. Salomé, and A.F. da Cunha, *CuxSnSx+1 (x = 2, 3) thin films grown by sulfurization of metallic precursors deposited by dc magnetron sputtering.* physica status solidi c, 2010. **7**(3-4): p. 901-904.
51. Berg, D.M., et al., *Raman analysis of monoclinic Cu2SnS3 thin films.* Applied Physics Letters, 2012. **100**(19): p. 192103.
52. Dimitrievska, M., et al., *Multiwavelength excitation Raman scattering study of polycrystalline kesterite Cu2ZnSnS4 thin films.* Applied Physics Letters, 2014. **104**(2): p. 021901.
53. Berg, D.M., et al., *Discrimination and detection limits of secondary phases in Cu 2 ZnSnS 4 using X-ray diffraction and Raman spectroscopy*. Thin Solid Films, 2014. **569**: p. 113-123.
54. Fontané, X., et al., *In-depth resolved Raman scattering analysis for the identification of secondary phases: Characterization of Cu2ZnSnS4 layers for solar cell applications.* Applied Physics Letters, 2011. **98**(18): p. 181905.

55. Altosaar, M., et al., *Cu2Zn1-xCdx Sn(Se1-ySy)4 solid solutions as absorber materials for solar cells.* Physica Status Solidi (a), 2008. **205**: p. 167-170.
56. Berg, D., et al., *Raman analysis of monoclinic Cu2SnS3 thin films.* Applied Physics Letters, 2012. **100**.
57. Fernandes, P.A., P.M.P. Salomé, and A.F. da Cunha, *Study of polycrystalline Cu2ZnSnS4 films by Raman scattering.* Journal of Alloys and Compounds, 2011. **509**(28): p. 7600-7606.
58. Price, L.S., et al., *Atmospheric Pressure Chemical Vapor Deposition of Tin Sulfides (SnS, Sn2S3, and SnS2) on Glass.* Chemistry of Materials, 1999. **11**(7): p. 1792-1799.
59. Grossberg, M., et al., *The role of structural properties on deep defect states in Cu2ZnSnS4 studied by photoluminescence spectroscopy.* Applied Physics Letters, 2012. **101**(10): p. 102102.
60. Hönes, K., et al., *Shallow defects in Cu2ZnSnS4.* Physica B: Condensed Matter, 2009. **404**(23): p. 4949-4952.
61. Chen, S., et al., *Classification of lattice defects in the kesterite Cu2ZnSnS4 and Cu2ZnSnSe4 earth-abundant solar cell absorbers.* Adv Mater, 2013. **25**(11): p. 1522-39.
62. Polizzotti, A., et al., *The state and future prospects of kesterite photovoltaics.* 2013.
63. Chen, S., et al., *Intrinsic point defects and complexes in the quaternary kesterite semiconductor Cu_ {2} ZnSnS_ {4}.* Phys. Rev. B, 2010. **81**.
64. Katagiri, H., et al., *Development of thin film solar cell based on Cu2ZnSnS4 thin films.* Solar Energy Materials and Solar Cells, 2001. **65**(1): p. 141-148.
65. Wibowo, R.A., et al., *Single step preparation of quaternary Cu2ZnSnSe4 thin films by RF magnetron sputtering from binary chalcogenide targets.* Journal of Physics and Chemistry of Solids, 2007. **68**(10): p. 1908-1913.
66. Tanaka, T., et al., *Preparation of Cu2ZnSnS4 thin films by hybrid sputtering.* Journal of Physics and Chemistry of Solids, 2005. **66**(11): p. 1978-1981.
67. Valle Rios, L.E., et al., *Existence of off-stoichiometric single phase kesterite.* Journal of Alloys and Compounds, 2016. **657**: p. 408-413.
68. Márquez, J., et al., *Systematic compositional changes and their influence on lattice and optoelectronic properties of Cu 2 ZnSnSe 4 kesterite solar cells.* Solar Energy Materials and Solar Cells, 2016. **144**: p. 579-585.

69. Pawar, S.M., et al., *Growth of void free Cu2ZnSnS4 (CZTS) thin films by sulfurization of stacked metallic precursor films.* Vacuum, 2014. **104**: p. 57-60.
70. Suryawanshi, M.P., et al., *A chemical approach for synthesis of photoelectrochemically active Cu2ZnSnS4 (CZTS) thin films.* Solar Energy, 2014. **110**: p. 221-230.
71. Wang, H., *Progress in Thin Film Solar Cells Based on Cu2ZnSnS4.* International Journal of Photoenergy, 2011. **2011**: p. 10.
72. Katagiri, H., et al., *Characterization of Cu2ZnSnS4 Thin Films Prepared by Vapor Phase Sulfurization.* Japanese Journal of Applied Physics, 2001. **40**: p. 500-504.
73. Xinkun, W., et al., *Photoelectric properties of Cu2ZnSnS4 thin films deposited by thermal evaporation.* Journal of Semiconductors, 2012. **33**.
74. Lee, Y.S., et al., *Cu2ZnSnSe4 Thin-Film Solar Cells by Thermal Co-evaporation with 11.6% Efficiency and Improved Minority Carrier Diffusion Length.* Advanced Energy Materials, 2015. **5**.
75. Abusnina, M., et al., *Fabrication and Characterization of CZTS Thin Films Prepared by the Sulfurization of RF-Sputtered Stacked Metal Precursors.* Journal of Electronic Materials, 2014. **43**.
76. Yoo, H. and J. Kim, *Growth of Cu2ZnSnS4 thin films using sulfurization of stacked metallic films.* Thin Solid Films, 2010. **518**(22): p. 6567-6572.
77. Han, J., et al., *Crystallization behaviour of co-sputtered Cu2ZnSnS4 precursor prepared by sequential sulfurization processes.* Nanotechnology, 2013. **24**: p. 095706.
78. Ge, J., et al., *Fabrication of Cu2ZnSnS4 absorbers by sulfurization of Sn-rich precursors.* Physica Status Solidi Applied Research, 2012. **209**: p. 1493-1497.
79. Shin, S.W., et al., *Studies on Cu 2ZnSnS 4 (CZTS) absorber layer using different stacking orders in precursor thin films.* Solar Energy Materials and Solar Cells - SOLAR ENERG MATER SOLAR CELLS, 2011. **95**: p. 3202-3206.
80. He, J., et al., *Cu2ZnSnS4 thin film solar cell utilizing rapid thermal process of precursors sputtered from a quaternary target: A promising application in industrial processes.* RSC Adv., 2014. **4**.
81. He, J., et al., *Effect of post-sulfurization on the composition, structure and optical properties of Cu2ZnSnS4 thin films deposited by sputtering from a single quaternary target.* Applied Surface Science, 2013. **264**: p. 133-138.

82. Ping, F., et al., *Effects of annealing treatment on the properties of CZTSe thin films deposited by RF-magnetron sputtering.* Journal of Alloys and Compounds, 2015. **625**: p. 171-174.
83. Sun, L., et al., *Comparative study on Cu2ZnSnS4 thin films deposited by sputtering and pulsed laser deposition from a single quaternary sulfide target.* Journal of Crystal Growth, 2012. **361**: p. 147-151.
84. Dhakal, T.P., et al., *Characterization of a CZTS thin film solar cell grown by sputtering method.* Solar Energy, 2014. **100**: p. 23-30.
85. Son, D.-H., et al., *Growth and Device Characteristics of CZTSSe Thin-Film Solar Cells with 8.03 % Efficiency.* Chemistry of Materials, 2015. **27**: p. 150707092429006.
86. Moholkar, A.V., et al., *Synthesis and characterization of Cu2ZnSnS4 thin films grown by PLD: Solar cells.* Journal of Alloys and Compounds, 2011. **509**(27): p. 7439-7446.
87. He, J., et al., *Composition dependence of structure and optical properties of Cu2ZnSn(S,Se)4 solid solutions: An experimental study.* Journal of Alloys and Compounds, 2012. **511**(1): p. 129-132.
88. Pawar, S., et al., *Effect of laser incident energy on the structural, morphological and optical properties of Cu2ZnSnS4 (CZTS) thin films.* Current Applied Physics - CURR APPL PHYS, 2010. **10**.
89. Tanaka, K., N. Moritake, and H. Uchiki, *Preparation of Cu2ZnSnS4 thin films by sulfurizing sol–gel deposited precursors.* Solar Energy Materials and Solar Cells, 2007. **91**(13): p. 1199-1201.
90. Tanaka, K., et al., *Cu2ZnSnS4Cu2ZnSnS4 thin film solar cells prepared by non-vacuum processing.* Solar Energy Materials and Solar Cells, 2009. **93**(5): p. 583-587.
91. Tanaka, K., et al., *Chemical composition dependence of morphological and optical properties of Cu2ZnSnS4 thin films deposited by sol–gel sulfurization and Cu2ZnSnS4 thin film solar cell efficiency.* Solar Energy Materials and Solar Cells, 2011. **95**(3): p. 838-842.
92. Todorov, T., et al., *Cu2ZnSnS4 films deposited by a soft-chemistry method.* Thin Solid Films, 2009. **517**(7): p. 2541-2544.
93. Ki, W. and H.W. Hillhouse, *Earth-Abundant Element Photovoltaics Directly from Soluble Precursors with High Yield Using a Non-Toxic Solvent.* Advanced Energy Materials, 2011. **1**(5): p. 732-735.
94. Todorov, T.K., K.B. Reuter, and D.B. Mitzi, *High-efficiency solar cell with Earth-abundant liquid-processed absorber.* Adv Mater, 2010. **22**(20): p. E156-9.

95. Barkhouse, D.A.R., et al., *Device characteristics of a 10.1% hydrazine-processed Cu2ZnSn(Se,S)4 solar cell.* Progress in Photovoltaics: Research and Applications, 2012. **20**(1): p. 6-11.
96. Todorov, T.K., et al., *Beyond 11% Efficiency: Characteristics of State-of-the-Art Cu2ZnSn(S,Se)4 Solar Cells.* Advanced Energy Materials, 2013. **3**(1): p. 34-38.
97. Todorov, T., et al., *Progress towards marketable earth-abundant chalcogenide solar cells.* Thin Solid Films, 2011. **519**(21): p. 7378-7381.
98. Guo, Q., et al., *Fabrication of 7.2% Efficient CZTSSe Solar Cells Using CZTS Nanocrystals.* Journal of the American Chemical Society, 2010. **132**(49): p. 17384-17386.
99. Zhou, H., et al., *CZTS nanocrystals: a promising approach for next generation thin film photovoltaics.* Energy & Environmental Science, 2013. **6**(10): p. 2822-2838.
100. Todorov, T.K., K.B. Reuter, and D.B. Mitzi, *High-Efficiency Solar Cell with Earth-Abundant Liquid-Processed Absorber.* Advanced Materials, 2010. **22**(20): p. E156-E159.
101. Riha, S.C., B.A. Parkinson, and A.L. Prieto, *Solution-Based Synthesis and Characterization of Cu2ZnSnS4 Nanocrystals.* Journal of the American Chemical Society, 2009. **131**(34): p. 12054-12055.
102. Guo, Q., H.W. Hillhouse, and R. Agrawal, *Synthesis of Cu2ZnSnS4 Nanocrystal Ink and Its Use for Solar Cells.* Journal of the American Chemical Society, 2009. **131**(33): p. 11672-11673.
103. Guo, Q., et al., *Fabrication of 7.2% Efficient CZTSSe solar cells using CZTS nanocrystals.* Journal of the American Chemical Society, 2010. **132**.
104. Steinhagen, C., et al., *Synthesis of Cu2ZnSnS4 Nanocrystals for Use in Low-Cost Photovoltaics.* Journal of the American Chemical Society, 2009. **131**(35): p. 12554-12555.
105. Khare, A., et al., *Size control and quantum confinement in Cu2ZnSnS4 nanocrystals.* Chemical Communications, 2011. **47**(42): p. 11721-11723.
106. Senthilnathan, V. and S. Ganesan, *Novel spray pyrolysis for dye-sensitized solar cell.* Journal of Renewable and Sustainable Energy, 2010. **2**(6): p. 063102.
107. Nakayama, N. and K. Ito, *Sprayed films of stannite Cu2ZnSnS4.* Applied Surface Science, 1996. **92**: p. 171-175.
108. Madarász, J., et al., *Thermal decomposition of thiourea complexes of Cu(I), Zn(II), and Sn(II) chlorides as precursors for the spray*

pyrolysis deposition of sulfide thin films. Solid State Ionics, 2001. **141-142**: p. 439-446.
109. Ramasamy, K., M.A. Malik, and P. O'Brien, *The chemical vapor deposition of Cu2ZnSnS4 thin films.* Chemical Science, 2011. **2**(6): p. 1170-1172.
110. Washio, T., et al., *6% Efficiency Cu2ZnSnS4-based thin film solar cells using oxide precursors by open atmosphere type CVD.* Journal of Materials Chemistry, 2012. **22**(9): p. 4021-4024.
111. Scragg, J.J., et al., *New routes to sustainable photovoltaics: evaluation of Cu2ZnSnS4as an alternative absorber material.* physica status solidi (b), 2008. **245**(9): p. 1772-1778.
112. Cunningham, D., M. Rubcich, and D. Skinner, *Cadmium telluride PV module manufacturing at BP Solar.* Progress in Photovoltaics: Research and Applications, 2002. **10**(2): p. 159-168.
113. Lincot, D., et al., *Chalcopyrite thin film solar cells by electrodeposition.* Solar Energy, 2004. **77**(6): p. 725-737.
114. Broggi, R.L., et al., *Study of an alkaline bath for tin deposition in the presence of sorbitol and physical and morphological characterization of tin film.* Journal of Applied Electrochemistry, 2006. **36**(4): p. 403-409.
115. Scragg, J.J., P.J. Dale, and L.M. Peter, *Synthesis and characterization of Cu2ZnSnS4 absorber layers by an electrodeposition-annealing route.* Thin Solid Films, 2009. **517**(7): p. 2481-2484.
116. Kurihara, M., et al., *Kesterite absorber layer uniformity from electrodeposited pre-cursors.* physica status solidi (c), 2009. **6**(5): p. 1241-1244.
117. Araki, H., et al., *Preparation of Cu2ZnSnS4 thin films by sulfurizing electroplated precursors.* Solar Energy Materials and Solar Cells, 2009. **93**(6-7): p. 996-999.
118. Araki, H., et al., *Preparation of Cu2ZnSnS4thin films by sulfurization of co-electroplated Cu-Zn-Sn precursors.* physica status solidi (c), 2009. **6**(5): p. 1266-1268.
119. Schurr, R., et al., *The crystallisation of Cu2ZnSnS4 thin film solar cell absorbers from co-electroplated Cu–Zn–Sn precursors.* Thin Solid Films, 2009. **517**(7): p. 2465-2468.
120. Ennaoui, A., et al., *Cu2ZnSnS4 thin film solar cells from electroplated precursors: Novel low-cost perspective.* Thin Solid Films, 2009. **517**(7): p. 2511-2514.

121. Pawar, S.M., et al., *Single step electrosynthesis of Cu2ZnSnS4 (CZTS) thin films for solar cell application.* Electrochimica Acta, 2010. **55**(12): p. 4057-4061.
122. Ahmed, S., et al., *A High Efficiency Electrodeposited Cu2ZnSnS4 Solar Cell.* Advanced Energy Materials, 2012. **2**(2): p. 253-259.
123. Yan, C., et al., *Cu2ZnSnS4 solar cells with over 10% power conversion efficiency enabled by heterojunction heat treatment.* Nature Energy, 2018. **3**(9): p. 764-772.
124. Sun, K., et al. *Towards 9% sulfide CZTS solar cells fabricated by a sol-gel process*. in *2018 IEEE 7th World Conference on Photovoltaic Energy Conversion (WCPEC) (A Joint Conference of 45th IEEE PVSC, 28th PVSEC & 34th EU PVSEC)*. 2018.
125. Hages, C.J., et al., *Controlled Grain Growth for High Performance Nanoparticle-Based Kesterite Solar Cells.* Chemistry of Materials, 2016. **28**(21): p. 7703-7714.
126. Giraldo, S., et al., *How small amounts of Ge modify the formation pathways and crystallization of kesterites.* Energy & Environmental Science, 2018. **11**(3): p. 582-593.
127. Taskesen, T., et al., *Device Characteristics of an 11.4% CZTSe Solar Cell Fabricated from Sputtered Precursors.* Advanced Energy Materials, 2018. **8**(16): p. 1703295.
128. Chernomordik, B.D., et al., *Microstructure Evolution During Selenization of Cu2ZnSnS4 Colloidal Nanocrystal Coatings.* Chemistry of Materials, 2016. **28**(5): p. 1266-1276.
129. Vauche, L., et al., *8.2% pure selenide kesterite thin-film solar cells from large-area electrodeposited precursors.* Progress in Photovoltaics: Research and Applications, 2016. **24**(1): p. 38-51.
130. Gang, M.G., et al., *Band Tail Engineering in Kesterite Cu2ZnSn(S,Se)4 Thin-Film Solar Cells with 11.8% Efficiency.* The Journal of Physical Chemistry Letters, 2018. **9**(16): p. 4555-4561.
131. Cabas-Vidani, A., et al., *High-Efficiency (LixCu1−x)2ZnSn(S,Se)4 Kesterite Solar Cells with Lithium Alloying.* Advanced Energy Materials, 2018. **8**(34): p. 1801191.
132. Schnabel, T., et al., *Solution-Based Preparation of Cu2ZnSn(S,Se)4 for Solar Cells—Comparison of SnSe2 and Elemental Se as Chalcogen Source.* IEEE Journal of Photovoltaics, 2015. **5**(2): p. 670-675.
133. Li, Z.-H., E.-S. Cho, and S.J. Kwon, *Molybdenum thin film deposited by in-line DC magnetron sputtering as a back contact for*

Cu(In,Ga)Se2 solar cells. Applied Surface Science, 2011. **257**(22): p. 9682-9688.
134. Scofield, J.H., et al., *Sputtered molybdenum bilayer back contact for copper indium diselenide-based polycrystalline thin-film solar cells.* Thin Solid Films, 1995. **260**(1): p. 26-31.
135. Bojinov, M., I. Betova, and R. Raicheff, *Kinetics of formation and properties of a barrier oxide film on molybdenum.* Journal of Electroanalytical Chemistry, 1996. **411**(1): p. 37-42.
136. Huang, Q., et al., *Electrodeposition of Indium on Copper for CIS and CIGS Solar Cell Applications.* Journal of The Electrochemical Society, 2011. **158**: p. D57-D61.
137. Khalil, M.I., et al., *CZTS absorber layer for thin film solar cells from electrodeposited metallic stacked precursors (Zn/Cu-Sn).* Applied Surface Science, 2016. **379**: p. 91-97.
138. Liu, C.-W., et al., *Effects of wetting ability of plating electrolyte on Cu seed layer for electroplated copper film.* Journal of Vacuum Science & Technology A - J VAC SCI TECHNOL A, 2004. **22**: p. 2315-2320.
139. Jiang, F., et al., *Pure Sulfide Cu2ZnSnS4Thin Film Solar Cells Fabricated by Preheating an Electrodeposited Metallic Stack.* Advanced Energy Materials, 2014. **4**(7): p. 1301381.
140. Scragg, J.J., D.M. Berg, and P.J. Dale, *A 3.2% efficient Kesterite device from electrodeposited stacked elemental layers.* Journal of Electroanalytical Chemistry, 2010. **646**(1-2): p. 52-59.
141. Lin, Y., et al., *Mechanistic aspects of preheating effects of electrodeposited metallic precursors on structural and photovoltaic properties of Cu2ZnSnS4 thin films.* Solar Energy Materials and Solar Cells, 2014. **120**: p. 218-225.
142. Jušk≐nas, R., et al., *Formation of intermetallic phases during ageing of Zn electroplate on the Cu substrate.* Applied Surface Science, 2004. **229**(1): p. 402-408.
143. Juškėnas, R., et al., *XRD studies of the phase composition of the electrodeposited copper-rich Cu–Sn alloys.* Electrochimica Acta, 2006. **52**(3): p. 928-935.
144. Koike, J., et al., *Cu$_{2}$SnS$_{3}$ Thin-Film Solar Cells from Electroplated Precursors.* Japanese Journal of Applied Physics, 2012. **51**: p. 10NC34.
145. Marcano, G., et al., *Raman spectrum of monoclinic semiconductor.* Solid State Communications, 2011. **151**(1): p. 84-86.

146. Temgoua, S., et al., *Effects of SnSe 2 secondary phases on the efficiency of Cu 2 ZnSn(S x ,Se 1−x) 4 based solar cells.* Thin Solid Films, 2015. **582**: p. 215-219.
147. Kim, K.M., et al., *Growth and characterization of coevaporated Cu2SnSe3 thin films for photovoltaic applications.* Thin Solid Films, 2013. **536**: p. 111-114.
148. Babu, G.S., et al., *Growth and characterization of Cu2SnSe3 thin films.* Materials Chemistry and Physics, 2006. **96**(2-3): p. 442-446.
149. Kuo, D.-H., et al., *Effect of post-deposition annealing on the performance of D.C. sputtered Cu2SnSe3 thin films.* Surface and Coatings Technology, 2010. **205**: p. S196-S200.
150. Avellaneda, D., M.T.S. Nair, and P.K. Nair, *Cu[sub 2]SnS[sub 3] and Cu[sub 4]SnS[sub 4] Thin Films via Chemical Deposition for Photovoltaic Application.* Journal of The Electrochemical Society, 2010. **157**(6): p. D346.
151. Kuo, D.-H., et al., *Single-step sputtered Cu2SnSe3 films using the targets composed of Cu2Se and SnSe2.* Thin Solid Films, 2010. **518**(24): p. 7218-7221.
152. Fan, J., et al., *Structural evolvement and thermoelectric properties of Cu(3-x)Sn(x)Se(3) compounds with diamond-like crystal structures.* Dalton Trans, 2014. **43**(44): p. 16788-94.
153. Rey, G., et al., *The band gap of Cu2ZnSnSe4: Effect of order-disorder.* Applied Physics Letters, 2014. **105**(11): p. 112106.
154. Sabli, N., Z.A. Talib, and H.S. Hilal, *Effect of under nitrogen annealing on photo-electrochemical characteristics of films deposited from authentic Cu 2 SnSe 3 sources by thermal vacuum under argon gas condensation.* International Journal of Hydrogen Energy, 2017. **42**(14): p. 9003-9010.
155. Li, W., et al., *The effect of ZnS segregation on Zn-rich CZTS thin film solar cells.* Journal of Alloys and Compounds, 2015. **632**: p. 178-184.
156. Scragg, J.J.S., et al., *Cu–Zn disorder and band gap fluctuations in Cu2ZnSn(S,Se)4: Theoretical and experimental investigations.* physica status solidi (b), 2016. **253**(2): p. 247-254.
157. Paris, M., et al., *Solid-state NMR and Raman spectroscopy to address the local structure of defects and the tricky issue of the Cu/Zn disorder in Cu-poor, Zn-rich CZTS materials.* Inorg Chem, 2014. **53**(16): p. 8646-53.

158. Dimitrievska, M., et al., *Resonant Raman scattering of ZnSxSe1−x solid solutions: the role of S and Se electronic states.* Physical Chemistry Chemical Physics, 2016. **18**(11): p. 7632-7640.
159. Rudisch, K., et al., *Order-disorder transition in B-type Cu2ZnSnS4 and limitations of ordering through thermal treatments.* Applied Physics Letters, 2016. **108**(23): p. 231902.
160. Krustok, J., et al., *Photoluminescence study of deep donor- deep acceptor pairs in Cu2ZnSnS4.* Materials Science in Semiconductor Processing, 2018. **80**: p. 52-55.
161. Tanaka, K., T. Shinji, and H. Uchiki, *Photoluminescence from Cu2ZnSnS4 thin films with different compositions fabricated by a sputtering-sulfurization method.* Solar Energy Materials and Solar Cells, 2014. **126**: p. 143-148.
162. Lafond, A., et al., *Crystal Structures of Photovoltaic Chalcogenides, an Intricate Puzzle to Solve: the Cases of CIGSe and CZTS Materials.* Zeitschrift für anorganische und allgemeine Chemie, 2012. **638**(15): p. 2571-2577.
163. Lafond, A., et al., *Crystal Structures of Photovoltaic Chalcogenides, an Intricate Puzzle to Solve: the Cases of CIGSe and CZTS Materials.* Z. Anorg. Allg. Chem., 2012. **638**: p. 2571–2577.
164. Juškėnas, R., et al., *XRD studies of an electrochemically co-deposited Cu–Zn–Sn precursor and formation of a Cu2ZnSnSe4 absorber for thin-film solar cells.* Journal of Alloys and Compounds, 2016. **655**: p. 281-289.
165. Leitão, J.P., et al., *Photoluminescence and electrical study of fluctuating potentials in Cu2ZnSnS4-based thin films.* Physical Review B, 2011. **84**(2).
166. Rey, G., et al., *On the origin of band-tails in kesterite.* Solar Energy Materials and Solar Cells, 2018. **179**: p. 142-151.

ACKNOWLEDGEMENTS/PADĖKA

Noriu padėkoti žmonai Julitai, kad mane pakenčia. Taip pat mamai, tečiui, sesei už kantrybę ir supratingumą ne tik studijų metu. Visiems draugams už palaikymą.

Ypatingai dėkoju savo darbo vadovui R. Juškėnui už kantrybę, patarimus, pagalbą ir už tai, kad visada atrasdavo laiko.

Noriu padėkoti Z. Mockui ir S. Kanapeckaitei už pagalbą elektrocheminėje pirmtako sluoksnių sintezėje, P. Kalinauskui už atliktus fotoelektrocheminius tyrimus, o R. Giraičiui už pirmtakų iškaitinimą ir selenidimą.

Taip pat norėčiau padėkoti SEM'o ekspertams A. Selskiui, A. Naujokaičiui ir G. Stalnioniui už morfologinius ir cheminės sudėties tyrimus. G. Niaurai už Raman tyrimus ir išsamų rezultatų aprašymą. Didelis dėkui XRD ekspertams V. Pakštui ir S. Stanionytei.

Bendrai noriu padėkoti visam mūsų medžiagų struktūrinės analizės skyriui už pagalbą, supratingumą ir palaikymą doktorantūros studijų laikotarpiu bei ruošiant disertaciją. Taip pat dėkoju FTMC už suteiktas sąlygas ir galimybę parengti šį darbą.

PUBLICATIONS

1. Remigijus Juškėnas, Zenius Mockus, Raimondas Giraitis, Algirdas Selskis, Giedrius Stalnionis, Stasė Kanapeckaitė, **Audrius Drabavičius**, Putinas Kalinauskas, Gediminas Niaura, „Structural and photoelectrochemical characterization of Cu_2SnSe_3 thin films fabricated by electrochemical co-deposition and selenization“.

2. **Audrius Drabavičcius**, Arnas Naujokaitis, Giedrius Stalnionis, Raimondas Giraitis, Zenius Mockus, Stasė Kanapeckaitė, Putinas Kalinauskas, Ramūnas Nedzinskas, Gediminas Niaura, Remigijus Juškėnas, „Photoelectrochemical, Raman spectroscopy, XRD and photoluminescence study of disorder in electrochemically deposited kesterite thin film“.

Paper I

Structural and photoelectrochemical characterization of Cu2SnSe3 thin films fabricated by electrochemical co-deposition and selenization

Remigijus Juškėnas, Zenius Mockus, Raimondas Giraitis, Algirdas Selskis, Giedrius Stalnionis, Stasė Kanapeckaitė, **Audrius Drabavičius**, Putinas Kalinauskas, Gediminas Niaura

Journal of Alloys and Compounds, 2018. 767: p. 345-352.

10.1016/j.jallcom.2020.153853.

Journal of Alloys and Compounds 767 (2018) 345–352

Contents lists available at ScienceDirect

Journal of Alloys and Compounds

journal homepage: http://www.elsevier.com/locate/jalcom

Structural and photoelectrochemical characterization of Cu_2SnSe_3 thin films fabricated by electrochemical co-deposition and selenization

Remigijus Juškėnas*, Zenius Mockus, Raimondas Giraitis, Algirdas Selskis, Giedrius Stalnionis, Stasė Kanapeckaitė, Audrius Drabavičius, Putinas Kalinauskas, Gediminas Niaura

State Research Institute Center for Physical Sciences and Technology, Savanoriu Av. 231, Vilnius, Lithuania

ARTICLE INFO

Article history:
Received 9 March 2018
Received in revised form
12 June 2018
Accepted 23 June 2018
Available online 12 July 2018

Keywords:
Cu_2SnSe_3
Electrochemical co-deposition
XRD
Raman spectroscopy

ABSTRACT

The Cu-Sn alloy as a precursor for Cu_2SnSe_3 (CTSe) thin films was electrochemically co-deposited from a modified electrolyte solution using magnetic steering. The Cu-Sn film on the Mo/glass substrate was continuous, smooth and contained no organic contaminants according to Raman spectroscopy. The current efficiency of Cu-Sn electrodeposition in the solution was about 90%, i.e. significantly higher than that previously reported. The Cu-Sn films with the Cu/Sn ratio in the range of 1.6–2.3 were selenized at temperatures of 350, 400, 450, 500 and 560 °C. The synthesized CTSe films were characterised by XRD, SEM, EDX and Raman spectroscopy. The photo-activity of the films was assessed by photoelectrochemical measurements in a 0.2 M $Eu(NO_3)_3$ aqueous solution. The conducted investigations revealed that the Cu_2SnSe_3 film with Cu/Sn = 1.9 selenized at a temperature of 500 °C demonstrated the best photoelectrochemical response and presented p type doping. The photo-activity of the film increased after additional annealing in air at a temperature of 200 °C. Raman spectroscopy studies of Cu_2SnSe_3 thin films revealed a rather insignificant difference between the spectra of cubic and monoclinic polymorphs, however, one of the bands in the low energy region could be treated as a marker of the monoclinic phase. The Raman spectra evidenced that nearly all of the studied Cu_2SnSe_3 films contained $SnSe_2$ the presence of which is detrimental for the photovoltaic characteristics of both Cu_2SnSe_3 and $Cu_2ZnSnSe_4$.

1. Introduction

The study of Cu_2SnSe_3 (CTSe) thin films formation may be of interest from at least two points of view: i) the usage of the film for fabrication of thin film solar cells and ii) the study of kesterite ($Cu_2ZnSnSe_4$) formation mechanism.

Firstly, CTSe was studied as a semiconductor material suitable for the application of an acousto-optic device in the infrared (IR) region [1–3]. It was determined that CTSe is formed in the monoclinic [1,2,4] or cubic [3] crystalline structures. This p-type semiconductor has a direct band gap in the range of 0.74–1.12 eV for the cubic structure [3] and 0.843 eV for the monoclinic one [1].

Since 2010 the CTSe and CTS (Cu_2SnS_3) studies have been mainly related to thin film solar cells [5–31] and thermoelectric materials [32–35].

Feasibility of CTS for the fabrication of thin film solar cells is well known [11,20,25]. The highest reached so far conversion efficiency for the CTS solar cell is 4.62% [20], while the conversion efficiency of CTSe based solar cell reaches a significantly lower value of 0.079% due to the excess hole concentration characteristic of CTSe [23]. It is determined that the highest hole concentration is in the CTSe of cubic structure, while the lowest one is in the monoclinic structure [34]. The authors showed that the CTSe crystalline structure evolves from the tetragonal via cubic to monoclinic structure, while the chemical composition changes from copper rich to tin rich. However, other authors found that the CTSe structure changes with precursor composition somewhat differently: the cubic structure is formed in copper or tin poor CTSe while the monoclinic one in Cu or Sn rich CTSe [35]. It is difficult to decide from XRD data if the CTSe contains the monoclinic structure only or both the monoclinic and cubic structures, since the highest intensity XRD peaks of both structures nearly coincide. Raman spectroscopy currently is helpless in this case since to the best of our knowledge the same Raman spectrum (bands at 179, 199, 233, 250 and 360 cm^{-1}) is attributed

* Corresponding author.
E-mail address: remigijus.juskenas@ftmc.lt (R. Juškėnas).

https://doi.org/10.1016/j.jallcom.2018.06.276
0925-8388/

to both of the abovementioned CTSe polymorphs: cubic [15,29,30] and monoclinic [13].

The CTSe/CTS thin films were fabricated by different approaches: the sputtering [5,6,8,16,17,23,28,29], evaporation [9,15,19–21,31], electrochemical deposition [10,11,14], chemical bath deposition [7,18,25], sol-gel deposition [22], successive ionic layer adsorption and reaction (SILAR) methods [30].

Many works are devoted to the studies of the kesterite formation pathways [36–41]. Some researchers have concluded that the CTSe/CTS takes place in the route of kesterite formation as an intermediate compound [38–40]. The CTSe has been used even as a precursor for $Cu_2ZnSnSe_4$ fabrication [19]. The kesterite formation is a complicated process. The study of the process could be simplified by at first studying separate selenization/sulphurization of Cu-Zn and Cu-Sn alloys of which the kesterite precursors sometimes are composed [41].

In the current work Cu-Sn films were electrochemically co-deposited on Mo/soda lime glass substrates and further selenized at temperatures in the range from 350 to 560 °C and characterised by XRD, SEM, x-ray (EDS) and Raman spectroscopy. The process of electrochemical co-deposition of Cu-Sn alloy has been improved in order to prepare a more compact and pure Cu-Sn precursor film. An attempt has been made to obtain Raman spectrum of pure cubic and monoclinic Cu_2SnSe_3 structures seeking to find a marker for these structures. A photoelectrochemical experiment was conducted to assess an impact of post-annealing on the photoelectrochemical activity of the synthesized CTSe layers.

2. Experimental

A Cu-Sn precursor layer was electrochemically co-deposited onto Mo/soda-lime glass substrates in a three-electrode glass electrolytic cell. Prior to the electrodeposition the Mo surface was cleaned as described in Ref. [41]. A platinum (purity 99.999%) plate of much larger dimensions than that of the working electrode was used as a counter electrode. The reference electrode (saturated Ag/AgCl/KCl) was placed near the working electrode through the Luggin capillary. All the potential E_c values reported in the paper were in respect to this electrode. A potentiostat/galvanostat REF 600 (Gamry Instruments) maintained potentiostatic conditions during electrodeposition.

The electrolyte solution was prepared using deionized water and contained $CuSO_4$·- 20 mM, $SnSO_4$ – 10 mM and 0.1 M of sodium citrate ($Na_3C_6H_5O_7 \cdot 2H_2O$). Hydroquinone (1 mM) was used as an antioxidant in the electrolyte solution. The pH of the solutions was adjusted to 5.75 with NaOH. All chemicals used in this work were of analytical grade. The electrolyte solution was kept at a constant temperature of 20 ± 1 °C during the electrodeposition. The solution was agitated with a magnetic stirrer. The Cu-Sn precursor layers were deposited at E_c −1.0 V in the potentiostatic mode for 230 s.

A detailed description of the selenization process was given previously [41]. The photoelectrochemical measurements of CTSe layer were performed in a three-electrode electrochemical cell supplied with a quartz window. An analog–digital converter (ADC) connected to PC was used for the data collection of photovoltamperometric and chronoamperometric measurements. Photovoltamperometrics of CTSe film electrodes were measured with respect to the Ag/AgCl/KCl electrode in an aqueous 0.2 M $Eu(NO_3)_3$ working solution. The solution was prepared from reagents of analytical grade and triply distilled water. Photovoltamperometric and chronoamperometric measurements were conducted using a potentiostat–galvanostat P-50-1 connected to a PC through ADC interface. The CTSe film surface was illuminated by White LED Lumiled 3 W. The light intensity at the CTSe film electrode surface was about 100 mW/cm^2, as measured with a VLP-2000 power meter. The area of CTSe film exposed to the solution was ~0.5 cm^2. Platinum wire was used as a counter electrode. All measurements were carried out at room temperature and normal pressure. All samples prior to photoelectrochemical measurements were etched for 30 s in a 5 wt% KCN aqueous solution to remove copper selenides.

The XRD studies were conducted using an x-ray diffractometer SmartLab (Rigaku) with a 9 kW rotating Cu anode x-ray tube. The primary x-ray beam was conditioned by a multilayer Ni/graphite monochromator CBO (cross beam optics) in the case of grazing incidence (GI) XRD measurements.

SEM characterization of CTSe films surface morphology, focused ion beam (FIB) prepared cross-sections and EDX analysis of the films were carried out in a dual beam system FE-SEM-FIB Helios Nanolab 650 (FEI Company) equipped with an x-ray spectrometer X-Max (Oxford Instruments).

Raman spectra were recorded using a confocal microspectrometer inVia (Renishaw, UK) equipped with thermoelectrically cooled (−70 °C) CCD camera and microscope. Spectra were excited with 532 nm (0.06 mW, 3000 lines/mm grating) and 632.8 nm (0.05 mW, 2400 lines/mm grating) laser radiations. Spectra in the C-H stretching vibration spectral range (2300–3500 cm^{-1}) were recorded by using 532 nm excitation and 1800 lines/mm grating. The Raman frequencies were calibrated using the silicon standard according to the line at 520.7 cm^{-1}. Spectra were taken using a 50×/0.75 NA objective lens. For the $SnSe_2$ and SnSe samples analysis, the 50×/50 NA long working distance objective was employed. The integration time was 400 or 800 s. Parameters of the bands were determined by fitting the experimental spectra with Gaussian-Lorentzian shape components using GRAMS/A1 8.0 (Thermo Scientific) software assuming linear baseline.

3. Results and discussion

3.1. Impact of electrolyte solution composition on the quality of the Cu-Sn precursor layer and CTSe film

In the case that the Cu-Sn precursor was fabricated by electrodeposition, typically sequential deposition of Cu and Sn layers was used [10]. However, the co-electrodeposition of Cu-Sn alloy is more convenient and faster [11]. The authors of the latter work used an electrolyte solution containing a rather large quantity of sodium citrate, namely, 0.5 M, which could lead to the incorporation of an appreciable quantity of citrate ion or its derivatives into the deposit. We reduced the quantity of citrate in the electrolyte solution down to 0.1 M. A further reduction in citrate concentration resulted in lower stability of the electrolyte solution. The quantities of $CuSO_4$ and $SnSO_4$ are presented in the Experimental section.

Fig. 1 depicts potentiostatic polarisation curves of the Mo/glass working electrode in the electrolyte solutions containing different quantities of $Na_3C_6H_5O_7$·: 0.5 M for dashed curves and 0.1 M for the solid ones. The lower curves correspond to stirred solutions. Vertical dashed lines indicate potential ranges, in which the electrodeposition of Cu, Cu and underpotential Sn, or Cu-Sn alloy takes place. Potential at which hydrogen electrochemical evolution starts is shown, as well. All of the studied Cu-Sn films were deposited at a cathodic potential E_c of −1.0 V, i.e., at the potential of limiting current density for Cu and Sn reduction. On the other hand, the electrochemical evolution of hydrogen was rather slow at this potential. Magnetic stirring of the electrolyte solutions increased current density by a factor of ~5.

The Cu/Sn ratio was varied by dissolution of an appropriate quantity of $SnSO_4$ according to the preliminary plotted linear

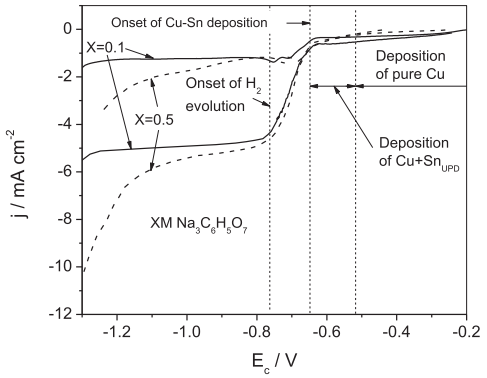

Fig. 1. The potentiostatic polarisation curves of Mo/glass working electrode in electrolyte solutions containing different quantity of $Na_3C_6H_5O_7\cdot$: 0.5 M for dashed curves and 0.1 M for solid ones. The lower curves correspond to stirred solutions.

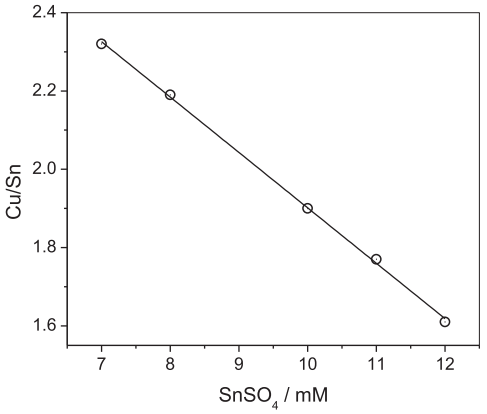

Fig. 2. An experimental dependency of Cu/Sn ration on the $SnSO_4$ concentration in the electrolyte solution containing 20 mM of $CuSO_4$, and 0.1 M of sodium citrate.

dependency based on our experimental data (Fig. 2). According to ref. [11], the best conversion efficiency yielded the CTS solar cells with the Cu/Sn ratio of about 1.9, so from here on we present results for Cu-Sn precursors and CTSe layers with this Cu/Sn ratio.

Fig. 3 shows top view SEM images of the Cu-Sn layers co-electrodeposited in the stirred solutions containing 0.5 M (left image) and 0.1 M (right image) of $Na_3C_6H_5O_7$. In both cases, the same electric charge was passed through the electrolytic cell. The film deposited from the solution with the lower content of citrate looks far more compact and smooth. Table 1 presents chemical composition of the Cu-Sn layers measured by EDX. The thickness of the layers derived from EDX data using dedicated software showed that the film from the solution with the lower concentration of $Na_3C_6H_5O_7$ was significantly thicker, i.e., the current efficiency in this solution was higher. Indeed, the measured current efficiency was 90 and 70% for the solutions with 0.1 and 0.5 M of sodium citrate, respectively.

The insertion of citrate or its derivatives into the Cu-Sn films was assessed by Raman spectroscopy. Fig. 4 compares Raman spectra of Cu-Sn films obtained from the solutions with high (0.5 M) and low (0.1 M) concentrations of sodium citrate. The film obtained by using the high concentration of citrate shows a well-defined Raman band near 2926 cm^{-1} (Fig. 4a). This band is associated with the C–H stretching vibration of CH_2 groups incorporated into the electrodeposited film [42]. Such a band is not visible in the Raman spectrum of the film obtained by using the solution with 0.1 M of $Na_3C_6H_5O_7$ (Fig. 4b).

Fig. 5 shows top view SEM micrographs of the surface and SEM images of the cross section of the CTSe films fabricated by selenization of Cu-Sn precursors co-electrodeposited from the solutions with different quantities of sodium citrate. The selenization of the depicted CTSe layers was conducted at a temperature of 500 °C. The left images are for the solution with 0.5 M and the right ones for those with 0.1 M. Alike the precursor, the CTSe layer from the solution with 0.1 M of $Na_3C_6H_5O_7\cdot$ is more compact and smooth. The cross-sectional image shows that the CTSe layer from the solution with 0.5 M of citrate contains more voids and its thickness is less even.

A good quality of Cu-Sn precursor layer deposited from the modified electrolyte solution suggests further usage of the solution for a fabrication of Cu-Sn-Zn precursor for CZTS(Se) solar cells by electrodeposition of only two sequential layers of Cu-Sn and Zn (or Cu-Zn) instead of three Cu, Sn and Zn.

3.2. Dependence of the phase composition of the CTSe film on the selenization temperature

The impact of selenization temperature on CTSe crystalline

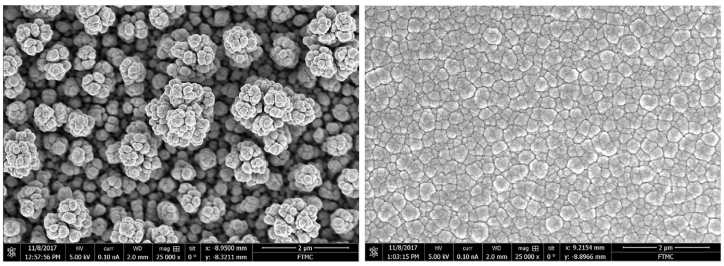

Fig. 3. The top view SEM images of the co-electrodeposited Cu-Sn films. Left image of Cu-Sn film from solution with 0.5 M of $Na_3C_6H_5O_7\cdot$ and right image with 0.1 M.

Table 1
Chemical composition (at. %) and thickness measured by EDX for Cu-Sn layers electrodeposited from electrolyte solutions with different quantity of sodium citrate.

Quantity of citrate	Chemical composition (at. %)					
	Without correction			After correction for thin film		Calculated thickness, nm
	Cu	Mo	Sn	Cu	Sn	
0.1 M	63.17	1.62	35.21	65.55	34.45	748
0.5 M	59.10	10.89	30.01	68.85	31.15	472

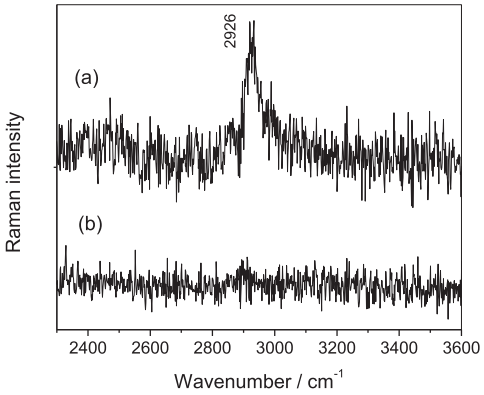

Fig. 4. Raman spectra of Cu-Sn films on Mo/glass substrate co-electrodeposited from the electrolyte solution containing sodium citrate: (a) 0.5 M, and (b) 0.1 M. Excitation wavelength is 532 nm (0.06 mW); integration time is 800 s.

structure and phase composition was studied using the Cu-Sn precursor deposited from the solution with 0.1 M of sodium citrate. Fig. 6 shows the XRD patterns of CTSe layers synthesized at temperatures in the range of 400–560 °C. The chemical composition of Cu-Sn precursors was 65.4 ± 1.0 at. % of Cu and 34.6 ± 1.0 at. % of Sn unless otherwise specified. After the selenization the Cu/Sn ratio increased to about 1.91–1.94 pointing to the loss of Sn during the selenization procedure.

At a temperature of 350 °C (the XRD pattern not presented) not the whole of the Cu-Sn precursor film was selenized during 20 min (at all the studied temperatures the selenization continued for 20 min). An intermetallic phase η-$Cu_{6.26}Sn_5$ (ICDD card # 00-047-1575) was present along with orthorhombic Cu_2Se (# 00-037-1187) and SnSe (# 00-048-1224) structures. Some of the XRD peaks could be attributed to Cu_2Se (# 01-088-2043) and Cu_2SnSe_3 (# 01-089-2879) with the cubic structure.

At a temperature of 400 °C the intermetallic Cu-Sn compounds became undetectable by XRD and broad peaks attributable to $MoSe_2$ (# 00-029-0914) emerged on the XRD pattern. It was quite obvious that cubic Cu_2SnSe_3 (# 01-089-2879) became the main phase in the CTSe film. However, small quantities of copper selenides $Cu_{1.8}Se$ (# 01-088-2046) and CuSe (# 00-049-1457) were also present.

When selenization temperature was increased up to 450 °C the XRD pattern of CTSe film presented peaks of cubic Cu_2SnSe_3 (# 01-089-2879) and one peak of CuSe (# 00-049-1457) at a 2Θ angle of 31.15°. The intensity of $MoSe_2$ peaks increased pointing to thickening of $MoSe_2$ layer.

At a selenization temperature of 500 °C the CTSe film was still comprised of the cubic Cu_2SnSe_3 and a small amount of CuSe phase. The thickness of $MoSe_2$ further increased. Meanwhile at a selenization temperature of 560 °C small XRD peaks at 2Θ angles of 15.35 and 19.88° emerged, which suggested the presence of Cu_2SnSe_3 with the monoclinic structure (# 00-056-1111, and # 04-012-4693). However, cubic Cu_2SnSe_3 could be also present because the highest intensity peaks of both the structures could fully overlap if the lattice parameter of the cubic phase equals to 0.569 nm. Fig. 7 shows a dependence of the cubic lattice parameter on the selenization temperature. The crystal lattice parameter of cubic Cu_2SnSe_3 was calculated from XRD patterns. We determined that the lattice parameter increased with selenization temperature from 0.5645 ± 0.0015 nm at a temperature of 385 °C up to 0.570 ± 0.002 nm at 560 °C (Fig. 7).

3.3. Raman spectroscopy of cubic and monoclinic Cu_2SnSe_3

Raman spectra of CTSe films selenized at temperatures of 500 °C (Fig. 8a) and 560 °C (Fig. 8b) were measured. Prior to Raman spectrum measurement, the copper selenides were dissolved in a 5% KCN aqueous solution. Raman spectra were deconvolved into separate bands using the Voigt function. The Raman spectrum for Cu_2SnSe_3 of cubic structure only (according to the XRD results in Fig. 6) contained bands (Fig. 8a), whose wavenumbers corresponded fairly well with those theoretically calculated for monoclinic Cu_2SnSe_3 [43] and are presented in Table 2.

All the bands in the spectrum from the cubic structure were slightly shifted to higher energies in comparison to the calculated values (except the main one (180.2 cm^{-1}), which was shifted in opposite direction). However, it is conceivable that these shifts are in the range of measurement error. The spectrum also presented a broad feature near 185.4 cm^{-1} attributable to $SnSe_2$ [15,45]. To be sure whether the $SnSe_2$ was present in the CTSe film, we measured a Raman spectrum from pure $SnSe_2$ and found that the spectrum presented two low intensity bands at 107.3 and 118.2 cm^{-1} and a high intensity one at 185.4 cm^{-1} (Fig. 9). A Raman spectrum from pure SnSe (Fig. 9) presented four high intensity bands (70.1, 109.0, 130.6, 150.0 cm^{-1}) and one low intensity feature (184.5 cm^{-1}). The spectra from the pure tin selenides confirmed that it was precisely $SnSe_2$ that was contained in the CTSe film.

The Raman spectrum from the CTSe film synthesized at a temperature of 560 °C (Fig. 8b) contained the same bands as the previous spectrum from probably only cubic Cu_2SnSe_3, however, all the bands were slightly shifted to lower energies in comparison to the calculated values (Table 2). This could point to the lower structure ordering in the sample [46]. Furthermore, the relative intensity of the band at 76.8 cm-1 was significantly increased in comparison with that at 77.8 cm^{-1} of the spectrum for cubic Cu_2SnSe_3 (Fig. 8a). That could mean that both the examined samples contained both cubic and monoclinic Cu_2SnSe_3, however, in the CTSe film selenized at a temperature of 500 °C prevailed the cubic polymorph, while in that selenized at a temperature of 560 °C dominated the monoclinic one.

In Ref. [44], devoted to the studies of the monoclinic Cu_2SnSe_3, only one band was detected in the low energy region, namely, at

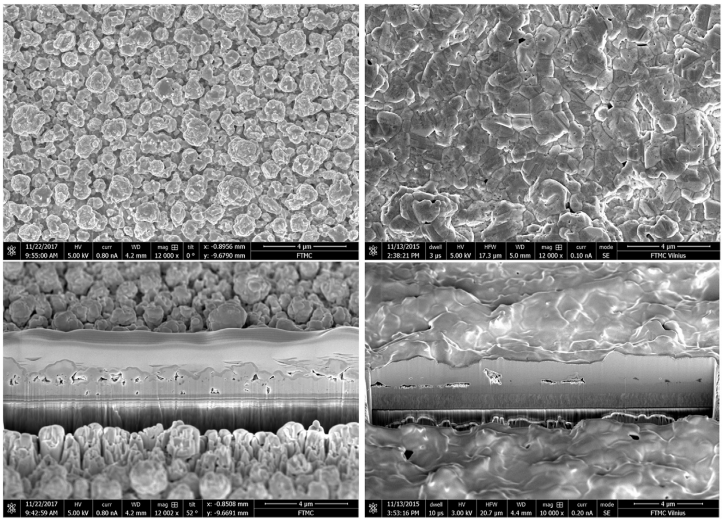

Fig. 5. SEM images of the surface and cross section of CTSe films fabricated using Cu-Sn precursors electrodeposited in solutions with different quantity of $Na_3C_6H_5O_7$: left images - 0.5 M and right images - 0.1 M.

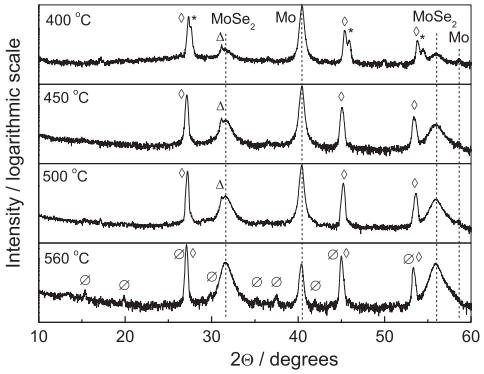

Fig. 6. The XRD patterns of CTSe layers synthesized at temperatures in the range of 400–560 °C. The chemical composition of Cu-Sn precursors was 65.4 ± 1.0 at.% of Cu and 34.6 ± 1.0 at.%. ◇ - cubic Cu_2SnSe_3; * - cubic $Cu_{1.8}Se$; Δ - hexagonal CuSe; ∅ - monoclinic Cu_2SnSe_3.

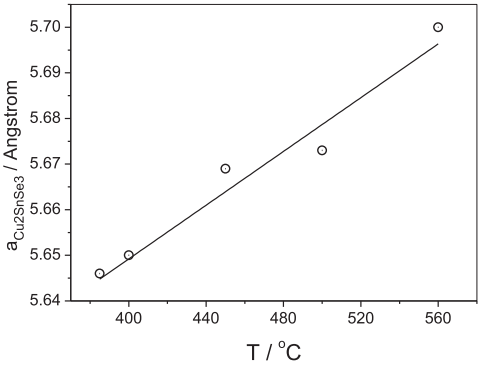

Fig. 7. The lattice parameter *a* of the cubic Cu_2SnSe_3 as a function of selenization temperature.

83 cm^{-1}. This value is rather close to that obtained by us, i.e. 76.8 cm^{-1}. We assume that this band could be a marker of the monoclinic structure since in the current work this band had a significantly higher intensity in the Raman spectrum of the film containing monoclinic Cu_2SnSe_3 in comparison to that containing only cubic Cu_2SnSe_3 according to the XRD data.

3.4. Photoelectrochemical studies of CTSe films

The photoelectrochemical studies of CTSe films synthesized at different temperatures were carried out by measuring pulses of photocurrent in a 0.2 M $Eu(NO_3)_3$ aqueous solution. Fig. 10 shows typical photocurrent pulses obtained at different cathodic potentials, E_c for CTSe films synthesized at a temperature of 500 °C (row a) and the same film after post-annealing in air at a temperature of 200 °C for 2 h (row b). Notation "On" in Fig. 10 indicates the moment light was switched on and the "Off" notation accordingly means the moment light was switched off. The photocurrent was negative which evidenced that all of the studied CTSe layers presented p doping type or p-type conductivity. The layers were fabricated on conductive back contact - Mo film, so it was impossible to apply Hall method to measure the doping level and

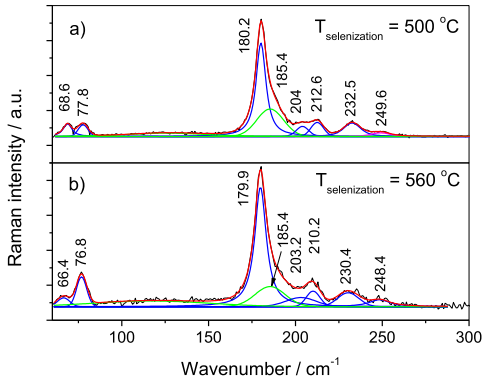

Fig. 8. Raman spectra from CTSe samples: (a) cubic structure, and (b) prevailed monoclinic structure. Excitation wavelength is 632.8 nm (0.05 mW); spectral region is 50–300 cm^{-1}.

Table 2
Wavenumbers of Raman spectra bands for different Cu_2SnSe_3 samples.

Spectrum	Band wavenumber, cm^{-1}						
Calc. [43]	67.7	78.6	181.6	203.8	211.7	230.5	–
Fig. 6a	68.7	77.7	180.2	204.1	212.6	232.7	249.1
Fig. 6b	66.4	76.8	179.9	203.2	210.2	230.4	248.4
Exper. [15]			179	199		233	250
Exper. [44]		83	178	204		231	244

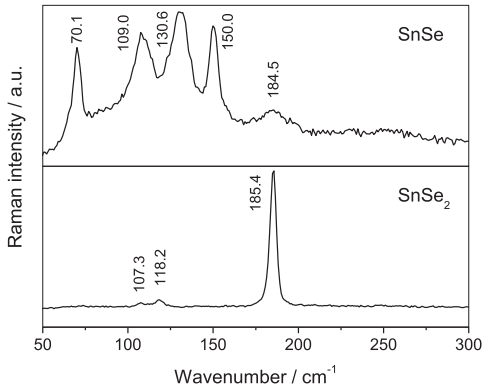

Fig. 9. Raman spectra of pure SnSe and pure $SnSe_2$. Excitation wavelength is 532 nm (0.06 mW); spectral region is 50–300 cm^{-1}.

conductivity as it was done by other researchers [3,6–8,15,21] for the CTSe films on a glass substrates.

Fig. 11 depicts a dependence of the photocurrent density, j_{photo} on selenization temperature. The j_{photo} values were measured at the cathodic potential $E_c = -0.8$ V, when photocurrent stopped changing after light was switched on. Prior to measurements, copper selenides were dissolved in a KCN solution. The largest value was revealed by the CTSe film selenized at a temperature of

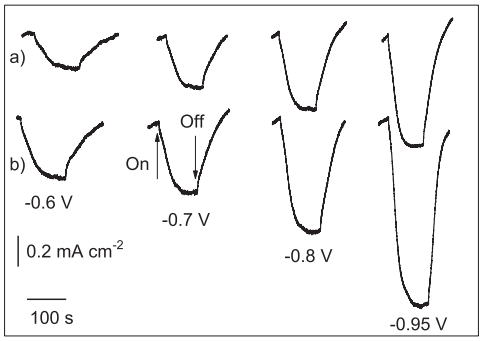

Fig. 10. Pulses of photocurrent in 0.2 M $Eu(NO_3)_3$ solution for CTSe film selenized at temperature of 500 °C. a) – as-synthesized; b) – after post annealing at temperature of 200 °C for 2 h.

500 °C. The film presented predominantly cubic Cu_2SnSe_3 (Fig. 6). The decrease in photocurrent with increase in selenization temperature is quite unexpected, since according to reference [34] cubic Cu_2SnSe_3 has a higher hole concentration as compared to the monoclinic one, and due to that the latter should be more photoactive. However, the photovoltaic performance depends not only on the hole concentration, but also on the presence of binary selenides [45], density of vacancy and antisite defects [46]. The photovoltaic performance depends also on serious resistance, which is related with the Mo back contact and thickness of $MoSe_2$ layer.

According to the results of examination of cross-sectional CTSe/Mo SEM images, the thickness of $MoSe_2$ increased with selenization temperature (Fig. 12). This dependence implies that the decrease in the photoactivity of CTSe film observed by us could be at least partly caused by an increasing thickness of the $MoSe_2$ layer.

Low electric resistance and a high concentration of holes in Cu_2SnSe_3 are mostly related with a high concentration of copper vacancy V_{Cu}. Some researchers applied low temperature post-annealing of Cu_2SnSe_3 in nitrogen gas [31] and annealing of Cu_2ZnSnS_4 in vacuum [46] in order to reduce the concentration of V_{Cu} vacancies or Cu_{Zn} and Zn_{Cu} antisite defects and consequently to improve the photovoltaic characteristics of the absorber layer. We tried this method for our films selenized at a temperature of 500 °C. The post-annealing of the film in air at a temperature of 100 °C even for 24 h had no impact on the photocurrent. However, the same heat treatment at a temperature of 200 °C yielded a significant increase in photocurrent already after 2 h and brought a further increase after 18 h of post-annealing (Fig. 13). The temperature of 200 °C is the critical temperature, T_C for kesterite [46]. At temperatures above T_C the kesterite is in the disordered equilibrium state, while below T_C the equilibrium ordering degree increases. The post-annealing of Cu_2SnSe_3 in nitrogen gas at temperatures in the range of 150–350 °C even lowered photoelectrochemical response [31]. This could be caused by undissolved copper selenides. During our studies we have noticed that CTSe gave a photoelectrochemical response lower by about 30%, if copper selenides were not dissolved in a KCN solution prior to the measurements.

4. Conclusions

The modified electrolyte solution developed in the current work made it possible to deposit a far more compact and smooth Cu-Sn precursor layer free from organic contaminants. The

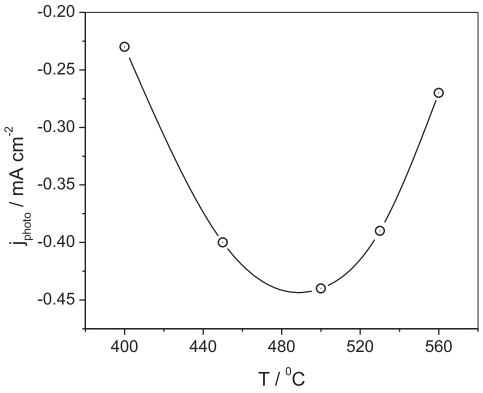

Fig. 11. Dependence of Cu_2SnSe_3 film photocurrent in 0.2 M $Eu(NO_3)_3$ solution at cathodic potential $E_c = -0.8$ V on the selenization temperature.

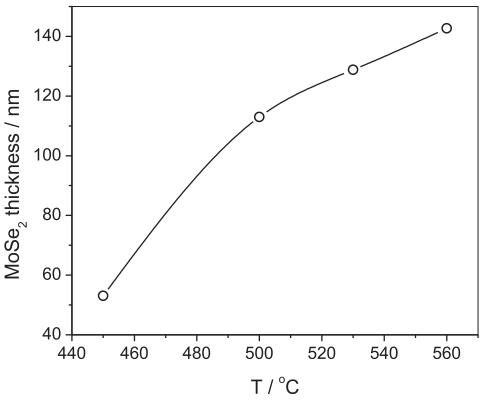

Fig. 12. The thickness of $MoSe_2$ layer as a function of the selenization temperature.

electrodeposition of Cu-Sn alloy in the modified electrolyte proceeds with ~90% current efficiency, the latter being about 20% higher than that in the electrolyte used by other researchers.

The usage of the obtained Cu-Sn precursor resulted in an improved quality of Cu_2SnSe_3 films, which exhibited a smoother surface and smaller density of voids. The XRD studies revealed that rather pure Cu_2SnSe_3 films were fabricated at selenization temperatures higher than 400 °C. In the selenization temperature range of 350–500 °C the cubic Cu_2SnSe_3 was detected by the XRD and its cubic lattice parameter linearly increased with temperature. The monoclinic Cu_2SnSe_3 was detected by XRD only in the film selenized at a temperature of 560 °C.

Raman spectra of the cubic and monoclinic Cu_2SnSe_3 looked rather similar. The main difference was observed in the low energy region of spectra: the band at about 77 cm^{-1} showed a much higher Raman intensity in the case of presence of monoclinic Cu_2SnSe_3; consequently, this band could be assumed as a marker of the monoclinic Cu_2SnSe_3 structure.

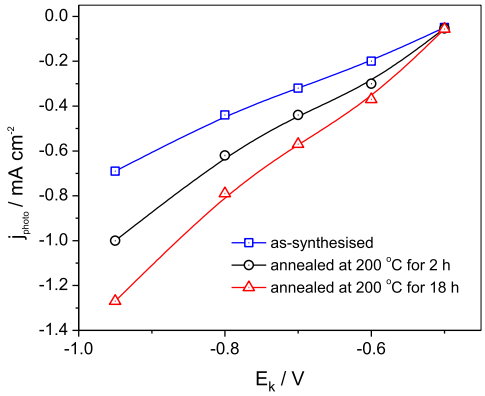

Fig. 13. Photocurrent of CTSe layer (Cu/Sn = 1.9) selenized at 500 °C for 20 min as a function of cathodic potential E_c in 0.2 M $Eu(NO_3)_3$ solution.

The largest photoelectrochemical response was yielded by Cu_2SnSe_3 synthesized at a selenization temperature of 500 °C. The photoelectrochemical performance of the film was improved by post-annealing in air at a temperature of 200 °C. It could be assumed that the improvement resulted from crystalline structure ordering and a decrease in density of V_{Cu}, however, further investigations must be carried out to reveal more reliable conclusions.

References

[1] G. Marcano, C. Rincón, L.M. de Chalbaud, D.B. Bracho, G. Sánchez Pérez, Crystal growth and structure, electrical, and optical characterization of the semiconductor Cu_2SnSe_3, J. Appl. Phys. 90 (2001) 1847–1853.
[2] G. Marcano, L.M. de Chalbaud, C. Rincon, G. Sanchez Perez, Crystal growth and structure of the semiconductor Cu_2SnSe_3, Mater. Lett. 53 (2002) 151–154.
[3] G. Suresh Babu, Y.B. Kishore Kumar, Y. Bharath Kumar Reddy, V. Sundara Raja, Growth and characterization of Cu_2SnSe_3 thin films, Mater. Chem. Phys. 96 (2006) 442–446.
[4] G.E. Delgado, A.J. Mora, G. Marcano, C. Rincon, Crystal structure refinement of the semiconducting compound Cu_2SnSe_3 from X-ray powder diffraction data, Mater. Res. Bull. 38 (2003) 1949–1955.
[5] D.-H. Kuo, W.-D. Haung, Y-Sh. Huang, J.-D. Wu, Y.-J. Lin, Effect of post-deposition annealing on the performance of D.C. sputtered Cu_2SnSe_3 thin films, Surf. Coating. Technol. 205 (2010) S196–S200.
[6] Dong-Hau Kuo, Wei-Di Haung, Ying-Sheng Huang, Jiun-De Wu, Yan-Jih Lin, Effect of post-deposition annealing on the performance of D.C. sputtered Cu_2SnSe_3 thin films, Surf. Coating. Technol. 205 (2010) S196–S200.
[7] David Avellaneda, M.T.S. Nair, P.K. Nair, Cu_2SnS_3 and Cu_4SnS_4 thin films via chemical deposition for photovoltaic application, J. Electrochem. Soc. 157 (2010) D346–D352.
[8] Dong-Hau Kuo, Wei-Di Haung, Ying-Sheng Huang, Jiun-De Wu, Yan-Jih Lin, Single-step sputtered Cu_2SnSe_3 films using the targets composed of Cu_2Se and $SnSe_2$, Thin Solid Films 518 (2010) 7218–7751.
[9] G. Hema Chandra, O. Lakshmana Kumar, R. Prasada Rao, S. Uthanna, Influence of substrate and selenization temperatures on the growth of Cu_2SnSe_3 films, J. Mater. Sci. 46 (2011) 6952–6959.
[10] Dominik M. Berg, Rabie Djemour, Levent Gütay, Susanne Siebentritt, Phillip J. Dale, Xavier Fontane, Victor Izquierdo-Roca, Alejandro Pérez-Rodriguez, Raman analysis of monoclinic Cu_2SnS_3 thin films, Appl. Phys. Lett. 100 (2012), 192103.
[11] Junpei Koike, Kotaro Chino, Naoya Aihara, Hideaki Araki, Ryota Nakamura, Kazuo Jimbo, Hironori Katagiri, Cu_2SnS_3 thin-film solar cells from electroplated precursors, Jpn. J. Appl. Phys. 51 (2012) 10NC34.
[12] Dominik M. Berg, Rabie Djemour, Levent Gütay, Susanne Siebentritt, Phillip J. Dale, Xavier Fontane, Victor Izquierdo-Roca, Alejandro Pérez-Rodriguez, Raman analysis of monoclinic Cu_2SnS_3 thin films, Appl. Phys. Lett. 100 (2012), 192103.
[13] Mahshid Ahmadi, Stevin S. Pramana, Sudip K. Batabyal, Chris Boothroyd, Subodh G. Mhaisalka, Yeng Ming Lam, Synthesis of Cu_2SnSe_3 nanocrystals for

solution processable photovoltaic cells, Inorg. Chem. 52 (2013) 1722–1728.
[14] W. Septina, S. Ikeda, A. Kyoraiseki, T. Harada, M. Matsumura, Single-step electrodeposition of a microcrystalline $Cu_2ZnSnSe_4$ thin film with a kesterite structure, Electrochim. Acta 88 (2013) 436–442.
[15] Min Kim Kang, Hitoshi Tampo, Hajime Shibata, Shigeru Niki, Growth and characterization of coevaporated Cu_2SnSe_3 thin films for photovoltaic applications, Thin Solid Films 536 (2013) 111–114.
[16] Zeguo Tang, Yuki Nukui, Kiichi Kosaka, Naoki Ashida, Hikaru Uegaki, Takashi Minemoto, Reduction of secondary phases in Cu_2SnSe_3 absorbers for solar cell application, J. Alloys Compd. 608 (2014) 213–219.
[17] Rachmat Adhi Wibowo, Stefan Moeckel, Hyesun Yoo, Astrid Hoelzing, Rainer Hock, Peter J. Wellmann, Formation of Cu_2SnSe_3 from stacked elemental layers investigated by combined in situ X-ray diffraction and differential scanning calorimetry techniques, J. Alloys Compd. 588 (2014) 254–258.
[18] C. Calderón, G. Gordillo, R. Becerra, P. Bartolo-Pérez, XPS analysis and characterization of thin films Cu_2ZnSnS_4 grown using a novel solution based route, Mater. Sci. Semicond. Process. 39 (2015) 492–498.
[19] Min Kim Kang, Kuang Hsiang Liao, Hitoshi Tampo, Hajime Shibata, Shigeru Niki, Cu2ZnSnSe4 thin-film solar cells fabricated using Cu_2SnSe_3 and ZnSe bilayers, Appl. Phys. Express 8 (2015), 042301.
[20] Mitsuki Nakashima, Junya Fujimoto, Toshiyuki Yamaguchi, Masanobu Izaki, Cu_2SnS_3 thin-film solar cells fabricated by sulfurization from NaF/Cu/Sn stacked precursor, Appl. Phys. Express 8 (2015), 042303.
[21] T. Srinivasa Reddy, R. Amiruddin, M.C. Santhosh Kumar, Deposition and characterization of Cu_2SnS_3 thin films by coevaporation for photovoltaic application, Sol. Energy Mater. Sol. Cell. 143 (2015) 128–134.
[22] Sandra Dias, Banavoth Murali, S.B. Krupanidhi, Transport properties of solution processed Cu_2SnS_3/AZnO hetero-structure for low cost photovoltaics, Sol. Energy Mater. Sol. Cell. 143 (2015) 152–158.
[23] Zeguo Tang, Kenta Aoyagi, Yuki Nukui, Kiichi Kosaka, Hikaru Uegaki, Jakapan Chatana, Daisuke Hironiwa, Takashi Minemoto, Reaction path for formation of Cu_2SnSe_3 film by selenization of Cu–Sn precursor, Sol. Energy Mater. Sol. Cell. 143 (2015) 311–318.
[24] Walelign Wubet, Dong-Hau Kuo, Effects of copper excess and copper deficiency on the structural and electrical properties of bulk Cu_xSnSe_3 with x=1.6–2.2, J. Solid State Chem. 226 (2015) 120–125.
[25] J. Li, C. Xue, Y. Wang, G. Jiang, W. Liu, C. Zhu, Cu_2SnS_3 solar cells fabricated by chemical bath deposition-annealing of SnS/Cu stacked layers, Sol. Energy Mater. Sol. Cell. 144 (2016) 281–288.
[26] Mirjana Dimitrievska, Andrew Fairbrother, Edgardo Saucedo, Alejandro Pérez-Rodríguez, Victor Izquierdo-Roca, Secondary phase and Cu substitutional defect dynamics in kesterite solar cells: impact on optoelectronic properties, Sol. Energy Mater. Sol. Cell. 149 (2016) 304–309.
[27] G. Rey, T.P. Weiss, J. Sendler, A. Finger, C. Spindler, F. Werner, M. Melchiorre, M. Hála, M. Guennou, S. Siebentritt, Ordering kesterite improves solar cells: a low temperature post-deposition annealing study, Sol. Energy Mater. Sol. Cell. 151 (2016) 131–138.
[28] Wei-Chao Chen, Venkatesh Tunuguntla, Hsien-Wen Li, Cheng-Ying Chen, Shao-Sian Li, Jih-Shang Hwang, Chin-Hao Lee, Li-Chyong Chen, Kuei-Hsien Chen, Fabrication of $Cu_2ZnSnSe_4$ solar cells through multi-step selenization of layered metallic precursor film, Thin Solid Films 618 (2016) 42–49.
[29] Albert Daniel Saragih, Dong-Hau Kuo, Investigation of Mg dopant in Cu_2SnSe_3 thin films for photovoltaic applications, J. Alloys Compd. 683 (2016) 542–546.
[30] A.S.T.A.M. Aykut, Structural and optical characterization of Cu_2SnSe_3 thin films prepared by SILAR method, Thin Solid Films 615 (2016) 324–328.
[31] Nordin Sabli, Zainal Abidin Talib, Hikmat S. Hilal, Effect of under nitrogen annealing on photo-electrochemical characteristics of films deposited from authentic Cu_2SnSe_3 sources by thermal vacuum under argon gas condensation, Int. J. Hydrogen Energy 42 (2017) 9003–9010.
[32] E.J. Skoug, J.D. Cain, D.T. Morelli, Thermoelectric properties of the Cu_2SnSe_3–Cu_2GeSe_3 solid solution, J. Alloys Compd. 506 (2010) 18–21.
[33] Jing Fan, Wilder Carrillo-Cabrera, Akselrud Lev, Iryna Antonyshyn, Lidong Chen, Yuri Grin, New monoclinic phase at the composition Cu_2SnSe_3 and its thermoelectric properties, Inorg. Chem. 52 (2013) 11067–11074.
[34] Jing Fan, Walter Schnelle, Iryna Antonyshyn, Igor Veremchuk, Wilder Carrillo-Cabrera, Xun Shi, Yuri Grin, Lidong Chen, Structural evolvement and thermoelectric properties of $Cu_{3-x}Sn_xSe_3$ compounds with diamond-like crystal structures, Dalton Trans. 43 (2014) 16788–16794.
[35] Maa Rui, Guanghua Liua, Jiangtao Lia, Yuyang Lia, Kexin Chenc, Yemao Hana, Min Zhoua, Laifeng Li, Effect of secondary phases on thermoelectric properties of Cu_2SnSe_3, Ceram. Int. 43 (2017) 7002–7010.
[36] C.M. Fella, A.R. Uhl, C. Hammond, I. Hermans, Y.E. Romanyuk, A.N. Tiwari, Formation mechanism of $Cu_2ZnSnSe_4$ absorber layers during selenization of solution deposited metal precursors, J. Alloys Compd. 567 (2013) 102–106.
[37] R. Schurr, A. Hölzing, R. Hock, Real-time investigations on the formation reactions during annealing of sulfurized Cu–Sn precursors, Thin Solid Films 519 (2011) 7412–7741.
[38] F. Hergert, R. Hock, Predicted formation reactions for the solid-state syntheses of the semiconductor materials Cu_2SnX_3 and Cu_2ZnSnX_4 (X = S, Se) starting from binary chalcogenides, Thin Solid Films 515 (2007) 5953–5956.
[39] R.A. Wibowo, W.H. Jung, M.H. Al-Faruqi, I. Amal, K.H. Kim, Crystallization of $Cu_2ZnSnSe_4$ compound by solid state reaction using elemental powders, Mater. Chem. Phys. 124 (2010) 1006–1010.
[40] R.A. Wibowo, S.A. Moeckel, H. Yoo, C. Hetzner, A. Hoelzing, P. Wellmann, R. Hock, Intermetallic compounds dynamic formation during annealing of stacked elemental layers and its influences on the crystallization of $Cu_2ZnSnSe_4$ films, Mater. Chem. Phys. 142 (2013) 311–317.
[41] R. Juskėnas, G. Niaura, Z. Mockus, S. Kanapeckaitė, R. Giraitis, R. Kondrotas, A. Naujokaitis, G. Stalnionis, V. Pakštas, V. Karpavičienė, XRD studies of an electrochemically co-deposited Cu-Zn-Sn precursor and formation of a $Cu_2ZnSnSe_4$ absorber for thin-film solar cells, J. Alloys Compd. 655 (2016) 281–289.
[42] Ganganath S. Perera, Sumudu A. Athukorale, Felio Perez, Charles U. Pittman Jr., Dongmao Zhang, Facile displacement of citrate residues from gold nanoparticle surfaces, J. Colloid Interface Sci. 511 (2018) 335–343.
[43] N.B.M. Amiri, A. Postnikov, Secondary phase Cu_2SnSe_3 vs. kesterite $Cu_2ZnSnSe_4$: similarities and differences in lattice vibration modes, J. Appl. Phys. 112 (2012), 033719.
[44] G. Marcanoa, C. Rincón, S.A. López, G. Sánchez Pérez, J.L. Herrera-Pérez, J.G. Mendoza-Alvarez, P. Rodríguez, Raman spectrum of monoclinic semiconductor Cu_2SnSe_3, Solid State Commun. 151 (2011) 84–86.
[45] Solange Temgoua, Romain Bodeux, Negar Naghavi, Sébastien Delbos, Effects of $SnSe_2$ secondary phases on the efficiency of $Cu_2ZnSn(S_x,Se_{1-x})_4$ based solar cells, Thin Solid Films 582 (2015) 215–219.
[46] G. Rey, A. Redinger, J. Sendler, T.P. Weiss, M. Thevenin, M. Guennou, B. El Adib, S. Siebentritt, The band gap of $Cu_2ZnSnSe_4$: effect of order-disorder, Appl. Phys. Lett. 105 (2014) 112106.

Paper II

Photoelectrochemical, Raman spectroscopy, XRD and photoluminescence study of disorder in electrochemically deposited kesterite thin film.

Audrius Drabavičius, Arnas Naujokaitis, Giedrius Stalnionis, Raimondas Giraitis, Zenius Mockus, Stasė Kanapeckaitė, Putinas Kalinauskas, Ramūnas Nedzinskas, Gediminas Niaura, Remigijus Juškėnas.

Journal of Alloys and Compounds, 2020. 824: p. 153853.

DOI: 10.1016/j.jallcom.2018.06.276.

Journal of Alloys and Compounds 824 (2020) 153853

Contents lists available at ScienceDirect

Journal of Alloys and Compounds

journal homepage: http://www.elsevier.com/locate/jalcom

Photoelectrochemical, Raman spectroscopy, XRD and photoluminescence study of disorder in electrochemically deposited kesterite thin film

Audrius Drabavičius*, Arnas Naujokaitis, Giedrius Stalnionis, Raimondas Giraitis, Zenius Mockus, Stasė Kanapeckaitė, Putinas Kalinauskas, Ramūnas Nedzinskas, Gediminas Niaura, Remigijus Juškėnas

State Research Institute Center for Physical Sciences and Technology, Savanoriu av. 231, Vilnius, Lithuania

ARTICLE INFO

Article history:
Received 9 September 2019
Received in revised form
13 January 2020
Accepted 14 January 2020
Available online 15 January 2020

Keywords:
CZTS
Thin film
Kesterite
XRD
Raman spectroscopy
Photoelectrochemical response

ABSTRACT

Photo-electrochemical measurements, Raman spectroscopy, XRD with Cu $K_{\alpha 1}$ radiation and photoluminescence (PL) spectroscopy studies were used for evaluating of photo-electric activity of the kesterite thin films and its relation with Cu and Zn atoms disorder. The kesterite films were synthesized using the electrochemical deposition of Cu-Sn and Zn layers on Mo/soda-lime glass substrates and subsequent sulfurization. The photo-electrochemical current density was measured as a function of the potential under chopped illumination in 0.1 M $Eu(NO_3)_3$ aqueous solution. All the methods showed the medium level of order, i.e. neither completely disordered nor highly ordered. However, the results of Raman spectroscopy predicted the stoichiometry of kesterite different from the one revealed by XRD. The XRD data showed the presence of defects $[2Cu_{Zn}^{-} + Sn_{Zn}^{2+}]$, while Raman spectroscopy predicted $[2Zn_{Cu}^{+} + Zn_{Sn}^{2+}]$ defects. Based on the results obtained it has been concluded that XRD revealed more plausible information on the kesterite stoichiometry and the point defects as compared to Raman spectroscopy under current experimental conditions.

1. Introduction

It is well known that kesterite is an attractive material as an absorber for thin-film solar cells due to the low cost, availability, and non-toxicity of comprising chemical elements (metallic constituents). However, even though researchers from all over the world have been working on research and fabrication of kesterite solar cells for as long as 10 years, the record conversion efficiency of these cells has merely reached 12.6% [1]. Perovskite solar cells pushed them into the shadow in just a few years, reaching the efficiency of 23.7% [2]. However, there are still many researchers working on the issues of kesterite solar cells. The scientific community is trying to find reasons why the CIGS ($CuInGaSe_2$) record efficiency (22.9% [3]) is almost twice as high as that of kesterite. Most attention is paid to point defects and their complexes or clusters, some of which could be responsible for low open-circuit voltage, V_{OC} and for detrimental recombination phenomena in the kesterite solar cells [4–9]. The presence of point defects such as vacancies V_{Cu}, V_{Zn}, antisite defects Cu_{Zn}, Zn_{Cu}, Zn_{Sn}, Sn_{Zn}, intrinsic atoms Cu_i, Zn_i causes a disorder in the tetragonal kesterite structure [10–12]. Depending on the concentration of defects, the types of kesterite structure are divided into ordered, partly ordered and disordered ones [13,14]. According to a more precise definition of the characteristic types of defects and their association with the chemical composition of CZTS (Cu_2ZnSnS_4) absorber, the structures of kesterite are divided into A, B, C, D, E and F types [4,15]. The classification of the off-stoichiometric kesterites structures is based on the formation of certain point defect clusters depending on the chemical composition: the Cu-poor Zn-rich chemical composition with $V_{Cu} + Zn_{Cu}$ is referred to as type A kesterite structure; B – the Cu-poor Sn-poor composition with $Zn_{Sn} + 2Zn_{Cu}$; C – the Cu-rich Sn-rich composition with $2Cu_{Zn} + Sn_{Zn}$; D – the Cu-rich Zn-poor composition with $Cu_{Zn} + Cu_i$; E - Cu-poor Sn-rich composition with $2V_{Cu} + Sn_{Zn}$ is referred to as type E; and F – Cu-rich Zn-rich composition with $Zn_{Sn} + Cu_{Sn} + Cu_i$ [4,15]. The concentration of point defects, their type or order/disorder of kesterite structure has

* Corresponding author.
E-mail address: audrius.drabavicius@ftmc.lt (A. Drabavičius).

https://doi.org/10.1016/j.jallcom.2020.153853
0925-8388/

been assessed by various techniques: scanning transmission electron microscopy (STEM) [16], Raman spectroscopy [17–20], a solid state nuclear magnetic resonance (NMR) [11,18], X-ray diffraction (XRD) [9,15], anomalous X-ray diffraction [21], neutron diffraction [22], photoluminescence spectroscopy [23].

The disorder or point defects are usually analyzed in the CZTS samples synthesized from the powders of individual chemical elements, sulfides of Cu, Zn and Sn [11,12,15,18,21,22] or in sputtered CZTS thin films [14,23]. To the best of our knowledge, there is only one work, which examined order/disorder by Raman spectroscopy in the CZTS film manufactured by the approach of electrochemical deposition [24]. We already noticed in our previous work [25] that a phase composition and structure of CZTSe films strongly depends on the approach of precursor formation.

In the current work, CZTS thin films were fabricated by electrodeposition and subsequent sulphurization. The photovoltaic activity of the films was assessed by measuring a photoelectrochemical (PEC) response in 0.1 M $Eu(NO_3)_3$ solution. For the first time, the origin and the number of point defects in the kesterite synthesized using electrochemical deposition have been studied not only by the near-resonant Raman spectroscopy, photoluminescence (PL) spectroscopy but also by a high-resolution XRD using Cu $K_{\alpha 1}$ radiation.

2. Experimental

The CZTS films were formed using the electrochemical deposition of stacked precursor layers similarly like in the work [26], except we used different electrolyte solutions, which were agitated with a magnetic stirrer during the deposition. The precursors were deposited on Mo/soda-lime glass substrates. The details on co-electrodeposition of a Cu-Sn (Cu 65 at. %, Sn 35 at. %) layer of about 500 nm in thickness and the procedures of the preparation of Mo surface prior to the electrodeposition were presented in Refs. [25,27], respectively. A topmost layer of Zn was deposited from commercial chloride solution LIKONDA ZnRN at a current density of 30 mA cm^{-2}. The kesterite films of Cu-poor Zn-poor, Cu-poor Zn-stoichiometric, and Cu-poor Zn-rich compositions were formed by depositing Zn layers of different thickness: 170, 200 and 240 nm, respectively. After the electrodeposition, Cu-Sn/Zn precursor layers were pre-annealed at a temperature of 350 °C for 60 min under atmospheric pressure of the gas mixture (Ar 95% + H_2 5%). A sulfurization of the precursors was conducted in a graphite container with 150 mg of sulfur powder. The container was placed into one zone quartz tube furnace and heated for 15 min in Ar gas 6.0 at atmospheric pressure and a temperature of 580 °C. The temperature ramping rate was 2° s^{-1}. The samples were naturally cooled down to room temperature in a furnace.

The chemical composition of CZTS films was investigated in a dual beam system FE-SEM-FIB Helios Nanolab 650 (FEI Company) equipped with an EDX spectrometer X-Max (Oxford Instruments).

PEC analysis of kesterite films was carried out in a three-electrode electrochemical cell using an aqueous 0.1 M $Eu(NO_3)_3$ solution and chopped illumination by White LED Lumiled 3W. More details are presented in Refs. [27,28].

XRD measurements were carried out using an X-ray diffractometer SmartLab (Rigaku) equipped with a 9 kW rotating Cu anode X-ray tube. The kesterite lattice parameters and quantity of ZnS were measured using a CALSA (Crystal Array on Logarithmic Spiral Analyser) analyzer on a diffracted beam, which enables registration of powder XRD patterns in Cu $K_{\alpha 1}$ radiation (λ = 1.5405929 Å). The accuracy of the adjustment of the diffractometer was tested using a certified standard SRM 660b (powder of LaB_6).

Raman spectra were recorded using a confocal microspectrometer inVia (Renishaw, UK) equipped with a thermoelectrically cooled (−70 °C) CCD camera and a microscope. Spectra were excited with 785 nm (1 mW, 1200 lines mm^{-1} grating), 532 nm (0.06 mW, 3000 lines mm^{-1} grating) and 325 nm (0.1 mW, 2400 lines mm^{-1} grating) laser radiations. The Raman frequencies were calibrated using the silicon standard according to the line at 520.7 cm^{-1} (532 nm excitation) and Teflon Raman spectrum (325 nm excitation). Spectra were taken using a 50x/0.75 NA (785 and 532 nm) and 15x/0.32 (325 nm) objective lens. The integration time was 100 s (785 nm) and 400 s (532 and 325 nm). Parameters of the bands were determined by fitting the experimental spectra with Gaussian-Lorentzian shape components using GRAMS/A1 8.0 (Thermo Scientific) software assuming linear baseline.

Photoluminescence (PL) spectra were recorded at 3–300 K temperatures using a self-made experimental setup. CZTS film samples were mounted on the cold finger of a closed-cycle cryostat (SHI-4, Janis Research) and excited using a pulsed UV laser (266 nm/ 4.66 eV, <0.6 ns, >0.7 kW). Then near-infrared (NIR) luminescence was dispersed by a 500 mm grating monochromator (Andor Shamrock SR-500i-D1; 600 l/mm, blaze @ 1000 nm) and focused into a thermoelectrically-cooled InGaAs photodetector. The electrical signal was then processed using conventional lock-in techniques. For the low temperatures (up to 250 K), the asymmetrical spectra were analyzed by two Gaussian bands. Moreover, full-range of temperature-dependent spectra allowed estimation of the activation energy (E_a). Furthermore, from the excitation power-dependent spectra, potential fluctuation parameter γ was calculated.

3. Results and discussion

Three groups of kesterite films, which differ in chemical composition (Cu-poor Zn-poor, Cu-poor Zn stoichiometric, and Cu-poor Zn-rich) were studied in the current work. The chemical compositions were determined after a treatment of CZTS samples in KCN and HCl aqueous solutions [29]. Table 1 presents chemical compositions and atomic ratios Cu/(Zn + Sn), Zn/Sn of one representative of each group. The chemical compositions of the samples presented in the Table were closest to the average ones in the group. Hereinafter the results of the study of these particular samples are presented in the work and are labelled as in Table 1.

Fig. 1 depicts the results of the measurement of photocurrent density j_{ph} as a function of the CZTS/Mo electrode potential E vs Ag/AgCl/KCl reference electrode. Fig. 1 presents j_{ph} values at a potential of −0.5 V for all three samples to clearly show that the highest photo-response revealed exactly the Stoichiometric CZTS sample and Zn-poor one yielded the lowest j_{ph}. The shape of j_{ph} pulses has spikes at the moments of light switch-on and switch-off. According to Ref. [30], the size of the spike could be related to slow recombination kinetics of trap states, which is why the current density which could be a result of this phenomenon was assigned as j_{tr}. An example of the photo-current pulse is shown in Fig. 2. That is a fragment of j ~ f(E) dependence measured for the Stoichiometric CZTS sample. Fig. 2 shows which part of total current density was attributed to the photo-current j_{ph} and which to that of j_{tr}, i.e., spike. The j_{tr} values were 0.044 ± 0.007, 0.025 ± 0.005 and

Table 1
Chemical composition (at.%) and atomic ratios of CZTS samples studied in the work.

Sample	Cu	Zn	Sn	S	Cu/(Zn + Sn)	Zn/Sn
Zn-rich	18.48	14.48	11.32	55.72	0.72	1.28
Stoichiometric	17.86	12.15	11.94	58.05	0.74	1.02
Zn-poor	18.89	10.81	12.8	57.5	0.80	0.84

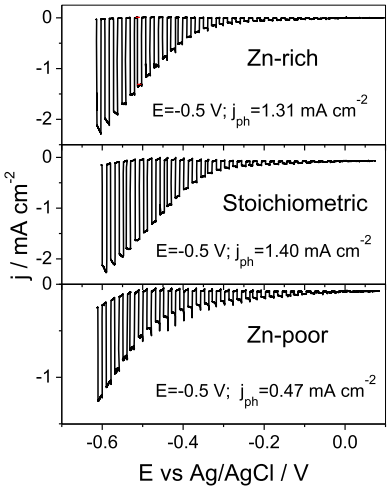

Fig. 1. Photoelectrochemical current density j_{ph} as a function of potential E of CZTS films in a 0.1 M $Eu(NO_3)_3$ solution under chopped illumination. The potential scan rate is 1 mV s^{-1}. Light intensity is 100 mW cm^{-2}.

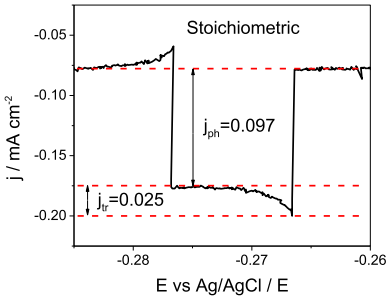

Fig. 2. The fragment of measured j ~ f(E) dependence for the Stoichiometric CZTS sample in a 0.1 M $Eu(NO_3)_3$ solution under chopped illumination. The potential scan rate is 1 mV s^{-1}. Light intensity is 100 mW cm^{-2}.

0.040 ± 0.007 mA cm^{-2} for Zn-rich, Stoichiometric and Zn-poor samples, respectively. The Stoichiometric CZTS sample revealed the lowest j_{tr}.

We have found that the recombination effect decreased after the processing of the as-synthesized CZTS film in KCN then in HCl and again in KCN solutions, as shown in Fig. 3. The processing not only decreased the recombination at the interface CZTS/$Eu(NO_3)_3$ solution but also increased j_{ph} value by a factor of about 7 at a potential of −0.5 V for the Stoichiometric CZTS sample. These changes could be attributed to the dissolution of copper and zinc sulfides in KCN and HCl solutions, respectively [29]. The dissolution of Cu_2S and ZnS resulted in an increased active surface of the CZTS film [31] because these secondary phases on the CZTS surface could act as traps or as a resistive barrier for minority carriers in p-type CZTS [32]. The dissolution of Cu_2S and ZnS located on the CZTS surface makes it possible to use j_{ph} as a parameter suitable for the

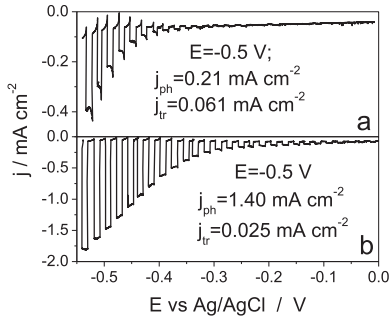

Fig. 3. Current density as a function of the potential for the Stoichiometric CZTS sample in a 0.1 M $Eu(NO_3)_3$ solution under chopped illumination: a) for as-synthesized sample; b) for the same sample after its treatments in the KCN and HCl solutions.

evaluation of photovoltaic efficiency of the CZTS film in bulk since all of the films had undergone the same surface treatment in KCN and HCl solutions.

The origin and the number of point defects as well as the ordering level S (S = 0 – fully disordered, 1 – fully ordered) of the studied CZTS films, was evaluated using Raman spectroscopy at first. Fig. 4 shows the Raman spectra of three CZTS samples measured using a near-resonant excitation wavelength of 785 nm. The parameters Q and Q′ were derived from these spectra, where $Q = I_{288}/I_{304}$ and $Q' = I_{338}/(I_{367} + I_{375})$ and I_i is the respective kesterite Raman band integral intensity [18]. The results obtained are presented in Table 2.

The values of the parameters Q and Q′ of three CZTS samples according to Ref. [18] are attributable to B_S – type structure, which represents off-stoichiometric ($Cu_{1.95}Zn_{1.06}Sn_{0.99}S_4$) ordered kesterite obtained by slow cooling. The disordered B_Q – type of an off-stoichiometric structure was formed by fast cooling or quenching in ice bath [18]. The parameters Q and Q′ for the latter type of kesterite structure should be ≤ 1.0. Point defect clusters [$2Zn_{Cu}^{+} + Zn_{Sn}^{2-}$] are characteristic of the B-type structure [18]. Ordering level S has a linear dependence on parameter Q according to Ref. [14] so we derived S values for the studied samples graphically using the dependence presented in Fig. 2 of Ref. [14] and Q values of our samples presented in Table 2. All three samples have

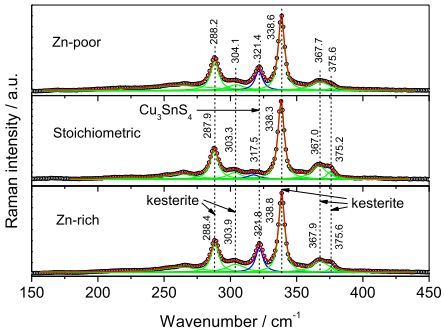

Fig. 4. Raman spectra of the studied CZTS films. Excitation wavelength is 785 nm.

Table 2
Atomic ratios, Q and Q′ parameters, structure types according Ref. [18] and the ordering level according Ref. [23].

Sample	Cu/(Zn + Sn)	Zn/Sn	Q	Q′	Type of structure	S
Stoichiometric	0.66	1.02	2.5	2.0	B_S	0.45
Zn-rich	0.72	1.28	1.5	2.1	B_S	0.28
Zn-poor	0.80	0.84	2.4	2.5	B_S	0.44

nearly the same ordering level S values of 0.28–0.45. These values are characteristic of the CZTS formed using the tube furnace process [33].

Two more Raman spectrum parameters can be used to assess the order/disorder state of kesterite and those are full width at half maximum (FWHM) of the bands at 287 and 338 cm^{-1} [14]. Table 3 presents FWHM ranges for the slow cooled (the ordered) and quenched (the disordered) kesterite samples from Ref. [14] and FWHM values measured for our samples.

The FWHM values of the studied CZTS samples are inside or quite near the range expected for the slow cooled or the ordered kesterite. Based on FWHM values, the Zn-rich CZTS sample possessed the most ordered structure. On the other hand, this CZTS film contained the largest quantity of Cu_3SnS_4 secondary phase as seen in the Raman spectra (Fig. 3). The band at ~320 cm^{-1} is attributable to orthorombic Cu_3SnS_4 secondary phase and the normalised intensities of the band were 11.5, 39.5 and 33.5 a.u. for Stoichiometric, Zn-rich and Zn-poor samples, respectively.

To assess the presence of ZnS in the CZTS samples, the Raman spectrum was measured using an excitation wavelength of 325 nm, which provides the possibility to obtain resonantly enhanced Raman spectrum for ZnS (Fig. 5). The intense bands near 698.4, 1045.3, 1394.5, and low intensity feature at 1743.3 cm^{-1} are associated with the second, third, fourth, and fifth order peaks of fundamental longitudinal optical (LO) phonon mode of ZnS at 351.5 cm^{-1}, respectively [34,35]. The lower intensity bands visible at 633, 981.8, and 1318.4 cm^{-1} are due to higher order combination bands of the fundamental LO and transverse optical (TO) phonon modes of ZnS [35]. Because of resonance Raman enhancement, even a small amount of ZnS on the surface of the studied samples can be detected. The spectra revealed that the Zn-rich sample possessed the largest quantity of ZnS secondary phase while the Zn-poor sample possessed the lowest one.

The XRD measurements of the as-synthesized CZTS films using Cu $K_{\alpha 1,2}$ radiation were used to determine the phase composition of the CZTS films. These measurements revealed that all the films contained off-stoichiometric kesterite $Cu_{1,885}Zn_{1,058}SnS_4$ (ICDD #01-080-8226) and the secondary phase Cu_2S (#00-002-1284). Fig. 6 (lower curve) presents the XRD pattern for the as-synthesized Stoichiometric CZTS sample as an example. This XRD pattern tells nothing about the presence of ZnS and ternary secondary phases since all of the high intensity peaks of these phases nearly fully overlap with those of kesterite. However, XRD pattern of the same sample measured after the treatment in a KCN solution (Fig. 6, upper pattern) showed that the Cu_2S phase was fully dissolved which points to the fact that Cu_2S was located on the CZTS film surface only.

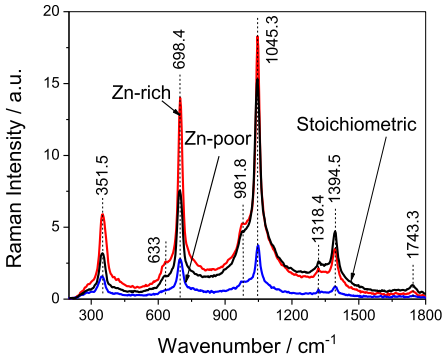

Fig. 5. Raman spectra of the studied CZTS films. Excitation wavelength is 325 nm.

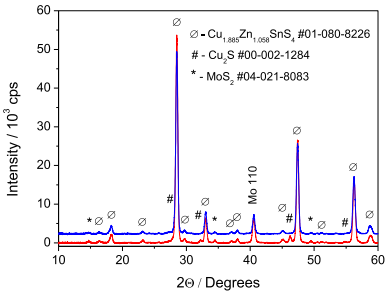

Fig. 6. The XRD patterns of CZTS sample Stoichiometric measured using Cu $K_{\alpha 1,2}$ radiation: lower (red) pattern of as-synthesized, upper (blue) after the treatment in a KCN solution. (For interpretation of the references to color in this figure legend, the reader is referred to the Web version of this article.).

Fig. 6 presents the XRD patterns for the Stoichiometric CZTS sample, for which Raman spectroscopy revealed the lowest quantity of orthorhombic Cu_3SnS_4 (CTS). However, XRD patterns of Zn-rich and Zn-poor samples also did not indicate the presence of this phase, although on the Raman spectra the band of the orthorhombic Cu_3SnS_4 was clearly visible. This could be due to higher sensitivity of Raman spectroscopy for this phase, i.e. the excitation wavelength of 785 nm could be near-resonant for this compound since the second harmonic of the 1st order Raman signal at 321 cm^{-1} is seen at the wavenumber of 642 cm^{-1}. The bands of the orthorhombic Cu_3SnS_4 were not seen on the Raman spectrum of Zn-poor sample when the excitation wavelength of 532 nm was used (Fig. 7). It can be assumed that CTS was formed in a Zn-rich sample as a consequence of the formation of a large amount of

Table 3
FWHM ranges of bands 287 and 338 cm^{-1} for slow cooled and quenched kesterite samples from Ref. [23] and FWHM values for CZTS samples measured in the current work. Excitation wavelength 785 nm. FWHM values in cm^{-1}.

Raman band	Slow cooled CZTS [23]	Quenched CZTS [23]	CZTS Stoichiometric	CZTS Zn-rich	CZTS Zn-poor
287 cm^{-1}	5.9–7.0	14.0–20.2	7.8	7.2	7.4
338 cm^{-1}	3.8–5.5	8.0–9.2	5.5	5.3	5.5

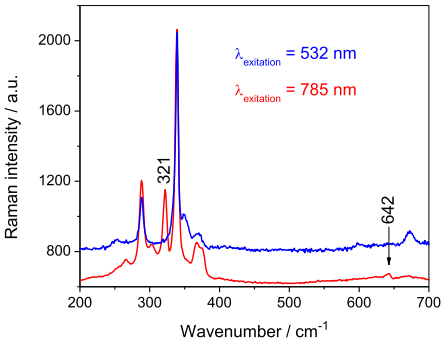

Fig. 7. Raman spectra for the CZTS sample Zn-poor. The upper spectrum – excitation wavelength 532 nm, the lower one – 785 nm.

ZnS in the sample, and the formed ZnS, apparently, did not participate in the formation of kesterite, contributing to the formation of orthorhombic Cu_3SnS_4.

SEM and EDX studies of Stoichiometric and Zn-rich samples supported the results of the XRD and Raman spectroscopy. Fig. 8 depicts the samples SEM images of FIB-made cross-sections and elements depth profiles. The cross-section image of the Stoichiometric CZTS sample evidenced that white colored inclusions of ZnS were distributed in the bulk of the CZTS layer and quantity of the inclusions is larger than in the Zn-rich sample. Furthermore, the ZnS inclusions were located closer to the CZTS layer surface in the latter sample. The depth profiles of Cu, S, Zn, and Sn presented on the Fig. 8 evidenced that white inclusions were ZnS and showed that there was no significant gradient in the distribution of the elements along the direction from the surface to the Mo back contact.

Much more informative and precise are the XRD patterns measured using Cu $K_{\alpha 1}$ radiation. These measurements enabled to determine the quantity of ZnS in the CZTS samples, to extract precise values of kesterite lattice parameters and to assess the disorder level in the kesterite structure. Fig. 9 depicts a fragment of XRD pattern of the Zn-rich CZTS sample. The kesterite XRD peaks 220 and 204 and ZnS (#00-005-0566) peak 220 are well resolved so their 2Θ angle, the integral intensity and FWHM can be measured with sufficient precision. A quantity (in volume %) of ZnS in the samples was calculated using integral intensities of peaks CZTS 220 and ZnS 220. The results obtained are presented in Table 4. It is worth mentioning that the treatment of CZTS films in an HCl solution did not change ZnS quantity determined by XRD which means that ZnS located on the CZTS film surface presented only a very small part of the total ZnS quantity.

Fig. 10 depicts a fragment of the XRD pattern of the Stoichiometric CZTS sample. The pattern presents kesterite peaks 200 and 004. The difference between $2\Theta_{max}$ values at the intensity maximum of the peaks reveals the order/disorder level in the kesterite structure: the difference for ordered Cu-poor Zn-rich

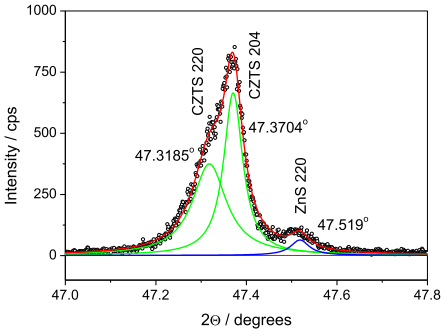

Fig. 9. Fragment of XRD pattern of the Zn-rich CZTS sample, measured in Cu $K_{\alpha 1}$ radiation.

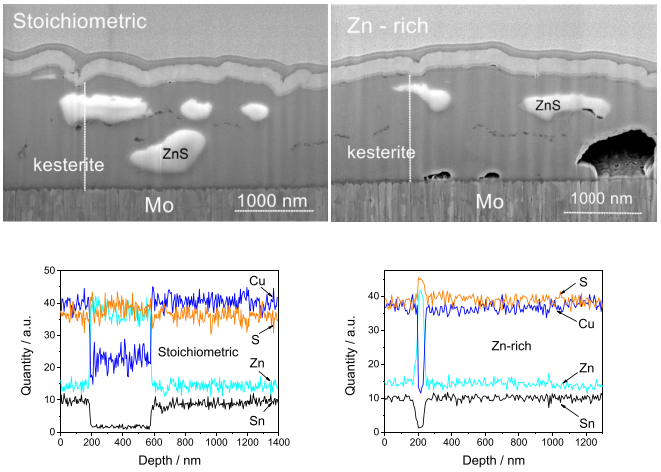

Fig. 8. SEM images of FIB-made cross-sections and the elements depth profiles of Stoichiometric and Zn-rich CZTS samples.

Table 4
Lattice parameters a and c, difference between kesterite XRD peaks 200 and 400, FWHM of the peaks, a crystallite size D_{200} and quantity of ZnS calculated using XRD patterns measured with Cu $K_{\alpha 1}$ radiation.

Sample	a, Å	c, Å	$(2\Theta_{004}\text{-}2\Theta_{200})$	FWHM 200	FWHM 004	D_{200}, nm	ZnS, vol. %
Stoichiometric	5.4288	10.8288	0.089 ± 0.005°	0.0913°	0.0340°	157	13.9
Zn-rich	5.4281	10.8308	0.080 ± 0.004°	0.1187°	0.0327°	107	6.6
Zn-poor	5.4281	10.8319	0.076 ± 0.006°	0.1290°	0.0384°	95	2.3

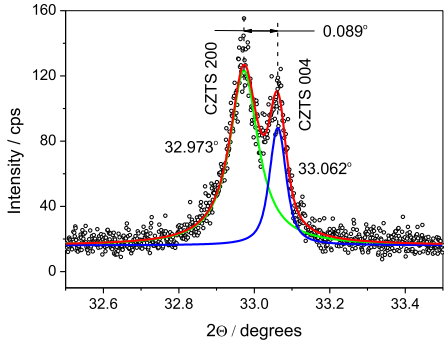

Fig. 10. Fragment of XRD pattern of the Stoichiometric CZTS sample, measured with Cu $K_{\alpha 1}$ radiation.

kesterite with the A-type structure reaches the value of 0.119°, whereas that for disordered Cu-rich Zn-poor kesterite with C-type structure is only 0.061° [9]. The difference between $2\Theta_{max}$ values was measured for all three samples and the results obtained were in the range of 0.076–0.089° (Table 4). These results correspond well to the moderate values of ordering level S similar to those already derived from Raman spectroscopy in the current work.

The kesterite lattice parameters a and c were calculated using $2\Theta_{max}$ values of peaks 200 and 004, respectively. The kesterite lattice parameters of all the studied samples yielded lower values than those characteristic of the stoichiometric or off-stoichiometric Cu-poor kesterite [9]. Comparing the lattice parameters of the samples studied in the current work with the parameters for off-stoichiometric kesterites presented in Ref. [9], we have found that they were best matched to the a and c values of Cu-rich Zn-poor off-stoichiometric kesterite, $Cu_{2.078}Zn_{0.909}Sn_{1.022}S_{4.000}$. The kesterite has about the same value of the difference between 200 and 004 peaks – 0.085°. Such off-stoichiometric C-type kesterite contains $[2Cu_{Zn}^{-} + Sn_{Zn}^{2+}]$ clusters of intrinsic point defects [15], which are very detrimental to the performance of kesterite solar cells.

The crystallites size D_{200} was calculated using the Scherer equation and the FWHM values of the kesterite XRD peak 200. As an instrumental broadening the FWHM value of the LaB_6 peak 110 was subtracted from the FWHM values of the kesterite peak 200. The FWHM values of kesterite peak 004 were of the same magnitude as that of the LaB_6 standard which means D_{004} was larger than 250 nm for all of the studied samples. It is worth noting that for all samples the FWHM values of kesterite peaks with indices h00, hk0 have always been about 2–4 times larger than FWHM of peaks with h0l or 00l indices. This indicates a lower ordering of kesterite structure in the crystallographic directions of <100> and <110> compared to those of <001> and <h0l>. It appears that the crystallites size in directions <100> and <110> could be a rather sensitive parameter for the evaluation of the disorder level in kesterite unlike the averaged crystallite size independent of crystallographic direction.

The comparison of the crystallites size D_{200} with photocurrent density values has shown that Stoichiomeric CZTS sample, which exhibited the largest size of crystallites, revealed the highest j_{ph} and lowest j_{tr} values. The j_{tr} spikes are a result of the recombination at the interface of kesterite/$Eu(NO_3)_3$ solution, therefore samples with larger crystallites and grains are expected to show lower j_{tr} values. This is well consistent with the results we have received, i.e. the lowest spikes were demonstrated by the sample with the largest crystallites and grains (Stoichiometric), whereas the highest in the sample with the poorest crystallinity (Zn-poor). The Stoichiometric CZTS sample also yielded the largest difference between kesterite XRD peaks 200 and 004 but it contained the largest amount of ZnS. A higher value of the difference means a less disordered kesterite structure, i.e. a higher S value. The ZnS inclusions should negatively affect the photovoltaic characteristics of the kesterite solar cell but according to Ref. [30] the inclusions near the surface of the absorber layer, may have a positive effect.

PL spectroscopy is widely used to explore the origin of point defects in a semiconductor material and has been used for kesterites [23,36,37]. Fig. 11 depicts PL spectra for Zn-rich and Stoichiometric CZTS samples measured at room temperature (300K). The approximation of experimental PL spectrum by the Gauss function yielded band maximum energies of 1.40 and 1.42 eV for the Stoichiometric and Zn-rich CZTS samples, respectively. According to Ref. [23], such PL band maxima value at room temperature suggests the band-to-tail (BT) recombination.

Temperature and excitation power-dependent PL band blue shift (Figs. 12 and 13, respectively) also evidenced the presence of BT recombination channel in the Stoichiometric and Zn-rich samples [37]. However, from the Arrhenius analysis (Fig. 14) it followed that an activation energy for the Stoichiometric sample ($E_a = 111 \pm 16$ meV) is significantly higher, as compared to the Zn-rich one ($E_a = 24 \pm 3$ meV). The E_a of about 120 meV is attributable to the acceptor defect formed by Cu_{Zn} antisite point defect while E_a of about 24 meV corresponds to shallow acceptor V_{Cu} [23]. These results are well combined with the chemical composition of the samples: the Stoichiometric sample was more rich in Cu than the Zinc-rich one.

The average depth of potential fluctuation (γ) is proportional to the concentration of ionized donors and acceptors [5]. Analysis of the exponential decay of the low-energy side of PL spectra at 3 K yielded the γ-values of 147 meV and $\gamma = 176$ meV for the Stoichiometric and Zn-rich samples, respectively. The potential fluctuations γ in a stoichiometric single phase kesterite on average is about 50 meV and sometimes even lower [36], though it can be as high as 172 meV [38]. The results of our PL studies are well in line with the results of XRD measurements, according to which our CZTS samples presented a C-type off-stoichiometric kesterite structure with point defects clusters $[2Cu_{Zn}^{-} + Sn_{Zn}^{2+}]$, i.e. ionized donors and acceptors. A lower value of $(2\Theta_{004} - 2\Theta_{200})$ was measured for the Zn-rich sample, indicating a higher disorder and a higher concentration of Cu_{Zn}^{-} defects in this sample compared to the Stoichiometric one. However, a high depth of potential fluctuation

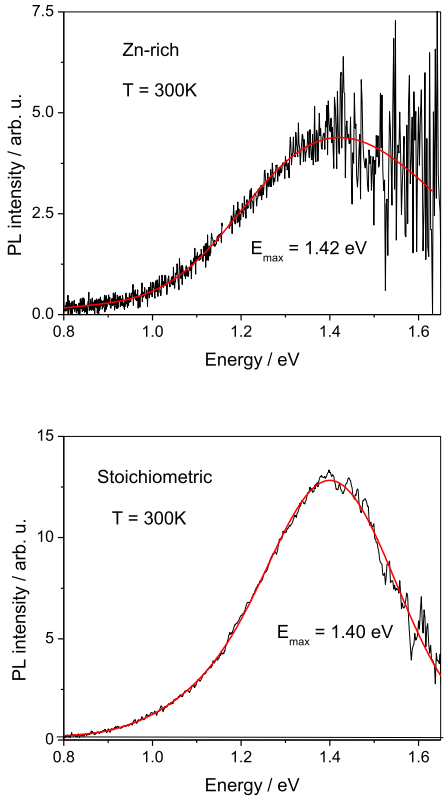

Fig. 11. Room temperature PL spectra for Zn-rich and Stoichiometric CZTS samples. Thicker (red) solid curve – approximation by Gauss function. (For interpretation of the references to color in this figure legend, the reader is referred to the Web version of this article).

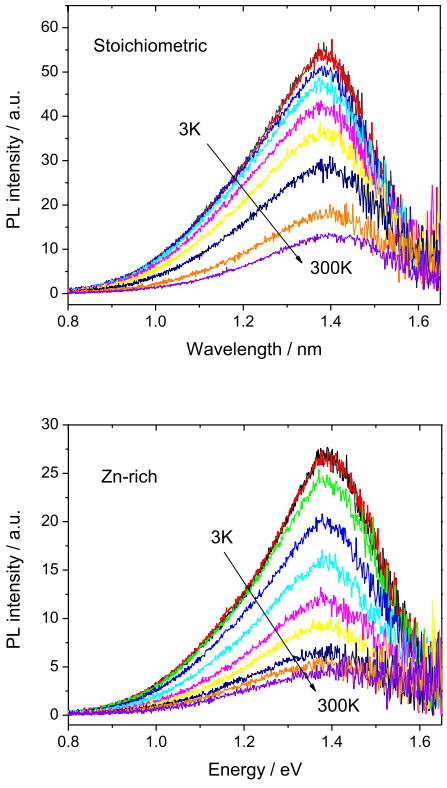

Fig. 12. Temperature dependent PL spectra for Stoichiometric and Zn-rich CZTS samples.

aggravated better understanding of PL processes of the structures studied, as optimal γ values should be < 25 meV for reliable analysis of the PL spectra [36]. This means that samples of higher crystallographic quality and phase purity should be studied to retrieve more plausible information on point defects present in the kesterite.

Summarizing the above one can see that the PEC analysis results correlate much better with those of the XRD studies rather than with the Raman spectroscopy ones. The highest value of j_{ph} and the lowest value of j_{tr} revealed the Stoichiometric CZTS sample. The sample yielded the largest difference between 2Θ positions of kesterite XRD peaks 004 and 200 (0.089°) as well as the largest crystallite size (157 nm), which evidenced the best crystalline structure and the lowest disorder as compared to the Zn-rich and Zn-poor CZTS samples. Nevertheless, Raman spectroscopy confirmed that the Stoichiometric CZTS sample could be an absorber of the highest quality, showing that it had the least amount of Cu_3SnS_4. The XRD and Raman spectroscopy have shown contradictory results in terms of the quantity of ZnS in the samples. This could be a result of a depth, from which the above mentioned methods bring information – the X-rays penetrates into kesterite much deeper than the laser radiation with wavelength of 325 nm.The XRD brings information throughout the entire layer thickness (of about 1500 nm) of the studied CZTS films and from a much larger area (of about 10 mm^2) compared to Raman spectroscopy, which provides information only from a 100 nm-thick layer several square microns in area. The presence of a larger amount of ZnS near the surface of the Zn-rich sample is fully understandable, as this sample had the thickest layer of zinc before the annealing. The results obtained could mean that ZnS in the Stoichiometric CZTS sample was located closer to the Mo substrate or was distributed throughout the entire layer thickness while in the Zn-rich sample ZnS was present closer to the CZTS film surface. These assumptions could be confirmed by the FIB-made cross-section SEM images of Stoichiometric and Zn-rich CZTS films shown in Fig. 8. Well visible white spots of ZnS inclusions (according to EDX) are both at the top of the kesterite layer and deeper in the CZTS film in the case of the Stoichiometric sample, while the ZnS inclusions are located mostly close to the surface in the Zn-rich sample.

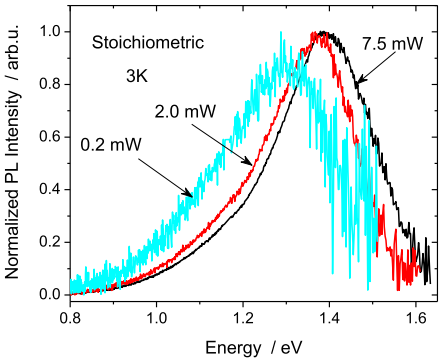

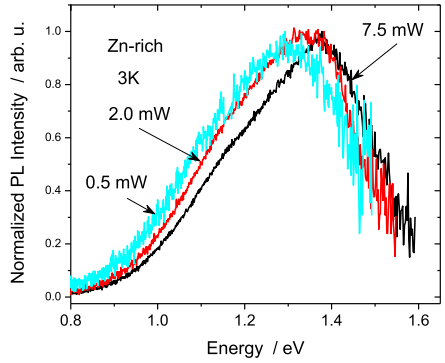

Fig. 13. The excitation power dependent PL spectra for Stoichiometric and Zn-rich CZTS samples.

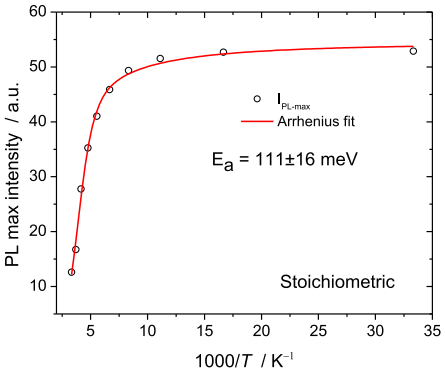

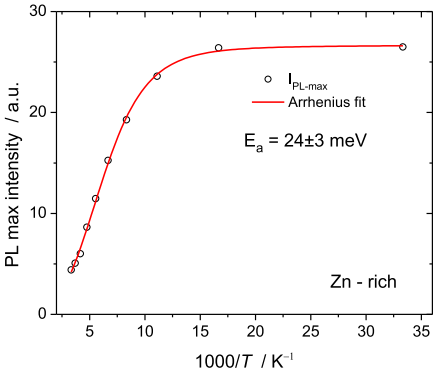

Fig. 14. Arrhenius plots for Stoichiometric and Zn-rich CZTS samples.

PL spectroscopy suggested the band-to-tail recombination and evidenced the presence of the ionized acceptors and donors, which could be point defects clusters $[2Cu_{\overline{Zn}} + Sn^{2}_{Zn}]$ predicted by the XRD results. However, it was not possible to reliably identify the type of point defects due to high values of potential fluctuations (γ) in the studied kesterite samples.

It is possible that the Raman spectroscopy gave less plausible information on the kesterite stoichiometry and the ordering level due to the presence of secondary phases in the samples. The XRD characterizes the structure of namely kesterite and the results are less affected by the presence of secondary phases if at all.

4. Conclusions

The PEC analysis of Zn-rich, nearly stoichiometric and Zn-poor CZTS films has shown that the highest photocurrent density j_{ph} and the smallest spikes (j_{tr}) revealed a nearly stoichiometric CZTS film. This CZTS film exhibited the largest crystallites in [100] direction and the highest ordering level according to the value of the distance between kesterite XRD peaks 200 and 004. This sample contained the smallest amount of the ternary secondary phase Cu_3SnS_4, but, the largest quantity of ZnS. According to XRD data, off-stoichiometric kesterite $Cu_{2.078}Zn_{0.909}Sn_{1.022}S_{4.000}$ was formed in every sample, irrespective of Zn/Sn ratio in the film.

The values of Q and Q′ parameters predicted kesterite of different stoichiometry as well as point defects of different types. We assume the XRD methods using Cu $K_{\alpha 1}$ radiation revealed more plausible information both on the kesterite stoichiometry and the point defects than Raman spectroscopy, at least under conditions employed in the work. Further experiments are needed to get more reliable and quantitative information on the order level in the kesterite using the above XRD approach.

CRediT author statement

Audrius Drabavičius: Conceptualization, Formal analysis, Investigation, Writing - original draft, Writing - review & editing, Visualization. **Arnas Naujokaitis**: Formal analysis, Investigation. **Giedrius Stalnionis**: Formal analysis, Validation. **Raimondas Giraitis**: Investigation, Methodology. **Zenius Mockus**: Investigation, Resources, Formal analysis, Data curation. **Stasė Kanapeckaitė**: Validation, Investigation. **Putinas Kalinauskas**: Investigation, Validation. **Ramūnas Nedzinskas**: Investigation, Validation, Data curation. **Gediminas Niaura**: Validation, Investigation, Data

curation. **Remigijus Juškėnas**: Supervision, Project administration, Conceptualization, Writing - review & editing, Formal analysis.

Declaration of competing interest

The authors declare that they have no known competing financial interests or personal relationships that could have appeared to influence the work reported in this paper.

References

[1] Wei Wang, Mark T. Winkler, Oki Gunawan, Tayfun Gokmen, Teodor K. Todorov, Yu Zhu, David B. Mitzi, Device characteristics of CZTSSe thin-film solar cells with 12.6% efficiency, Adv. Energy Mater. 4 (2014) 1301465.

[2] Hui-Seon Kim, Anders Hagfeldt, Nam-Gyu Park, Morphological and compositional progress in halide perovskite solar cells Chem, Commun. Now. 55 (2019) 1192–1200.

[3] Jyh-Lih Wu, Yoshiaki Hirai, Takuya Kato, Takuya Kato, Veronica Bermudez, Record efficiency for thin-film polycrystalline solar cells up to 22.9% achieved by Cs-treated Cu(in,Ga)(Se,S)$_2$, IEEE J. Photovolt. 9 (1) (2018) 325–330.

[4] Stéphane Bourdais, Christophe Choné, Delatouche Bruno, Alain Jacob, Gerardo Larramona, Camille Moisan, Alain Lafond, Fabrice Donatini, Germain Rey, Susanne Siebentritt, Aron Walsh, Gilles Dennler, Is the Cu/Zn disorder the main culprit for the voltage deficit in kesterite solar cells? Adv. Energy Mater. 6 (2016) 1502276.

[5] G. Rey, G. Larramona, S. Bourdais, C. Choné, B. Delatouche, A. Jacob, G. Dennler, S. Siebentritt, On the origin of band-tails in kesterite, Sol. Energy Mater. Sol. Cells 179 (2018) 142–151.

[6] Shoushuai Gao, Yi Zhang, Jianping Ao, Xiuling Li, Shuang Qiao, Ying Wang, Shuping Lin, Zhaojing Zhang, Dongxiao Wang, Zhiqiang Zhou, Guozhong Sun, Shufang Wang, Yun Sun, Insight into the role of post-annealing in air for high efficient $Cu_2ZnSn(S,Se)_4$ solar cells, Sol. Energy Mater. Sol. Cells 182 (2018) 228–236.

[7] SeongYeon Kim, JunHo Kim, R. Tanka, Rana, Kang-Woo Kim, Myeung-Hoi Kwon. Characterization of CBO and defect states of CZTSe solar cells prepared by using two-step process, Curr. Appl. Phys. 18 (2018) 191–199.

[8] Maykel Courel, A. Arce-Plaza, D.O. Oseguera-Galindo, O. Vigil-Galán, The path to improve kesterite solar cell efficiency, Gen. Chem. 4 (2018) 180015.

[9] Alain Lafond, Léo Choubrac, Catherine Guillot-Deudon, Philippe Deniard, Stephane Jobic, Crystal structures of photovoltaic chalcogenides, an intricate puzzle to solve: the cases of CIGSe and CZTS materials, Z. Anorg. Allg. Chem. 638 (15) (2012) 2571–2577.

[10] Shiyou Chen, X.G. Gong, Aron Walsh, Su-Huai Wei, Crystal and electronic band structure of Cu_2ZnSnX_4 (X=S and Se) photovoltaic absorbers: first-principles insights, Appl. Phys. Lett. 94 (2009), 041903.

[11] Léo Choubrac, Michae Paris, Alain Lafond, Catherine Guillot-Deudon, Xavier Rocquefelte, Stéphane Jobic, Multinuclear (^{67}Zn, ^{119}Sn and ^{65}Cu) NMR spectroscopy – an ideal technique to probe the cationic ordering in Cu_2ZnSnS_4 photovoltaic materials, Phys. Chem. Chem. Phys. 15 (2013) 10722–10725.

[12] S. Schorr, The crystal structure of kesterite type compounds: a neutron and X-ray diffraction study, Sol. Energy Mater. Sol. Cells 95 (6) (2011) 1482–1488.

[13] R. Caballero, E. Garcia-Llamas, J.M. Merino, M. Leon, I. Babichuk, V. Dzhagan, V. Strelchuk, M. Valakh, Non-stoichiometry effect and disorder in Cu_2ZnSnS_4 thin films obtained by flash evaporation: Raman scattering investigation, Acta Mater. 65 (2014) 412–417.

[14] Katharina Rudisch, Yi Ren, Charlotte Platzer-Björkman, Jonathan Scragg, Order-disorder transition in B-type Cu_2ZnSnS_4 and limitations of ordering through thermal treatments, Appl. Phys. Lett. 108 (2016) 231902.

[15] Laura Elisa Valle Rios, Kai Neldner, Galina Gurieva, Susan Schorr, Existence of off-stoichiometric single phase kesterite, J. Alloy. Comp. 657 (2016) 408–413.

[16] B.G. Mendis, M.D. Shannon, M.C.J. Goodman, J.D. Major, R. Claridge, D.P. Halliday, K. Durose, Direct observation of Cu, Zn cation disorder in Cu_2ZnSnS_4 solar cell absorber material using aberration corrected scanning transmission electron microscopy, Prog. Photovolt. Res. Appl. 22 (2014) 24–34.

[17] Jonathan J.S. Scragg, Léo Choubrac, Alain Lafond, Tove Ericson, Charlotte Platzer-Björkman, A low-temperature order-disorder transition in Cu_2ZnSnS_4 thin films Appl, Phys. Lett. 104 (2014), 041911.

[18] Michaël Paris, Leo Choubrac, Alain Lafond, Catherine Guillot-Deudon, Stéphane Jobic, Solid-state NMR and Raman spectroscopy to address the local structure of defects and the tricky issue of the Cu/Zn disorder in Cu-poor, Zn-rich CZTS materials, Inorg. Chem. 53 (2014) 8646–8653.

[19] S. Exarhos, E. Palmes, L. Mangolini, Structural homogenization and cation ordering in CZTS films during sulfurization as probed via in-situ Raman, Thin Solid Films 684 (2019) 21–30.

[20] I.S. Babichuk, M.O. Semenenko, S. Golovynskyi, R. Caballero, O.I. Datsenko, I.V. Babichuk, Ji Li, Guiwen Xu, Ran Qiu, Chun Huang, Rui Hu, I. Golovynska, V. Ganus, Baikui Li, Junle Qu, M. Leon, Control of secondary phases and disorder degree in Cu_2ZnSnS_4 films by sulfurization at varied subatmospheric pressures, Sol. Energy Mater. Sol. Cells 200 (2019) 109915.

[21] Daniel M. Többens, Galina Gurieva, Sergiu Levcenko, Thomas Unold, Susan Schorr, Temperature dependency of Cu/Zn ordering in CZTSe kesterites determined by anomalous diffraction, Phys. Status Solidi B 253 (10) (2016) 1890–1897.

[22] A. Ritscher, M. Hoelzel, M. Lerch, The order-disorder transition in Cu_2ZnSnS_4 – a neutron scattering investigation, J. Solid State Chem. 238 (2016) 68–73.

[23] L. Van Puyvelde, J. Lauwaert, P.F. Smet, S. Khelifi, T. Ericson, J.J. Scragg, D. Poelman, R. Van Deun, C. Platzer-Björkman, H. Vrielinck, Photoluminescence investigation of Cu_2ZnSnS_4 thin film solar cells, Thin Solid Films 582 (2015) 146–150.

[24] B. Unveroglu, G. Zangari, Photoelectrochemical behavior of bismuth-containing Cu_2ZnSnS_4 (CZTS) absorber layers for photovoltaic applications, J. Electrochem. Soc. 166 (5) (2019) H3040–H3046.

[25] R. Juškėnas, G. Niaura, Z. Mockus, S. Kanapeckaitė, R. Giraitis, R. Kondrotas, A. Naujokaitis, G. Stalnionis, V. Pakštas, V. Karpavičienė, XRD studies of an electrochemically co-deposited Cu–Zn–Sn precursor and formation of a $Cu_2ZnSnSe_4$ absorber for thin-film solar cells, J. Alloy. Comp. 655 (2016) 281–289.

[26] M.I. Khalil, O. Atici, A. Lucotti, S. Binetti, A. Le Donne, L. Magagnin, CZTS absorber layer for thin film solar cells from electrodeposited metallic stacked precursors (Zn/Cu-Sn), Appl. Surf. Sci. 379 (2016) 91–97.

[27] R. Juškėnas, Z. Mockus, R. Giraitis, A. Selskis, G. Stalnionis, S. Kanapeckaitė, A. Drabavičius, P. Kalinauskas, G. Niaura, Structural and photoelectrochemical characterization of Cu_2SnSe_3 thin films fabricated by electrochemical co-deposition and selenization, J. Alloy. Comp. 767 (2018) 345–352.

[28] P. Kalinauskas, E. Norkus, Z. Mockus, R. Giraitis, R. Juškėnas, Electrochemical and photoelectrochemical characterization of Cu_2SnSe_3 thin films deposited on Mo/glass substrates, J. Electrochem. Soc. 166 (5) (2019) H3107–H3111.

[29] Andrew Fairbrother, Eric García-Hemme, Victor Izquierdo-Roca, Xavier Fontané, A. Fabián, Pulgarín-Agudelo, Osvaldo Vigil-Galán, Alejandro Pérez-Rodríguez, Edgardo Saucedo, Development of a selective chemical etch to improve the conversion efficiency of Zn-rich Cu_2ZnSnS_4 solar cells, J. Am. Chem. Soc. 134 (2012) 8018–8021.

[30] Diego Colombara, Crossay Alexandre, David Regesch, Cedric Broussillou, Thomas Goislard de Monsabert, Pierre-Philippe Grand, J. Phillip, Dale, Prediction of photovoltaic p–n device short circuit current by photoelectrochemical analysis of p-type CIGSe films, Electrochem. Commun. 48 (2014) 99–102.

[31] Néstor Guijarro, Mathieu S. Prévot, Xavier A. Jeanbourquin, Xiaoyun Yu, Sivula Kevin, Autodecomposition approach for the low-temperature mesostructuring of nanocrystal semiconductor electrodes, Chem. Mater. 27 (2015) 6337–6344.

[32] Wei Li, Jian Chen, Yan Chang, Xiaojing Hao, The effect of ZnS segregation on Zn-rich CZTS thin film solar cells, J. Alloy. Comp. 632 (2015) 178–184.

[33] Jonathan J.S. Scragg, Jes K. Larsen, Mukesh Kumar, Clas Persson, Jan Sendler, Susanne Siebentritt, Charlotte Platzer Björkman, Cu–Zn disorder and band gap fluctuations in $Cu_2ZnSn(S,Se)_4$: theoretical and experimental investigations, Phys. Status Solidi B 253 (2016) 247–254.

[34] M. Dimitrievska, A. Fairbrother, X. Fontane, T. Jawhari, V. Izquierdo-Roca, E. Saucedo, A. Pérez-Rodríguez, Multiwavelength excitation Raman scattering study of polycrystalline kesterite Cu_2ZnSnS_4 thin films, Appl. Phys. Lett. 104 (2014), 021901.

[35] M. Dimitrievska, H. Xie, A.J. Jackson, X. Fontané, M. Espindola-Rodriguez, E. Saucedo, A. Pérez-Rodriguez, A. Walsh, V. Izquierdo-Roca, Resonant Raman scattering of ZnS_xSe_{1-x} solid solutions: the role of S and Se electronic states, Phys. Chem. Chem. Phys. 18 (2016) 7632–7640.

[36] J. Krustok, T. Raadik, M. Grossberg, M. Kauk-Kuusik, V. Trifiletti, S. Binetti, Photoluminescence study of deep donor- deep acceptor pairs in Cu2ZnSnS4, Mater. Mat. Sci. Semicond. Proc. 80 (2018) 52–55.

[37] KunihikoTanaka, Tomokazu Shinji, HisaoUchiki, Photoluminescence from Cu2ZnSnS4 thin films with different compositions fabricated by a sputtering-sulfurization method, Sol. Energy Mater. Sol. Cells 126 (2014) 143–148.

[38] J.P. Leitão, N.M. Santos, P.A. Fernandes, P.M.P. Salomé, A.F. da Cunha, J.C. González, G.M. Ribeiro, F.M. Matinaga, Phys. Rev. B 84 (2011), 024120.

Vilnius University Press
9 Saulėtekio Ave., Building III, LT-10222 Vilnius
Email: info@leidykla.vu.lt, www.leidykla.vu.lt
Print run copies 17